N° d'ordre :

RÉPUBLIQUE ALGÉRIÈNNE DÉMOCRATIQUE & POPULAIRE

MINISTÈRE DE L'ENSEIGNEMENT SUPERIEUR & DE LA RECHERCHE SCIENTIFIQUE

UNIVERSITÉ DJILLALI LIABÈS
FACULTÉ DES SCIENCES EXACTES
SIDI BEL ABBÈS

THÈSE
DE DOCTORAT

Présentée par : DJERMOUNI Mostefa

Spécialité : Physique

Option : Sciences et Génie des Matériaux

Intitulée

Electronic Structure and Magnetic Properties in Perovskite-Related Materials

Soutenue le 09/06/2015
Devant le jury composé de :

Président :
TADJER Abdelkader — Prof. (U. Sidi Bel Abbès, Algeria)

Examinateurs :
AOURAG Hafid — Prof. (U. Tlemcen, Algérie)
HAYN Roland — Prof. (U. Aix-Marseille, France)
BEJAR Moez — Prof. (U. Monastir, Tunisie)
BOUKORTT Abdelkader — Prof. (U. Mostaganem, Algérie)

Directeur de thèse :
ZAOUI Ali — Prof. (U. Sidi Bel Abbès, Algérie)

Electronic structure and magnetic properties of prerovskite-related materials

Mostefa DJERMOUNI

University Djilalli Liabes of Sidi Bel-Abbes

This dissertation is submitted for the degree of

Doctor of Science

Supervisor: Pr. Ali ZAOUI

June 2015

Graduation committee

- **Chairman:** Prof. Abdelkader TADJER (University of Sidi Bel-Abbes)
- **Examinator:** Prof. Hafid AOURAG (University of Tlemcen)
- **Examinator:** Prof. Roland HAYN (University of d'Aix Marseille)
- **Examinator:** Prof. Moez BEJAR (University of Monastir, Tunisia)
- **Examinator:** Prof. Abdelkader BOUKORTT (University of Mostaganem)
- **Supervisor:** Prof. Ali ZAOUI (University of Sidi Bel-Abbes)

Day of the defense: Friday 5^{th} June, 2015

This thesis is dedicated to

My parents,

who have always loved me unconditionally and whose good examples have taught me to work hard for the things that I aspire to achieve.

My wife,

who has been a constant source of support and encouragement during the challenges of life. I am truly thankful for having you in my life.

My brothers and sisters,

There is no such thing as fun for the whole family.

Acknowledgements

First and foremost, praises and thanks to the God, the Almighty, for His showers of blessings throughout my research work to complete the research successfully.
I would like to express my deep and sincere gratitude to my research supervisor, Prof. Ali ZAOUI, Director of Computational Material Physics Laboratory (LPCM) where I carried out my research, all my thanks for the patient guidance, encouragement and advice he has provided throughout my time as his student. I have been extremely lucky to have a supervisor who cared so much not only about my work but about myself also, and who responded to my questions and queries so promptly. I thank you also for giving me the freedom of choose in my research, with an appreciable confidence in my work. I would also like to thank him for his friendship, empathy, and great sense of humor. I am extending my heartfelt thanks to his family for their acceptance and patience during the discussion I had with him on research work and thesis preparation.
Besides my supervisor, I would like to thank Prof. Roland HAYN, Professor at Aix-Marseille university, France, and committee member in my thesis, thank you for his encouragement and insightful comments and questions. I also want to thank the rest of my thesis committee for taking the time to review this work: Prof. Abdelkader TADJER from university of Sidi Bel-Abbes, Algeria "Chairman of thesis committee"; Prof. Hafid AOURAG, Professor at University of Tlemcen, Algeria; Prof. Moez BEJAR from university of Monastir, Tunisia ; Prof. Abdelkader BOUKORTT from university of Mostaganem, Algeria.
I would also like to thank Dr. Belkacem BENSEDDIK, Dr. Youcef CHERCHAB and Mr. Hmida HADROUG, for their helpful assistance in linguistic correction of this thesis.
A very special thanks goes out to my friends and research colleagues in LPCM, in particular Abbes HALLOUCHE and Ameur DAHANI, for lending me a helping hand, whenever and wherever needed.
My sincere thanks also go to my family for the support they provided me through my entire life and in particular, I must acknowledge my parents and best friend, Nasreddine, without whose love, encouragement and editing assistance, I would not have finished this thesis.

Finally, without the support of my wife I would never have succeeded. I must to thank her for her continued support, encouragement, quiet patience and unwavering love.

Abstract

This thesis deals with interconnections between composition, structure and properties, in materials like perovskites and alloys. Our investigation has been based on the bulk materials such as $SrTiO_3$, $LaCoO_3$, $BiCoO_3$, and inverse perovskites $R\mathrm{Rh}_3\mathrm{C}$. We have presented a theoretical study of selected solids using *ab* inition methods based on the density functional theory (DFT).
This thesis is subdivided into three major works. The first work is entitled "Defect in Perovskite: $SrTiO_{3-x}$", the second work is entitled "Perovskite alloy: $Bi_{1x}La_xCoO_3$" and the third work is entitled "Anti Perovskites : RRh3C". The main results of the thesis are:

- In the first work, we have performed a detailed investigation of the structural and electronic properties of single and double oxygen vacancy defects in bulk $SrTiO_3$ using first principles LDA method. Removal of one oxygen atom from the lattice reduces two Ti^{4+} to Ti^{3+} and replaces two octahedra with two square-pyramids. The similarity of t_{2g} orbitals (xy, xz, yz) in the defect wavefunction of all Ti atoms of the supercell confirms the existence of an ionic conductivity in the $SrTiO_{3x}$. However, the contribution of deep e_g ($3z^2 - r^2$) in defect wavefunction confirms the electronic conductivity. $SrTiO_3$ is thus considered a mixed electronic-ionic conductor.

- In the second work, using the first-principles DFT method and LSDA+U calculations, we have performed a detailed investigation on the structural and magnetic ground states of strongly correlated perovskites, $BiCoO_3$, $LaCoO_3$ and their alloys $Bi_{1-x}La_xCoO_3$.
  We have found that the structural stability of this alloy between tetragonal-AFM-C and rhombohedral-NM undergoes a strongly discontinuous transition between a Tetragonal-phase and a Rhombohedral-phase at $x \simeq 0.345$, this structural transition is associated with a spin state transition from HS magnetic state to LS nonmagnetic state.

- In the last work, we have performed the first-principles DFT calculations for intermetallic antiperovskites (inverse perovskites) $R\mathrm{Rh_3C}$ (R = rare earth: La-Gd) compounds.
  From the calculated band structures, densities of states and valence charge densities, the hybridization between $d - t_{2g}$ of Rh ion and $p - p_x, p_y$ of C atom creates a covalent bonding. Also, the d orbital (electron) of Rh creates the Rh-C bonding with C atom, and other electrons participate to metallic bonding with rare earth atoms. This particular result is absent in the conventional perovskites materials which make the properties of antiperovskites different.

Keywords: density functional theory, electronic structure, LSDA+U, perovskite structure, phase transition, structural stability, magnetic structure.

Résumé

Cette thèse étude la relation entre la composition, la structure et les propriétés, dans les matériaux pérovskites et leurs alliages. Notre recherche a été basée sur les composés pérovskites parents $SrTiO_3$, $LaCoO_3$, $BiCoO_3$ et les pérovskites inverse $R\mathrm{Rh}_3\mathrm{C}$ (R: Terre rare).
Nous avons présenté une étude théorique sur les matériaux solides choisis à l'aide d'une méthode *ab initio* basée sur la théorie de la fonctionnelle de la densité (DFT).
Cette thèse est subdivisée en trois travaux majeurs. Le premier travail est intitulé "Les défauts dans les pérovskites: $SrTiO_{3-x}$"; le second travail est intitulé "L'alliage pérovskite: $Bi_{1-x}La_xCoO_3$"; et le troisième travail est intitulé "Anti-pérovskites: $R\mathrm{Rh}_3\mathrm{C}$".
Les principaux résultats de la thèse sont:

- Dans la première investigation, nous avons effectué une étude détaillée de propriétés structurales et électroniques du composé en bulk $SrTiO_3$; ainsi que les propriétés de défauts lacunaires monoatomique et diatomique du $SrTiO_{3-x}$ en utilisant la méthode de premier principe LDA. La suppression d'un atome d'oxygène dans la maille conventionnelle fait réduire la valence de titane du Ti^{4+} à Ti^{3+} et remplace deux octaèdres avec deux pyramides carrés. La similarité des orbitales $t_{2g}(xy, xz, yz)$ de la fonction d'onde du défaut avec tous les atomes de Ti dans la supercellule confirme l'existence d'une conductivité ionique dans le $SrTiO_{3-x}$. Cependant, la contribution des états profonds $e_g(3z^2 - r^2)$ dans la fonction d'onde du défaut confirme la conductivité électronique. Le $SrTiO_{3-x}$ est donc considéré comme étant un conducteur mixte "électronique-ionique".

- Dans le second travail, en utilisant la méthode de premier principe DFT et le calcul LSDA+U, nous avons effectué une investigation approfondie de l'état fondamental structurale et magnétique des pérovskites fortement corrélés $BiCoO_3$, $LaCoO_3$ et leurs alliages $Bi_{1-x}La_xCoO_3$.
  Dans la stabilité structurale de l'alliage, nous avons trouvé une transition fortement discontinue entre la phase quadratique et la phase rhomboédrique à $x = 0,345$.

Cette transition structurale est associée à une transition magnétique de l'état magnétique HS à l'état non-magnétique LS.

- Dans le dernier travail, nous avons effectué un calcul DFT pour des composés intermétalliques anti-pérovskites (perovskites inverses) $R\mathrm{Rh_3C}$ (R = terre rare: La-Gd).
  A travers le calcul de la structure de bande, la densité d'états et la densité de charge de valence, nous avons trouvé qu'une liaison covalente a été crée par l'hybridation entre l'orbitale t_{2g} de l'atome Rh et les états $p - px, py$ du carbon. En outre, l'orbitale d de Rh (electron) créé avec l'atome C une liaison covalente Rh-C et les autre électrons de cette orbitale participent à la liaison métallique avec les atomes de terre rares. Ce caractère particulier est absent dans les pérovskites conventionnelles, ce qui rend les propriétés des anti-pérovskites différentes.

Mots-clés: Théorie de la fonctionnelle de la densité, structure électronique, LSDA+U, structure pérovskite, transition de phase, stabilité structurale, structure magnétique.

List of Publications

Publications related to the Thesis

- **M. Djermouni**, A. Zaoui , S. Kacimi, B. Bouhafs, "Vacancy defects in strontium titanate: Ab initio calculation", Computational Materials Science **49** 904–909 (2010).

- **M. Djermouni**, S. Kacimi and A. Zaoui, " Electronic and magnetic structure of carbides $R\mathrm{Rh_3C}$", Phys. Status Solidi B, **248**, 8, 1925-1932 (2011).

Other publications

- F. Zazoua, S. Kacimi, **M. Djermouni** and A. Zaoui, " Ab initio full-potential study of mechanical properties and magnetic phase stability of rare earth diboride compounds", J. Appl. Phys. **110**, 014908 (2011).

- **M. Djermouni**, M. Belhadj, S. Kacimi and A. Zaoui, " Ab-initio study of electronic and magnetic structure of intermetallic $\mathrm{RE_5Ge_3}$ compounds", Modern Physical Letter B, **25**, 32 (2011).

- W. Hasni, A. Boukortt, B. Bekkouche, S. Kacimi, **M. Djermouni** and A. Zaoui, " B-cation effect in electronic structure and magnetic properties of $\mathrm{Ce}B\mathrm{O_3}$ ($B =$ Ga, In) compounds from first principles study", Physica B: Condensed Mater, **407**, 901–906 (2012).

- S. Kacimi, A. Boukortt, B. Bekkouche, F. Zazoua, **M. Djermouni** and A. Zaoui, " Magnetic structure and bonding of rare-earth diboride compounds $\mathrm{RB_2}$: First-principles calculations", Phys. Status Solidi B, **249**, 7, 1470–1476 (2012).

- H. Mehnane, B. Bekkouche, S. Kacimi, A Hallouche, **M. Djermouni** and A. Zaoui, " First-principles study of new half Heusler for optoelectronic applications", Superlattices and Microstructures, **51**, 772 (2012).

- A. Mir, B. Bekkouche, A. Boukortt, S. Kacimi, **M. Djermouni** and A. Zaoui, " Enhancement of Ferromagnetic Ordering Curie Temperature in N-Doped MgO under Hydrostatic Pressure", Modeling and Numerical Simulation of Material Science, **2**, 37-42 (2012).

- D. Mekam, S. Kacimi, **M. Djermouni**, M. Azzouz and A. Zaoui, " Ab-initio calculations on RE–TM–O_3 perovskites: A comparative study of cation effect", Results in physics, **2**, 156-163 (2012).

- M. Moussa, **M. Djermouni**, S. Kacimi, M. Azzouz, A. Dahani and A. Zaoui, " First-principles calculations of structural, magnetic phase stability and electronic properties of RVO_4 compounds", Computational Materials Science, **68**, 361-366 (2013).

- S. Kacimi, D. Mekam, **M. Djermouni**, M. Azzouz, A. Hallouche and A. Zaoui, " Electronic structure and magnetism in ternary gadolinium-based cubic inverse perovskites", Materials Science semiconductor processing, **26**, 1971-1976 (2013).

- S. Abbaoui, A. Zaoui, S. Kacimi, **M. Djermouni** and M. Bououdina, " Theoretical investigation of the magnetic ordering and the superconducting state in rare earth iron pnictides", Int. J. Comp. Mat. Sci. Eng. **03**, 1450020 (2014).

- N. Benayad, **M. Djermouni** and A. Zaoui, " Electronic structure of new superconductor $La_{0.5}Th_{0.5}OBiS_2$: DFT study", Computational Condensed Matter **1**, 19-25 (2014).

- A. Benidris, A. Zaoui, M. Belhadj, **M. Djermouni** and S. Kacimi, " Structure and Magnetic Properties of $RESn_3$ Compounds: GGA+U Calculations", Journal of Superconductivity and Novel Magnetism DOI: 10.1007/s10948-015-3016-7, (2015).

Table of contents

List of figures

List of tables

Chapter 1

Introduction

Since its theoretical foundation in the mid-1960's [13, 14], Density Functional Theory (DFT) is being used in computational solid state physics to calculate structural, magnetic and ground state properties of real materials from first principle[1].
In this thesis we will use Density Functional Theory to study different perovskites materials. A short introduction for each subject is given here, a more elaborated one at the beginning of the respective chapters.
The first study is devoted to oxygen vacancies in $SrTiO_3$ with different concentrations by means of first-principles simulations. These types of point defect represent very common imperfections in ABO_3-type perovskite oxides diversifying their chemistry and leading to a broad range of possible technological applications.
Our first step was to examine basic properties of perfect $SrTiO_3$ crystals. Afford significant insight into the electronic properties and chemical bonding of $SrTiO_3$ and give several predictions about the perfect $SrTiO_3$, we have examined these properties, especially around the Fermi level, to clarify the picture of this system in the non-stoichiometric cases.
We also investigated the electronic structure and nature of bonding around the oxygen vacancies in the next step. We have used a supercell model to calculate the band structure, the incorporation of one or two oxygen vacancies in supercell gives rise to variety of unique density of state functions depending on the distribution of defects in the supercell. Metallic behavior is thus predicted in every case.
$SrTiO_3$ is one of the simplest perovskite, it's a perfect ionic perovskite due to total filled shell (this so called d^0 perovskites).

[1]Reference text: Veerle Vanhoof's thesis, "Density Functional Theory Studies for Transition Metals: Small (Fe,Co)-clusters in fcc Ag, and the Spin Density Wave in bcc Chromium.", Katholieke university Leuven (2006).

When we substitute the alkali metal (A-cation) with a large size atom such as rare earths; and so, the B-cation by a magnetic atom such as transition metals, the situation becomes complicated, and these complicated properties reveal to an exciting phenomena.
In our second study, we have investigated strongly correlated materials, $BiCoO_3$ and $LaCoO_3$, where we have encountered new effects in perovskites.
In this part, we seek the origin of the giant tetragonal FE distortion in the ambient phase of $BiCoO_3$ and identify the nature of the La-substitution-induced spin-state transition, using local density approximation plus Hubbard U (LSDA+U) calculations. Our results show that the structural stability of this alloy between tetragonal-AFM-C and rhombohedral-NM undergoes a strongly discontinuous transition between a Tetragonal-phase and a Rhombohedral-phase at $x \simeq 0.345$, this structural transition is associated with a spin state transition from HS magnetic state to LS nonmagnetic state, these transitions are mainly due to the changes in different effects such as, crystal field, Jahn-Teller, and *lone pair* effects.
On the other hand, BO_6 cluster plays a crucial role in perovskites, a change in this environment structure, making the material totally different. One of these cases the so-called inverse perovskite (anti-perovskite).
Intermetallic antiperovskites closely related to $MgCNi_3$ are therefore subject to investigations, both in the search for new superconductors and in the pursuit of a better understanding of the interplay between superconductivity and magnetism. It was suggested that carbon-containing antiperovskites may be good candidates.
Systematic investigation of the synthesis and fundamental properties of nonoxide perovskite-type compounds is necessary. The ternary carbides of rare-earth metal R-Rh-C system have also received considerable attention in the superconductivity and magnetism field. So, most interest is limited to the synthesization and structural analysis and the absence in the literature of any information about the *ab*-initio electronic and magnetic structure of these compounds has led us to study these new materials. And for comparison with Ref. [12], the magnetic stability of $R\mathrm{Rh_3C}$ compounds for R = La, Ce, Pr, Nd, Pm, Sm, Eu, and Gd is studied.
Otherwise, the choice of the method used in this thesis is based on some basis. The "homogeneous electron gas" *ansatz* fails if one wants to describe strongly correlated perovskites, e.g. consider transition metal oxides as $LaCoO_3$, or $BiCoO_3$. In those compounds a strong coulomb repulsion in the incompletely screened d states exists, which is neither included in LSDA nor in GGA. Thence a metallic behaviour is obtained, while experiments verify Mott insulators. The inclusion of local Coulomb repulsion remedies this discrepancy between theory and experiment. This method is known as the

LSDA+U approach. This method, however, is strongly dependents on the choice of the interaction parameters which sometimes have been evaluated using *ab*-initio (constrained) calculations. Anyway, no general procedure is well established to calculate these effective interaction parameters entering the theory and this situation is also reflected in the LSDA+U-like approaches. In fact, the few method which have been proposed to extract the effective electronic interactions from first principle (constrained) calculations [15], did not give very reliable results, so that their value is usually determined by seeking a good agreement of the calculated properties with the experimental results in a semiempirical way.

This thesis is organized as follows:

Firstly, in chapter 2 some definitions and notations of crystallography are outlined. The aim here is to introduce the models used for the study of the bulk of the materials investigated during this thesis.

Chapter 3 is divided in two principle sections. In the first section we outline the basic foundations of the ground-state density functional theory. We introduce the Hohenberg-Kohn theorem and the Kohn-Sham equations and finally we describe superficially the main approximations for the exchange-correlation functional. In the second section we highlight in detail the main computational method FP-LAWP+*lo* used in our simulations and the numerical parameters used during the whole thesis.

In chapter 4 a current knowledge of material perovskites properties is briefly presented.

Chapter 5 shows a detail investigation of the electronic structure and nature of bonding around the oxygen vacancies in $SrTiO_3$.

Chapter 6 is divided in three parts; at first, we have Studied in detail the electronic structure and magnetic stability of each parent ($BiCoO_3$ and $LaCoO_3$). Secondly, we have compared both materials in both structures (tetragonal and rhombohedric). Finally, we have carried out a detailed study about $Bi_{1-x}La_xCoO_3$ alloy in both structures, in order to identify a magneto-structural transition.

In the end, chapter 7 presents the results of a systematic study by means of the full-potential linearized augmented planewave (FLAPW) method of newly synthesized non-oxide antiperovskites RRh$_3$C (R = rare earth: La-Gd) and discuss the trends in their structural, electronic and magnetic properties depending on the rare earth cations.

Chapter 2

Backgrounds

2.1 Crystalline Solids

In the first part of this chapter[1], some definitions and notations of crystallography are outlined. The aim here is to introduce the models used for the study of the bulk of the materials investigated during this thesis. It should be noted that this discussion is limited to crystalline solids.

2.1.1 Crystal Lattices

A crystal lattice is a mathematical concept, which can be described as an infinite pattern of points, each of which has the same surroundings in the same orientation. In 3-dimensions, if any lattice point is chosen to be the origin, the position of any other lattice point can be defined by the vector $\vec{T}$ such that:

$$\vec{T} = m\vec{a} + n\vec{b} + p\vec{c} \tag{2.1}$$

where $\vec{a}$, $\vec{b}$ and $\vec{c}$ are vectors often known as basis vectors, which form a parallelepiped that defines the unit cell of the lattice. These vectors describe the length of each side of the unit cell (a_0, b_0 and c_0) and, together with the angles between them, are collectively known as the unit cell parameters. These angles are called α, β and γ, where α lies between $\vec{b}$ and $\vec{c}$, β lies between $\vec{a}$ and $\vec{c}$ and γ lies between $\vec{a}$ and $\vec{b}$. The unit cell is not a unique entity, it is chosen conveniently to reveal a crystal's underlying symmetry. In Equation 2.1, m, n and p are any rational numbers.
There are 14 possible lattices (in 3-dimensions) which are known as Bravais lattices (or sometimes direct lattices). These have been illustrated in Figure 2.1.

[1]Reference text: Thesis of Mark Robert Michel, "Electronic Structure Study of Copper-containing Perovskites", University College London (2010)

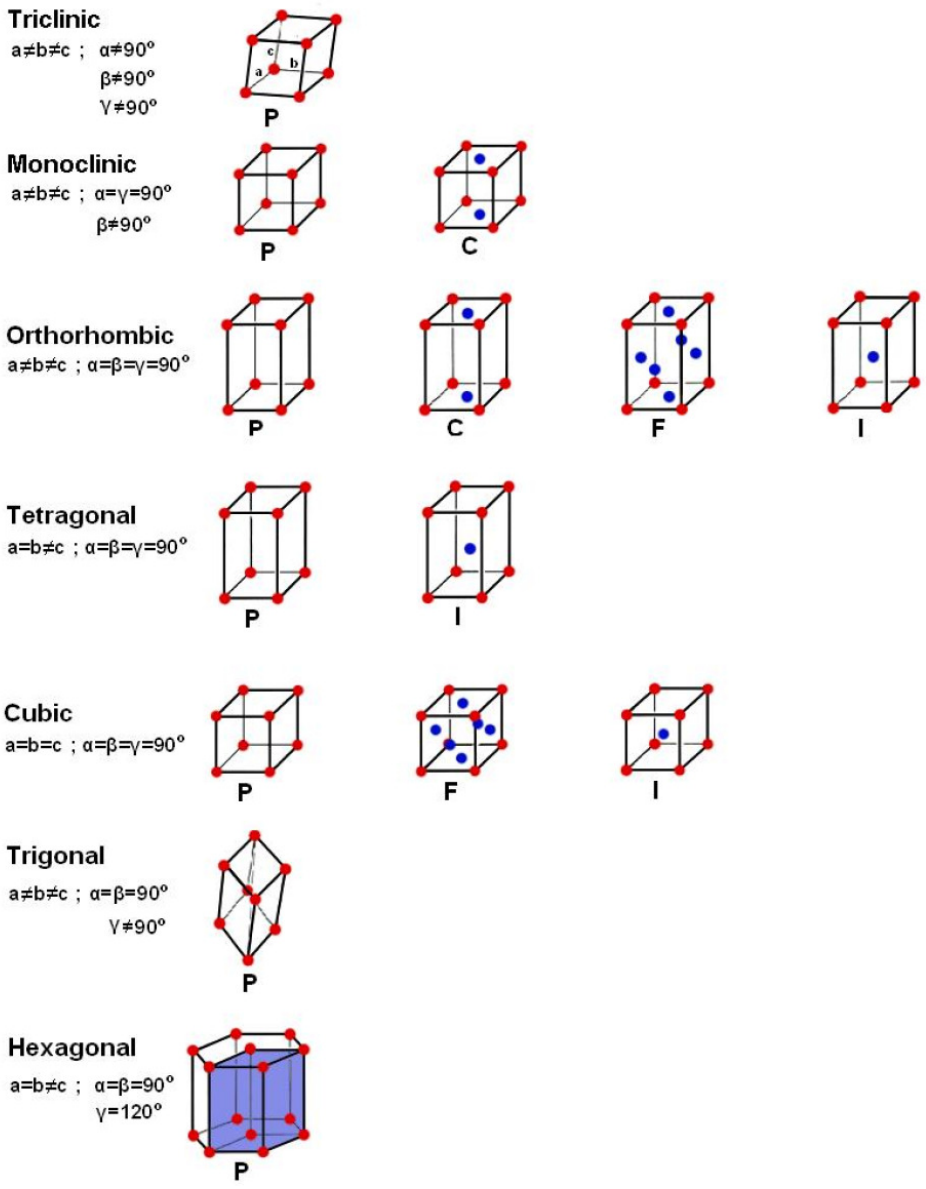

Figure 2.1: **The Bravais lattices.** - The a, b and c directions are as shown in the Triclinic case. Image adapted from Ref [16].

There are 7 different classes of a, b, c, α, β and γ that are needed to define all of the Bravais lattices. These are labelled in Figure 2.1.
The Bravais lattices are further denoted by the number of lattice points contained in a unit cell. The simplest is known as the primitive lattice and is denoted as P in Figure 2.1. This is the smallest type of unit cell and the only one which contains only one lattice point. A unit cell that contains lattice points in the corner and in the center of the cell (2 lattice points) is known as body-centered unit cell and is labelled I. A unit cell containing lattice points in the center of each its faces (4 lattices points) is called a face-centered unit cell and is labelled F. There are also unit cells containing a lattice point on one of the face centers which is called A-face centered if the faces cut the a-axes, B-face centered if the faces cut the b-axes and C-face centered if the faces cut the c-axes.

2.1.2 Crystal Structures

The Bravais lattices allow any crystal structure to be built by positioning one or more atoms on each lattice point. The atom or atoms that sit on each lattice point are usually called the basis or the motif. This is the smallest fragment of the crystal structure that, when repeated, can create the whole structure. The motif, for example, could be an atom or a molecule. Therefore, a crystal structure is formed of both a lattice and a basis. It is important to note here the distinction between the crystal lattice and crystal structure. A crystal lattice is simply a lattice of points in space formed by repeating units, a purely mathematical concept. The crystal structure is formed by placing a basis down on each point of a lattice. An identical arrangement and orientation of the basis is found at each lattice point. Hence the crystal is formed by repeating the basis in space according to a given Bravais lattice[17].
The axes used to describe the crystal structure are the same as those outlined so far. The position of an atom within the unit cell can be described by fractional coordinates. These provide a position which is a fraction (in each direction) of the unit cell lengths, a_0, b_0 and c_0. So for example if we have an Oxygen atom at position (1/2, 1/2, 1/2) it is located halfway along the a axis, halfway along the b axis and halfway along the c axis, i.e. it is located in the center of the unit cell[18].
So far, we have seen how a unit cell can be constructed from one of fourteen different Bravais lattices by adding an atom or a set of atoms to each lattice point known as a basis. An entire crystal structure can then be constructed by repeating this unit cell in 3-dimensions. Therefore, one can build a crystalline system by defining the unit cell type (e.g. Tetragonal), the unit cell parameters (a_0, b_0, c_0, α, β and γ) and the fractional positions of all the unit cell atoms.

We will now see how there are several symmetry operations available which lead to the existence of a finite number of classes known as point and space groups.

2.1.3 Symmetry, Point Groups and Space Groups

A solid, such as a crystal structure, can be classified in terms of the collection of symmetry elements that can be attributed to the given shape. Its internal symmetry can be described by the combination of axes of rotation and mirror planes. It is a collection of such symmetry operations, applied to a point in space (leaving one point fixed), that is given the name of a point group. The various possible symmetry elements under consideration are inversion center, reflection plane, rotation axis and rotation-inversion axis. It should be noted that translation plays no part here since it does not leave one point fixed. The combination of these symmetry elements leads to 32 possible crystallographic point groups.
As aforementioned, one can place a basis of atoms or molecules on the points of a Bravais lattice. It follows that adding these introduces more and more possible combinations of symmetry operations. The number of possible Bravais lattices, together with the various point groups, give a total of 230 different space groups. That is to say that by considering the combinations of the 32 point groups, the screw axes (simultaneous rotation and translation), glide planes (combination of a reflection and a translation in a plane) and the different Bravais lattices we arrive at 230 space groups. We can then attribute a particular real crystal to one of these space groups. Each group is represented by a combination of numbers, letters and symbols which are chosen to represent the symmetry elements of the structure[19].
The space group provides much information about a system including the type of unit cell and all or some of the fractional coordinates of the atoms in the cell. To fully build the crystal structure one must additionally known the type of atoms within the cell, the unit cell parameters and the fractional coordinates of the atoms that are not fixed by the space group symmetry.

2.1.4 Miller Indices

The facets and internal planes through a crystal lattice or structure can be described by Miller Indices. If a unit cell of a crystal is defined by vectors $\vec{a}$, $\vec{b}$ and $\vec{c}$, then any crystal plane that intercepts the axes proportional to $\vec{a}/h$, $\vec{b}/k$ and $\vec{c}/l$ respectively is denoted by its Miller indices (hkl). These indices describe not just one plane, but all parallel planes. The values of h, k and l are multiples of the unit cell lattice parameters,

a_0, b_0 and c_0. Therefore, the set of planes which lie parallel to the unit cell edge is given the relevant h, k or l value zero. Some examples of these Miller indices are the 001, 110 and 111 planes which are illustrated in Figure 2.2. The 001 indices represent the set of planes that lie parallel to the a-axes and b-axes and intersect the unit cell at position 1c. Planes cutting the a-axes and b-axis at 1a and 1b are the 110 planes, and planes cutting the a-axes, b-axes and c-axes at 1a 1b and 1c are called the 111 planes. Indices of higher multiples of the axes exist, for example, the 122 planes will cut the unit cell edges at 1a, 1/2b and 1/2c.

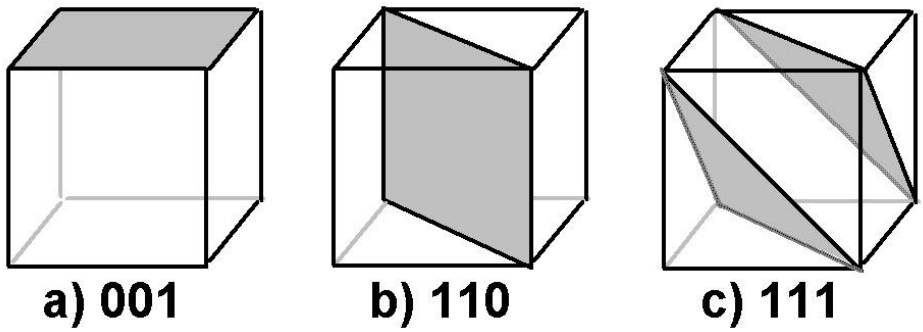

Figure 2.2: **Miller indices.** - Examples of some Miller indices of lattice planes a) 001, b) 110 and c) 111.

2.1.5 Reciprocal Lattice and Reciprocal Space

For each Bravais lattice, a corresponding reciprocal lattice may be postulated which possesses the same symmetry. Where the Bravais lattice may be described as existing in real space, the reciprocal lattice exists in reciprocal space. This idea was created in order to simplify the process of describing the physical properties of many systems.
To derive the reciprocal lattice we define new lattice vectors $\vec{a}^*$, $\vec{b}^*$, $\vec{c}^*$ whose directions are perpendicular to the end faces of the Bravais lattice unit cell. The lengths of these new lattice vectors are the inverse of the perpendicular distance from the lattice origin to the end faces of the Bravais lattice unit cell. The reciprocal lattice points are associated with a set of planes described by the Miller indices (hkl). The position of the (hkl) spot in the reciprocal lattice is related to the orientation of these planes and the spacing between them, d_{hkl}. In fact the lengths of the vectors of the reciprocal space can be written as:

$$a^* = \frac{1}{d_{100}},\ b^* = \frac{1}{d_{010}},\ c^* = \frac{1}{d_{001}}, \tag{2.2}$$

For example, the cubic, tetragonal and orthorhombic lattices are equivalent to:

$$a^* = \frac{1}{a_0},\ b^* = \frac{1}{b_0},\ c^* = \frac{1}{c_0}, \tag{2.3}$$

For crystals possessing different symmetries the relationship between the Bravais and reciprocal lattice is more complex. The important point to note is that the use of reciprocal space allows the physical properties of many systems to be more easily described.
Just as the Bravais lattices have primitive cells, there is also a primitive cell of a given reciprocal lattice. This is called the first Brillouin zone.

2.1.6 K-Points and the Brillouin Zone

In order to understand the concepts of the next chapter it is convenient to introduce the concept of k-points here. There are an infinite number of k-points in the Brillouin zone. Electronic structure calculations performed on crystalline solids require the evaluation of integrals over the Brillouin zone, that cannot be performed analytically. This problem is overcome by the fact that k-points that are sufficiently close together contain similar information; we can therefore replace the integration with a summation over a finite number of k-points. The amount of points required to obtain converged properties will depend on the size and nature of the system. For example, metallic systems tend to require more k-points (to capture the shape of the Fermi surface properly) than a large band-gap insulator. A common recipe for choosing the number of k-points was that developed by Monkhorst and Pack[20], which is particularly well suited for metallic systems, but is applied more generally to all crystalline solids.

2.1.7 Modeling Solids and Bulk Calculations

We have now seen how a crystalline solid can be constructed by applying translational and point symmetry operations to a finite number of atoms describing its unit cell. During this thesis we have been interested in studying bulk materials. Let us now discuss how this can be done in practice by making use of the concept of periodic boundary conditions (PBC). For the majority of this thesis, calculations were performed on the bulk properties of materials; an explicit description of each atom of a typical solid would involve calculations on a large amount of atoms, of the order of Avogadro's number ($\sim 6 \times 10^{23}$). Calculations on this scale are clearly not computationally feasible. We also have the issue of surface effects. Unless the chosen bulk size is adequately large (too large to simulate) the ratio between the number of surface atoms and total number of atoms would be large enough to cause surface effects to be more important than they should.

These problems are overcome by the application of periodic boundary conditions (PBC) which enable crystalline solids to be characterized in a more manageable way. In this way a unit cell is chosen including the minimal number of atoms which contains the whole symmetry of the system. This is used with the lattice vectors indicating the size of the unit cell and the direction of replication to reproduce an infinite crystalline structure. This cell is able to interact with an infinite lattice of identical image cells surrounding it in each Cartesian direction. Any movement or action from an atom in the main cell is replicated precisely by the equivalent atoms in the surrounding 'image' cells. Here we have a situation where each particle interacts, not only with other particles in its cell but with their images in nearby cells. This is advantageous as information about the atoms in each cell do not need to be stored. It is only necessary to store information on the molecules in the unit cell. If an atom were to leave the cell there would be an equivalent atom entering from the opposite side. Therefore the entire solid is reproduced by just repeating this unit cell in all Cartesian directions.

2.1.8 Magnetic Structures

Magnetic order in bulk materials can have a large effect on the crystal structure. Let us therefore discuss magnetism and how it is incorporated into the crystallographic structures discussed above.

It is possible to occupy positions of a crystal lattice with any element, some of which may contain unpaired electrons. As a result of the spin on these atoms we are presented with the phenomenon of magnetism where each atom has a magnetic dipole associated with it. These dipoles can exist with different alignments such as paramagnetic, ferrimagnetic, ferromagnetic (FM) or anti-ferromagnetic (AFM)[21]. Paramagnetic compounds have magnetic dipoles which are completely unaligned in random directions. A ferromagnetic structure is one that undergoes a phase transition from a high temperature phase that does not have a macroscopic moment to a low temperature phase that has a spontaneous magnetization. This spontaneous magnetization remains even in the absence of an applied magnetic field. This is due the randomly aligned magnetic dipole moments of the atoms in the paramagnetic high temperature phase tending to line up in the same direction. This is shown in Figure 2.3 along with two other possible orderings, AFM and ferrimagnetic. Ferromagnetism has been successfully rationalized by two theories, the Curie-Weiss localized-moment theory[22] and the Stoner band theory of magnetism[23]. Weiss proposed that a "molecular field" acts to align magnetic moments and we now understand this to be the quantum mechanical exchange energy (see Chapter 3) which causes electrons with parallel spins (and therefore with parallel magnetic moments)

to have a lower energy than electrons with anti-parallel spins. It is below a cut-off temperature known as the Curie temperature, T_c, that the molecular field of a material is so strong that it remains magnetized even in the absence of an applied magnetic field (the analogous cut-off for AFM materials is known as the Neel temperature, T_N, i.e. the temperature above which an AFM material becomes paramagnetic).
In an AFM structure the magnetic dipole moments of the atoms are ordered anti-parallel to one another. This leads to a net zero magnetization and hence they are not as sought after for technological applications. There can often be more than one type of AFM arrangement available to a structure. For example, the magnetic dipoles can alternate in direction along the 111, 110 or 001 planes. Ferrimagnets are similar to AFM materials in that the dipoles align antiparallel. The difference is that in a Ferrimagnet some of the dipole moments are larger than others so the material has a net overall magnetization; hence these can be useful for device implementation.
When describing an AFM structure it is not always possible to use the same unit cell as used for an isostructural paramagnetic or diamagnetic unit cell. For example if there are three magnetic ions in a unit cell it is not possible to have an equal number of spin up and down ions. Therefore a multiple cell must be created. In this example a double unit cell is the best solution from a computational point of view where the cell is doubled along one direction. This allows for three alpha and three beta spin and hence a proper AFM magnetic structure. .

2.2 Physics and Chemistry of Solids

2.2.1 Introduction

Before we can hope to construct models of materials, we need to be able to understand their chemistry. The second part of this chapter[2] is intended to outline the three most pertinent examples of phenomena in physical chemistry that will be relevant to our modeling of material systems. The first is a set of laws from atomic physics, called Hund's rules which determine the electronic configuration of the ground state of atoms. Since we will be working with crystalline materials, it is unreasonable to expect these laws to survive. Surprisingly, most of them do, but the crystalline environment has its own set of energy scales which compete with Hund's rules. The energy of the crystal field interaction is enough to beat some of the energy scales set by Hund's rules. These

[2]Reference text: Thesis of M.I. Brammall, "Stoner Criteria in Transition Metal Oxides and Heavy Fermions", School of Physics and Astronomy, University of Birmingham (2011)

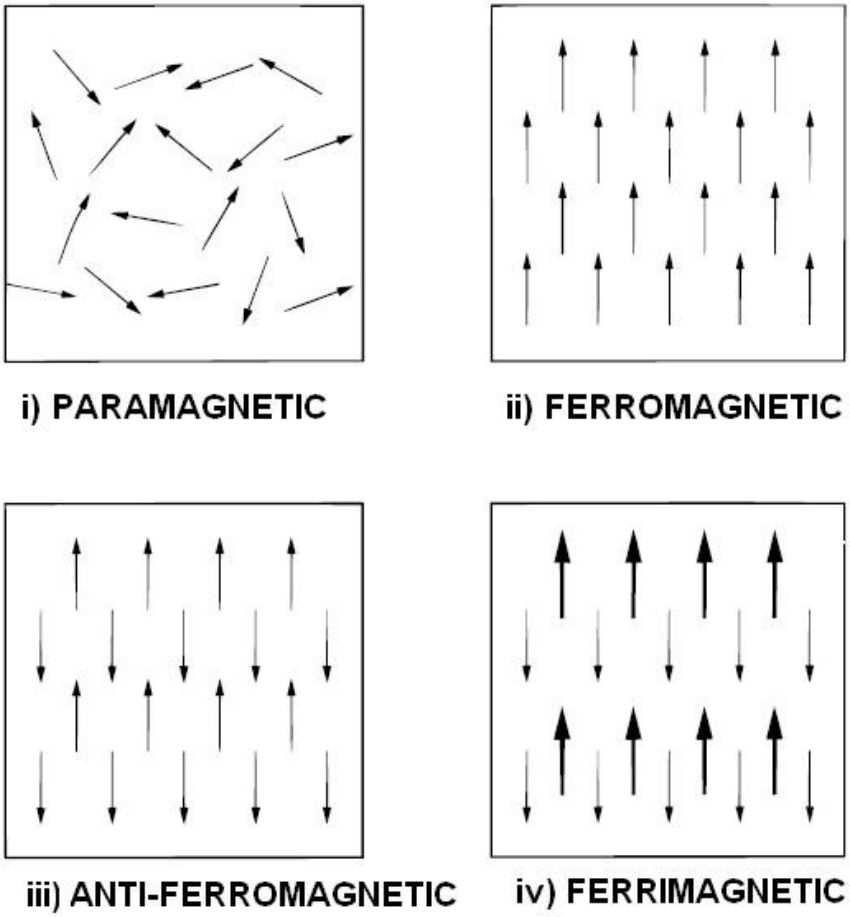

Figure 2.3: **Magnetic Structures.** - Example of the possible ordering of dipoles in magnetic structures. Image adapted from Ref. [24].

are the crystal field levels, and divide our space of orbitals into a set of irreducible representations of the symmetry group of the crystal. In most of the examples we look at, the crystallographic point group will be the cubic group, usually written as O_h.
Since we will discuss mostly problems of orbital ordering, we will have occasion to refer to the Jahn-Teller effect. This is an effect that lifts the degeneracy of electronic levels by causing an orbital ordering to distort the crystal. Jahn and Teller demonstrated that a non-linear molecule with degeneracy would distort to remove the degeneracy. Orbital ordering is the typical mechanism for this lifting of degeneracy, and so the Jahn-Teller effect is relevant to us.

2.2.2 Hund's Rules

Hund's rules are derived purely from phenomenological considerations[25]. They are rules for determining the configuration of the spin and orbital angular momentum of electrons in an atom possessing an incomplete degenerate outer shell. Some of the rules survive when we consider molecules in a crystalline environment, and a discussion of this will follow this section.
Hund's rules form a hierarchy for determining the spin and orbital ground-state configurations of the atoms. We list the rules in order here:

1. The total spin S should be maximal.

2. The orbital angular momentum L should be maximal, with constraints provided by the first rule and Pauli exclusion.

3. The total angular momentum J should be $|L - S|$ for less than half-filled shells, and $|L + S|$ for more than half-filled shells.

We may be concerned about applying Hund's rule to a solid where there is a lower degree of symmetry than that of an atom in free space. However, some of Hund's rules can survive and be relevant in solids. This is due to the relatively high-energy scale for the first rule, and the slightly lower energy scale for the second rule.
Even though the rules are empirical in nature, there is some justification on a theoretical level for their existence, which we discuss here, along with some implications.

2.2.2.1 The First Rule

The largest relevant atomic physics energy arises from exchange. Due to the Pauli principle, when two electrons have parallel spins they must have an antisymmetric spatial

wavefunction, whereas when the electrons have an antisymmetric spin wavefunction then they must have a symmetric spatial wavefunction. We express this by

$$\Psi(r_1, r_2, ..., r_n) \;=\; \Psi(r_{\sigma(1)}, r_{\sigma(2)}, ..., r_{\sigma(n)}) \tag{2.4}$$

for the symmetric case and

$$\Psi(r_1, r_2, ..., r_n) \;=\; \mathrm{sgn}(\sigma)\Psi(r_{\sigma(1)}, r_{\sigma(2)}, ..., r_{\sigma(n)}) \tag{2.5}$$

where $\sigma(i)$ is a permutation of the *ith*-coordinate, and $\mathrm{sgn}(\sigma)$ is the sign of the permutation, with +1 corresponding to even permutations and -1 to odd permutations.
Since the electron-electron interaction takes the form

$$\int d^3r_1 \int d^3r_2 |\psi(r_1, r_2)|^2 \frac{e^2}{|r_1 - r_2|} \tag{2.6}$$

the wave function for parallel spins has a lower energy as it vanishes where the interaction is maximal. This interaction leads to Hund's first rule which is that the total spin of an open shell is maximal.

2.2.2.2 The Second Rule

The next most important energy scale controls the choice of orbitals and competes directly with the crystal-field energy scale in transition metals. The physical source of the energy is again electrostatic. A classical explanation is that electrons orbiting an atom are less likely to meet if the electrons orbit the atom in the same sense. Hund's second rule is thus that the orbital angular momentum is maximized, subject to the restriction of Fermi statistics.
The second Hund's rule aligning the orbital angular momentum is on a similar energy scale to the spin energy but is a fraction of it. Subject to crystal-field splitting interfering with Hund's second rule, the orbital angular momentum is quenched in transition metals. The rare earth elements, on the other hand, have such localized f-electrons that often the third Hund's rule is also observed.

2.2.2.3 The Third Rule

The third Hund's rule originates from relativistic effects and is usually small. The effect is to induce a coupling between an electron's spin and its orbital angular momentum, also called spin-orbit coupling. The result is that for the first half of the shell the total

spin and total angular momentum are anti-parallel, whereas for the second half they are parallel.

$$\begin{aligned} j &= |l-s|, n < M \\ j &= l+s, n > M \end{aligned} \tag{2.7}$$

For Ce the spin-orbit coupling energy is around 0.25 eV and for Yb the spin-orbit energy is of the order of 1 eV. In comparison transition metals typically have spin-orbit couplings of around 0.1 eV.
It is important to realize that the role of the crystal field in the rare-earths is not to stabilize the cubic harmonics, but is more subtle. The spin-orbit effects win and so we cannot separate the spin from the orbital angular momentum. It is the different rather more complicated j_z states which are split by the crystal field.

2.2.3 Crystal Field Theory

In a spherically symmetric atom, the orbitals within a given shell are energetically degenerate, as discussed above. In a crystalline environment, we cannot expect this degeneracy to be present. The breaking of this symmetry is the subject of crystal field theory. It was developed in 1929 by Hans Bethe[26]. The basic idea is that electrons in a crystalline environment are effected by the electrostatic field of the surrounding ions. This electrostatic field is called the crystal field. The origin of the splitting originates from the anisotropic charge distribution of the orbitals, and hence of the charge distribution. For a simple example, consider a transition metal oxide with a perovskite crystal structure. We restrict attention to the active $L = 2$ d-shell. In the $\hat{x}^2 - \hat{y}^2$ and $3\hat{z}^2 - \hat{r}^2$ orbitals, the orbitals will point directly at the oxygen anions, and therefore will experience a strong coulombic repulsion. The $\hat{x}\hat{y}$, $\hat{y}\hat{z}$, and $\hat{z}\hat{x}$ orbitals, however, point in between the oxygen anions, and so will experience less coulomb repulsion. There is therefore an energetic difference between these sets of orbitals, and we have lost the 5-fold orbital degeneracy. We now have a set of three degenerate orbitals and a set of two degenerate orbitals with a splitting between the two.
In this section, we will develop these ideas more concretely. The splitting of the levels is determined by the representations of the group of symmetries of the crystal. The levels are grouped according to irreducible representations of the point group of the crystal. Group theory can only tell us the splittings of the orbitals, and not the energetics so we are unable to determine the sequence of the levels. An alternative is to look at inelastic neutron scattering data, and this is often used when using group theoretic methods

become complicated. This happens quickly for f-electron systems.
There is a systematic nomenclature for labelling point groups which is used throughout the literature, and that is Mulliken symbols. There is an account of the nomenclature in the book [27] by for the reader who is curious of the meaning of these symbols. For our purposes, there are only two irreducible representations of groups of interest. That is the t_{2g} and e_g irreducible representations of the cubic group. The $L = 2$ d-orbitals form a five dimensional vector space, while the order of the cubic group is 48. Since the dimension of an irreducible representation of a finite group must divide the order of the group, we find that the five dimensional d-orbital vector space decomposes into an irreducible doublet representation and an irreducible triplet representation.
Take as an example $LaMnO_3$. The crystal structure is perovskite. There is a octahedron of oxygen atoms surrounding every manganese atom. The platonic dual to an octahedron is a cube, and so the octahedral group is isomorphic to the cubic group, and hence their irreducible representations will be isomorphic. The t_{2g} and e_g representations of these groups are thus identical, and we can talk of the same orbitals in the representations.
The story does not end here. There are also weak and strong crystal field splittings. In the weak case, the high-spin state is realized where, taking the case of cubic splittings for d-orbitals, the t_{2g} sector is half-filled first, then the e_g sector is half-filled. This is repeated for the next half.
For the strong-field case, the low-spin state is realized. Following the last example, the t_{2g} sector is completely filled, and then the e_g sector is filled. For the 3d elements, the former situation is realized up to cobalt, and the latter for the elements past cobalt. Cobalt containing compounds are interesting, since both situations can be realized.

2.2.4 The Jahn-Teller Effect

If we consider a set of orbitals lying in a shell, say the d-orbitals, then we expect the orbitals to be split by a crystal field, which depends on the symmetry of the crystalline environment. In the case of d-orbitals in a cubic environment, we have splittings into the t_{2g} and e_g representations. If we consider the motion of a hole in an otherwise filled d-shell in a cubic environment, say Cu^{2+}, then there will be a degeneracy in the orbital ground state between the $\hat{x}^2 - \hat{y}^2$ orbital and the $3\hat{z}^2 - \hat{r}^2$ orbital, providing there is no further lifting of the degeneracy. However, Jahn and Teller [[28], [29]] formulated and proved a theorem which describes when a further lifting of the degeneracy is energetically favorable.
The problem of the lifting of the orbital degeneracy was first tackled by Landau with phenomenological arguments. He argued that the ordering of orbitals will induce a

distortion of the crystal, and this distortion of the crystal will cost an energy $E_1 \propto \alpha(\delta z)^2$, for some energy scale α and distortion δd. This will induce a splitting between the $3\hat{z}^2 - \hat{r}^2$ and the $\hat{x}^2 - \hat{y}^2$ orbital. It is then energetically favorable for two electrons to lie in the $3\hat{z}^2 - \hat{r}^2$ orbital than the $\hat{x}^2 - \hat{y}^2$ orbital which gains an energy $E_2 \propto \beta\delta d$ with some separate energy scale β. The total energy associated with distorting the crystal and repopulating the electronic levels is $E_1 + E_2 = \alpha(\delta d)^2 - \beta\delta d$ and this energy is minimized for a distortion of the order $\delta d = \frac{\beta}{2\alpha}$.

Things were not as simple as this, however. The situation was complicated by molecules with linear geometries and orbitally degenerate ground states, such as CO_2, not showing Jahn-Teller distortions. The splitting between the orbital levels in CO_2 is $\propto (\delta d)^2$, and therefore no Jahn-Teller distortion will occur.

The doubts thrown over the simple physical arguments provided by Landau were rigorously resolved by Jahn and Teller, who used group and representation theoretic methods to prove that the only molecules with an orbitally degenerate ground state that do not distort to lift the degeneracy are those with a linear geometry. However, as with most group theoretic methods employed in physics, it can only tell us the nature of the splittings leading to the crystalline distortion. It cannot tell us the magnitude of such effects.

2.2.5 Double Exchange

Double-exchange was first proposed by Zener [30]. We take as an example to illustrate the double exchange mechanism, and one that will be especially important to us later, the exchange between an Mn^{4+} and an Mn^{3+} ion mediated by an intermediate oxygen atom. The situation is illustrated in Figure 2.4. .

Double-exchange tells us that electrons move most easily if electrons do not have to reorient spins when moving between ions in order to avoid paying Hund's rule energies. Delocalization reduces the energy, and so this leads to ferromagnetic correlations between neighboring ions. For us, it will be one of the most used exchange mechanisms, notably when we discuss exchange in saturated ferromagnets.

In the case of a saturated ferromagnet, double exchange enables us to avoid describing the spin degree of freedom in itinerant magnets. The spin is guaranteed to be of one species only, and though the assignment of up or down to the z component of a spin is arbitrary, it will be fixed and it will be polarized due to the large Hund's rule penalty for hopping, as an example, an electron in the e_g sector on Mn^{3+} to the empty e_g sector on Mn^{4+}. The only degree of freedom left for the electron is which e_g orbital to hop into.

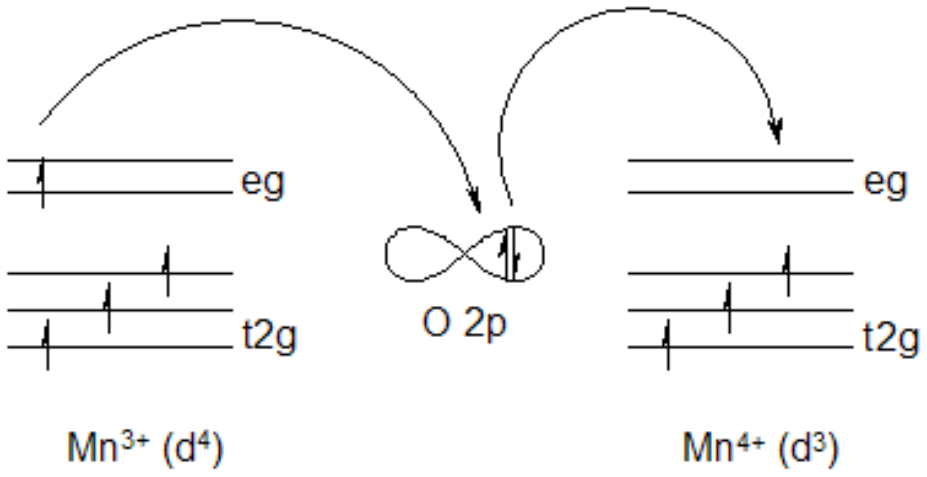

Figure 2.4: **Double Exchange** - in an Mn-O-Mn chain.

Chapter 3

Methods & Concepts

3.1 Introduction

On the nanoscale, materials around us have surprisingly simple structures: The standard model of solid state physics and chemistry only knows of two types of particles, namely the nuclei making up the periodic table and the electrons. Only one kind of interaction between them needs to be considered, namely the electrostatic interaction. Even magnetic forces are important only in rare occasions. All other fundamental particles and interactions are irrelevant for chemistry. The behavior of these particles can be described by the Schrödinger equation (or better the relativistic Dirac equation), which is easily written down. However, the attempt to solve this equation for any system of interest fails miserably due to what Walter Kohn termed the exponential wall [31].
To obtain an impression of the powers of the exponential wall, imagine the wave function of a N_2 molecule, having two nuclei and fourteen electrons. For N particles, the Schrödinger equation is a partial differential equation in 3N dimensions. Let us express the wave function on a grid with about 100 points along each spatial direction and let us consider two spin states for each electron. Such a wave function is represented by $2^{14}\ 100^{3\times 16} \approx 10^{100}$ complex numbers. A data server for this amount of data, made of current terabyte hard disks, would occupy a volume with a diameter of 10^{10} light years! [1].
Treating the nuclei as classical particles turned out to be a good approximation, but the quantum nature of the electrons cannot be ignored. A great simplification is to describe electrons as noninteracting quasi particles. Instead of one wave function in 3N

[1]This chapter was inspired from following reference text: Eva Pavarini, Erik Koch, Dieter Vollhardt, and Alexander Lichtenstein, "The LDA+DMFT approach to strongly correlated materials", Lecture Notes of the Autumn School 2011 Hands-on LDA+DMFT (Forschungszentrum Jülich GmbH), ISBN 978-3-89336-734-4

dimensions, one only needs to describe N wave functions in three dimensions each, a dramatic simplification from 10^{100} to 10^7 numbers

While the independent-particle model is very intuitive, and while it forms the basis of most text books on solid-state physics, materials physics, and chemistry, the Coulomb interaction between electrons is clearly not negligible.

Here, density-functional theory [13, 14] comes to our rescue: it provides a rigorous mapping from interacting electrons onto a system of non-interacting electrons. Unfortunately, the exact mapping is utterly complicated, and this is where all the complexity goes. Luckily, there are simple approximations that are both intuitive and surprisingly accurate. Furthermore, with the help of clever algorithms, density-functional calculations can be performed on current computers for large systems with several hundred atoms in a unit cell or a molecule. The microscopic insight gained from density functional calculations is a major source of progress in solid state physics, chemistry, material science, and biology.

In the first part of this chapter, we will try to familiarize the novice reader with the basics of density functional theory, provide some guidance into common approximations and give an idea of the type of problems that can be studied with density functional theory.

Beyond this chapter, I recommend the insightful review articles on density functional theory by Jones and Gunnarsson [32], Baerends [33], von Barth [34], Perdew [35], Cohen [36], and their collaborators.

Solving the one-particle Schrödinger equation, which results from density-functional theory, for real materials is a considerable challenge. Several avenues have been developed to their solution. This is the field of electronic structure methods, which will be discussed in the second part of this chapter. This part is taken from earlier versions by Clemens Först, Johannes Kästner and Peter E. Blöchl [37, 38].

3.2 Basic of density-functional theory

The dynamics of the electron wave function is governed by the Schrödinger equation $i\hbar\partial_t|\Psi\rangle = \hat{H}|\Psi\rangle$ with the N-particle Hamiltonian $\hat{H}$.

$$\hat{H} = \sum_{j=1}^{N}\left(\frac{-\hbar^2}{2m_e}\vec{\nabla}_j^2 + v_{ext}\left(\vec{r}_j\right)\right) + \frac{1}{2}\sum_{j\neq 1}^{N}\frac{e^2}{4\pi\epsilon_0\left|\vec{r}_i-\vec{r}_j\right|}. \tag{3.1}$$

With m_e we denote the electron mass, with ϵ_0 the vacuum permittivity, e is the elementary charge and $\hbar$ is the Planck quantum divided by 2π. The Coulomb potentials of the nuclei have been combined into an external potential $v_{ext}\left(\vec{r}\right)$.

All N-electron wave functions $\Psi(\vec{x}_1,\ldots,\vec{x}_N)$ obey the Pauli principle, that is they change

their sign, when two of its particle coordinates are exchanged.
We use a notation that combines the position vector $\vec{r} \in R^3$ of an electron with its discrete spin coordinate $\sigma \in \{\uparrow, \downarrow\}$ into a single vector $\vec{x} := (\vec{r}, \sigma)$. Similarly, we use the notation of a four-dimensional integral $\int d^4x := \sum_\sigma \int d^3r$ for the sum over spin indices and the integral over the position. With the generalized symbol $\delta(\vec{x} - \vec{x'}) := \delta_{\sigma,\sigma'}\delta(\vec{r} - \vec{r'})$ we denote the product of Kronecker delta of the spin coordinates and Dirac's delta function for the positions. While, at first sight, it seems awkward to combine continuous and discrete numbers, this notation is less error prone than the notation that treats the spin coordinates as indices, where they can be confused with quantum numbers. During the first reading, the novice can ignore the complexity of the spin coordinates, treating $\vec{x}$ like a coordinate. During careful study, he will nevertheless have the complete and concise expressions.

3.2.1 One-particle reduced density matrix and two-particle density

In order to obtain the ground state energy $E = \langle\Psi|\hat{H}|\Psi\rangle$ we need to performed 2^N integrations in $3N$ dimensions each, i.e.

$$E = \int d^4x_1 \ldots \int d^4x_N \Psi^* (\vec{x}_1, \ldots, \vec{x}_N) \hat{H} \Psi (\vec{x}_1, \ldots, \vec{x}_N) . \tag{3.2}$$

However, only two different types of integrals occur in the expression for the energy, so that most of these integrations can be performed beforehand leading to two quantities of physical significance.

- One of these quantities is the one-particle reduced density matrix $\rho^{(1)}(\vec{x}, \vec{x'})$, which allows one to evaluate all expectation values of one-particle operators such as the kinetic energy and the external potential,

$$\rho^{(1)}(\vec{x}, \vec{x'}) := N \int d^4x_2 \ldots \int d^4x_N \Psi (\vec{x}, \vec{x}_2, \ldots, \vec{x}_N) \Psi^*(\vec{x'}, \vec{x}_2, \ldots, \vec{x}_N). \tag{3.3}$$

- The other one is the two-particle density $n^{(2)}(\vec{r}, \vec{r'})$, which allows to determine the interaction between the electrons,

$$n^{(2)}(\vec{r}, \vec{r'}) := N(N-1) \sum_{\sigma,\sigma'} \int d^4x_3 \ldots \int d^4x_N |\Psi(\vec{x}, \vec{x'}, \vec{x_3}, \ldots, \vec{x}_N)|^2. \tag{3.4}$$

If it is confusing that there are two different quantities depending on two particle coordinates, note that the one-particle reduced density matrix $\rho^{(1)}$ depends on two

$\vec{x}$-arguments of the same particle, while the two-particle density $n^{(2)}$ depends on the positions of two different particles.
With these quantities the total energy is

$$\begin{aligned} E &= \int d^4x' \int d^4x \delta(\vec{x'} - \vec{x}) \left(\frac{-\hbar^2}{2m_e} \vec{\nabla}^2 + v_{ext}(\vec{r}) \right) \rho^{(1)}(\vec{x}, \vec{x'}) \\ &+ \frac{1}{2} \int d^3r \int d^3r' \frac{e^2 n^{(2)}(\vec{r}, \vec{r'})}{4\pi\epsilon_0 |\vec{r} - \vec{r'}|}, \end{aligned} \tag{3.5}$$

where the gradient of the kinetic energy operates on the first argument $\vec{r}$ of the density matrix.

3.2.2 One-particle reduced density matrix and natural orbitals

In order to make oneself familiar with the one-particle reduced density matrix, it is convenient to diagonalize it. The eigenstates $\varphi_n(\vec{r})$ are called natural orbitals [39] and the eigenvalues $\bar{f}_n$ are their occupations. The index n labelling the natural orbitals may stand for a set of quantum numbers.
The density matrix can be written in the forms

$$\rho^{(1)}(\vec{x}, \vec{x'}) = \sum_n \bar{f}_n \varphi_n(\vec{x}) \varphi_n^*(\vec{x'}). \tag{3.6}$$

The natural orbitals are orthonormal one-particle orbitals, i.e.

$$\int d^4x \varphi_m^*(\vec{x}) \varphi_n(\vec{x}) = \delta_{m,n}. \tag{3.7}$$

Due to the Pauli principle, occupations are non-negative and never larger than one [40]. The natural orbitals already point the way to the world of effectively non-interacting electrons.
The one-particle density matrix provides us with the electron density

$$n^{(1)}(\vec{n}) = \sum_\sigma \rho^{(1)}(\vec{x}, \vec{x}) = \sum_\sigma \sum_n \bar{f}_n \varphi_n^*(\vec{x}) \varphi_n(\vec{x}). \tag{3.8}$$

With the natural orbitals, the total energy Eq.3.5 obtains the form

$$\begin{aligned} E = \sum_n \bar{f}_n \int d^4x \, \varphi_n^*(\vec{x}) \frac{-\hbar^2}{2m} \vec{\nabla}^2 \varphi_n(\vec{x}) &+ \int d^3r \, v_{ext}(\vec{r}) n^{(1)}(\vec{r}) \\ &+ \frac{1}{2} \int d^3r \int d^3r' \frac{e^2 n^{(2)}(\vec{r}, \vec{r'})}{4\pi\epsilon_0 |\vec{r} - \vec{r'}|}. \end{aligned} \tag{3.9}$$

3.2.3 Two-particle density and exchange-correlation hole

The physical meaning of the two-particle density $n^{(2)}(\vec{r},\vec{r'})$ is the following: For particles that are completely uncorrelated, meaning that they do not even experience the Pauli principle, the two particle density would be[2] the product of one-particle densities, i.e. $n^{(2)}(\vec{r},\vec{r'}) = n^{(1)}(\vec{r})n^{(1)}(\vec{r'})$. If one particle is at position $\vec{r_0}$,the density of the remaining $N-1$ particles is the conditional density

$$\frac{n^{(2)}\left(\vec{r_0},\vec{r}\right)}{n^{(1)}\left(\vec{r_0}\right)}.$$

The conditional density is the electron density seen by one of the electrons at $\vec{r_0}$. This observer electron obviously only sees the remaining $N-1$ electrons.
It is convenient to express the two-particle density by the hole function $h(\vec{r},\vec{r'})$, i.e.

$$n^{(2)}(\vec{r},\vec{r'}) = n^{(1)}(\vec{r})\left[n^{(1)}(\vec{r'}) + h(\vec{r},\vec{r'})\right]. \tag{3.10}$$

One electron at position $\vec{r}$ does not "see" the total electron density $n^{(1)}$ with N electrons, but only the density of the $N-1$ other electrons, because it does not see itself. The hole function $h\left(\vec{r_0},\vec{r}\right)$ is simply the difference of the total electron density and the electron density seen by the observer electron at $\vec{r_0}$.
The division of the two-particle density in Eq. 3.10 suggests that we split the electron-electron interaction into the so-called Hartree energy

$$E_H \overset{def}{=} \frac{1}{2}\int d^3r \int d^3r' \frac{e^2 n^{(1)}\left(\vec{r}\right) n^{(1)}(\vec{r'})}{4\pi\epsilon_0|\vec{r}-\vec{r'}|} \tag{3.11}$$

and the potential energy of exchange and correlation

$$U_{xc} \overset{def}{=} \int d^3r n^{(1)}(\vec{r})\frac{1}{2}\int d^3r' \frac{e^2 h(\vec{r},\vec{r'})}{4\pi\epsilon_0|\vec{r}-\vec{r'}|}. \tag{3.12}$$

Keep in mind that U_{xc} is not the exchange correlation energy. The difference is a kinetic energy correction that will be discussed later in Eq.3.19.
The hole function has a physical meaning: An electron sees the total density minus the electrons accounted for by the hole. Thus each electron not only experiences the electrostatic potential of the total electron density $n^{(1)}(\vec{r})$, but also the attractive potential of its own exchange correlation hole $h(\vec{r_0},\vec{r})$.
A few facts for this hole density are apparent:

[2] This is correct only up to a term that vanishes in the limit of infinite particle number.

1. Because each electron of a N-electron system sees $N-1$ other electrons, the hole function integrates to exactly minus one electronic

$$\int d^3r h(\vec{r_0},\vec{r}) = -1 \tag{3.13}$$

irrespective of the position $\vec{r_0}$ of the observing electron.

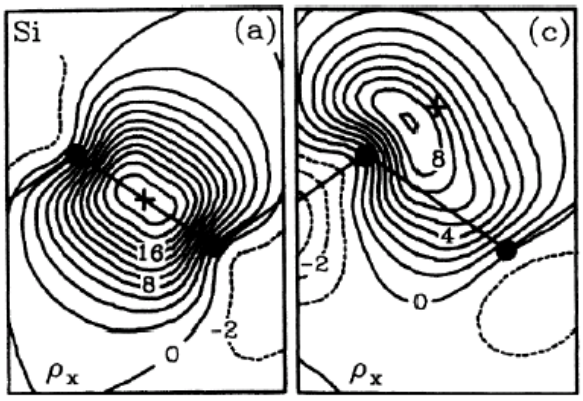

Figure 3.1: **Exchange hole in silicon** - The cross indicates the position of the observer electron. The black spheres and the lines indicate the atomic positions and bonds in the (110) plane. Reprinted figure with permission from Mark S. Hybertsen and Steven G. Louie, Physical Review B 34, 5390 (1986). Copyright 1986 by the American Physical Society.

2. The density of the remaining $N-1$ electrons can not be larger than the total electron density. This implies

$$h\left(\vec{r_0},\vec{r}\right) \geq -n^{(1)}(\vec{r}). \tag{3.14}$$

3. Due to the Pauli principle, no other electron with the same spin as the observer electron can be at the position $\vec{r_0}$. Thus the on-top hole $h\left(\vec{r_0},\vec{r_0}\right)$ obeys the limits [41].

$$-\frac{1}{2}n^{(1)}(\vec{r_0}) \geq h(\vec{r_0},\vec{r_0}) \geq -n^{(1)}(\vec{r_0}). \tag{3.15}$$

4. Assuming locality, the hole function vanishes at large distances from the observer electron at $\vec{r_0}$, i.e.

$$h(\vec{r_0},\vec{r}) \to 0 \qquad for \qquad |\vec{r}-\vec{r_0}| \to \infty. \tag{3.16}$$

With locality I mean that the density does not depend on the position or the presence of an observer electron, if the latter is very far away.

3.2.4 A selfmade functional

It is fairly simple to make our own density functional[3]: For a given density,we choose a simple shape for the hole function, such as a spherical box. Then we scale the value and the radius such that the hole function integrates to 1, and that its value is opposite equal to the spin density at its center. The electrostatic potential of this hole density at its center is the exchange-correlation energy for the observer electron. Our model has an exchange correlation energy[4] of

$$U_{xc}[n^{(1)}] \approx -\frac{1}{2}\int d^3r\, n^{(1)}(\vec{r})\left(\frac{3}{4}\frac{e^2}{4\pi\epsilon_0}\sqrt[3]{\frac{2\pi}{3}}\left(n^{(1)}(\vec{r})\right)^{\frac{1}{3}}\right) \sim \int d^3r\left(n^{(1)}(\vec{r})\right)^{\frac{4}{3}} \quad (3.17)$$

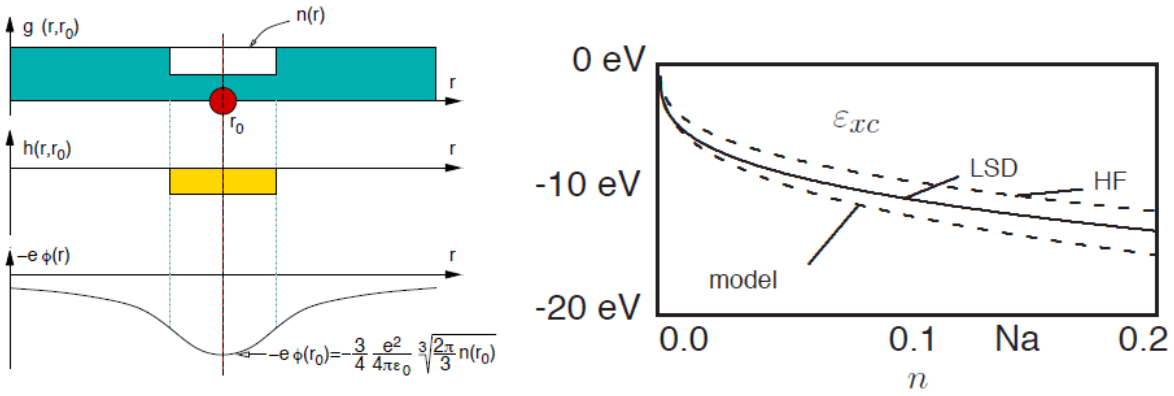

Figure 3.2: **Exchange correlation energy** - Left: Scheme to demonstrate the construction of the exchange correlation energy from a simple model. Right: exchange correlation energy per electron ϵ_{xc} as function of electron density from our model, Hartree-Fock approximation and the exact result. The symbol "Na" indicates the density of Sodium.

The derivation is an elementary exercise. The resulting energy per electron ϵ_{xc} is given on the right-hand side of Fig.3.2 indicated as "model" and compared with the exact result indicated as "LSD" and the Hartree-Fock result indicated as "HF" for a homogeneous electron gas.

The agreement with the correct result, which is surprisingly good for such a crude model, provides an idea of how robust the density-functional theory is with respect to approximations. While this model has been stripped to the bones, it demonstrates the way physical insight enters the construction of density functionals. Modern density functionals are far more sophisticated and exploit much more information [42], but the basic method of construction is similar.

[3] A functional $F[y]$ maps a function $y(x)$ to a number F. It is a generalization of the function $F(\vec{y})$ of a vector $\vec{y}$, where the vector index of $\vec{y}$ is turned into a continuous argument x.

[4] For this model we do not distinguish between the energy of exchange and correlation and its potential energy contribution

3.2.5 Kinetic energy

While the expression for the kinetic energy in Eq. 3.9 seems familiar, there is a catch to it. In order to know the natural orbitals and the occupations we need access to the many-particle wave function or at least to its reduced density matrix.
A good approximation for the kinetic energy of the interacting electrons is the kinetic energy functional $T_s[n^{(1)}]$ of the ground state of non-interacting electrons with the same density as the true system. It is defined by

$$\begin{aligned} T_s[n^{(1)}] \;=\; & \min_{\{f_n\in[0,1],|\psi_n\rangle\}} \Bigg\{ \sum_n f_n \int d^4x\; \psi_n^*(\vec{x}) \frac{-\hbar^2\vec{\nabla}^2}{2m} \psi_n(\vec{x}) \\ & + \int d^3r\; v_{eff}(\vec{r}) \left(\left[\sum_n f_n \sum_\sigma \psi_n^*(\vec{x})\psi_n(\vec{x}) \right] - n^{(1)}(\vec{r}) \right) \\ & - \sum_{n,m} \Lambda_{m,n} \Big(\langle\psi_n|\psi_m\rangle - \delta_{n,m} \Big) \Bigg\}. \end{aligned} \tag{3.18}$$

Note that $f_n \neq \bar{f}_n$ and that the so-called Kohn-Sham orbitals $\psi_n(\vec{x})$ differ[5] from the natural orbitals $\varphi_n(\vec{x})$. Natural orbitals and Kohn-Sham wave functions are fairly similar, while the occupations f_n of Kohn-Sham orbitals differ considerably from those $\bar{f}_m$ of the natural orbitals. The effective potential $v_{eff}(\vec{r})$ is the Lagrange multiplier for the density constraint. $\Lambda_{m,n}$ is the Lagrange multiplier for the orthonormality. Diagonalization of Λ yields a diagonal matrix with the one-particle energies on the diagonal.

This kinetic energy $T_s[n^{(1)}]$ is a unique functional of the density, which is the first sign that we are approaching a density-functional theory. Also it is the introduction of this kinetic energy, where we made for the first time a reference to a ground state. Density functional theory as described here is inherently a ground-state theory.

Why does the true kinetic energy of the interacting system differ from that of the non-interacting energy? Consider the hole function of a non-interacting electron gas. When inserted into Eq. 3.12 for U_{xc} the potential energy of exchange and correlation, we obtain a contribution to the total energy that is called exchange energy. The interaction leads to a second energy contribution that is called correlation energy. Namely, when the interaction is switched on, the wave function is deformed in such a way that the Coulomb repulsion between the electrons is reduced. This makes the hole function more compact. However, there is a price to pay when the wave functions adjust to reduce

[5] To be precise, Kohn-Sham orbitals are the natural orbitals for non-interacting electrons of a given density.

the Coulomb repulsion between the electrons, namely an increase of the kinetic energy: Pushing electrons away from the neighborhood of the reference electrons requires that work be performed against the kinetic pressure of the electron gas,which raises the kinetic energy. Thus, the system has to find a compromise between minimizing the electrostatic repulsion of the electrons and increasing its kinetic energy. As a result, the correlation energy has a potential-energy contribution and a kinetic-energy contribution.

This tradeoff can be observed in Fig.3.2. The correct exchange correlation energy is close to our model at low densities, while it becomes closer to the Hartree-Fock result at high densities. This is consistent with the fact that the electron gas can easily be deformed at low densities, while the deformation becomes increasingly costly at high densities due to the larger pressure of the electron gas.

The difference between T_s and the true kinetic energy is combined with the potential energy of exchange and correlation U_{xc} from Eq.3.12 into the exchange correlation energy E_{xc}, i.e.

$$E_{xc} = U_{xc} + \sum_n \bar{f}_n \int d^4x \; \varphi_n^*(\vec{x}) \frac{-\hbar^2}{2m} \vec{\nabla}^2 \varphi_n(\vec{x}) - T_s[n^{(1)}]. \tag{3.19}$$

Note, that the $\varphi_n(\vec{x})$ and the $\bar{f}_n$ are natural orbitals and occupations of the interacting electron gas, and that they differ from the Kohn-Sham orbitals[6] $\psi_n(\vec{x})$ and occupations f_n.

3.2.6 Total energy

The total energy obtains the forms

$$\begin{aligned} E \;=\; & \min_{|\Phi\rangle,\{|\psi_n\rangle,f_n\in[0,1]\}} \left\{ \sum_n f_n \int d^4x \; \psi_n^*(\vec{x}) \frac{-\hbar^2\vec{\nabla}^2}{2m} \psi_n(\vec{x}) \right. \\ & + \int d^3r \; \upsilon_{eff}(\vec{r}) \left(\left[\sum_n f_n \sum_\sigma \psi_n^*(\vec{x}) \psi_n(\vec{x}) \right] - n(\vec{r}) \right) + \int d^3r \; \upsilon_{ext}(\vec{r}) n^{(1)}(\vec{r}) \\ & \left. + \frac{1}{2} \int d^3r \int d^3r' \frac{e^2 n^{(1)}(\vec{r}) n^{(1)}(\vec{r'})}{4\pi\epsilon_0 |\vec{r} - \vec{r'}|} + E_{xc} - \sum_{n,m} \Lambda_{m,n} \Big(\langle \psi_n | \psi_m \rangle - \delta_{n,m} \Big) \right\}. \end{aligned} \tag{3.20}$$

In order to evaluate the total energy with Eq.3.20, we still have to start from the many-particle wave function $|\Phi\rangle$. Only the many-particle wave function allows us to evaluate

[6] They are however different from the natural orbitals of interacting electrons at the same density.

the one-particle density $n^{(1)}(\vec{r})$ and the exchange correlation energy E_{xc}. Kohn-Sham orbitals $|\psi_n\rangle$ and occupations f_n are obtained by an independent minimization for each density.

If, however, we were able to express the exchange-correlation energy E_{xc} as a functional of the density alone, there would be no need for the many-particle wave function at all and the terrors of the exponential wall would be banned. We could minimize Eq.3.20 with respect to the density, Kohn-Sham orbitals and their occupations.

Let us, for the time being, simply assume that $E_{xc}[n^{(1)}]$ is a functional of the electron density and explore the consequences of this assumption. Later, I will show that this assumption is actually valid.

The minimization in Eq.3.20 with respect to the one-particle wave functions yields the Kohn- Sham equations

$$\left[\frac{-\hbar^2}{2m_e}\vec{\nabla}^2 + v_{eff}(\vec{r}) - \epsilon_n\right]\psi_n(\vec{x}) = 0 \quad \text{with} \quad \int d^4x\, \psi_m(\vec{x})\psi_n(\vec{x}) = \delta_{m,n}. \tag{3.21}$$

The Kohn-Sham energies ϵ_n are the diagonal elements of the Lagrange multiplier Λ, when the latter is forced to be diagonal.

The requirement that the derivative of the total energy Eq.3.20 with respect to the density vanishes, yields an expression for the effective potentials

$$v_{eff}(\vec{r}) = v_{ext}(\vec{r}) + \int d^3r' \frac{e^2 n^{(1)}(\vec{r'})}{4\pi\epsilon_0|\vec{r} - \vec{r'}|} + \frac{\delta E_{xc}[n^{(1)}]}{\delta n^{(1)}(\vec{r})}. \tag{3.22}$$

Both equations, together with the density constraint

$$n^{(1)}(\vec{r}) = \sum_n f_n \sum_\sigma \psi_n^*(\vec{x})\psi_n(\vec{x}), \tag{3.23}$$

form a set of coupled equations, that determine the electron density and the total energy. This set of coupled equations, Eqs.3.21, 3.22, and 3.23, is what is solved in the so-called self-consistency loop. Once the set of self-consistent equations has been solved, we obtain the electron density and we can evaluate the total energy. In practice, one often makes the assumption that the non-interacting electrons in the effective potential closely resemble the true interacting electrons, and extracts a wealth of other physical properties from the Kohn-Sham wave functions $|\psi_n\rangle$ and the Kohn-Sham energies ϵ_n. However, there is little theoretical backing for this approach and, if it fails, one should not blame density functional theory!

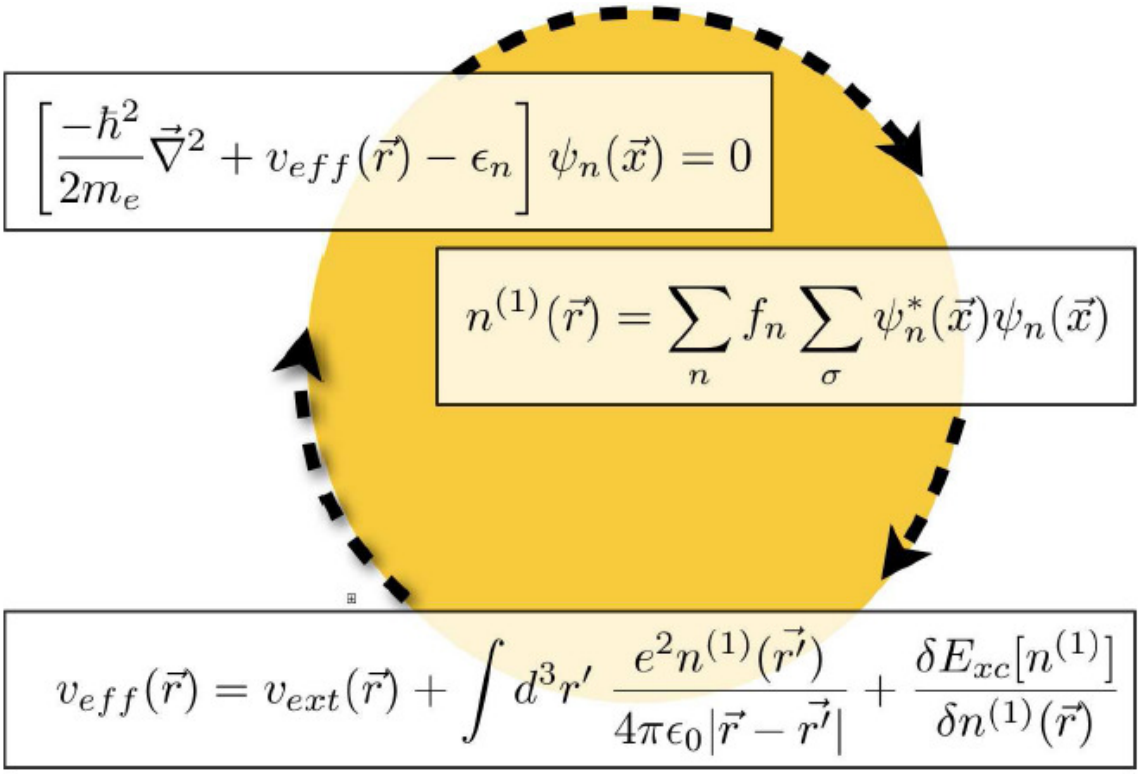

Figure 3.3: **Self-consistency cycle** -

3.2.7 Is there a density functional?

The argument leading to the self-consistent equations, Eqs.3.21, 3.22, and 3.23, relied entirely on the hope that exchange correlation functional can be expressed as a functional of the electron density. In fact, this can easily be shown, if we restrict us to ground state densities. The proof goes back to the seminal paper by Levy [43, 44].
Imagine that one could construct all fermionic many-particle wave functions. For each of these wave functions, we can determine in a unique way the electron density

$$n^{(1)}(\vec{r}) = N \sum_\sigma \int d^3x_2 \ldots \int d^3x_N |\Psi(\vec{x}, \vec{x}_2, \ldots \vec{x}_N)|^2. \tag{3.24}$$

Having the electron densities, we sort the wave functions according to their density. For each density, I get a mug $M[n^{(1)}]$ that holds all wave functions with that density, which is written on the label of the mug.
Now we turn to each mug $M[n^{(1)}]$ in sequence and determine for each the wave function with the lowest energy. Because the external potential energy is the same for all wave functions with the same density, we need to consider only the kinetic energy operator $\hat{T}$

and the operator $\hat{W}$ of the electron-electron interaction, and we do not need to consider the external potential.

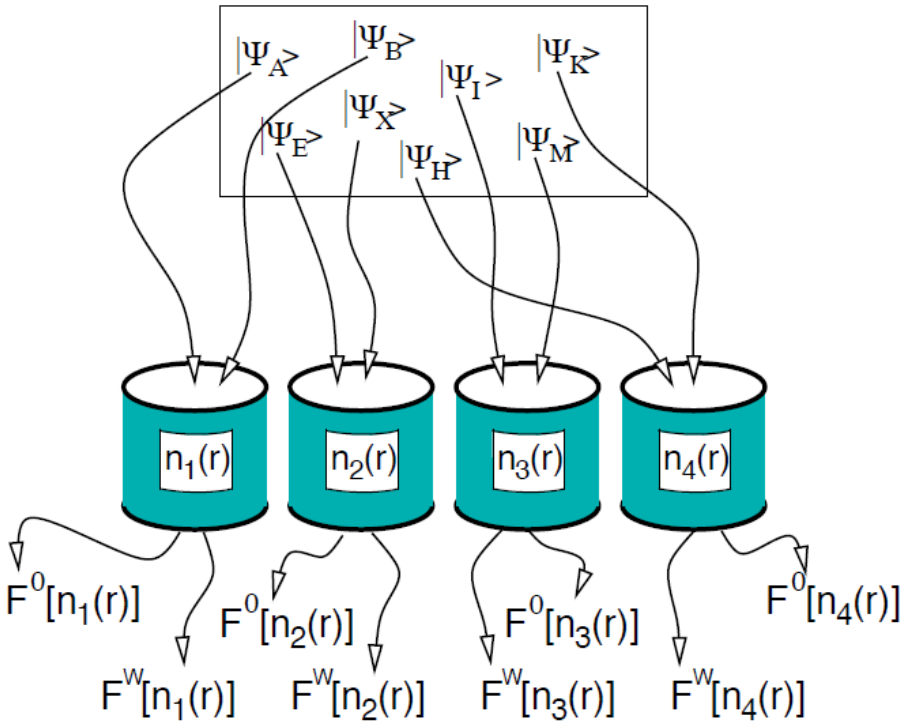

Figure 3.4: **Functional proof** - Illustration for Levy's proof that there exists a density functional.

$$F^{\hat{W}}[n^{(1)}] = \min_{|\psi\rangle \in M[n^{(1)}]} \langle \Psi | \hat{T} + \hat{W} | \Psi \rangle \tag{3.25}$$

$F^{\hat{W}}[n^{(1)}]$ is the universal density functional. It is universal in the sense that it is an intrinsic property of the electron gas and absolutely independent of the external potential. Next, we repeat the same construction as that for a universal density functional, but now we leave out the interaction $\hat{W}$ and consider only the kinetic energy $\hat{T}$.

$$F^{0}[n^{(1)}] = \min_{|\psi\rangle \in M[n^{(1)}]} \langle \Psi | \hat{T} | \Psi \rangle \tag{3.26}$$

The resulting functional $F^0[n^{(1)}]$ is nothing but the kinetic energy of non-interacting electrons $T_s[n^{(1)}]$.
Now we can write down the total energy as functional of the density

$$E[n^{(1)}] = F^{\hat{W}}[n^{(1)}] + \int d^3r \; v_{ext}(\vec{r}) n^{(1)}(\vec{r}) \tag{3.27}$$

When we compare Eq.3.27 with Eq.3.20, we obtain an expression for the exchange correlation energy.

$$E_{xc}[n^{(1)}] = F^{\hat{W}}[n^{(1)}(\vec{r})] - F^{0}[n^{(1)}(\vec{r})] - \frac{1}{2}\int d^3r \int d^3r' \frac{e^2 n^{(1)}(\vec{r}) n^{(1)}(\vec{r'})}{4\pi\epsilon_0 |\vec{r} - \vec{r'}|} \tag{3.28}$$

This completes the proof that the exchange correlation energy is a functional of the electron density. The latter was the assumption for the derivation of the set of self-consistent equations, Eqs.3.21, 3.22, and 3.23 for the Kohn-Sham wave functions $\psi_n(\vec{x})$.

With this, I finish the description of the theoretical basis of density-functional theory. We have seen that the total energy can rigorously be expressed as a functional of the density or, in practice, as a functional of a set of one-particle wave functions, the Kohn-Sham wave functions and their occupations. Density functional theory per se is not an approximation and, in contrast to common belief, it is not a mean-field approximation. Nevertheless, we need to introduce approximations to make density functional theory work. This is because the exchange correlation energy $E_{xc}[n^{(1)}]$ is not completely known. These approximations will be discussed in the next section.

3.3 Jacob's ladder of density functionals

The development of density functionals is driven by mathematical analysis of the exact exchange correlation hole [35, 42], physical insight and numerical benchmark calculations on real systems. The functionals evolved in steps from one functional form to another, with several parametrizations at each level. Perdew pictured this development by Jacob's ladder leading up to heaven [35, 45]. In his analogy the different rungs of the ladder represent the different levels of density functionals leading to the unreachable, ultimately correct functional.

3.3.1 LDA, the big surprise

The first density functionals used in practice were based on the local-density approximation (LDA). The hole function for an electron at position $\vec{r}$ has been approximated by the one of a homogeneous electron gas with the same density as $n^{(1)}(\vec{r})$. The exchange correlation energy for the homogeneous electron gas has been obtained by quantum Monte Carlo calculations [46] and analytic calculations [47]. The local density approximation has been

generalized early to local spin-density approximation (LSD) [48].
Truly surprising was how well the theory worked for real systems. Atomic distances could be determined within a few percent of the bond length and energy differences in solids were surprisingly good.
This was unexpected, because the density in real materials is far from homogeneous. Gunnarsson and Lundquist [49] explained this finding with sumrules that are obeyed by the local density approximation: Firstly, the exchange correlation energy depends only on the spherical average of the exchange correlation hole. Of the radial hole density only the first moment contributes, while the second moment is fixed by the sum-rule that the electron density of the hole integrates to -1. Thus we can use

$$\int d^3r \frac{e^2 h(\vec{r}_0, \vec{r})}{4\pi\epsilon_0 |\vec{r} - \vec{r}_0|} = -\frac{e^2}{4\pi\epsilon_0} \frac{\int_0^\infty dr\ r \langle h(\vec{r}_0, \vec{r'}) \rangle_{|\vec{r'} - \vec{r}_0| = r}}{\int_0^\infty dr\ r^2 \langle h(\vec{r}_0, \vec{r'}) \rangle_{|\vec{r'} - \vec{r}_0| = r}} \tag{3.29}$$

where the angular brackets imply the angular average of $\vec{r'} - \vec{r}_0$. This dependence on the hole density is rather insensitive to small changes of the hole density. Even for an atom, the *spherically averaged* exchange hole closely resembles that of the homogeneous electron gas [32]. The main deficiency of the LDA was the strong overbinding with bond energies in error by about one electron volt. On the one hand, this rendered LDA useless for most applications in chemistry. On the other hand, the problem was hardly visible in solid state physics where bonds are rarely broken, but rearranged so that errors cancelled.

3.3.2 GGA, entering chemistry

Being concerned about the large density variations in real materials, one tried to include the first terms of a Taylor expansion in the density gradients. These attempts failed miserably. The culprit has been a violation of the basic sum rules as pointed out by Perdew [50]. The cure was a cutoff for the gradient contributions at high gradients, which lead to the class of generalized gradient approximations (GGA) [51].
Becke [52] provides an intuitive description for the workings of GGA's, which I will sketch here in a simplified manner: Becke uses an *ansatz* $E_{xc} = \int d^3r\ A(n(\vec{r}))F(x(\vec{r}))$ for the exchange-correlation energy where $n(\vec{r})$ is the local density and $x = |\vec{\nabla} n|/n^{\frac{4}{3}}$ is a dimensionless reduced gradient. Do not confuse this symbol with the combined position-and-spin coordinate $\vec{x}$. The function A is simply the LDA expression and $F(x)$ is the so-called enhancement factor. The large-gradient limit of $F(x)$ is obtained from

a simple physical argument: Somewhat surprisingly, the reduced gradient is largest

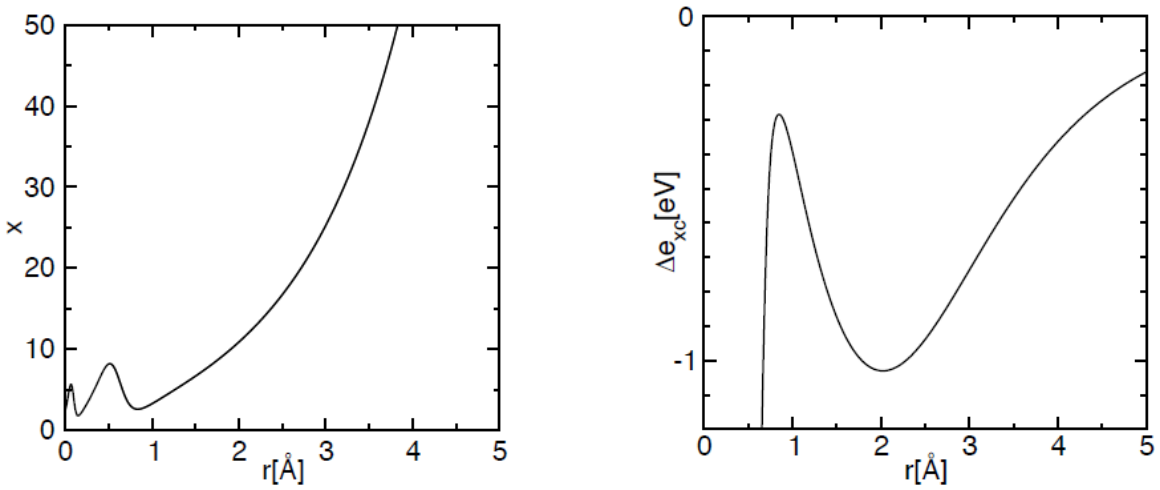

Figure 3.5: **Gradient correction** - Left figure: reduced density gradient $x = |\vec{\nabla} n|/n^{\frac{4}{3}}$ of a silicon atom as function of distance from the nucleus demonstrating that the largest reduced gradients occur in the exponential tails. Right figure: additional contribution from the gradient correction (PBE versus PW91 LDA) of the exchange correlation energy per electron. The figure demonstrates that the gradient correction stabilizes the tails of the wave function. The covalent radius of silicon is at 1.11Å

not near the nucleus but in the exponentially decaying charge-density tails as shown in Fig.3.5. For an electron that is far from an atom, the hole is on the atom, because a hole can only be dug where electrons are. Thus the Coulomb interaction energy of the electron with its hole is $-\frac{e^2}{4\pi\epsilon_0 r}$, where r is the distance of the reference electron from the atom. The enhancement factor can now be obtained by enforcing this behavior for exponentially decaying densities.

As a result, the exchange and correlation energy per electron in the tail region of the electron density falls of with the inverse distance in GGA, while it has a much faster, exponential decay in the LDA. Thus, the the tail region is stabilized by GGA. This contribution acts like a negative "surface energy".

When a bond between two atoms is broken, the surface is increased. In GGA this bond-breaking process is more favorable than in LDA, and, hence, the bond is weakened. Thus the GGA cures the overbinding error of the LDA.

These gradient corrections greatly improved the bond energies and made density functional theory useful also for chemists. The most widely distributed GGA functional is the Perdew- Burke-Ernzerhof (PBE) functional [53].

3.3.3 Meta GGA's

The next level of density functionals are the so-called meta GGA's [54–56] that include not only the gradient of the density, but also the second derivatives of the density. These functionals can be reformulated so that the additional parameter is the kinetic energy density instead of the second density derivatives. Perdew recommends his TPSS functional [57].

3.3.4 Hybrid functionals

Another generation of functionals are hybrid functionals [58, 59], which replace some of the exchange energy by the exact exchange

$$E_X^{HF} = -\frac{1}{2}\sum_{m,n} \bar{f}_m \bar{f}_n \int d^4x \int d^4x' \frac{e^2 \psi_m^*(\vec{x})\psi_n(\vec{x})\psi_n^*(\vec{x'})\psi_m(\vec{x'})}{4\pi\epsilon_0|\vec{r}-\vec{r'}|} \tag{3.30}$$

where $\bar{f}_n$ and the $\psi_n(\vec{x})$ are the Kohn-Sham occupations and wave functions, respectively. The motivation for this approach goes back to the adiabatic connection formula [49, 60, 61]

$$E_{xc}[n(r)] = \int_0^1 d\lambda\, U_{xc}^{\lambda\hat{W}}[n(r)] = \int d^3r\, n(r) \int_0^1 d\lambda \frac{1}{2} \int d^3r' \frac{h_\lambda(\vec{r},\vec{r'})}{4\pi\epsilon|\vec{r}-\vec{r'}|} \tag{3.31}$$

which expresses the exchange correlation energy as an integral of the potential energy of exchange and correlation over the interaction strength. Here the interaction in the Hamiltonian is scaled by a factor λ, leading to a λ-dependent universal functional $F^{\lambda\hat{W}}[n^{(1)}]$. The interaction energy can be expressed by

$$\begin{aligned} F^{\hat{W}}[n] &= F^0[n] + \int_0^1 d\lambda \frac{d}{d\lambda} F^{\lambda\hat{W}}[n] \\ &= T_s[n] + \frac{1}{2}\int d^3r' \frac{e^2 n(\vec{r})n(\vec{r'})}{4\pi\epsilon_0|\vec{r}-\vec{r'}|} + \int_0^1 d\lambda\, U_{xc}^{\lambda\hat{W}}[n] \end{aligned} \tag{3.32}$$

which leads via Eq.3.28 to Eq.3.31. Using perturbation theory, the derivative of $F^{\lambda\hat{W}}[n]$ simplifies to the expectation value of the interaction $\langle\Psi(\lambda)|\hat{W}|\Psi(\lambda)\rangle$, which is the potential energy of exchange and correlation evaluated for a many-particle wave function obtained for the specified given interaction strength. The underlying idea of the hybrid functionals is to interpolate the integrand between the end points. In the non-interacting limit, i.e.

for $\lambda = 0$ the integrand $U_{xc}^{\lambda\hat{W}}$ is exactly given by the exact exchange energy of Eq.3.30. For the full interaction, on the other hand, the LDA or GGA functionals are considered correctly. Thus a linear interpolation would yields

$$E_{xc} = \frac{1}{2}(U_{xc}^{0} + U_{xc}^{\hat{W}}) = \frac{1}{2}(E_X^{HF} + U_{xc}^{\hat{W}}) = E_{xc}^{GGA} + \frac{1}{2}(E_X^{HF} - E_X^{GGA}) \tag{3.33}$$

Depending on whether the λ-dependence is a straight line or whether it is convex, the weight factor may be equal or smaller than $\frac{1}{2}$. Perdew [62] has given arguments that a factor $\frac{1}{4}$ would actually be better than a factor $\frac{1}{2}$.
Hybrid functionals perform substantially better than GGA functionals regarding binding energies, band gaps and reaction energies. However, they are flawed for the description of solids. The reason is that the exact exchange hole in a solid is very extended. These long-range tails are screened away quickly when the interaction is turned on, because they are cancelled by the correlation. Effectively, we should use a smaller mixing factor for the long range part of the exchange hole. This can be taken into account, by cutting off the long-range part of the interaction for the calculation of the Hartree-Fock exchange [63]. This approach improves the results for band gaps while reducing the computational effort [64].
The effective cancellation of the long-ranged contribution of exchange with a similar contribution from correlation, which is also considered properly already in the LDA, is one of the explanation for the superiority of the LDA over the Hartree-Fock approximation. The most widely used hybrid functional is the B3LYP functional [65], which is, however, obtained from a parameter fit to a database of simple molecules. The functional PBE0 [66, 67] is born out of the famous PBE GGA functional and is a widely distributed parameter-free functional.

3.3.5 LDA+U and local hybrid functionals

Starting from a completely different context, Anisimov et. al. [68] introduced the so-called LDA+U method, which, as described below, has some similarities to the hybrid functionals above.
The main goal was to arrive at a proper description of transition metal oxides, which tend to be Mott insulators, while GGA calculations predict them often to be metals. The remedy was to add a correlation term[7] [69] borrowed from the Hubbard model and

[7] The expression given here looks unusually simple. This is due to the notation of spin orbitals, which takes care of the spin indices.

to correct the resulting double counting of the interactions by E_{dc}.

$$E = E^{GGA} + \frac{1}{2}\sum_R \sum_{\alpha,\beta,\gamma,\delta,\in C_R} U_{\alpha,\beta,\gamma,\delta}\Big(\rho_{\gamma,\alpha}\rho_{\delta,\beta} - \rho_{\delta,\alpha}\rho_{\gamma,\beta}\Big) - E_{dc} \tag{3.34}$$

$$U_{\alpha,\beta,\gamma,\delta} = \int d^4x \int d^4x' \frac{e^2 \chi^*_\alpha(\vec{x})\chi^*_\beta(\vec{x'})\chi^*_\gamma(\vec{x})\chi_\delta(\vec{x})}{4\pi\epsilon_0|\vec{r}-\vec{r'}|} \tag{3.35}$$

$$\rho_{\alpha,\beta} = \langle\pi_\alpha|\psi_n\rangle f_n \langle\psi_n|\pi_\beta\rangle \tag{3.36}$$

where $|\chi_\alpha\rangle$ are atomic tight-binding orbitals and $|\pi_\alpha\rangle$ are their projector functions.[8] The additional energy is a Hartree-Fock exchange energy, that only considers the exchange for specified sets of local orbitals. The exchange term does only consider a subset of orbitals C_R for each atom R and it ignores the contribution involving orbitals centered on different atoms.

Novak et al. [70] made the connection to the hybrid functionals explicit and restricted the exact exchange contribution of a hybrid functional to only a shell of orbitals. While in the LDA+U method the bare Coulomb matrix elements are reduced by a screening factor, in the hybrid functionals it is the mixing factor that effectively plays the same role. Both LDA+U and the local hybrid method have in common that they radically remove the contribution of off-site matrix elements of the interaction. Tran et al. [71] applied this method to transition metal oxides and found results that are similar to those of the full implementation of hybrid functionals.

3.3.6 Van der Waals interactions

One of the major difficulties for density functionals is the description of van der Waals forces, because it is due to the quantum mechanical synchronization of charge fluctuations on distinct molecules. I refer the reader to the work made in the group of Lundqvist [72–74].

[8] Projector functions obey the biorthogonality conditional $\langle\chi_\alpha|\pi_\beta\rangle = \delta_{\alpha,\beta}$. Within the sub-Hilbert space of the tight-binding orbitals, i.e. for wave functions of the form $|\psi\rangle = \sum_\alpha |\chi_\alpha\rangle c_\alpha$, the projector functions decompose the wave function into tight binding orbitals, i.e. $|\psi\rangle = \sum_\alpha |\chi_\alpha\rangle\langle\pi_\alpha|\psi\rangle$. A similar projection is used extensively in the projector augmented-wave method described later.

3.4 Benchmarks, successes and failures

The development of density functionals has profited enormously from careful benchmark studies. The precondition is a data set of test cases for which reliable and accurate experimental data exist. The most famous data sets are the G1 and G2 databases [75–78] that have been set up to benchmark quantum-chemistry codes. Becke [59, 79–82] set a trend by using these large sets of test cases for systematic studies of density functionals. In order to separate out the accuracy of the density functionals, it is vital to perform these calculations on extremely accurate numerical methods. Becke used basis set free calculations that were limited to small molecules, while being extremely accurate. Paier et. al. [64, 83–85] have later performed careful comparisons of two methods, Gaussian and the projector augmented-wave method, to single out the error of the electronic structure method.
Overall, the available density functionals predict molecular structures very well. Bond distances agree with the experiment often within one percent. Bond angles come out within a few degrees. The quality of total energies depends strongly on the level of functionals used. On the LDA level bonds are overestimated in the 1 eV range, on the GGA level these errors are reduced to a about 0.3 eV, and hybrid functionals reduce the error by another factor of 2. The ultimate goal is to reach chemical accuracy, which is about 0.05 eV. Such an accuracy allows to predict reaction rates at room temperature within a factor of 10.
Band gaps are predicted to be too small with LDA and GGA. The so-called band gap problem has been one of the major issues during the development of density functionals. Hybrid functionals clearly improve the situation. A problem is the description of materials with strong electron correlations. For LDA and GGA many insulating transition metal oxides are described as metals. This changes again for the hybrid functionals, which turns them into antiferromagnetic insulators, which is a dramatic improvement.

3.5 Electronic structure methods

In this second part of this chapter, I will address the problem of how to solve the Kohn-Sham equations and how to obtain the total energy and other observables. It is convenient to use a slightly different notation: Instead of treating the nuclei via an external potential, we combine all electrostatic interactions into a single double integral.

This brings the total energy into the form

$$E\Big[\{\psi_n(\vec{r})\},\{\vec{R}_R\}\Big] = \sum_n f_n\langle\psi_n|\frac{\hat{\vec{p}}^2}{2m_e}|\psi_n\rangle + \frac{1}{2}\int d^3r\int d^3r'\,\frac{e^2\Big(n(\vec{r})+Z(\vec{r})\Big)\Big(n(\vec{r'})+Z(\vec{r'})\Big)}{4\pi\epsilon_0|\vec{r}-\vec{r'}|} + E_{xc}[n], \tag{3.37}$$

where $Z(\vec{r}) = -\sum_R Z_R\delta\Big(\vec{r}-\vec{R}_R\Big)$ is the nuclear charge density expressed in electron charges.
Z_R is the atomic number of a nucleus at position $\vec{R}_R$.
The electronic ground state is determined by minimizing the total energy functional $E[\Psi_n]$ of Eq.3.37 at a fixed ionic geometry. The one-particle wave functions have to be orthogonal. This constraint is implemented with the method of Lagrange multipliers. We obtain the ground-state wave functions from the extremum condition for

$$Y\Big[\{|\psi_n\rangle\},\Lambda\Big] = E\Big[\{|\psi_n\rangle\}\Big] - \sum_{n,m}\Big[\langle\psi_n|\psi_m\rangle-\delta_{n,m}\Big]\Lambda_{n,m} \tag{3.38}$$

with respect to the wave functions and the Lagrange multipliers $\Lambda_{n,m}$. The extremum condition for the wave functions has the form

$$\hat{H}|\psi_n\rangle f_n = \sum_m |\psi_m\rangle\Lambda_{n,m}, \tag{3.39}$$

where $\hat{H} = \frac{1}{2m_e}\hat{\vec{p}}^2 + \hat{v}_{eff}$ is the effective one-particle Hamilton operator.
The corresponding effective potential depends itself on the electron density via

$$v_{eff}(\vec{r}) = \int d^3r'\,\frac{e^2\Big(n(\vec{r'})+Z(\vec{r'})\Big)}{4\pi\epsilon_0|\vec{r}-\vec{r'}|} + \mu_{xc}(\vec{r})\ , \tag{3.40}$$

where $\mu_{xc}(\vec{r}) = \frac{\delta E_{xc}[n(\vec{r})]}{\delta n(\vec{r})}$ is the functional derivative of the exchange and correlation functional.
After a unitary transformation that diagonalizes the matrix of Lagrange multipliers Λ, we obtain the Kohn-Sham equations

$$\hat{H}|\psi_n\rangle = |\psi_n\rangle\epsilon_n\,. \tag{3.41}$$

The one-particle energies ϵ_n are the eigenvalues of the matrix with the elements $\Lambda_{n,m}(f_n + f_m)/(2f_n f_m)$ [86].
The one-electron Schrödinger equations, namely the Kohn-Sham equations given in Eq.3.21, still pose substantial numerical difficulties: (1) in the atomic region near the nucleus, the kinetic energy of the electrons is large, resulting in rapid oscillations of the wavefunction that require fine grids for an accurate numerical representation. On the other hand, the large kinetic energy makes the Schrödinger equation stiff, so that a change of the chemical environment has little effect on the shape of the wavefunction. Therefore, the wavefunction in the atomic region can be represented well already by a small basis set. (2) In the bonding region between the atoms the situation is opposite. The kinetic energy is small and the wavefunction is smooth. However, the wavefunction is flexible and responds strongly to the environment. This requires large and nearly complete basis sets.
Combining these different requirements is non-trivial and various strategies have been developed.

- The atomic point of view has been most appealing to quantum chemists. Basis functions are chosen that resemble atomic orbitals. This choice exploits that the wavefunction in the atomic region can be described by a few basis functions, while the chemical bond is described by the overlapping tails of these atomic orbitals. Most techniques in this class are a compromise of, on the one hand, a well adapted basis set, where the basis functions are difficult to handle, and, on the other hand, numerically convenient basis functions such as Gaussians, where the inadequacies are compensated by larger basis sets.

- Pseudopotentials regard an atom as a perturbation of the free electron gas. The most natural basis functions for the free electron gas are plane waves. Plane-wave basis sets are in principle complete and suitable for sufficiently smooth wavefunctions. The disadvantage of the comparably large basis sets required is offset by their extreme numerical simplicity. Finite plane-wave expansions are, however, absolutely inadequate to describe the strong oscillations of the wavefunctions near the nucleus. In the pseudopotential approach the Pauli repulsion by the core electrons is therefore described by an effective potential that expels the valence electrons from the core region. The resulting wavefunctions are smooth and can be represented well by plane waves. The price to pay is that all information on the charge density and wavefunctions near the nucleus is lost.

- Augmented-wave methods compose their basis functions from atom-like wavefunctions in the atomic regions and a set of functions, called envelope functions, appropriate for the bonding in between. Space is divided accordingly into atom-centered spheres, defining the atomic regions, and an interstitial region in between. The partial solutions of the different regions are matched with value and derivative at the interface between atomic and interstitial regions.

The projector augmented-wave method is an extension of augmented wave methods and the pseudopotential approach, which combines their traditions into a unified electronic structure method.
After describing the underlying ideas of the various approaches, let us briefly review the history of augmented wave methods approach. We do not discuss the atomic-orbital based methods and pseudopotential approach, because our focus is the APW method and its ancestors.

3.5.1 The APW method

Although the pseudopotential method is extremely useful, there are reasons why alternatives could be attractive. Is the introduction of the pseudopotential completely innocent? What do you do if you are interested in information that is inherently contained in the region near the nucleus (hyperfine fields for instance, or core level excitations)? Can the basis set be made more efficient? Therefore, we will search for a basis set that uses other functions than plane waves, and that does not require the introduction of a pseudopotential. Such a basis set will have to be more efficient, but of course we do not want it to be biased. Our first example of this will be the *Augmented Plane Wave* (APW) basis set. Right from the beginning it has to be said that the APW-method itself is of no practical use any more today. But for didactical reasons it is advantageous to discuss APW first, before going to its successors, LAPW and APW+lo [9].
The ideas that lead to the APW basis set are very similar to what made us to introduce the pseudopotential. In the region far away from the nuclei, the electrons are more or less 'free'. Free electrons are described by plane waves[10]. Close to the nuclei, the electrons behave quite as they were in a free atom, and they could be described more efficiently by

[9] Reference text: Stefaan Cottenier , "Density Functional Theory and the Family of (L)APW-methods: a step-by-step introduction", ISBN 978-90-807215-1-7

[10] Plane waves are eigenfunctions of a Hamiltonian with zero potential.

atomic like functions. Space is therefore divided now in two regions: around each atom[11] a sphere with radius R_α is drawn (call it S_α). Such a sphere is often called a *muffin tin sphere*, the part of space occupied by the spheres is the *muffin tin sphere*. The remaining space outside the spheres is called the *interstitial region* (call it I). One augmented plane wave (APW) used in the expansion of $\psi_{\vec{k}}^n$ is defined as:

$$\phi_{\vec{K}}^{\vec{k}}(\vec{r},E) = \begin{cases} \frac{1}{\sqrt{V}} e^{i(\vec{k}+\vec{K}).\vec{r}} & \vec{r} \in I \\ \\ \sum_{l,m} A_{lm}^{\alpha,\vec{k}+\vec{K}} u_l^\alpha(r',E) Y_m^l(\hat{r}') & \vec{r} \in S_\alpha \end{cases} \tag{3.42}$$

The symbols $\vec{k}$, $\vec{K}$ and $\vec{r}$ keep their usual meaning, V is the volume of the unit cell. Note that the APW basis set is $\vec{k}$-dependent, as was the plane wave basis set. The position

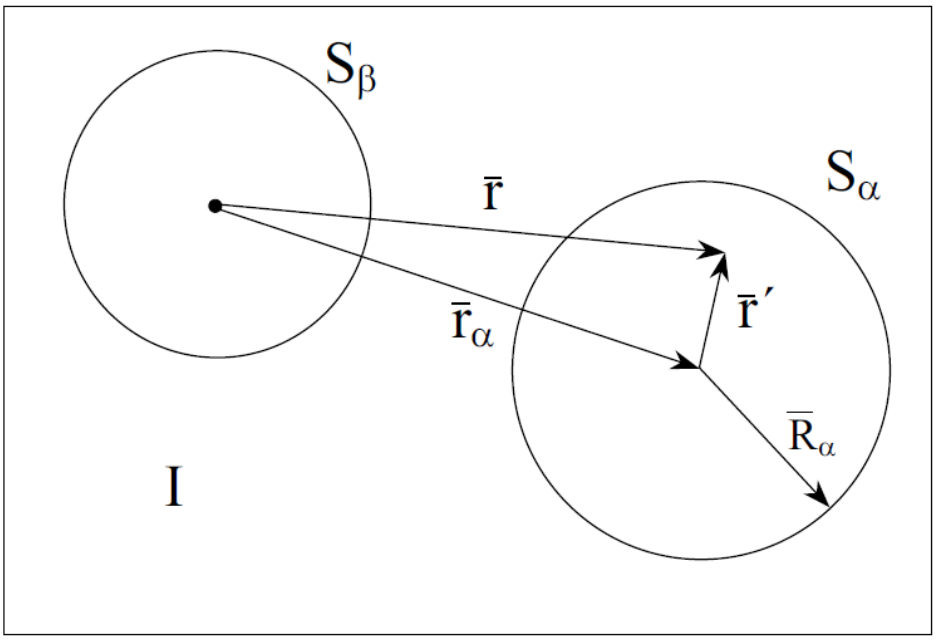

Figure 3.6: **APW method** - Division of a unit cell in muffin tin regions and the interstitial region, for a case with two atoms. The black dot is the origin of the axis system (which may but need not to coincide with the nucleus of an atom).

inside the spheres is given with respect to the center of each sphere by $\vec{r}' = \vec{r} - \vec{r}_\alpha$ (see Fig.3.6). The length of $\vec{r}'$ is r', and the angles θ' and ϕ' specifying the direction of $\vec{r}'$ in spherical coordinates, are indicated as $\hat{r}'$. The Y_m^l are spherical harmonics. The $A_{lm}^{\alpha,\vec{k}+\vec{K}}$ are yet undetermined parameters, as is E. The latter has the dimension of energy. The

[11] Mark the different atoms in the unit cell by a label α. This label is different for all atoms in the unit cell, not just for all inequivalent atoms.

u_l^α are solutions to the radial part of the Schrödinger equation for a free atom α, and this at the energy E. For a true free atom, the boundary condition that $u_l^\alpha(r, E)$ should vanish for $r \to \infty$, limits the number of energies E for which a solution u_l^α can be found. But as this boundary condition does not apply here, we can find a numerical solution for any E. Hence, the u_l^α themselves do not correspond to something physical, but that doesn't harm: they are only part of a basis function, not of the searched eigenfunction itself. And because they are close to how the actual eigenfunction will look like in that region of the crystal, they will do their job as basis function very efficiently.
If an eigenfunction would be discontinuous, its kinetic energy would not be well-defined. Such a situation can therefore never happen, and we have to require that the plane wave outside the sphere matches the function inside the sphere over the complete surface of the sphere (in value, not in slope). That seems a weird thing to do: a plane wave is oscillating and has a unique direction built in, how can it match another function based on spherical harmonics over the entire surface of a sphere? To see how this is possible, we expand the plane wave in spherical harmonics about the origin of the sphere of atom α:

$$\frac{1}{\sqrt{V}} e^{i(\vec{k}+\vec{K}).\vec{r}} = \frac{4\pi}{\sqrt{V}} e^{i(\vec{k}+\vec{K}).\vec{r}_\alpha} \sum_{l,m} i^l j_l \left(\left| \vec{k} + \vec{K} \right| |\vec{r}'| \right) Y_m^{l*} \left(\hat{\vec{k} + \vec{K}} \right) Y_m^l (\hat{r}') \tag{3.43}$$

$j_l(x)$ is the Bessel function of order l. Requiring this at the sphere boundary (where $\vec{r}' = \vec{R}_\alpha$, which defines $\vec{R}_\alpha$) to be equal to the lm-part of Eq.3.42 easily yields:

$$A_{lm}^{\alpha, \vec{k}+\vec{K}} = \frac{4\pi i^l e^{i(\vec{k}+\vec{K}).\vec{r}_\alpha}}{\sqrt{V} u_l^\alpha(\vec{R}_\alpha, E)} j_l \left(\left| \vec{k} + \vec{K} \right| R_\alpha \right) Y_m^{l*} \left(\hat{\vec{k} + \vec{K}} \right) \tag{3.44}$$

This uniquely defines the $A_{lm}^{\alpha, \vec{k}+\vec{K}}$, apart from the still undetermined E. In principle there are an infinite number of terms in Eq.3.43, which would force us to use an infinite number of $A_{lm}^{\alpha, \vec{k}+\vec{K}}$ in order to create the matching. In practice we will have to truncate at some value l_{max}. What would be a reasonable choice? For a given l_{max}, $Y_m^{l_{max}}(\theta, \phi)$ can have at most $2l_{max}$ nodes along a great circle (i.e. $\theta = 0 \to 2\pi$ for any fixed ϕ) of the α-sphere (see Fig.3.6). Converted into nodes per unit of length, this is $2l_{max}/(2\pi R_\alpha) = l_{max}/(\pi R_\alpha)$. If a plane wave should match with this, there should be plane waves with at least a similar number of nodes per unit of length available. The plane wave with the shortest period $2\pi/K_{max}$ has $2/(2\pi/K_{max}) = K_{max}/\pi$ nodes per unit of length. The cut-off for the plane waves (K_{max}) and for the angular functions (l_{max}) are of comparable quality if the number of nodes per unit of length is identical. This yields the condition $R_\alpha K_{max} = l_{max}$. This allows to determine a good l_{max} for a given K_{max}. A finite value for l_{max} means

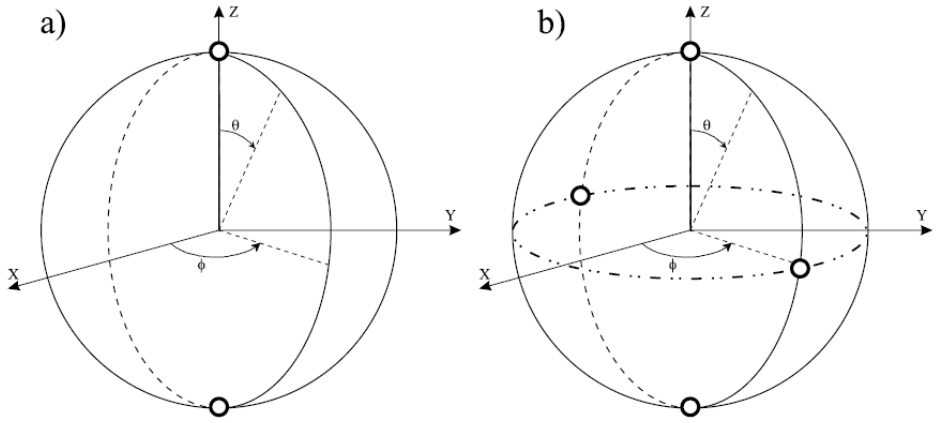

Figure 3.7: **In a) and b)** - a great circle for some arbitrary value of ϕ is drawn. The points on the circle for which a) $Y_{m=2}^{l=2}$ or b) $Y_{m=1}^{l=2}$ is zero, are indicated by white points. In a) there are no other points on which $Y_{m=2}^{l=2}$ is zero. In b) all other such points for $Y_{m=1}^{l=2}$ fall on a horizontal circle with $\theta = \pi/2$ (point-dashed circle). In both cases, the number of zeros along a great circle is at most $2.l$. Remember: $Y_{m=2}^{l=2} = \frac{1}{4}\sqrt{\frac{15}{2\pi}}\sin^2\theta e^{2i\phi}$ and $Y_{m=1}^{l=2} = -\sqrt{\frac{15}{8\pi}}\sin\theta\cos\theta e^{i\phi}$.

that for each APW the matching at the sphere boundaries will not be exact, but good enough to work with. It is not useful to make l_{max} larger than the condition $R_\alpha K_{max}$ requires, as it would lead to unstable behavior at the sphere boundary (you can compare this with fitting a polynomial of high order through a limited number of points: the fit will be 'perfect', but not very meaningful). Therefore, it is also clear now that the muffin tin radii for the different atoms should not be too different: if they were, a value for l_{max} that is suitable for each atom would not exist.

Now you should be able to visualize the meaning of a single APW $\phi_{\vec{K}}^{\vec{k}}(\vec{r}, E)$ of Eq.3.42: it is an oscillating function that runs through the unit cell. Whenever it encounters an atom on its path, the simple oscillating behavior is changed into something more complex inside the muffin tin sphere of that atom. Nevertheless, the function values inside and outside the sphere smoothly match, which is taken care of by a set of $\sum_{l=1}^{l_{max}} 2l_{max} + 1$ coefficients $A_{lm}^{\alpha,\vec{k}+\vec{K}}$ that is different for each atom (the atom determines α , the APW under consideration determines $\vec{k}$ and $\vec{K}$, all l up to l_{max} are present, with the corresponding values of m).

At first sight, it looks like we can now use the APW's as a basis set, and proceed in the same way as for the plane wave basis set in order to determine the coefficients $c_{\vec{K}}^{n,\vec{k}}$ in the expansion of the searched eigenfunction. However, this does not work. We did not settle the parameter E yet. It turns out that in order to describe an eigenstate $\psi_{\vec{K}}^{n}(\vec{r})$ accurately with APW's, one has to set E equal to the eigenvalue (or band energy) $\epsilon_{\vec{K}}^{n}$ of

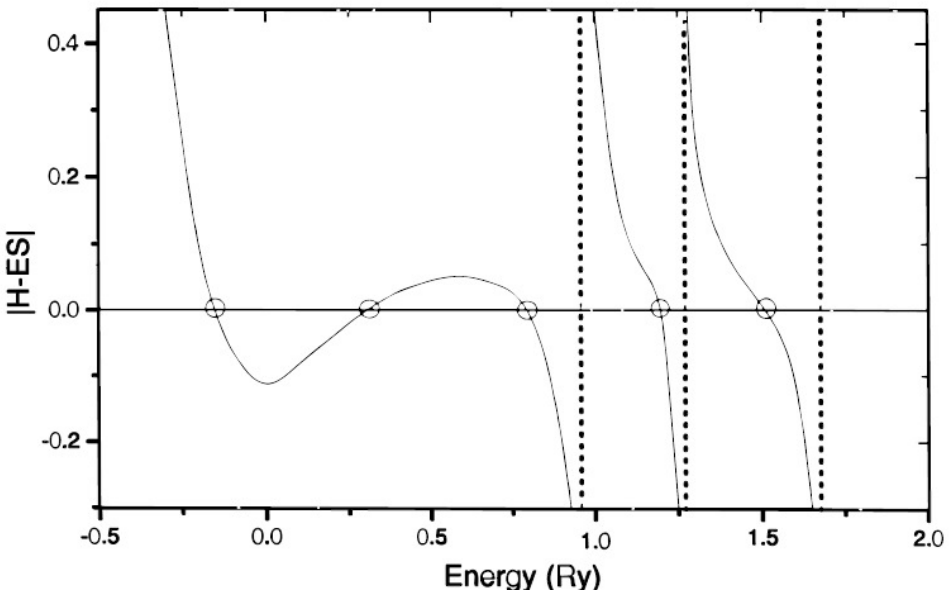

Figure 3.8: **A suggestive visualization of how the roots of the secular equation are searched.** - picture copied from reference [87].

that state. But this is exactly what we are trying to determine! We are hence forced to start with a guessed value for $\epsilon^n_{\vec{K}}$ and take this as E. Now we can determine the APW's, and construct the Hamiltonian matrix elements and overlap matrix (the APW's are not orthogonal). The secular equation is determined, and our guessed $\epsilon^n_{\vec{K}}$ should be a root of it. Usually it is not, hence we have to try a second guess. Due to this new E , the APW's have to be determined again, and similarly for all matrix elements. With the help of root determination algorithms, this guessing continues until a root -say $\epsilon^{n=1}_{\vec{K}}$- is found. And then the whole procedure starts over for $\epsilon^{n=2}_{\vec{K}}$, etc. (see Fig.3.8 and Fig.3.9). In practice, $K_{max} \approx 3.5\, au^{-1}$ is needed for sufficient accuracy. This is less than the typical value of 5.5 for plane waves and pseudopotentials. The basis set size can be estimated to be about P = 131 for APW, compared to roughly P = 270 for plane waves. The calculation time (mainly determined by matrix diagonalization) scales with the third power of the basis set size, which would suggest APW to be 10 times faster than pseudopotentials. However, with a plane wave basis set, P eigenvalues are found by a single diagonalization, while with APW one diagonalization is needed for every eigenvalue. This makes the APW method inherently slow, much slower than the pseudopotential method.

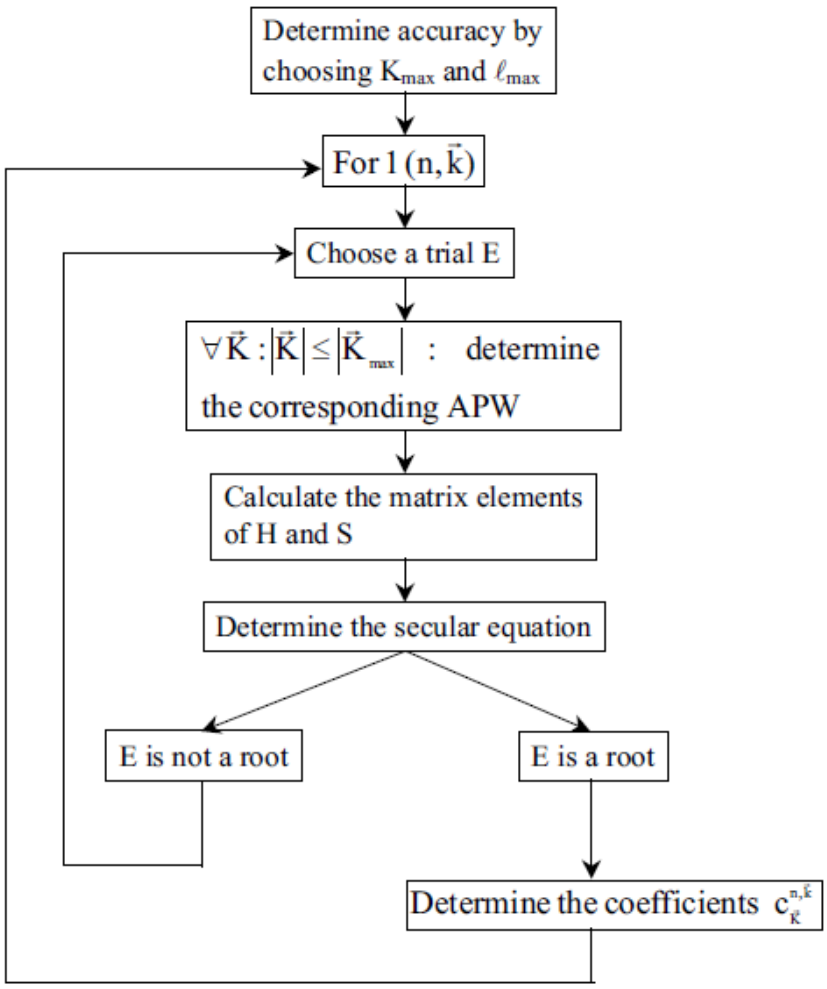

Figure 3.9: **The APW scheme.** - Flowchart of the APW method.

3.5.2 The LAPW method

3.5.2.1 The regular LAPW method

The problem with the APW method was that the $u_l^\alpha(r', E)$ have to be constructed at the - yet unknown - eigenenergy $E = \epsilon_{\vec{k}}^n$ of the searched eigenstate. It would be helpful if we were able to recover $u_l^\alpha(r', \epsilon_{\vec{k}}^n)$ on the fly from known quantities. That is exactly what the *Linearized Augmented Plane Wave* method enables us to do. If we have calculated u_l^α at some energy E_0 , we could make a Taylor expansion to find it at energies not far away from it:

$$u_l^\alpha(r', \epsilon_{\vec{k}}^n) = u_l^\alpha(r', E_0) + (E_0 - \epsilon_{\vec{k}}^n) \underbrace{\left.\frac{\partial u_l^\alpha(r', E)}{\partial E}\right|_{E=E_0}}_{\dot{u}_l^\alpha(r', E_0)} + O(E_0 - \epsilon_{\vec{k}}^n)^2 \tag{3.45}$$

Substituting the first two terms of the expansion in the APW for a fixed E_0 gives the definition of an LAPW. This has a price: the energy difference $(E_0 - \epsilon_{\vec{k}}^n)$ is unknown, and hence a yet undetermined $B_{lm}^{\alpha,\vec{k}+\vec{K}}$ has to be introduced:

$$\phi_{\vec{K}}^{\vec{k}}(\vec{r}) = \begin{cases} \frac{1}{\sqrt{V}} e^{i(\vec{k}+\vec{K}).\vec{r}} & \vec{r} \in I \\ \sum_{l,m} \left(A_{lm}^{\alpha,\vec{k}+\vec{K}} u_l^\alpha(r', E_0) + B_{lm}^{\alpha,\vec{k}+\vec{K}} \dot{u}_l^\alpha(r', E_0) \right) Y_m^l(\hat{r}') & \vec{r} \in S_\alpha \end{cases} \tag{3.46}$$

In order to determine both $A_{lm}^{\alpha,\vec{k}+\vec{K}}$ and $B_{lm}^{\alpha,\vec{k}+\vec{K}}$, we will require that the function in the sphere matches the plane wave both in value and in slope at the sphere boundary. This can be done by using an expression similar to Eq.3.43 and its radial derivative. This results in a 2×2 system from which both coefficients can be solved.
Eq.3.46 is not the final definition of an LAPW yet. Imagine we want to describe an eigenstate $\psi_{\vec{k}}^n$ that has predominantly p-character ($l = 1$) for atom α. This means that in its expansion in LAPW's, the $A_{(l=1)m}^{\alpha,\vec{k}+\vec{K}}$ are large. It is therefore advantageous to choose E_0 near the center of the p-band. In this way, the $O(E_0 - \epsilon_{\vec{k}}^n)^2$–term in Eq.3.45 will remain small, and cutting after the linear term is certainly allowed. We can repeat this argument for every physically important l (s-, p-, d- and f-states, i.e. up to $l = 3$) and for every atom. As a result, we should not choose one universal E_0, but a set of well-chosen $E_{1,l}^\alpha$ up to $l = 3$ (the meaning of the index '1' will become clear in subsection.3.5.2.2.

For higher l , a fixed value can be kept. The final definition of an LAPW is then:

$$\phi^{\vec{k}}_{\vec{K}}(\vec{r}) \;=\; \begin{cases} \frac{1}{\sqrt{V}} e^{i(\vec{k}+\vec{K}).\vec{r}} & \vec{r} \in I \\ \sum_{l,m} \left(A^{\alpha,\vec{k}+\vec{K}}_{lm} u^{\alpha}_{l}(r', E^{\alpha}_{1,l}) + B^{\alpha,\vec{k}+\vec{K}}_{lm} \dot{u}^{\alpha}_{l}(r', E^{\alpha}_{1,l}) \right) Y^{l}_{m}(\hat{r}') & \vec{r} \in S_\alpha \end{cases} \tag{3.47}$$

With the $E^{\alpha}_{1,l}$ being fixed, the basis functions can be calculated once and for all. The same procedure as used for the plane wave basis set can now be applied. One diagonalization will yield P different band energies for this $\vec{k}$.

The accuracy of a plane wave basis set was determined by K_{max}. For the APW or LAPW basis set, it is not incorrect to use the same criterion. However, a better quantity to judge the accuracy here is the product $R^{min}_{\alpha} K_{max}$ between the smallest muffin tin radius and K_{max}. This can be understood as follows. If the smallest muffin tin radius is increased, the closest point a plane wave can come to a nucleus moves farther away from the nucleus. The part of the wave function that need not to be described with plane waves any more, in general will have displayed the steepest behavior, steeper than anywhere else in the interstitial region (it was closest to the nucleus). Less plane waves are needed to describe the remaining, smoother parts of the wave function. K_{max} can be reduced, and a good rule of thumb is that the product $R^{min}_{\alpha} K_{max}$ should remain constant in order to have comparable accuracy. Reducing K_{max} means reducing the size of the matrices, and because matrix diagonalization is very expensive, a larger R^{min}_{α} can significantly reduce the computation time. R^{min}_{α} cannot be too large on the other hand, as the spherical harmonics are not suited to describe the wave functions in the region far away from the nuclei.

Compared to a plane wave basis set, the LAPW basis set can be much smaller. The required K_{max} turns out to be $K_{max} = \frac{7.5 \leftrightarrow 9.0}{R^{min}_{\alpha}} \approx 4\text{au}^{-1}$, depending on the desired accuracy. This yields $P \approx 195$ as basis set size, compared to $P \approx 270$ for plane waves. The calculation time (mainly determined by matrix diagonalization) scales with the third power of the basis set size, which makes LAPW in this respect about 2 to 3 times faster than plane waves. There are other aspects however that slow down LAPW[12], such that in the end it is comparable in speed with plane waves.

[12] The non-orthogonal basis set for instance.

3.5.2.2 LAPW with Local Orbitals (LAPW+LO)

It was not explicitly stated so far which electron states are calculated with the LAPW method. Does it make sense to calculate the 1s orbital of Fe in bcc-Fe? No, because this electron is extremely well bound to the nucleus (-514 Ry), and will behave almost exactly as if it were in a free Fe atom. Such a state is called a *core state*. The criterion for a core state is that it does not participate directly in chemical bonding with other atoms. Therefore, it must be contained entirely in the muffin tin sphere. States that leak out of the muffin tin sphere, are called *valence states*. Valence states participate in chemical bonds, and these states are treated by LAPW. Core states are treated as in free atoms, but subject to the potential due to the valence states.
When applying this definition, it frequently happens that states with the same l but a different principal quantum number n are both valence states. For instance, due to hybridization, Fe in bcc-Fe will have a non-negligible amount of 4p-character in its valence states that are about 0.2 Ry below the Fermi level. But the 3p-states that are 4.3 Ry below the Fermi level are not entirely confined in the core too. Such low-lying valence states are called *semi-core* states. It is not clear how $E^{Fe}_{1,(l=1)}$ should be chosen: close to 3p, close to 4p, at an intermediate value, ...? None of the choices is optimal. This dilemma is solved by adding another type of basis function to the LAPW basis set, called a *local orbital* (LO). A local orbital is defined as:

$$\phi^{lm}_{\alpha,LO}(\vec{r}) = \begin{cases} 0 & \vec{r} \notin I \\ \left(A^{\alpha,LO}_{lm} u^{\alpha}_{l}(r', E^{\alpha}_{1,l}) + B^{\alpha,LO}_{lm} \dot{u}^{\alpha}_{l}(r', E^{\alpha}_{1,l}) + C^{\alpha,LO}_{lm} u^{\alpha}_{l}(r', E^{\alpha}_{2,l})\right) Y^{l}_{m}(\hat{r}') & \vec{r} \in S_{\alpha} \end{cases} \tag{3.48}$$

A local orbital is defined for a particular l and m, and for a particular atom α. A local orbital is zero in the interstitial region and in the muffin tin spheres of other atoms, hence its name *local* orbital. In the muffin tin sphere of atom α, the same $u^{\alpha}_{l}(r', E^{\alpha}_{1,l})$ and $\dot{u}^{\alpha}_{l}(r', E^{\alpha}_{1,l})$ as in the LAPW basis set are used, with as linearization energy $E^{\alpha}_{1,l}$ a value suitable for the highest of the two valence states (4p in our example)[13]. The lower valence state that is much more free-atom-like is sharply peaked at an energy $E^{\alpha}_{2,l}$. A single radial function $u^{\alpha}_{l}(r', E^{\alpha}_{2,l})$ at that same energy will be sufficient to describe it. Local orbitals are not connected to plane waves in the interstitial region, they have hence no $\vec{k}$- or $\vec{K}$-dependence. The three coefficients $A^{\alpha,LO}_{lm}$, $B^{\alpha,LO}_{lm}$ and $C^{\alpha,LO}_{lm}$ are determined by requiring that the LO is normalized, and has zero value and zero slope at the muffin

[13] Linearization energies for two atoms that are equivalent, are taken to be equal.

tin boundary (= it does not leak out of the muffin tin sphere).
Adding local orbitals increases the LAPW basis set size. If for each atom local orbitals for p- and d-states are added, the basis set increases with 3+5=8 functions per atom[14]in the unit cell. This number is rather small compared to typical LAPW basis set sizes of a few hundred functions. The slightly increased computational time is a small price to be paid for the much better accuracy that local orbitals offer, and therefore they are always used.

3.5.3 The APW+lo method

3.5.3.1 The 'pure'APW+lo basis set

The problem with the APW method was the energy dependence of the basis set. This energy dependence could be removed in the LAPW+LO method, at the cost of a somewhat larger basis set size[15]. In the APW+lo method that will be described now, the basis set will be energy independent and still have the same size as in the APW method. In this sense, APW+lo combines the good features of APW and LAPW+LO.
The APW+lo basis set contains two kinds of functions. The first kind are APW's, with a set of fixed energies $E^{\alpha}_{1,l}$:

$$\phi^{\vec{k}}_{\vec{K}}(\vec{r}) = \begin{cases} \frac{1}{\sqrt{V}} e^{i(\vec{k}+\vec{K}).\vec{r}} & \vec{r} \in I \\ \sum_{l,m} A^{\alpha,\vec{k}+\vec{K}}_{lm} u^{\alpha}_{l}(r', E^{\alpha}_{1,l}) Y^{l}_{m}(\hat{r}') & \vec{r} \in S_{\alpha} \end{cases} \tag{3.49}$$

We know from the discussion in Section.3.5.1 that with fixed energies this basis set does not give a good description of the eigenfunctions. The basis set is therefore augmented with a second type of functions. These are *local orbitals*, but another type as the one used in connection with the LAPW method. We abbreviate them therefore as 'lo' instead

[14]Indeed, the more atoms in the unit cell, the more LO's have to be added. In contrast to this, the number of LAPW's does not depend on the number of atoms in the unit cell, but - for a fixed $R^{min}_{\alpha} K_{max}$ and cell symmetry - on the volume of the unit cell, independent on how many atoms appear in it (more atoms mean just more sets of coefficients $A^{\alpha,\vec{k}+\vec{K}}_{lm}$ and $B^{\alpha,\vec{k}+\vec{K}}_{lm}$).
[15]Due to LAPW itself, and due to adding local orbitals.

of as 'LO'. Their definition is:

$$\phi^{lm}_{\alpha,lo}(\vec{r}) = \begin{cases} 0 & \vec{r} \notin I \\ \left(A^{\alpha,lo}_{lm} u^{\alpha}_{l}(r', E^{\alpha}_{1,l}) + B^{\alpha,lo}_{lm} \dot{u}^{\alpha}_{l}(r', E^{\alpha}_{1,l})\right) Y^{l}_{m}(\hat{r}') & \vec{r} \in S_{\alpha} \end{cases} \tag{3.50}$$

The same set of energies $E^{\alpha}_{1,l}$ is used as for the corresponding APW's (although this is not strictly needed). The two coefficients $A^{\alpha,lo}_{lm}$ and $B^{\alpha,lo}_{lm}$ are determined by normalization, and by requiring that the local orbital has zero value at the muffin tin boundary (not zero slope). Hence, both the APW and the local orbital are continuous at the sphere boundary, but for both their first derivative is discontinuous.
For accurate results, the APW+lo basis set appears to require a size that is comparable to the APW method ($K_{max} \approx 3.5\ au^{-1}$, $P \approx 130$). This is less than in the LAPW+LO method ($K_{max} \approx 4\ au^{-1}$, $P \approx 200$). Nevertheless, P eigenvalues are obtained by a single diagonalization, as in LAPW+LO.

3.5.3.2 Mixed LAPW/APW+lo basis sets

The reason why LAPW needs a higher K_{max} than APW+lo can be traced back to a few states that are hard for LAPW. They are:

- Valence d- and f-states.
- States in atoms that have a muffin tin sphere that is much smaller than others spheres in the unit cell.

It is advantageous to treat those states with APW+lo, and keep using LAPW for all other states. Why? Using APW+lo for a state means that per atom $2l + 1$ local orbitals are added to the basis set. This makes an APW+lo basis set for the same $R^{min}_{\alpha} K_{max}$ considerably larger than the LAPW basis set. This is compensated by the fact that a lower $R^{min}_{\alpha} K_{max}$ is needed for accurate results, but nevertheless, it is better to use these extra basis functions only there where they are useful. Such an approach leads to a mixed LAPW/APW+lo basis set: for all atoms α and values of l, equation.3.46 is used. But for one or more atoms α_0 ($r \in S_{\alpha_0}$) and one or more l_0, equation.3.49 is used. Corresponding $\phi^{l_0 m}_{\alpha_0}$ according to equation.3.50 are then added to the basis set. Such a mixed basis set is the recommended choice in WIEN2k[16].

[16] LAPW-code for electronic structure calculation.

3.5.3.3 APW+lo with Local Orbitals (APW+lo+LO)

With APW+lo basis functions, the same problem with semi-core states appears as described in subsection.3.5.2.2. It will be remediated in the same way: by adding Local Orbitals (LO). The definition of a local orbital for APW+lo is:

$$\phi^{lm}_{\alpha,LO}(\vec{r}) = \begin{cases} 0 & \vec{r} \notin I \\ \left(A^{\alpha,LO}_{lm} u^{\alpha}_{l}(r', E^{\alpha}_{1,l}) + C^{\alpha,LO}_{lm} u^{\alpha}_{l}(r', E^{\alpha}_{2,l})\right) Y^{l}_{m}(\hat{r}') & \vec{r} \in S_{\alpha} \end{cases} \tag{3.51}$$

In contrast to the LO for LAPW, there is no derivative of u^{α}_{l} here. The two coefficients $A^{\alpha,LO}_{lm}$ and $C^{\alpha,LO}_{lm}$ are determined by the requirement that the LO is normalized, and has zero value (not zero slope) at the sphere boundary.

Chapter 4

Literature note about Perovskites

4.1 Introduction

The mineral $CaTiO_3$ was discovered in the Ural Mountains by geologist Gustav Rose in 1839 and given the name perovskite in honor of the eminent Russian mineralogist, Count Lev Alexevich von Perovski[1]. The name perovskite is now used to refer to any member of a very large family of compounds that has the formula ABC_3 and for which the B ion is surrounded by an octahedron of C ions. Perovskites ($MgSiO_3$ and $FeSiO_3$) are the most abundant compounds in the Earth's crust.
The compounds with the formula ABO_3, with O = oxygen and B =a transition metal ion, are a subclass of the transition metal oxides that belong to the perovskite family. Table 4.1 provides a brief list of some well-studied ABO_3 perovskites. Many of the perovskites are cubic or nearly cubic, but they often undergo one or more structural phase transitions, particularly at low temperatures.
The perovskite oxides are extremely interesting because of the enormous variety of solid-state phenomena they exhibit. These materials include insulators, semiconductors, metals, and superconductors. Some have delocalized energy-band states, some have localized electrons, and others display transitions between these

two types of behavior. Many of the perovskites are magnetically ordered and a large variety of magnetic structures can be found.
The electronic properties of the perovskites can be altered in a controlled manner by

[1]This chapter was inspired from this reference text: Thomas Wolfram, Sinasi Ellialtioglu, "Electronic and Optical Properties of d-Band Perovskites", Cambridge University Press (2006), ISBN-13: 978-0-521-85053-7

Table 4.1: Some perovskite and related oxides.

Insulating	**Metallic**	**Magnetic**	**Superconducting**	
			$SrTiO_3$(n-type)	
WO_3	ReO_3	$PbCrO_3$	Na_xWO_3	(t)
$NaTaO_3$	$NaWO_3$	$LaCrO_3$	K_xWO_3	(t)
$SrTiO_3$	$KMoO_3$	$CaMnO_3$	K_xWO_3	(h)
$BaTiO_3$	$SrNbO_3$	$LaMnO_3$	Rb_xWO_3	(h)
$KTaO_3$	$LaTiO_3$	$LaCoO_3$	Cs_xWO_3	(h)
$LiNbO_3$	$LaWO_3$	$LaFeO_3$	Li_xWO_3	(h)

t = tetragonal, h = hexagonal

substitution of ions into the A or B sites, or by departures from ideal stoichiometry.
The electronic energy bands of the perovskites are very unusual in that they exhibit two-dimensional behavior that leads to unique structure in properties such as the density of states, Fermi surface, dielectric function, phonon spectra and the photoemission spectra. The perovskites are also important in numerous technological areas. They are employed in photochromic, electrochromic, and image storage devices. Their ferro- electric and piezoelectric properties are utilized in other device applications including switching, filtering, and surface acoustic wave signal processing.
Many of the perovskites are catalytically active. Development of perovskite catalyst systems for the oxidation of carbon monoxide and hydrocarbons, and the reduction of the oxides of nitrogen have been proposed. The perovskites are also employed in electrochemical applications including the photoelectrolysis of water to produce hydrogen.
Scientific studies of the perovskites date back many years. The physical properties of the tungsten bronzes were investigated as early as 1823 [88]. However, it is only in recent years that experimental and theoretical information on the electronic structure has begun to become available. Energy band calculations [89], neutron diffraction and inelastic scattering data [90], photoemission spectra [91], optical spectra [92], and transport data [93] are now available for materials such as ReO_3, WO_3, $NaWO_3$, $SrTiO_3$, $BaTiO_3$, $KMoO_3$, $KTaO_3$, $LaMnO_3$, $LaCoO_3$, and a variety of other perovskites.
Surface studies of single-crystal perovskites have been performed using photoelectron spectroscopies that indicate that the surface properties are extremely complex and interesting [94].
In this chapter[1] we present brief discussions of some of the properties of the perovskite

[1]This chapter was inspired from this reference text: Thomas Wolfram, Sinasi Ellialtioglu, "Electronic and Optical Properties of d-Band Perovskites", Cambridge University Press (2006), ISBN-13: 978-0-521-85053-7

oxides. The discussions are qualitative and intended only to give the reader a general impression of the types of factors that must be considered. More quantitative discussions are given in later chapters.
In Section 4.2 we describe the structural features of the perovskites. Sections 4.3 through 4.6 give a qualitative discussion of the electronic states starting from a simple ionic model and then adding ligand field, covalency, and band effects. Section 4.7 deals briefly with localized d-electron states and why many perovskites do not have conventional energy bands. In Section 4.8 we touch upon the multiplet configurations of localized d electrons and their role in determining the magnetic properties. The last section, 4.9, is a summary of some of the technological applications of the perovskites.

4.2 The perovskite structure

The formula unit for the cubic perovskite oxides is ABO_3 where A and B are metal cations and O indicates an oxygen anion. The structure, illustrated in Figure 4.1 is simple cubic ($O_h^1, Pm\bar{3}m$) with five atoms per unit cell. The lattice constant, $2a$, is close to 4 Å for most of the perovskite oxides.
The B cation is a transition metal ion such as Ti, Ni, Fe, Co, or Mn. It is located at the center of an octahedron of oxygen anions. The B site has the full cubic (O_h) point group symmetry. The A cation may be a monovalent, divalent, or trivalent metal ion such as K, Na, Li; Sr, Ba, Ca; or La, Pr, Nd. The A ion is surrounded by 12 equidistant oxygen ions. The A site also has the point group O_h.

The oxygen ions are not at sites of cubic point group symmetry. Focusing attention on the oxygen ion marked with an "× "in Figure 4.1 it may be seen that the site symmetry is D_4^h. The B-O axis is a fourfold axis of symmetry and there are several reflection planes; the yz-plane and planes passing through the edges containing A sites. The transition metal ion (B site) will experience a cubic ligand field that lifts the fivefold degeneracy of the d-orbital energies. The oxygen ions experience an axial ligand field that splits the $2p$-orbital energies into two groups. These splittings are described in the next section.
Well-known examples of cubic perovskites are $SrTiO_3$, $KTaO_3$, and $BaTiO_3$ (above the ferroelectric transition temperature). Many of the perovskites that we shall want to include in our discussions are slightly distorted from the ideal cubic structure. If the distortions are moderate the general features are not significantly different from those of the cubic materials. $BaTiO_3$ and $SrTiO_3$ both have structural transitions to a tetragonal

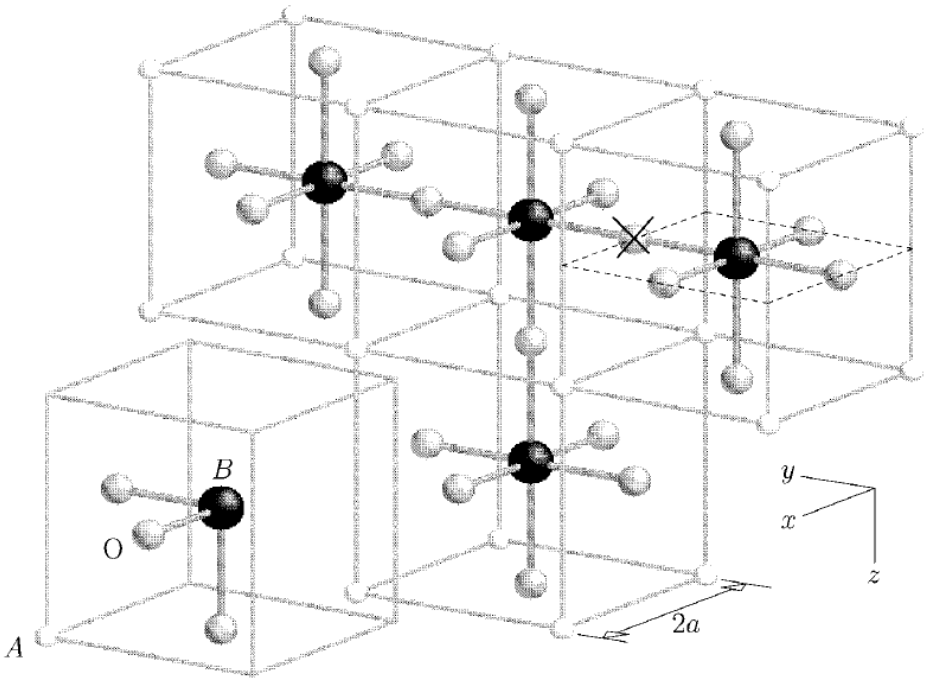

Figure 4.1: - The crystal structure of perovskite oxides with ABO_3 formula unit.

symmetry at certain critical temperatures. Tetragonal and orthorhombic distortions are very common among the perovskites.
In our discussions we shall also include substituted or mixed compounds of the form $(A^1_x A^2_{1-x})BO_3$ and oxygen-deficient perovskites, ABO_{3-x}. Including distorted, substituted, and non-stoichiometric compounds, the class of materials under consideration is very large. Within this broad class, examples may be found that display almost any solid-state phenomena known.

4.3 Ionic model

The perovskite oxides are highly ionic, but they also possess a significant covalent character. The ionic model is an oversimplified picture but it serves well as a starting point for thinking about the electronic properties. The ionic model assumes that the A and B cations lose electrons to the oxygen anions in sufficient numbers to produce O^{2-} ions. The usual chemical valence is assumed for the A cations; K^+, Ca^{2+}, and La^{3+}, for example. The ionic state of the transition metal ion is determined by charge neutrality. If the charge of the B ion is denoted by q_B and that of the A ion by q_A then $q_B = 6 - q_A$ where the three oxygen ions contribute the factor of 6. A list of the common A ions and

their valence states is given in Table 4.2.
Once the charge state of the B ion is determined the number of d electrons remaining is determined from the atomic electronic configuration (Table 4.2). For example, for $SrTiO_3$ we have Sr^{2+} and O^{2-} so that the titanium ion is Ti^{4+}. The electronic configuration of neutral titanium atom is [Ar] $3d^2 4s^2$. To form Ti^{4+} the outer four electrons are removed leaving the closed-shell Ar core [Ar]. Since O^{2-} has the [Ne] configuration, all of the ions of $SrTiO_3$ have closed-shell configurations. The electronic configuration of W is [Xe] $5d^4 6s^2$. Thus in WO_3 the W^{6+} ion has a closed-shell [Xe] core; however, for $NaWO_3$ the W^{5+} ion has a d^1 configuration. The electronic configurations of relevant transition metal ions are given in Table 4.2.
According to the ionic model when all of the ions have closed-shell configurations the material is an insulator.

If the B ion retains d electrons then the perovskite may be a metallic conductor depending on other factors to be discussed. $NaWO_3$ or ReO_3 each have d^1 configurations and are good metals. For compounds such as Na_xWO_3 it is assumed that there will be x d electrons per unit cell.That is, the Na donates its electron and the W ions donate the remaining electrons needed to form O^{2-} ions. One may imagine that there are $(1-x)$ W^{6+} and x W^{5+} ions distributed at random or on an ordered array or that each tungsten ion has an average valence of $W^{(6-x)+}$. The proper picture can not be decided from the ionic model but depends on other considerations. For Na_xWO_3 experiments show that metallic d bands are formed so that we may picture an average valency of $(6-x)+$. However, among the perovskites examples of ordered and random arrays of mixed valence B ions can also be found.

4.4 Madelung and electrostatic potentials

Starting from the ionic model, other important effects that determine the electronic properties can be added. The ionic model described above would apply to isolated or free ions. The ions are, of course, not isolated but interact in several different ways. One such interaction is through the electrostatic fields due to the charges on the ions. The most important electrostatic effect is the Madelung potential. The A and B ions are surrounded by negatively charged oxygen ions. The electrons orbiting these ions therefore experience repulsive electrostatic (Madelung) potentials. Conversely, the electrons orbiting the oxygen ions are surrounded by positively charged cations and they experience an attractive Madelung potential. The “site Madelung potentials”are defined

Table 4.2: Cations commonly found in perovskite-type oxides. In parentheses is the coordination number, Z, if the radii given are not for 12 coordination; HS and LS refer to high spin and low spin, respectively. The effective ionic radii (in Å) are from R. D. Shannon, Acta Cryst. A 32, 751 (1976).

Dodecahedral *A* site (Z =12)			**Octahedral *B* site (Z =6)**		
Ion	Electrons	Radius	Ion	Electrons	Radius
Na^{+}	$2p^6$	1.39	Na^{+}	$1s^2$	0.76
K^{+}	$3p^6$	1.64	Cu^{2+}	$3d^9$	0.73
Rb^{+}	$4p^6$	1.72	Mg^{2+}	$2d^6$	0.72
Ag^{+}	$2d^{10}$	1.28 (8)	Zn^{2+}	$2d^{10}$	0.74
Ca^{2+}	$3p^6$	1.34	Ti^{3+}	$3d^1$	0.67
Sr^{2+}	$4p^6$	1.44	V^{3+}	$3d^2$	0.64
Ba^{2+}	$5p^6$	1.61	Cr^{3+}	$3d^3$	0.615
Pb^{2+}	$6s^2$	1.49	Mn^{3+}(LS)	$3d^4$	0.58
La^{3+}	$4d^{10}$	1.36	Mn^{3+}(HS)	$3d^4$	0.645
Pr^{3+}	$4f^2$	1.18 (8)	Fe^{3+}(LS)	$3d^5$	0.55
Nd^{3+}	$4f^3$	1.27	Fe^{3+}(HS)	$3d^5$	0.645
Bi^{3+}	$6s^2$	1.17 (8)	Co^{3+}(LS)	$3d^6$	0.5456
Ce^{4+}	$5p^6$	1.14	Co^{3+}(HS)	$3d^6$	0.61
Th^{4+}	$6p^6$	1.21	Ni^{3+}(LS)	$3d^7$	0.56
			Ni^{3+}(HS)	$3d^7$	0.60
			Rh^{3+}	$4d^6$	0.665
			Ti^{4+}	$3p^6$	0.605
			Mn^{4+}	$3d^3$	0.53
			Ru^{4+}	$4d^4$	0.62
			Pt^{4+}	$5d^6$	0.625
			Nb^{5+}	$4p^6$	0.64
			Ta^{5+}	$5p^6$	0.64
			Mo^{6+}	$4p^6$	0.59
			W^{6+}	$5p^6$	0.60

as the electrostatic potentials at the different lattice sites due to all of the other ions. For example, the Madelung potential at a B site located at $\vec{R}_B^0$ is

$$V_M(\vec{R}_B^0) = \sum_{\vec{R}_O} \frac{e^2|q_O|}{|\vec{R}_B^0 - \vec{R}_O|} - \sum_{\vec{R}_A} \frac{e^2|q_A|}{|\vec{R}_B^0 - \vec{R}_A|} - \sum_{\vec{R}_B \neq \vec{R}_B^0} \frac{e^2|q_B|}{|\vec{R}_B^0 - \vec{R}_B|}. \tag{4.1}$$

In 4.1, eq_O, eq_A, and eq_B are the charges on the oxygen, A, and B ions, respectively, and $\vec{R}_O$, $\vec{R}_A$, and $\vec{R}_B$ are the vectors for the corresponding lattice sites. The site Madelung potentials are very large for the perovskites because of the large ionic charges. Typical Madelung potentials are 30-50 eV for the B site. For $A^{2+}B^{4+}O_3^{2-}$ perovskites the (full ionic) site potentials [95] are: $V_M(B) = +45.6eV$, $V_M(A) = +19.9eV$, and $V_M(O) = -23.8eV$. A table of Madelung potentials can be found in Reference texts[1].
The stability of the perovskite structure is largely due to the energies associated with the Madelung potentials. The attractive potential at the oxygen sites allows the oxygen ions to bind a pair of electrons. In effect the site potential adds to the electron affinity of the oxygen ion. The affinity of O^- for the second electron is actually positive. This means that the second electron would not be bound on a free oxygen ion. O^{2-} is stable in the lattice because of the attractive site Madelung potential. Conversely, a d electron is bound to a Ti^{4+} ion with an (ionization) energy of 43 eV. In the absence of the repulsive site Madelung potential, donation of an electron from the Ti^{3+} to an O^- ion in $SrTiO_3$ would be energetically very unfavorable. The site Madelung potential adds to the ionization energy so that the d electron would have an effective binding energy of $-43 + 45.6 = +2.6eV$ (unbound) for $SrTiO_3$ with the full ionic charges.
Thus, it is seen that the Madelung potentials are responsible for the ionic configurations. An orbital centered on an ion has a finite radial extent so that an electron in such an orbital would sample the electrostatic field over a distance comparable to the ionic radius. In order to determine the complete effect of the electrostatic field on the electron state we need to know the behavior of the field as a function of position near each ion site. If we use the point ion model then,

$$\begin{aligned} V_{(\vec{r})} &= -\frac{e^2|q_B|}{|\vec{r} - \vec{R}_B^0|} + V_{es}(\vec{r}), \\ V_{es}(\vec{r}) &= \sum_{\vec{R}_B \neq \vec{R}_B^0} \frac{e^2|q_B|}{|\vec{r} - \vec{R}_B|} - \sum_{\vec{R}_A} \frac{e^2|q_A|}{|\vec{r} - \vec{R}_A|} - \sum_{\vec{R}_A} \frac{e^2|q_O|}{|\vec{r} - \vec{R}_O|}. \end{aligned} \tag{4.2}$$

[1]This chapter was inspired from this reference text: Thomas Wolfram, Sinasi Ellialtioglu, "Electronic and Optical Properties of d-Band Perovskites", Cambridge University Press (2006), ISBN-13: 978-0-521-85053-7

The potential near $\vec{R}_B^0$ can be found by expanding $V_{es}(\vec{r})$ in terms of spherical harmonics centered at $\vec{R}_B^0$. The potential $V_{es}(\vec{r})$ then takes the form of an electric multipole expansion. The monopole term is just the site Madelung potential. Thus, as we have described, the site Madelung potential produces a shift in the energy of an electron localized on the site.

The higher-order multipoles (dipole, quadrupole, etc.) create an electrostatic field (with the point group symmetry of the site) which leads to a lifting of the orbital degeneracies. The effect of the cubic electrostatic field at the B ion site is to split the fivefold degenerate d states into two groups as shown in Figure 4.2(c). The e_g group is doubly degenerate corresponding to the d orbitals having wavefunctions with angular symmetry $(x^2-y^2)/r^2$ and $(3z^2-r^2)/r^2$. The threefold degenerate t_{2g} group corresponds to the states (xy/r^2), (xz/r^2), and (yz/r^2).

The oxygen $2p$ states are split by the axial electrostatic field into a doubly degenerate level denoted by $p_\perp$ and a non-degenerate $p_\parallel$ state. The notation $p_\perp$ and $p_\parallel$ refer to $2p$ orbitals oriented perpendicular and parallel to a $B-O$ axis, respectively.

The lowest unoccupied state of the A ion is an s state. Its energy is shifted by the monopole (Madelung potential) but unaffected by the other multipole terms because it is a spatially non-degenerate function with spherical symmetry at a site of cubic symmetry.

The particular level ordering shown in Figure 4.2 may be understood by considering the orientation of orbitals relative to the charge distributions on neighboring ions. The e_g orbitals have lobes directed along the $B-O$ axis and directly into the negative charge clouds of oxygen ions. The t_{2g} orbitals have lobes pointed perpendicular to the $B-O$ axis between the negative oxygen ions. As a result the e_g states experience a greater repulsion than the t_{2g} states and consequently lie at a higher energy. Similar reasoning suggests that the $p_\parallel$ states lie below the $p_\perp$ states when it is noted that B ion cores appear as positively charged centers.

In insulating perovskites such as $SrTiO_3$ the p states are completely filled while the d states are completely empty. The energy difference, E_g, between the t_{2g} and $p_\perp$ states is approximately equal to the energy gap. Metallic and semiconducting materials have the d states partially filled. $NaWO_3$ or ReO_3 have a single electron in a t_{2g} state.

In most but not all cases the energy bands involving the s state of the A ion are at energies much higher than the primary valence and conduction bands of a perovskite and therefore these bands are unoccupied. As a result the s state of the A ion usually does not play any significant role in determining the electronic properties. This is not to say that the A ion is not important. The electrostatic potentials of the A ions have a strong influence on the energy of the $p-d$ valence and conduction bands. Furthermore, the

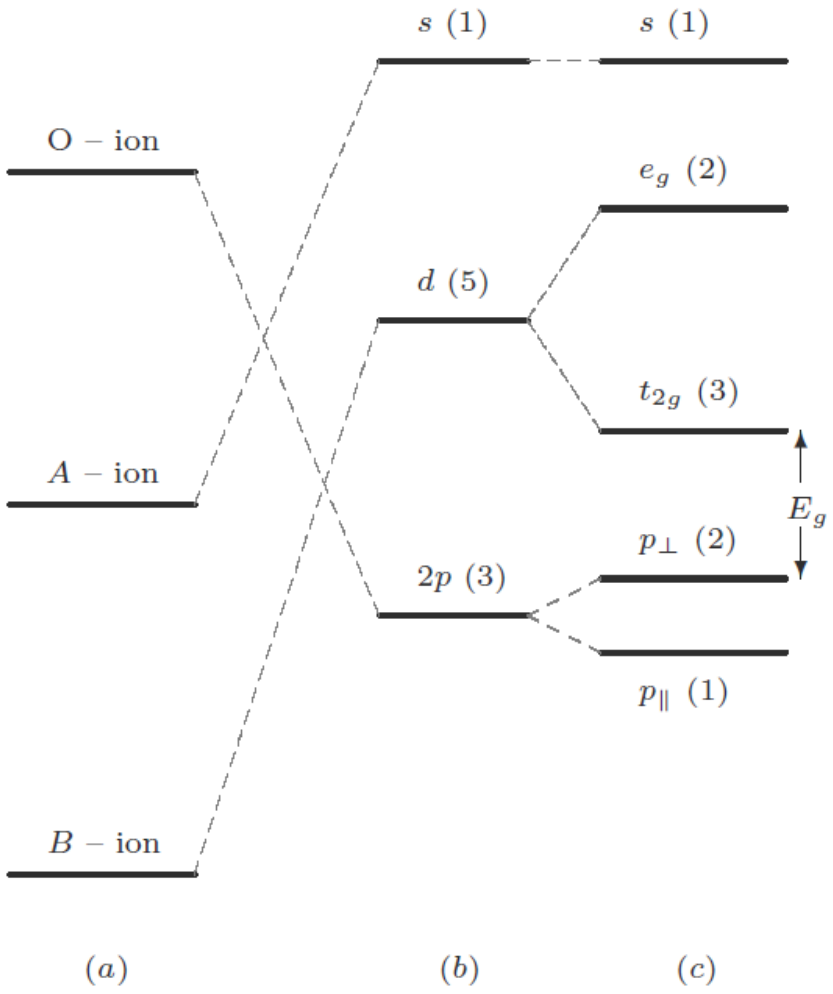

Figure 4.2: **Effect of the electrostatic potentials on the ion states** - (a) free ions, (b) Madelung potential, and (c) electrostatic splittings.

size of the A ion is a significant factor in determining whether the crystal structure is distorted from the ideal cubic form. Nevertheless, given a particular perovskite structure and the effective electrostatic potentials acting on the B and O sites, the orbitals of the A ion may usually be omitted from electronic structure calculations. This leads to a major conceptual simplification because the electronic properties of the perovskites may be regarded as arising solely from the BO_6 part of the ABO_3 structure. This implies, for example, that the electronic structure of $BaTiO_3$ and $SrTiO_3$ should be essentially the same. According to the same reasoning the electronic *structure* of Na_xWO_3 should be independent of x. This does not mean that the properties are the same, but only that the available electronic states are the same. Obviously, the properties of WO_3 are completely different from those of $NaWO_3$; the former is an insulator and the latter is a metal. However, as a first approximation the only effect of the sodium is to donate electrons which occupy the t_{2g} states of the tungsten ion.

4.5 Covalent mixing

In addition to electrostatic interactions, the ions can interact because of the overlap of the electron wavefunctions. This leads to hybridization between the p and d orbitals and the formation of covalent bonds between the transition metal ions and the oxygen ions. It is frequently assumed that the covalent mixing in insulating materials such as $SrTiO_3$ is negligible. This is not correct. Nearly all of the physical and chemical properties of the perovskites are significantly affected by covalency.
To understand covalent mixing we consider a *cluster* of atoms consisting of a transition metal ion and its octahedron of oxygen ions. The wavefunctions of the cluster can be written in the form:

$$\psi^{(n)}(\vec{r}) = \sum_{\alpha} a_{\alpha}^{(n)} \varphi_{d\alpha}(\vec{r}) + \sum_{\vec{R}_i} \sum_{\beta} b_{i\beta}^{(n)} \varphi_{p\beta}(\vec{r} - \vec{R}_i), \tag{4.3}$$

where $\psi^{(n)}(\vec{r})$ is the cluster wavefunction for the nth eigenstate. $\varphi_{d\alpha}(\vec{r})$ is a d orbital on the B ion of α-type ($\alpha = xy, xz, ...$,etc.) and $\varphi_{p\beta}(\vec{r} - \vec{R}_i)$ is a p orbital centered at an oxygen ion located at $\vec{R}_i$ of the βth-type ($\beta = x, y, orz$). The coefficients $a_{\alpha}^{(n)}$ and $b_{i\beta}^{(n)}$ are constants which specify the amplitudes of the different orbitals which compose the nth eigenstate.

For the ionic model the wavefunctions are either pure d orbital ($b_{i\beta}^{(n)} = 0$) or pure p orbital ($a_{\alpha}^{(n)} = 0$). For the cluster the wavefunctions are still predominantly d or p

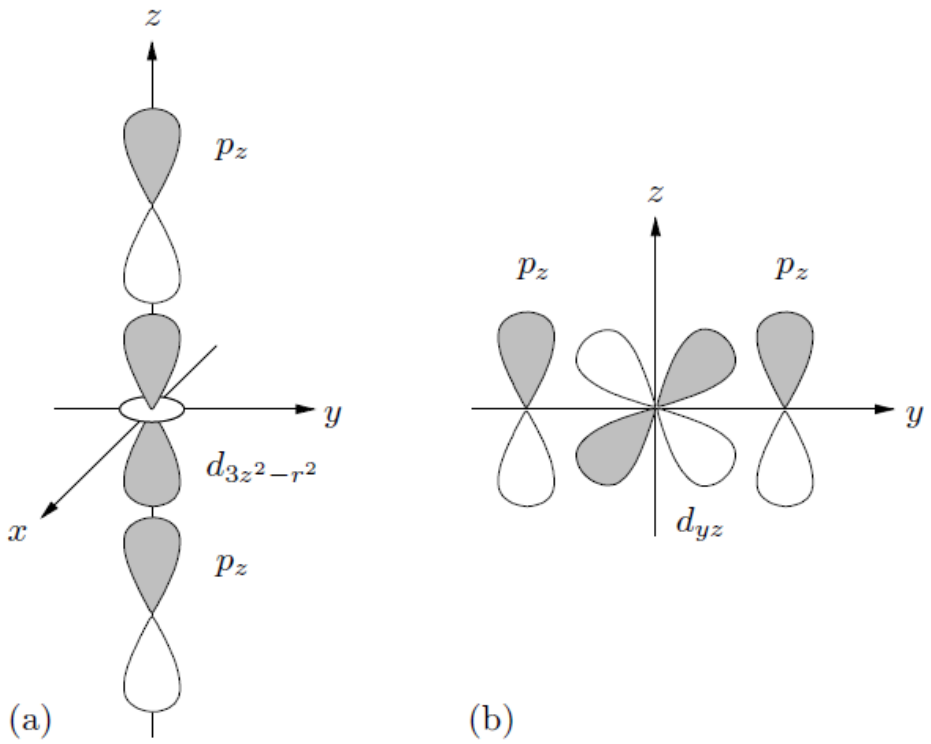

Figure 4.3: Overlap between cation d orbitals and anion p orbitals (a) Sigma overlap and (b) pi overlap.

orbital in character but there is a significant covalent mixing between the two ($b_{i\beta}^{(n)}$ and $a_{\alpha}^{(n)} \neq 0$). The mixing comes about because of the overlap between d orbitals centered on the cation and the p orbitals on neighboring oxygen ions. There are two types of $p-d$ overlap. The first is overlap between the d orbitals of the e_g type with p orbitals of the $p_{\parallel}$ type. This overlap is called "sigma"overlap. The second type, "pi"overlap occurs between t_{2g}-type d orbitals and $p_{\perp}$ orbitals. These two types of overlap are illustrated in Figure 4.3. The overlap between t_{2g} and $p_{\parallel}$ orbitals or between e_g and $p_{\perp}$ orbitals vanishes by symmetry. If only the p and d orbitals are considered then there are 23 cluster states for a transition metal ion and the octahedron of oxygen ions. These 23 cluster states arise from admixtures of the 23 basis states; 5 d orbitals and 18 p orbitals, three on each of the six oxygen ions.

The cluster energy levels [96] are illustrated in Figure 4.4. The labels given to the cluster energy levels indicate the group theoretical irreducible representations to which the wavefunctions belong. The prefix numbers are used to distinguish different levels which have the same symmetry properties. The degeneracies of the levels are indicated by the numbers in parentheses.

It is noted that the cation d orbitals are still split into the e_g and t_{2g} groups. These,

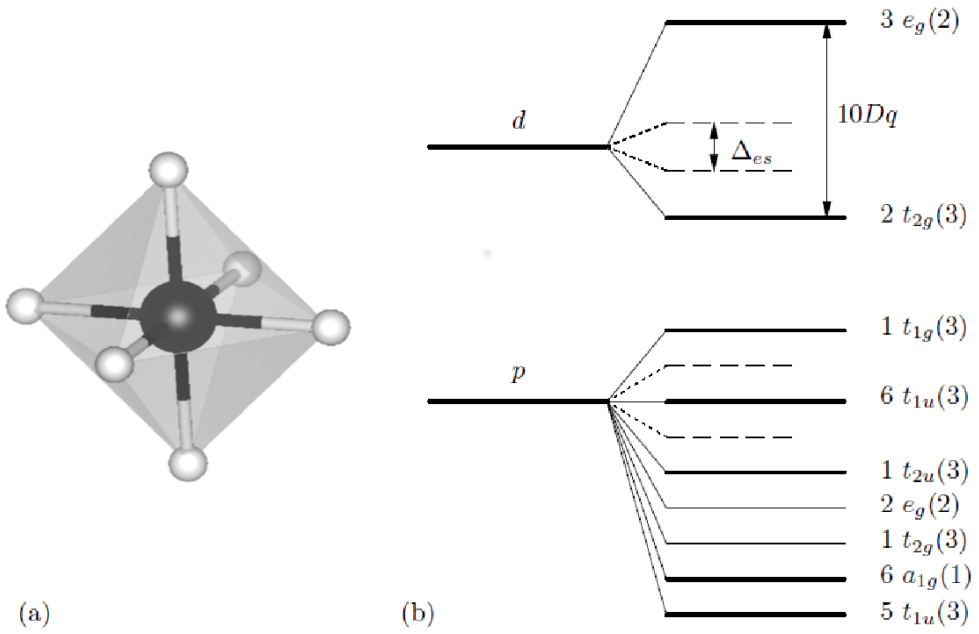

Figure 4.4: (a) BO_6 cluster and (b) the cluster levels. The dashed levels are for the electrostatic model. Δ_{es} is the electrostatic splitting.

so-called "ligand-field states"differ from those of the electrostatic model (Fig. 4.2) in two significant ways. First, the wavefunctions are no longer just d orbitals. They are admixtures of p and d orbitals. A second difference is that the splitting between the e_g and t_{2g} groups is much larger than for the electrostatic model. The cluster *ligand-field splitting* denoted by $10Dq$ is due to both electrostatic and covalent effects. The covalent contribution to $10Dq$ is usually much larger than the electrostatic contribution, Δ_{es}. Typically $10Dq$ is 2-3 eV in magnitude.

The ligand-field states, $3e_g$ and $2t_{2g}$, have wavefunctions in which the d orbitals combine out-of-phase with the p orbitals. The interference between the orbitals leads to a depletion of charge between the B and O ions. For this reason these states are called *antibonding* states. *Bonding* states are formed from in-phase combinations of the d and p orbitals. These states have wavefunctions that correspond to an accumulation of charge between the B and O ions. The bonding states are the $2e_g$ and $1t_{2g}$ levels (shown in Fig. 4.4). These states have hybridized wavefunctions, typically 70% p orbital and 30% d orbital. The percentage d-orbital admixture is a measure of the covalent bonding.

The remaining cluster levels have wavefunctions that are combinations of p orbitals located on the six oxygen ions. They do not hybridize with the d orbitals and therefore they do not contribute to the metal-oxygen bonding. Such states are called *non-bonding* states. Wavefunctions of the three types of cluster states are illustrated in Figure 4.5.

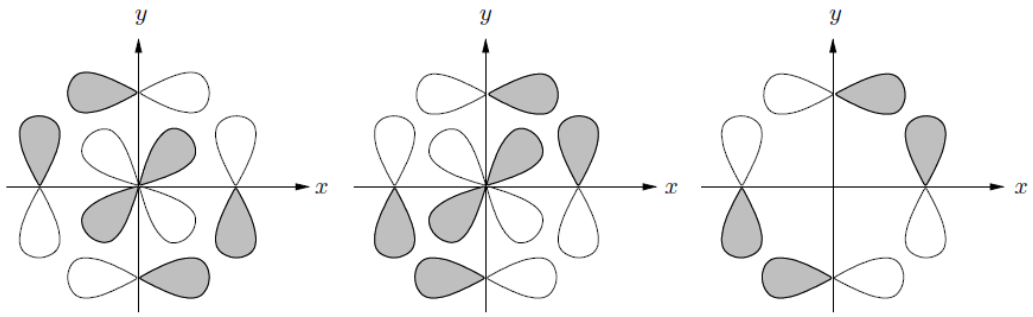

(a) $2t_{2g}$ (b) $1t_{2g}$ (c) $1t_{1g}$

Figure 4.5: Cluster states: (a) antibonding, (b) bonding, and (c) non-bonding.

It is important to note that electrons occupy d orbitals on the cation even when the $3e_g$ and $2t_{2g}$ levels are unoccupied. This is because of the covalent mixing of the d orbitals into the filled valence states below the $2t_{2g}$ level. This covalency effect is significant even for "ionic"insulators such as $SrTiO_3$. The ionic model implies that the titanium ion is Ti^{4+} with a d^0 configuration. Cluster models would give an effective valence such as $Ti^{3+}(d^1)$.

4.6 Energy bands

In the preceding section we considered a cluster model for the perovskites in which the transition metal ion interacts with the nearest-neighbor oxygen ions. The covalent mixing between the cation and anion wavefunctions leads to a partial occupation of d orbitals which, in the ionic model, were empty. A mechanistic interpretation of the covalent mixing is that the overlap between cation and anion wavefunctions provides a means of transferring electrons back and forth between the ions. Clearly, for an extended crystal structure the same mechanism will allow electrons to be shared between cations in adjacent clusters. Each oxygen of a given cluster is shared by adjacent cations. Cations can interact with each other through the intervening oxygen ion. An electron on a cation may be transferred to the oxygen ion and then from the oxygen ion to the second cation. When such processes occur the electrons become delocalized and electron energy bands are formed. It is important to note that the formation of d-electron bands requires two independent electron transfer processes. The delocalization of d electrons therefore is second order in the $p-d$ overlap (or the probability of p to d electron transfer). This is quite different from a typical monoatomic metal where delocalization is first order in the

atomic overlap. For cubic perovskites the cation-cation separation is nearly 4Å. This is too large for a significant direct overlap between cation orbitals and therefore band formation occurs by transfer of electrons between cations and anions whose separation is only about 2Å.

In considering the energy bands of a perovskite it is appropriate to divide the crystal into unit cells each with the formula unit ABO_3. (The unit cell is shown in Fig. 4.1.) As discussed previously, the s states of the A ion can be neglected. Therefore, there will be 14 energy bands corresponding to the five d orbitals and nine p orbitals of each unit cell. The wavefunctions of the band states are characterized by a wavevector $\vec{k}$ and are of the form

$$\Psi_{\vec{k}}(\vec{r}) = \sum_{\vec{R}_d}\sum_{\alpha} a_\alpha(\vec{k})e^{i\vec{k}.\vec{R}_d}\varphi_{d\alpha}(\vec{r}-\vec{R}_d) + \sum_{\vec{R}_p}\sum_{\beta} b_\beta(\vec{k})e^{i\vec{k}.\vec{R}_p}\varphi_{p\beta}(\vec{r}-\vec{R}_p). \tag{4.4}$$

In eq. 4.4, $a_\alpha(\vec{k})e^{i\vec{k}.\vec{R}_d}$ and $b_\beta(\vec{k})e^{i\vec{k}.\vec{R}_p}$ are respectively the amplitudes of the d and p orbitals of symmetries α and β located at the lattice sites $\vec{R}_d$ and $\vec{R}_p$.

An energy band diagram for a typical perovskite is shown in Figure 4.6 for a model which includes only the interactions between nearest-neighbor ions [97]. For this simple model the energy bands divide into a set of sigma bands and a set of pi bands. The sigma bands involve only the e_g d orbitals and the $p_\parallel$ oxygen orbitals. The pi bands involve only the t_{2g} d orbitals and the $p_\perp$ oxygen orbitals.

The sigma bands have five branches: two distinct σ-type valence (bonding) bands, two distinct σ^*-type conduction (antibonding) bands and a single σ^0-type non-bonding band. The pi bands have nine branches: three equivalent π-type valence (bonding) bands, three equivalent π^*-type conduction (antibonding) bands, and three equivalent π^0-type non-bonding bands.

The bonding and antibonding (σ; σ; π; π^*) bands have wavefunctions whose $p-d$ admixture varies as a function of the wavevector $\vec{k}$. At $\Gamma(\vec{k}=0)$ in the first Brillouin zone (see the inset in Fig. 4.6) the wavefunctions are pure p or pure d orbital in composition. The states at Γ have no covalent character and therefore correspond to the levels derived from the ionic model including the electrostatic potentials (Fig. 4.2(c)). As $\vec{k}$ varies along $\Gamma \rightarrow$ X $\rightarrow$ M $\rightarrow$ R the covalent mixture of the p and d orbitals increases. It is maximum at the point R, at the corner of the Brillouin zone. The states at R are very similar to the "g"states of the cluster model (i.e., $2t_{2g}$; $3e_g$, etc.). Thus the ionic model underestimates the covalency and the cluster model overestimates the covalency of the perovskites. The separation between the σ^* and π^* bands at Γ, $\Delta_{es}(d)$, corresponds to

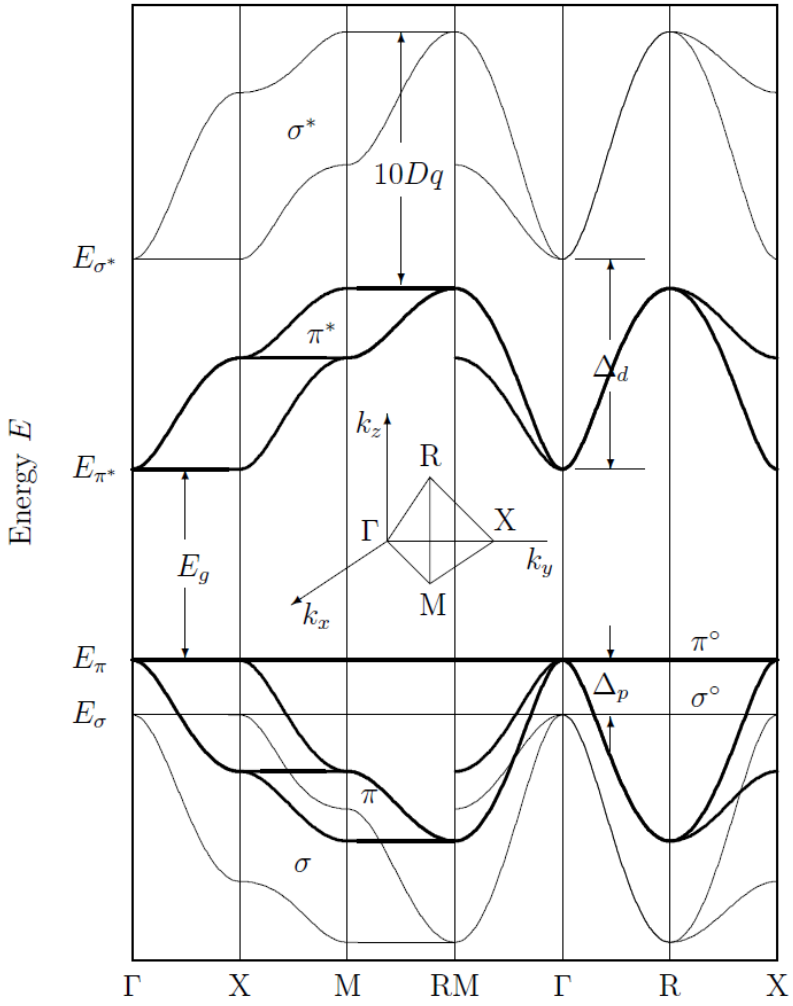

Figure 4.6: Energy bands for a typical perovskite showing the dispersion for $\vec{k}$-vectors along various lines in the Brillouin zone (inset) according to the LCAO model with nearest-neighbor interactions. The lighter curves are the pi bands and the darker curves are the sigma bands. The energies, E_g, $10Dq$, Δ_d, and Δ_p are the band gap, total (cluster) ligand-field splitting, d-orbital ligand-field splitting, and the p-orbital ligand-field splitting, respectively.

the electrostatic contribution to the ligand-field splitting. The separation at R is the total ligand-field band splitting and is approximately equal to $10Dq$.
The non-bonding band states for σ^0 and π^0 involve only oxygen $2p$ orbitals and therefore do not involve metal-oxygen covalent mixing. The band and cluster models produce similar non-bonding states.
The energy separation between the π^* and π^0 bands at Γ is the fundamental band gap, E_g. It varies between 1 and 4 eV and is largest for the insulating perovskites. Covalent mixing decreases with increasing band gap. The magnitude of the band gap is a measure of the ionicity of a perovskite. For example, the band gap of $SrTiO_3$ is 3.25 eV and that of ReO_3 is about 1 eV. This means that $SrTiO_3$ is much more ionic than ReO_3.
Insulating perovskites (e.g., $SrTiO_3$, $BaTiO_3$, or WO_3) have filled valence bands; that is, the σ; π; σ^0, and π^0 bands are completely occupied with electrons. The conduction bands (σ^* and π^*) are empty. Metallic perovskites such as $NaWO_3$ or ReO_3 have one electron per unit cell in the π^* conduction band. Examples of metallic compounds with two electrons in the π^* band are $CaMoO_3$, $BaMoO_3$, and $SrMoO_3$. Perovskites with more than two d electrons tend to form localized-states similar to those of the cluster model rather than delocalized band states.
Insulating perovskites can be rendered semiconducting or metallic by several means. Reduction in a hydrogen atmosphere produces oxygen vacancies. The vacancies act as donor centres; two electrons being donated by each vacancy (hydrogen itself may also remain in the lattice and act as a donor). Electron concentrations in the range of $10^{16} - 10^{20}$ electrons/cm^3 can be produced in this way. Reduced insulating perovskites are n-type semiconductors with the Fermi level very near to the bottom of the π^* conduction band. n-type $SrTiO_3$ has been found to be a superconductor at temperatures below 0.3K [98].
Insulating perovskites can also be doped by substituting appropriate ions into either the B or A sites. The tungsten bronzes Na_xWO_3, K_xWO_3, Li_xWO_3, and H_xWO_3 are special cases in which donor ions are substituted into the empty A sites of insulating WO_3. Electron concentrations of the order of 10^{22} electrons/cm^3 are obtained in this case. Many of the bronze compositions are superconductors.
One of the reasons perovskites are particularly valuable for research is that the electronic properties can be varied in a controlled fashion to produce almost any desired feature. The Fermi level in $SrTiO_3$ can be varied over a 3 eV range by going from cation- to anion-deficient compositions. The basic band structure does not change appreciably so the properties of such compositions are easily understood and interpreted in terms of a fixed band structure; that is the “rigid-band”approximation is valid. The rigid-band model is

also applicable to the tungsten bronzes, and mixed compounds of the $A_x^{(1)}A_{1-x}^{(2)}BO_3$ type where $A^{(1)}$ and $A^{(2)}$ are different cations.

4.7 Localized *d* electrons

In the preceding section we indicated how the localized cluster states are delocalized because of the overlap of wavefunctions between adjacent clusters. The d-band formation is due to the transfer of electrons between cations via intervening oxygen ions. These electrons become delocalized and have an equal probability (proportional to $|e^{i\vec{k}.\vec{R}}|^2 = 1$) of being found at any cation site. The band model neglects any possible spatial correlation between d electrons. The potential experienced by a given electron is assumed to be the same at every lattice site and equal to the average potential of the ion core and all other electrons. The usual one-electron band model explicitly ignores the fact that at any given instant of time a non-average number of electrons may be occupying the orbital of an ion. However, during the lifetime of the "non-average"ionic state the electrons on the site will experience a non-average potential. In particular, the intra-atomic Coulomb repulsion of an electron on a non-average site will be different from that at an average site.
Consider the situation in which we start with two metal ions each having n electrons. The electron-electron repulsion energy among the n electrons at each site is $\frac{1}{2}Un(n-1)$ where U is the Coulomb integral. If we transfer an electron from one site to the other there will be $n-1$ electrons on one site and $n+1$ on the other. The electron-electron repulsion energy will be $\frac{1}{2}Un(n+1)$ on the site with the extra electron and $\frac{1}{2}U(n-2)(n-1)$ on the other site. There is a change in the repulsion energy at one site of $\frac{1}{2}U[n(n+1)-n(n-1)] = nU$. At the other site the change in energy is $\frac{1}{2}U[(n-2)(n-1)-n(n-1)] = -Un+U$. Therefore, the net change is an additional repulsive energy equal to U. Thus, there is a Coulomb energy barrier to the creation of non-average ionic states.
Band formation is favorable because the delocalization of an electron reduces its kinetic energy (provided that the electron can occupy a state near the bottom of the band). For such a case the reduction in kinetic energy increases as the band width increases.
It is clear from what has been said that energy band formation will only be favorable if the reduction in kinetic energy is larger than the increase in the Coulomb energy. A variety of models which include a form of the Coulomb correlation energy have been used to find a criterion for the validity of the band model [99]. In general it is found that band theory applies when $W \geq U$ where W is the band width. For W less than U, localized d-electron states are energetically favored. The precise criterion is model-dependent.

The localized electron criterion leads to interesting possibilities for the perovskites. The band width of the σ^* band is substantially larger than that of the π^* band and consequently, for a number of perovskites, the t_{2g} states are localized while the e_g states form σ and σ^* energy bands; $LaNiO_3$ with filled t_{2g} states and a single electron in the σ^* band is an example [100].

4.8 Magnetism in the perovskites

The occurrence of magnetism in the perovskites is closely connected to the existence of localized d electrons. In almost all cases where magnetism exists the d electrons are localized and possess localized spins. In such cases the local electronic configuration becomes an important consideration. One must be concerned with the multiplet structure. The tendency toward the formation of a multiplet configuration with a net spin arises from intra-atomic exchange and correlation. In atomic theory, Hund's rule states that the lowest-energy configuration corresponds to the state of maximum multiplicity or maximum spin and orbital angular momentum. Hund's rule is qualitatively applicable to the perovskites with localized d electrons. There are, however, some significant differences between atomic theory and the theory applicable to ions of the solid. The major differences between free ions and the cations in a solid perovskite are:

1. the fivefold degenerate d states are split into the e_g and t_{2g} groups with a splitting of $10Dq$;

2. the energy differences between different electronic configurations are not as widely separated as for the free ions;

3. there is significant covalent mixing between the d-ion orbitals and the neighboring oxygen ion p orbitals.

As a consequence of 1 and 3 the electronic configuration of the cation should be specified in terms of the one-electron cluster states $3e_g$ and $2t_{2g}$. For simplicity the numerical descriptors of these states may be omitted. The d-electron configuration may then be specified by $(t_{2g}^n e_g^m)$, where n and m are the occupations of the $2t_{2g}$ and $3e_g$ levels, respectively.
The effect of 2 is that different valence states and different electronic configurations of the cation are closer in energy to each other than for the free ion. This is a result of

polarization and electron screening of the Coulomb interactions. On applying Hund's rule to a perovskite cation the ligand-field splitting must be taken into account. When the number of d electrons, $m+n$, is between 4 and 7, Hund's rule can be violated if the ligand-field splitting is greater than the intra-atomic exchange energy. Consider, for example, $LaMnO_3$ which has Mn^{3+} ions with four d electrons. The intra-atomic exchange favours the "high-spin"configuration ${}^5E_g = (t_{2g} \uparrow^3 e_g \uparrow)$. However, occupying the e_g state involves a loss of binding energy equal to the ligand-field splitting. Therefore, the "low-spin"configuration ${}^3T_{2g} = (t_{2g} \uparrow^3 t_{2g} \downarrow)$ is competitive. Assuming a constant exchange, J, between parallel spin electrons, the intra-atomic exchange involves

$$E_{ex} = -J \sum_{i>j} \vec{s}_i . \vec{s}_j$$

where $\vec{s}_i$ and $\vec{s}_j$ are the spins of the occupied states. The ${}^5E_g$ has an exchange energy $-\frac{3}{2}J$ while for the ${}^3T_{2g}$, $E_{ex} = -\frac{3}{4}J$. However, the ${}^3T_{2g}$ has a ligand-field energy of $10Dq$. Therefore, the difference in the energies of the two configurations is

$$E({}^5E_g) - E({}^3T_{2g}) = -\frac{3}{4}J + 10Dq \equiv \Delta E.$$

When $\Delta E < 0$ the high spin state ${}^5E_g$ (spin=2) is lower in energy than the low spin state ${}^3T_{2g}$ (spin=1). If $\Delta E > 0$ then the low spin state is favored. Experiments on d^4 ions in perovskites show that the low spin state is usually favored. This indicates that the ligand-field splitting is larger than the intra-atomic exchange and Hund's rule does not apply.

When the cations possess localized spins, then long-range magnetic ordering can occur. The principal mechanism of spin-spin interactions is superexchange. Superexchange involves the antiferromagnetic coupling between nearest-neighbor cations by exchange of electrons with the intervening oxygen ion.

Examples of magnetically ordered perovskites are $LaCrO_3$, $PbCrO_3$, $CaMnO_3$, $LaFeO_3$, and many others. Those named above form the simple G-type magnetic cell in which the spins of nearest-neighbor cations are antiparallel. Many other types of magnetic ordering also occur among the magnetic perovskites.

As a final comment on localized d electrons we mention the importance of the Jahn-Teller effect. This effect is the spontaneous distortion of a cubic structure such as that of perovskites. When the cation electronic configuration is orbitally degenerate, the ground state will in some cases, be unstable to small distortional displacements. This Jahn-Teller

distortion occurs because the electronic energy decreases linearly with displacement while the elastic energy increases as the square of the displacement. A minimum in the total energy always occurs for a small but finite distortional displacement.

4.9 Some applications of perovskite materials

The technological uses of perovskite and perovskite-related materials are extensive and we will not attempt to review the field. In this section we shall only briefly mention some of the common applications. References are given to only a few representative papers in the vast literature.

The piezoelectric insulating perovskites such as $BaTiO_3$, $PbTiO_3$, $PbZrO_3$, $Pb(Zr_xTi_{1-x})O_3$ (PZT), and $LiNbO_3$ have been employed extensively as solid-state device materials. Some solid-state applications include switching devices, infrared detectors, and a large variety of signal processing devices [101]. These materials are employed as substrates for the generation of bulk and surface acoustic (elastic) waves. Because of their piezoelectric properties, acoustic waves are accompanied by an oscillating electric field [102, 103]. It is possible to generate acoustic waves by applying an oscillating electric field to the substrate and conversely an acoustic wave may be detected by the electric field it generates. The coupling between the elastic displacement and the electromagnetic field is nonlinear and produces second-harmonic electric fields [104]. These properties have been employed to design a number of acoustic wave signal processing devices, including time delay lines, filters, acoustic wave image devices and nonlinear convolution and correlation devices.

The nonlinear optical properties of the perovskite insulators are used for the generation of second-harmonic optical waves. The second-harmonic generation coefficient of $PbTiO_3$ is among the highest known [105]. Other applications of the insulators include photochromic, electrochromic, image storage, and display devices [105]. In the photochromic applications the transparent host materials are doped with impurity transition metal ions or rare earth ions. The impurity ions have several localized levels lying within the band gap of the substrate that correspond to different valence states. The valence state of the impurity ion can be changed by photoexcitation. Impurity ions are selected for which one valence state has an absorption band in the visible while the second does not. Colored images can be “written”by a light beam that causes photoexcitations of these metastable valence states. The images can be erased by a second light beam of a different wavelength which depopulates the metastable states. For electrochromic devices, the

valence states are changed by shifting the quasi-Fermi level or by reducing the material electrochemically. A thin film of WO_3 may be changed from transparent to a deep blue color by electrochemically converting W^{6+} ions to W^{5+} ions.
There is also interest in the surface chemical properties of the perovskites. Many are excellent gas-phase catalysts and in addition several are photocatalytic and electrocatalytic.
Interest in the catalytic properties of the perovskites began with the suggestion that the rare earth cobalt oxides, $RCoO_3$ (R=rare earth ion) might prove useful as substitutes for Pt-based automotive exhaust catalysts [102, 103]. Strong catalytic activity and a high degree of selectivity have been found for a large variety of perovskite materials [106].
Many energetically favorable (exothermic) gas-phase reactions do not occur spontaneously but require a catalyst in order to occur. The detailed mechanisms of catalytic action are not known in most cases, but some general features are understood. There are two principal factors which inhibit an exothermic reaction. The first is related to the symmetry of the reactant and product states. As two molecules come together in a chemical reaction the orbitals of the complex must evolve from those of the reactants to those of the products. One can imagine a continuously changing set of hybridized molecular orbitals for the reacting molecules. It frequently happens that the occupied orbitals of the ground state of the product can not evolve from a hybridization of the occupied orbitals of the reactants. An example is the hydrogenation of ethylene to form ethane. The bonds associated with the hydrogen atoms of ethane evolve from a hybridization of empty anti- bonding states of the reacting hydrogen and ethylene molecules, and not from the occupied bonding states. Electron flow from the occupied bonding states to the empty antibonding states is forbidden by symmetry consideration. Reactions can be classified as symmetry-“allowed”or symmetry-“forbidden”in much the same way as optical translations [107]. Reactions that are “forbidden”are inhibited by a symmetry-imposed barrier.
Another barrier encountered is associated with the charge transfer involved in the reaction. As charge flows from the reactant states to the ground state of the product, the molecules must often pass through a transient polar configuration. Such polar configurations are usually energetically unfavorable because the electron affinity of a molecule is small compared to its ionization energy. The inhibition to charge transfer acts as an additional barrier to the chemical transformation.
The catalytic properties of the perovskites are directly related to the presence of coordinatively unsaturated transition metal ions on the surface. The term coordinatively unsaturated, refers to the fact that an ion on the surface will often have less than its

normal complement of six oxygen ligands. Such ions provide active sites for adsorption of reactant molecules because in this way the ion can attain its normal number of ligands. The symmetry of the d orbitals is favorable for interaction with both the bonding and antibonding states of most molecules.

It is generally believed that chemisorption of one or more of the reactant molecules to form a surface complex is a precursor to a catalyzed reaction. The role of the surface complex in catalysis is twofold: d orbitals can hybridize with the reactant molecule orbitals in such a way as to provide a symmetry-allowed path for the reactions [108]. In addition, the adsorption of the reaction species greatly facilitates charge transfer processes. When molecules condense on a solid substrate the ionization energy of the molecular levels is reduced due to a process known as extra-atomic relaxation [109]. Furthermore the barrier to charge transfer is reduced by the solid-state effects of polarization and electron screening. It is also possible for charge transfer to occur via the transition metal ion. The catalyst ion acts as an intermediary to accept (donate) electrons from the reactants and to donate (accept) electrons to the product. This process involves a valence fluctuation of the cation. Such fluctuations are of low energy compared to fluctuations of charge on free molecules. The energy required for a valence fluctuation can be minimized in systems such as the mixed or non-stoichiometric perovskites since they already contain mixed valence transition metal ions.

There are several factors that make the perovskites particularly attractive as catalyst systems for research. One factor is that they form a large class of structurally similar compounds whose electronic properties can be varied in a controlled way. This permits a systematic study of the effects of variations in electronic parameters on catalytic rate, for example. (Pt is an excellent catalyst but there is little that can be done to vary its electronic state and therefore to discover why it is such a good catalyst.) A second factor making the perovskites important as catalysts is that they are highly stable at high temperatures and in hostile chemical environments.

Voorhoeve et al. [106] have reported extensive studies on a variety of perovskite catalysts. Co, Mn, and Ru perovskites have been investigated as catalysts for the oxidation of carbon monoxide and hydrocarbons and for the reduction of the oxides of nitrogen. (Such catalytic conversions are important in removing pollutants from auto exhaust.) Particular examples of perovskite catalysts investigated include $SrRuO_3$, $LaRuO_3$, and the substituted system $(La_xK_{1-x})(Ru_yMn_{1-y})O_3$. The catalysts are very active and highly selective in the reduction of nitrogen oxides. The use of substituted systems permits a controlled variation of valence states for the cations. The electronic properties can be tailored for a particular application.

Another important feature of perovskite catalysts is that they can be designed to simultaneously catalyze reduction and oxidation reactions. An example of such a catalyst is $(La_{0.8}Sr_{0.2})(Co_{0.9}Ru_{0.1})O_3$. Several perovskite compositions have been found to be superior or comparable to commercial catalysts.

It is also noted that surface oxygen vacancies on a perovskite can serve as catalytically active sites. NO is believed to dissociate into adsorbed N by reaction at a vacancy site on manganite catalysts. The liberated oxygen from the NO molecule can fill the empty surface oxygen site. The vacancy can be restored by reaction with an reducing agent such as CO. Such sites are useful in catalysis systems where both reduction and oxidation processes are desired.

The perovskites have not yet emerged as commercially competitive catalysts, but have proved valuable in the study of the possible mechanisms of catalysis.

As a final topic in the applications of perovskites we mention their use as electrochemical electrodes.

Materials such as $LaCoO_3$, n-type $SrTiO_3$ and the tungsten bronzes have been utilized as anode materials in electrochemical cells. They are particularly useful because of their stability in an electrolyte. Nearly ideal reversible electrode behavior has been shown for $LaCoO_3$ and related compounds such as $(La_{0.5}Sr_{0.5})CoO_3$ [110].

A particularly interesting application is the photoelectrolysis of water. The electrochemical cell consists of an n-type anode such as $SrTiO_3$, $BaTiO_3$ or some substituted perovskite and a Pt counterelectrode [111–114]. The electrolyte may be either alkaline or acid aqueous solution. The electrodes are connected through an external circuit and the electrolysis process is driven photocatalytically by photons incident on the anode surface. In alkaline aqueous solution the anode reaction is

$$2p^+ + 2\,OH^- \longrightarrow \frac{1}{2}\,O_2 + H_2O$$

where p^+ designates a hole. Electron-hole pairs are generated in the oxide anode by absorption of incident photons with energies equal to or greater than the band gap. The electrons and holes are separated by the internal electric field of the oxide (due to band bending at the oxide-electrolyte interface). In n-type materials such as $SrTiO_3$ the band bending creates an electron depletion (hole accumulation) region at the surface. The holes combine with adsorbed hydroxyl ions to produce molecular oxygen and water as indicated by the anode reaction above. The electrons are discharged at the cathode, producing hydrogen.

The feasibility of photoelectrolysis for the production of hydrogen has been demonstrated

using band-gap photons with $\hbar\omega \sim 3\,\mathrm{eV}$ for several oxides. The first such experiments utilized n-type TiO_2 [114]. Later studies employed perovskites such as $SrTiO_3$ [112, 113]. These experiments have raised the exciting possibility of developing a solar-driven electrolysis system for the production of hydrogen fuel. The band-gap energy of $SrTiO_3$ or TiO_2 is too large for efficient solar-driven devices and therefore interest has been stimulated to search for another oxide with a smaller band gap. Methods of reducing the energy for creating electron-hole pairs in large band-gap materials are also being considered. One such method is the use of adsorbed sensitizing dye molecules. Surface states in the band-gap region offer another way for the generation of electron-hole pairs with less-than-band-gap radiation. Such surface states may also be involved in electrocatalyzing the anode reaction.

Chapter 5

Defect in Perovskite : $SrTiO_{3-x}$

5.1 Introduction and objective

One of the greatest challenges in solid state physics has been the development of a satisfactory explanation of the fundamental differences between an insulator and a metal. When a few atoms of the same kind are brought together to form a molecule, the individual atomic orbitals break the degeneracy and form molecular orbitals. In a solid, where the number of atoms per cubic centimeter normally is in the order of 10^{23}, the individual atomic orbitals may form continuous bands. As explained by the nearly free electron model [115], these bands split when the electronic wave functions Bragg-scatter off the periodic lattice and give rise to regions in energy where no electrons are allowed. With this fairly simple picture, the difference between an insulator and a metal is understood as a full band and a partly filled band, respectively. In a full band, an electron has to be excited, beyond the so called "bandgap", to the next unoccupied band leaving behind a positively charged "hole." This hole moves, in an applied field, in the opposite direction of the electron and in this way no net current will flow. In a metal, where the most lightly bound electrons only partly occupy the band, the electrons directly start to move in an applied field, creating a net current. If the partly filled band is close to empty, or close to full, one normally talks about a semimetal or a semiconductor at elevated temperatures[1]. In the first part of the twentieth century, when the quantum theory for solids was developed, experimentalists tried to prove the nearly free electron model. It was found that wide-bandgap insulators (for example noble element crystals or diamond with bandgaps

[1]Reference text: Thesis of B. P. Andreasson, "OXYGEN VACANCIES IN $SrTiO_3$: AN X-RAY ABSORPTION STUDY", ETH Zürich, Zürich, Switzerland (2009)

of about $\sim 5-6$ eV) and intrinsic semiconductors (for example silicon and germanium with bandgaps around 1 eV) behave fairly close to this simple model [116]. For materials with bandgaps around $2-3$ eV, for example the $3d$ transition metal oxides, the behavior is not that straight forward. Many binary $3d$ transition metal oxides with partly populated $3d$ bands were found to be semiconducting and even insulating [117]. The inability of the nearly free electron model to predict the insulating behavior in the $3d$ transition metal oxides with partly filled bands has since then puzzled the scientific community. It turned out that the localized character of the $3d$ orbitals was responsible for the insulating behavior. In the tightly bound $3d$ orbitals the coulombic interaction between the electrons cannot be neglected. The localized behavior of the $3d$ orbitals is in strong competition with the partly delocalized character of the hybridized oxygen $2p$ orbitals. Therefore, in the $3d$ transition metal oxides, the charge, spin, and orbital degrees of freedom, give rise to a variety of interesting properties. Many of these properties do not arise in the intrinsic $3d$ transition metal oxides. However, when the material has been doped, these properties are revealed. In the $3d$ transition metal oxides, doping can be done either by partly substituting an element for another (for example La^{3+} for Sr^{2+} in $SrTiO_3$ giving metallic conductivity[118]), or by introducing defects, such as oxygen vacancies [119]. It seems logical that a very small doping of electrons or holes would gradually induce metal-like behavior in an insulator. In practice, there is a critical doping level; normally the material remains insulating or semiconducting over a broad range of band filling. Many compounds show transitions between insulating and metallic states when different chemical or physical parameters are changed. The idea that one could controllably switch a material between an insulator and a metal is originated from the nearly free electron model. The gap between the bands, formed due to the periodic potential, is controlled by the interatomic distance. Changing this distance by external pressure or other means, it would be possible to alter the bandgap. Depending on the filling of the bands, the material may switch between a metal and an insulator. Pressure dependent metal-to-insulator transitions were found in metallic Sr and Yb [120]. Several different transition metal compounds have shown metal-to-insulator transitions when other parameters were changed, for example doping or temperature [121]. The field of solid state physics, where different conductivity phenomenons are studied in the $3d$ transition metal oxides, belongs to the field of "strongly correlated electrons physics". A comprehensive review on early progress in this field, where the irregularities in the expected behavior of the $3d$ transition metal oxides is thoroughly explained, can be found in reference [122].

The solid state physics revolution induced by the discovery of the transistor by Shockley,

Bardeen, and Brattain [123] in the late forties was the basis for the electronic industry. The accelerating demands on the performance of electronics refined the manufacturing processes giving a possibility to produce materials of very high purity. Increase of the quality in manufacturing has led to the miniaturization of electronic devices, where the number of transistors per chip, amount of storage space per area, roughly follows exponential growth (known as Moore's law [124]). All progress in the electronics industry since the introduction of the transistor has been based on current flow and storage of charge. Information is, in this mainly silicon based technology, processed by redirecting currents with transistors and stored by charging capacitor structures. If the limitations of this technology are reached, currents and charges would have to be determined accurately in structures smaller than a few nanometers. In such small structures, the quantum nature of the electron will become more important, making the determination of currents and charges difficult. Based on Moore's law, the industry predicts to break the 10 nm barrier in 2020 (information taken from "International Technology Roadmap for Semiconductors") If the current electronic device development continues, ground breaking technological advances and a new perspective on current technologies will be required in order to avoid a stagnation of the market within the next few decades. Naturally, current solid state physics research is therefore trying to implement some of the recent ground breaking scientific discoveries in commercial electronic devices.

A renewed interest in transition-metal oxides and an upswing for the studies of strongly correlated systems was caused by the discovery of high temperature superconductivity in the copper oxides [125]. Since then, the temperature at which the material turns superconducting has been increasing to above 130 K [126]. Although applications such as superconducting power transmission or the generation of magnetic fields do exist, so far there has been limited impact on everyday consumer electronics.

Many of the transition metal oxides have a very large relative permittivity, making them suitable for the dielectric layer of capacitors. Especially $BaTiO_3$ [127] and later $SrTiO_3$ [128] have had many technological applications as dielectric materials. The most interesting question to ask is: How much electric field can one apply to the dielectric before the material breaks down and becomes conducting? To answer this question, and to develop new materials suitable for analog electronic devices, a lot of research effort has been spent on studying the dielectric breakdown in perovskite titanates. The phenomenon of resistance degradation has been known since the fifties, with early reports on $(BeBa)TiO_3$ in 1951 [129].

One phenomenon, closely related to the development of electronic devices, is the magnetoresistance effect. In recent years, this phenomenon has been detected in several

manganese based oxides, where the resistivity can be changed with applied magnetic fields [130]. Due to the extreme differences in resistivity this phenomenon was termed colossal magnetoresistance. In the manganese oxide based magnetoresistance materials, when the material is close to a metal-to-insulator transition, the conductivity can be changed by several orders of magnitude with the application of a magnetic field. Possible applications for these colossal magnetoresistance compounds would be to replace the current metallic magnetoresistance materials used in the read head of computer hard-disks, if the working temperature could be raised to room temperature and above.

In several transition metal oxides, the intrinsic resistivity, as well as induced states with higher conductivity, can be switched between two or more stable states. This phenomenon was first discovered in insulating films, e.g., SiO_2 and Al_2O_3 [131, 132]. In these early measurements, oxide films were grown by oxidizing chosen regions of the material. When the fabrication methods for the growth of oxide films were developed, there was a renewed interest in these kind of phenomena [133]. This was also boosted by the fact that the electronics industry saw possible applications with this phenomenon. If the resistivity of a material can be switched between two stable states, information can be stored.

The electronics industry is focused on improving the density, durability, and reading-writing speeds of non-volatile memories. These are currently dominated by the Flash memories which are important for almost all electronics, especially in hand-held mobile devices. The current main focus in this research field now lies on materials for which one can change the resistivity by controllable means. The main trends of this field are explained in reference [134]. Suggested techniques to change the resistivity are: Resistivity change of a metal-oxide-metal structure with applied electric field [133]. The resistivity can also be switched in a magnetic tunnel junction using magnetic fields [135]. In chalcogenide glasses, based on different GeSbTe alloys, the resistivity is changed when the material is switched between a crystalline and an amorphous phase with heat pulses [136].

The main objective of the present chapter was the theoretical study of oxygen vacancies in $SrTiO_3$ with different concentrations by means of first-principles simulations. These types of point defect represent very common imperfections in ABO_3-type perovskite oxides diversifying their chemistry and leading to a broad range of possible technological applications.

Our first step was to examine basic properties of perfect $SrTiO_3$ crystals. This study give us a significant insight into the electronic properties and chemical bonding of $SrTiO_3$ and give several predictions about the perfect $SrTiO_3$, we have examined these properties, especially around the Fermi level, to clarify the picture of this system in the

non-stoichiometric cases.
We also investigated the electronic structure and nature of bonding around the oxygen vacancies in the next step. We have used a supercell model to calculate the band structure; the incorporation of one or two oxygen vacancies in the supercell gives rise to variety of unique density of state functions depending on the distribution of defects in the supercell. Metallic behavior is thus predicted in every case.

5.2 Materials and Computational details

5.2.1 Method

The calculations have been performed within DFT implemented in the WIEN2K code [137]. Atoms were represented by hybrid full-potential (linear) augmented plane-wave plus local orbitals (L/APW + lo) method [138]. The electronic configurations are taken [Ar] $3d^2$ $4s^2$ for Ti, [Kr] $5s^2$ for Sr and [He] $2s^2$ $2p^4$ for O. In this method wave functions, charge density, and potential are expanded in spherical harmonics within no overlapping muffin-tin spheres, and plane waves are used in the remaining interstitial region of the unit cell. In the code, the core and valence states are treated differently. Core states are treated within a multiconfiguration relativistic Dirac–Fock approach, while valence states are treated in a scalar relativistic approach. The exchange–correlation energy was calculated using the Perdew–Wang local density approximations (LDA) [139]. Very carefully step analysis is done to ensure convergence of the total energy in terms of the variational cutoff-energy parameter. At the same time we have used an appropriate set of k points to compute the total energy. We compute equilibrium lattice constants and bulk moduli by fitting the total energy versus volume to the Murnaghan [140] equation. The total energy was minimized using a set of 78, 63, 38, 26 k-points in the irreducible sector of Brillouin zone, equivalent to a $5 \times 5 \times 11$, $5 \times 5 \times 5$, $5 \times 5 \times 3$ and $5 \times 5 \times 2$ Monkhorst-Pack [20] grid in the unit cell respectively, and the value of 8 Ry for the cutoff energy were used. The self-consistent calculations are considered to be converged only when the calculated total energy of the crystal converged to less than 1 mRy. We have adopted the values of 2.5 bohr for Sr, 1.95 bohr for Ti, and 1.5 bohr for O, as Muffin-Tin radii (RMT). Density of states has been calculated using the linear tetrahedron method with Blöchl corrections [141].

5.2.2 The perfect perovskite $SrTiO_3$

$SrTiO_3$ crystallizes in a cubic perovskite lattice, titanium is in the center of the unit cell octahedrally surrounded by six oxygen ions and a strontium ion in each corner. $SrTiO_3$ has the perfect cubic perovskite structure at temperatures above $\sim$ 110 K, which means that all the oxygen octahedrons are sharing a corner with another oxygen octahedron. One unit cell of $SrTiO_3$ is displayed in figure 5.1. This structure is generally known as the "ABO_3"perovskite structure. A and B denote cations and are in $SrTiO_3$ represented by Sr and Ti. The crystallographic space group of $SrTiO_3$ is the cubic $PM\bar{3}M$ (221) structure, the length of the unit cell (lattice parameter **a** in figure 5.1) is 3.8996 Å at room temperature [142].

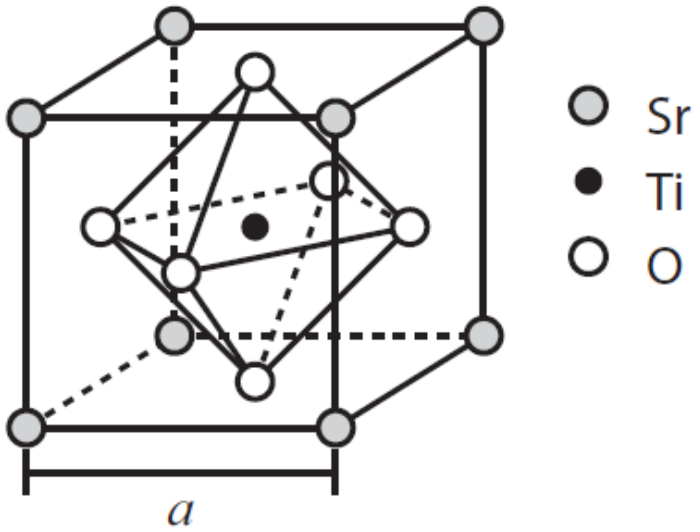

Figure 5.1: **The unit cell of the cubic perovskite $SrTiO_3$** - The positions of the ions in the unit cell are: Sr (000), Ti $(\frac{1}{2}\frac{1}{2}\frac{1}{2})$ and one O at $(0\frac{1}{2}\frac{1}{2})$, $(\frac{1}{2}0\frac{1}{2})$, and $(\frac{1}{2}\frac{1}{2}0)$ respectively. The lattice parameter is marked "a".

$SrTiO_3$ is known to have a structural phase transition below $\sim$ 110 K, where the cubic structure turns into a tetragonal structure. It has been suggested that this phase transition corresponds to a rotation of one rigid TiO_6 octahedron and a mirrored rotation of the next neighboring TiO_6 octahedron, thereby doubling the unit cell in all three crystallographic directions [143]. $SrTiO_3$ with its $3d^0$ electronic configuration is intrinsically a band insulator and paraelectric at room temperature. Paraelectric materials can be polarized by an electric field. $SrTiO_3$ remains paraelectric when lowering the temperature, with a sharp increase of the dielectric constant. Below 4 K the dielectric constant is very large

and does not vary. This was interpreted as a quantum mechanical phase, which stabilizes large ferroelectric fluctuations [144]. Furthermore, reduced, semiconducting $SrTiO_3$ was found to have a low-temperature superconducting phase, with transition temperatures ranging from 0.1 to 0.3 K, depending on the carrier concentrations [98, 145].

5.2.3 The oxygen vacancy in $SrTiO_3$

The oxygen vacancy V_O (also called the F center) is likely the most abundant defect in transition metal oxides and accounts for a rich variety of phenomena. To shed light on this pivotal defect, it is instructive to view it from different angles. Firstly, V_O may be considered from the electronic point of view as an electron or a hole trap/donor. In this respect, the position (shallow or deep) of vacancy's one-electron energy levels with respect to the conduction band is crucial for the electronic behavior and the optical properties of an oxygen non-stoichiometric material. The oxygen vacancies are believed to be largely responsible for leakage current [146], electrical breakdown [147] or degradation of transition metal oxide-based microelectronic devices [148, 149]. Also, the V_O are often implicated in deteriorating the performance of high-k gate oxides such as ZrO_2, HfO_2, trapping electrons and thereby reducing carrier mobility [149, 150]. Thus, the understanding of the V_O electronic properties and energetics of its formation in different charge states is of great practical importance.
As to the $SrTiO_3$ crystal in particular, oxygen vacancies are known to be a source of electron doping, thus making it n-type conductor. The change of oxygen concentration by only 10 ppm can change the conductivity of $SrTiO_3$ from a good n-type to a poor p-type. Furthermore, $SrTiO_3$ may even become superconducting in strongly oxygen-reduced atmosphere at $T \leq 0.35$ K. An appropriate tuning of the oxygen content also enables to switch the conductivity from the electronic to ionic type (see [151] and references therein).
Secondly, at elevated temperatures the V_O is a crucial ionic mobile carrier whose transport properties are of substantial practical relevance to solid oxide fuel cells, permeation membranes, oxygen gas sensors, etc. [152–155].
First-principles simulations of V_O in $SrTiO_3$ bulk were performed for 2×2×n (n = 1, 2, 3 and 4) supercells, for which the removing of the single and double oxygen ions allows to simulate the non-stoichiometric materials with formal compositions $SrTiO_{2.875}$ and $SrTiO_{2.750}$.

A supercell approach was used to simulate the effect of introducing vacancies into the

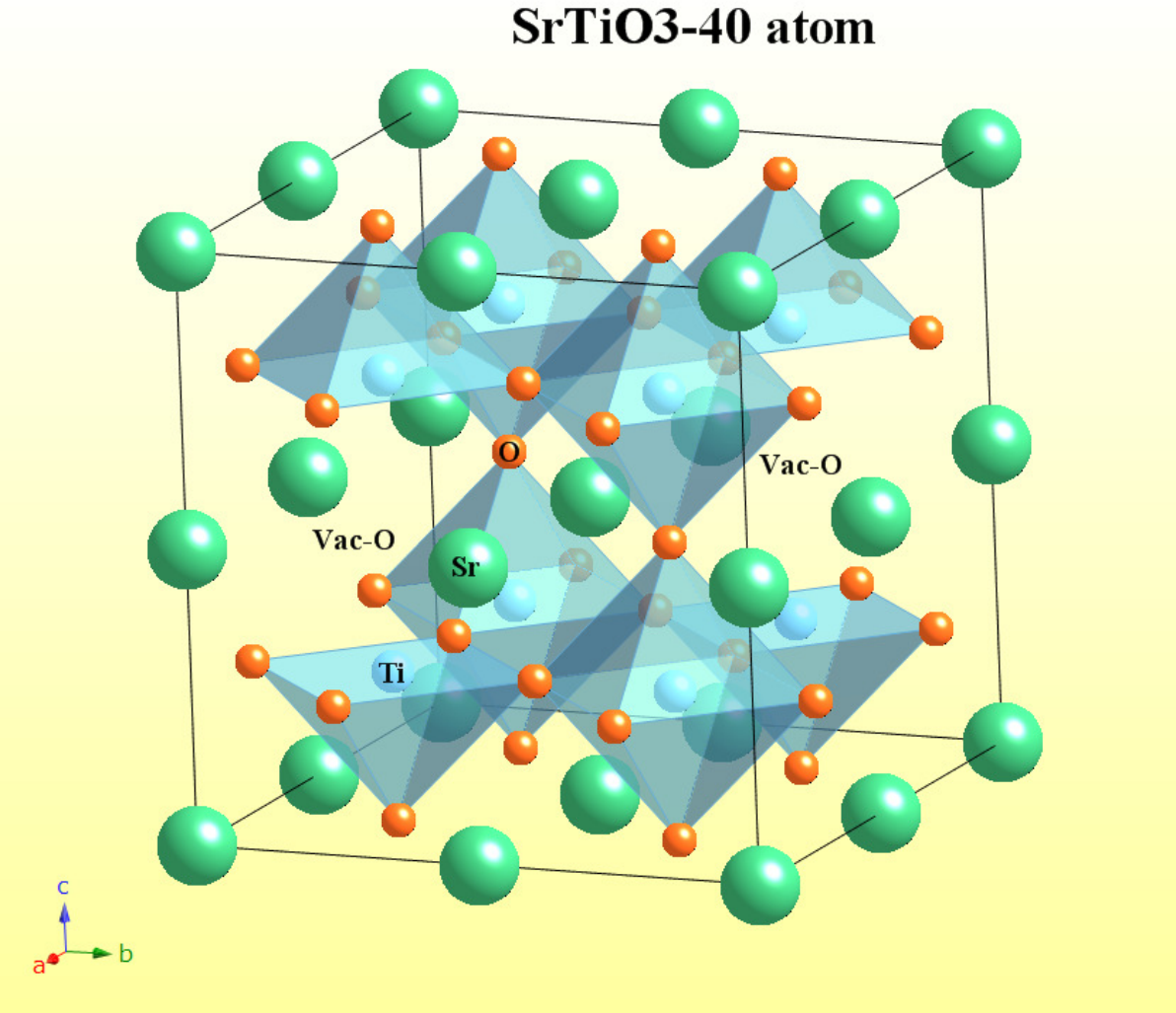

Figure 5.2: - Crystal structure of $SrTiO_3$ with double oxygen vacancy.

oxygen sublattice. Initial $SrTiO_3$ structure contained 20 (2×2×1), 40 (2×2×2), 60 (2×2×3) and 80 (2×2×4) atoms. A neutral vacancy was created by removing one then two neutral oxygen atoms from these supercells, this corresponds to vacancy concentration (x = 8.33% and x = 16.66%), (x = 4.16% and x = 8.33%), (x = 2.77% and x = 5.55%) and (x = 2.08% and x = 4.16%) for 2×2×n (n = 1, 2, 3 and 4) supercells respectively. Hence, the oxygen atom located at (1/4, 1/2, 1/2), (1/2, 1/4, 1/4), (1/4, 1/2, 1/2) and (1/4, 1/4, 1/4) for 2×2×n (n = 1, 2, 3 and 4) supercells respectively, (the fractional coordinates refer to the supercell), was taken out of the supercell. The supercell with doubled vacancy was constructed in a similar manner. Two neutral oxygen atoms residing in the $SrTiO_3$ supercell at (1/4, 1/2, 1/2), (3/4, 1/2, 1/2) positions for 20-atoms, (1/2, 1/4, 1/4), (1/2, 3/4, 3/4) positions for 40-atoms, (1/4, 1/2, 1/2), (3/4, 1/2, 1/2) positions for 60-atoms and (1/4, 1/4, 1/4), (3/4, 3/4, 3/4) positions for 80-atoms supercell, have been removed (see Figure 5.2).

5.3 Results and discussion

5.3.1 The pure perovskite $SrTiO_3$

The physical properties of strontium titanate have been studied extensively for well over thirty years. These research efforts have accumulated a profusion of facts leading to deeper understanding of some phenomena and greater bewilderment of others (compare, for example, [156] with [157] and [158] with [159]). This section reviews the current level of knowledge of bulk structure and properties of monocrystalline $SrTiO_3$.

At room temperature $SrTiO_3$ adopts the ideal cubic perovskite structure which may be described as a close packing of Sr^{+2} and O^{-2} ions with Ti^{+4} occupying one quarter of the octahedral interstices. Alternatively, one may consider the structure as a network of polyhedra, as illustrated in Figure 5.1, from which its simple cubic symmetry (crystallographic space group Pm-3m) is readily apparent. The basic structural unit is the Ti^{+4}-O_6^{+2} octahedron and the crystal consists of corner shared octahedra with Sr^{+2} occupying the icosahedral interstices. Each oxygen is coordinated to two Ti ions (linearly) and to four Sr ions, where the Ti-O bond length is smaller than the Sr-O bond length. There are eight other oxygen ions surrounding each oxygen with an O-O bond length equivalent to the Sr-O bond length.

5.3.1.1 Structural properties

Firstly, we have calculated the structural parameters using the DFT [31] as First-principles method and the Local density approximations (LDA) [139] for the exchange-correlation treatment. We have optimized the fundamental energy with varying the unit cell volume using the Murnaghan equation as equation of state (EOS) [140].
The results are compiled in Table 5.1, together with previous experimental and theoretical data for a comparison purpose.
The overall agreements with previous literatures are satisfactory. The lattice constant of 3.859 Å and the bulk moduli 203.25 GPa agree with the theoretical and experimental values (3.905 Å) so that the bond lengths are approximately 1.95Å and 2.76Å for the Ti-O bond and Sr-O (O-O) bond, respectively.
In studying the stability we are interested in the equilibrium volume and the formation energy defined as

$$E_{form}(SrTiO_3) = \frac{E_{total}(Sr_mTi_nO_p) - [m.E(Sr) + \frac{1}{2}n.E(Ti) + p.E(O_2)]}{m+n+p}$$

where m, n and p are the number of atoms used in the supercell and $\frac{1}{2}$ in Ti used because the unit cell of elemental bulk Ti contain two atoms. The reference state for Sr is the face-centered cubic (space group Fm-3m), for Ti it is the hexagonal structure (space group $P6_3/$ mmc) and for O it is monoclinic phase (space group C2/m).
The formation energy of pure $SrTiO_3$ is -4.869674 eV/atom. From this negative value, one can deduce that the $SrTiO_3$ system is structurally stable. It is clearly seen that the formation energy is converged at 2×2×3 supercell (see Table 5.1). This convergence reveal that the study of defect in $SrTiO_3$ require a supercell higher than 60 atoms.

5.3.1.2 Electronic properties

Early determinations of the electronic structure of strontium titanate, utilized the LCAO (linear combination of atomic orbitals) or FPLAPW approach or molecular-orbital (MO) methods based on a local density approximation for electron correlation. The limitations of both methods are well-known — the former underestimates the band gap energy while it is overestimated by the latter.

Table 5.1: Calculated values for the lattice parameter (a, in Å), bulk modulus (B, in GPa), the formation energies (E_{form}, in eV/atom) and vacancy formation energies (E_{vf}, in eV) for cubic perovskites $SrTiO_3$ obtained in our FLAPW-LDA calculations in comparison with available experimental and theoretical data.

	20 atoms	**40 atoms**	**60 atoms**	**80 atoms**
$SrTiO_3$				
a (Å)	3.8599, 3.863[160], 3.863[161], 3.922[162], 3.865[163], 3.900[142], 3.89[164]			
B (GPa)	203.253, 183.00[160], 198.00[161], 190.00[162], 200.00[163], 180.00[164]			
E_{form} (eV/atom)	-4.865595	-4.8679	-4.869674	-4.869021
$SrTiO_3$-V_O				
a (Å)	3.8567	3.8587	3.8592	3.8595
B (GPa)	188.174	196.195	198.585	199.247
E_{form} (eV/atom)	-4.646371	-4.6573	-4.80753	-4.821104
E_{vf} (eV)	8.385	8.425	8.531	8.654, 9.14[165], 8.74[166]
$SrTiO_3$-V_{2O}				
a (Å)	3.8477	3.8561	3.8582	3.8587
B (GPa)	174.656	188.3112	193.65	196.402
E_{form} (eV/atom)	-4.429029	-4.4368	-4.743411	-4.771483
E_{vf} (eV)	8.541	8.622	8.536	8.673

These calculations, however, afford significant insight into the electronic properties and chemical bonding of $SrTiO_3$ and several predictions based on these results are consistent with experimental observations [167]. Our calculated band gaps are less than experimental values (3.25 eV), which is typical for our LDA calculations (1.86 eV). Figure 5.3 shows the band structure for undoped $SrTiO_3$. The results depict $SrTiO_3$ as an indirect insulator with the top of the valence band at R and the bottom of the conduction band at Γ. The lowest conduction band from Γ to X is quite flat, which was found to be a common feature of many ABO_3 perovskite ferroelectrics [89, 163].

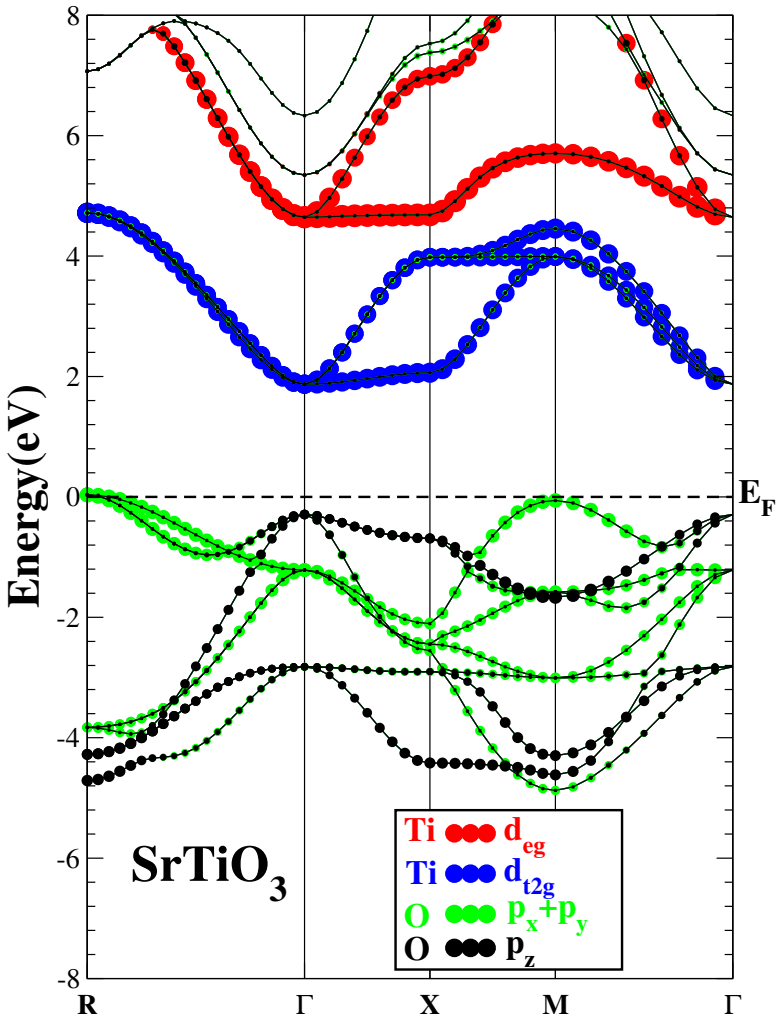

Figure 5.3: **Energy band structure of undoped $SrTiO_3$** - The zero of energy is set at the top of the valence band.

It is well known that the electronic properties of the doped systems can sensitively depend on the electronic structure near the top of valence band and near the bottom

of the conduction band. Figure 5.4 shows $|\Psi_R|^2$ and $|\Psi_\Gamma|^2$ throughout the Ti-O plane, respectively. Here Ψ_R and Ψ_Γ are electron wave functions at R point of the highest valence band and at Γ point of the lowest conduction band, respectively. It is clear that Ψ_R is predominantly composed of O $2p$ orbitals and Ψ_Γ is predominantly composed of Ti $3d$-t_{2g} orbitals.
In fact, because of the cubic crystal field produced by the six nearest-neighbor O atoms, the empty Ti $3d$ orbitals will split into three lower energy t_{2g} orbitals (xy, yz, zx) and two higher energy e_g orbitals ($3z^2$-r^2, x^2 -y^2). From Figure 5.3, this can be clearly seen by the threefold degenerate states at the conduction band minimum and the twofold degenerate states which are 2.3 eV higher in energy (at Γ).

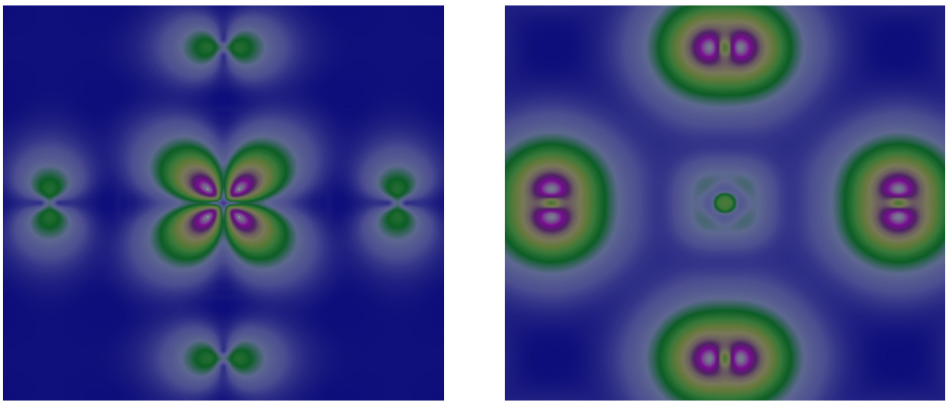

(a) (b)

Figure 5.4: **(a)** $|\Psi_\Gamma|^2$ of the lowest conduction band (Ti $3d - t_{2g}$ orbitals) and **(b)** $|\Psi_R|^2$ of the highest valence band (O $2p$ orbitals) in the Ti-O plane for undoped $SrTiO_3$.

5.3.2 Single and double oxygen vacancies

Now we examine the effect of O vacancy doping on the structural and electronic properties.

5.3.2.1 Structural properties

For undoped $SrTiO_3$, Introduction of the oxygen vacancies (V_O and V_{2O}) into $SrTiO_3$ matrix is accompanied by a very small rearrangement of neighboring atoms. From Table 5.1, one can see that the introduction of vacancies in $SrTiO_3$ leads to a reduction in volume and bulk moduli. The same trend is obtained by the authors of Ref [163]. our

calculated Sr-O and Ti-O distances are 2.757 Å and 1.950 Å, respectively. We find that introducing O vacancies leads to a slight distortion, For the 40 atom supercell, the vacancy-induced changes of the bond lengths are less than 0.06 Å for the Sr -O bond and 0.04 Å for the Ti-O bond. We observe that the nearest two Ti^{4+} cations and eight O^{2-} anions move toward the vacancy.
We have also calculated the formation energies of our defected systems as:

$$E_{form}(SrTiO_{2.875}) = \frac{E_{total}(Sr_mTi_nO_{p-1}) - [m.E(Sr) + \frac{1}{2}n.E(Ti) + (p-1).E(O_2)]}{m+n+(p-1)}$$

$$E_{form}(SrTiO_{2.750}) = \frac{E_{total}(Sr_mTi_nO_{p-2}) - [m.E(Sr) + \frac{1}{2}n.E(Ti) + (p-2).E(O_2)]}{m+n+(p-2)}$$

The indication of the stability of these compounds with the following values according to these calculations of vacancy formation energies, for $SrTiO_{2.875}$ and $SrTiO_{2.750}$ are -4.821104 eV/atom and -4.771483 eV/atom respectively for 2 supercell. It is clear that the single oxygen-deficient phase is less stable than the perovskite with double oxygen vacancies. This remark coincides with direct estimations of the vacancy formation energies (E_{vf}) as:

$$E_{vf} = E(SrTiO_3 : V_O) + E(V_O) - E(SrTiO_3)$$

The results obtained (Table 5.1) also confirm that the formation energy of double oxygen vacancy is the most energetically stable, adopting the minimal E_{vf} in all cases. when we compare between E_{form} and E_{vf} of 40 atoms with V_O and 80 atoms with V_{2O} we find that the double oxygen vacancy is more stable; this result confirm the existence of more than tow oxygen vacancies in the bulk of more than 40 atoms. Note that our estimation of E_{vf} is in a reasonable agreement with other available data [165, 166]. The convergence of the E_{form} and E_{vf} from the 40 atoms and more, neglect the effect between neighboring vacancies defects. In conclusion, The reduction of formation energy between single and double oxygen vacancies confirm that the $SrTiO_3$ perovskite structure cannot support further removal of oxygen from the lattice. Note, however, that this limiting phase has a reduced lattice point symmetry which suggests the lifting of energy band degeneracies.

5.3.2.2 Electronic properties

We are most interested in the doping-induced change of the band structure around the Fermi level.
examined deficiency in oxygen atoms on our stoichiometric supercell by the calculation of the band structures in both cases: single and double oxygen vacancies, which are shown in Figures 5.5a, 5.5b, 5.5c and 5.5d for 2×2×n (n = 1, 2, 3 and 4) supercells. These results show that the Fermi energy is moved at the more energetic levels and becomes a conductor. Our calculated band structures are in excellent agreement with those determined by Luo et al [168].
We are most interested in the doping-induced change of the band structure around the Fermi level. Figures 5.5a-(d) and 5.6 shows the band structure and DOS of $SrTiO_{1-x}$, respectively. For this case, the Fermi level is in the conduction band and the DOS at the Fermi level is no longer zero because of the carriers arising from O vacancies. Hence the doped system is metallic.

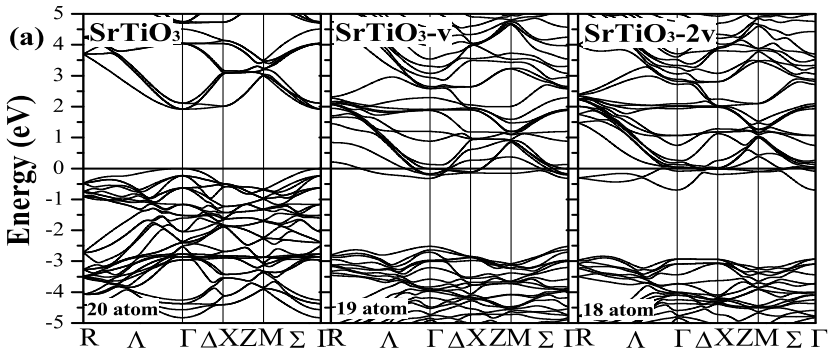

(a) 20 atoms

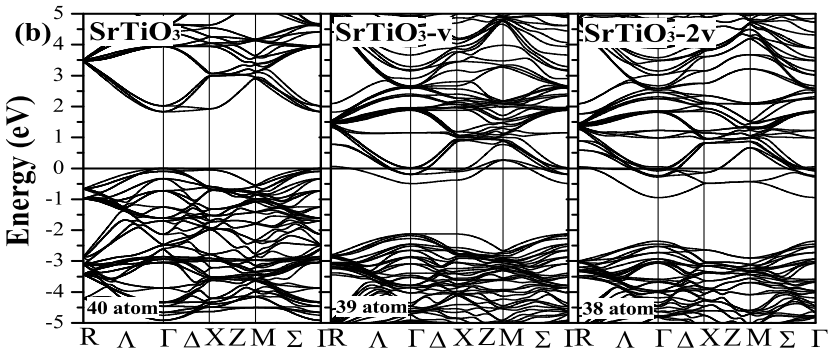

(b) 40 atoms

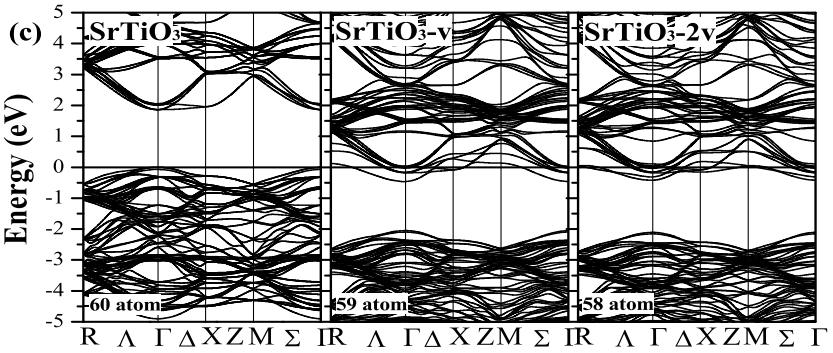

(c) 60 atoms

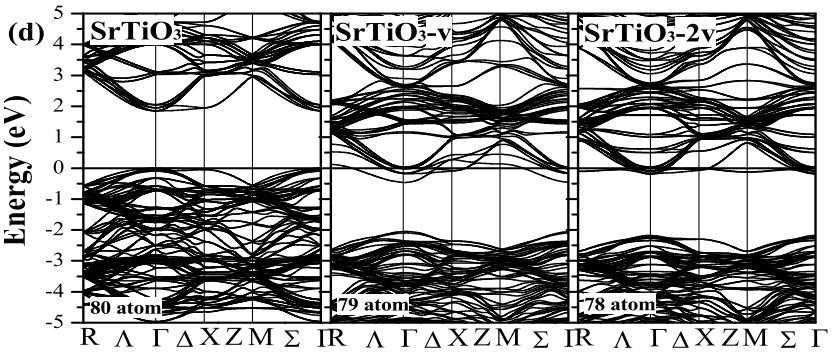

(d) 80 atoms

Figure 5.5: Calculated band structure of $SrTiO_3$ along several high-symmetry axis.

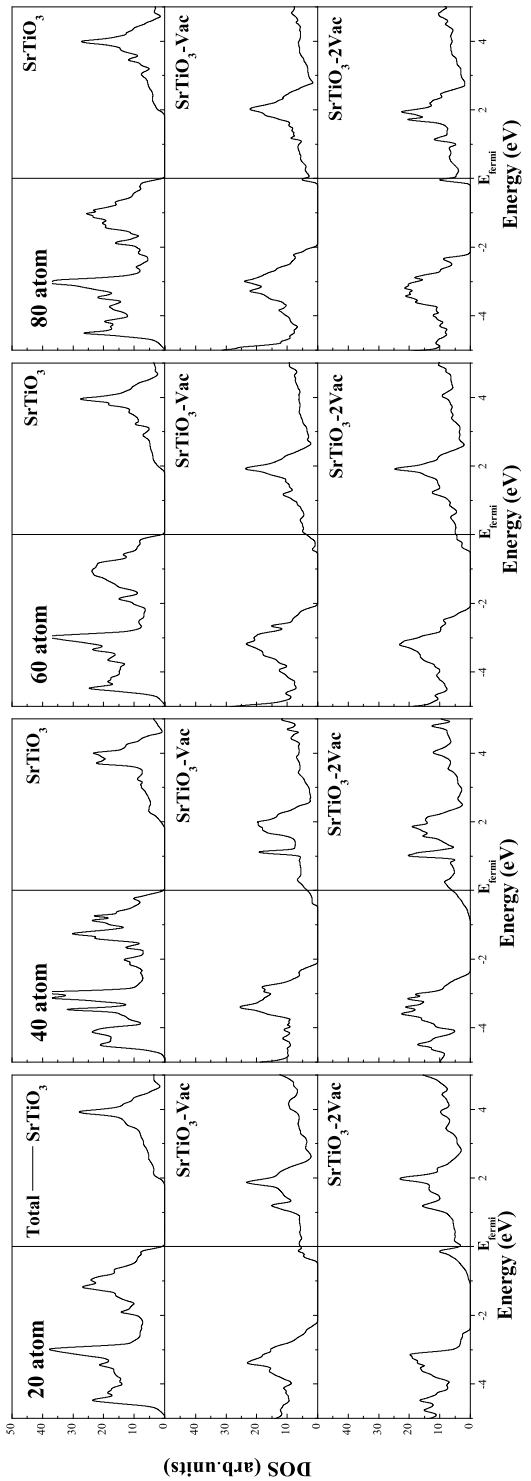

Figure 5.6: Calculated projected total DOS plots of $SrTiO_3$ with different supercells.

Based only on a comparison of the DOS, i.e., Figs. 5.6(undoped $SrTiO_3$) and 5.6(doped $SrTiO_3$), a supercell method appears to be proper for describing the effect of electron doping on electronic properties, Since a 2×2×n supercell is used in our calculations for doped $SrTiO_3$. It is clear that the calculation of undoped $SrTiO_3$ with 2×2×n supercell is important to consider the band folding effects while comparing the band structure of Figure 5.5a-(d) with that of undoped $SrTiO_3$ [shown in Fig. 5.3]. From Figure 5.3, we can see that the lowest level at X of the conduction bands is nondegenerate. For undoped $SrTiO_3$ in a 2×2×n supercell, there would be six low lying Γ levels, three are associated with the original degenerate Γ states and the other three arise from folded X states. These six states are much lower in energy than other levels in the conduction bands, and therefore have a large influence on the electronic properties.
It is noticed that there is an important density in the non-stoichiometric supercells compared with that of the stoichiometric supercells [shown in Fig. 5.6].
It is interesting to note that when there is one O vacancy in the 2×2×2 supercell, there are seven Γ levels near the Fermi level in the conduction bands, as shown in Fig. 5.5b, on the other hand, when there are two O vacancies in the 2×2×2 supercell, there are seven band of defect and the width bands is wider than one oxygen vacancy. One of the lowest conduction bands originate from the O vacancy. In order to clarify this point, we analyze the partial density of states (PDOS) [shown in Fig. 5.7] and the electronic charge density [shown in Fig. 5.8]. We find that, in the lowest conduction band, mostly the e_g type orbitals $(3z^2 - r^2)$, and this observation is confirmed in the charge density (Fig. 5.8 (a) of the lowest seven bands, when the charge is concentrate especially between the both Ti^{3+}, this orbital is less charged along the Ti-Vac-Ti direction in the 2×2×4 supercell (80 atoms); We can see that in the bands structure of 39 atoms Fig.5.5(b) and 79 atoms Fig.5.5(d).
The wave functions of the other six lowest conduction bands are predominantly composed of Ti $3d - t_{2g}$ orbitals, as shown in Figures 5.7 and 5.8 (b). For these six bands, all Ti atoms (no matter whether they are close to the vacancy or not) have similar contributions, which is also very similar to the picture shown in Figure 5.4(a) for undoped $SrTiO_3$. Therefore we may conclude that the lowest conduction band originates from a Ti $3d - e_g$ type defect state, and the other six conduction bands are associated with the band folding states of the three lower conduction bands (mainly Ti $3d - t_{2g}$ orbitals) of the undoped $SrTiO_3$. This again indicates that the effect of electron doping by introducing O vacancies cannot be correctly analyzed within a small supercell.

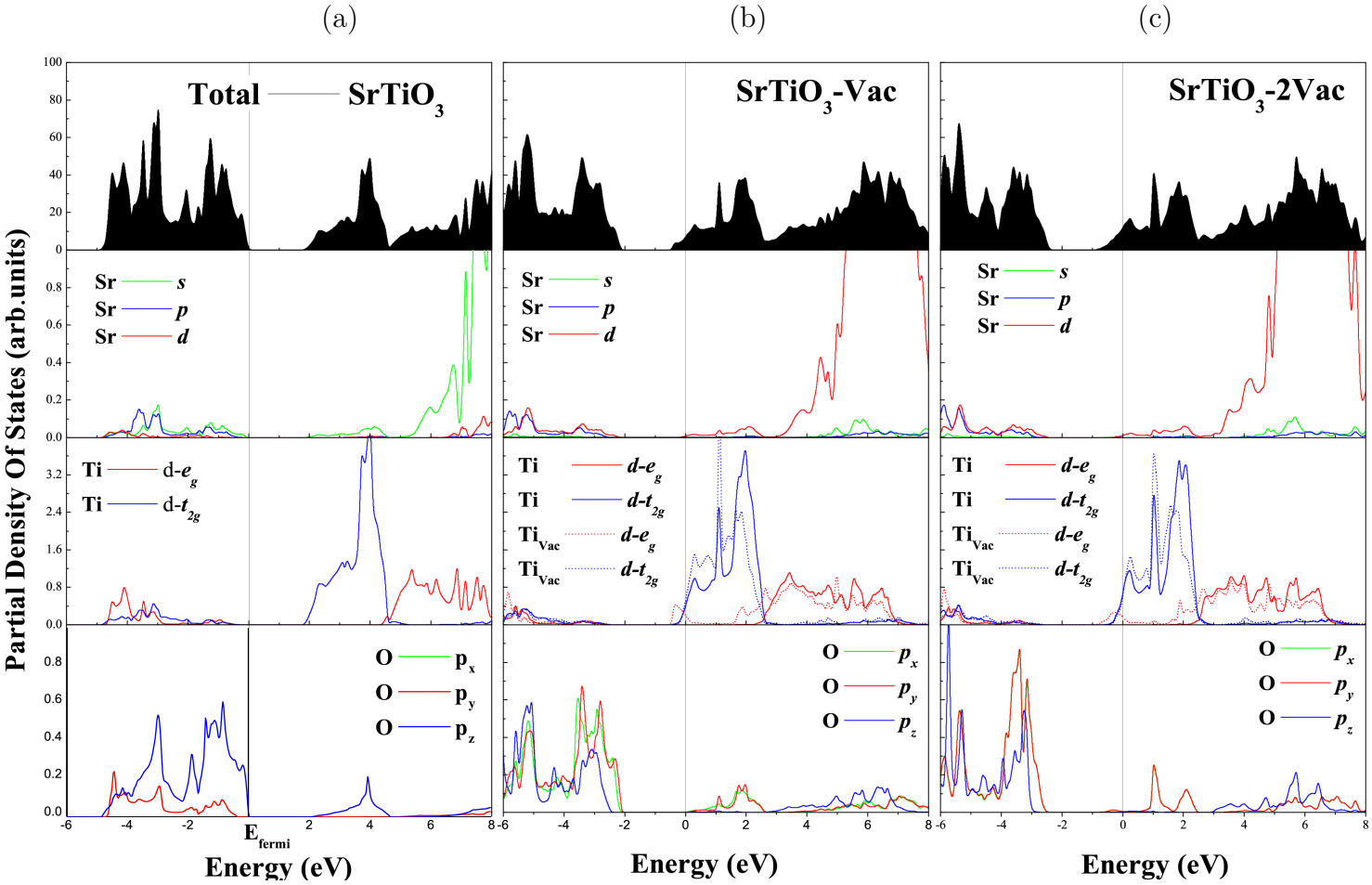

Figure 5.7: Calculated projected partial DOS plots of $SrTiO_3$ in 40 atoms supercells.

We note that in the 40 atom supercell calculations, the Ti $3d - e_g$ type defect states have lower energy than the Ti $3d - t_{2g}$ type conduction states. This is actually easy to understand, considering that the $3z^2 - r^2$ type orbital concentrates its charge density in a direction toward two of the nearest O atoms, while one of them (the one in the vacancy site) is missing.

From the energy dispersion of the defect state [Fig. 5.6(b)] and the spatial extension of the defect wave function [Fig. 5.8(a)], there is considerable interaction of the defect wave functions along the Ti-Vac-Ti direction between neighboring supercells. To address this problem, we had to investigate the band structure of $SrTiO_{3-x}$ with a doubled supercell (80 atoms). Compared to the 40 atom supercell, there are two important differences in the electronic band structure. First, the defect band dispersion becomes almost flat with a bandwidth of ≈0.3 eV, which is the result of reduced interaction between defect wave functions due to a larger supercell. Second, for the two Ti atoms next to the O vacancy, the distance to their other nearest-neighboring O atoms along the Ti-Vac-Ti is reduced by 0.06 Å compared to the undoped structure. The enhanced crystal field caused by the closer O atoms lifts up the e_g type defect states. Energy level of this shift is about ≈0.40 eV higher than the conduction band minimum and above the Fermi level. Thus the defect state becomes completely empty. In a publication [169], Ricci et al. observed

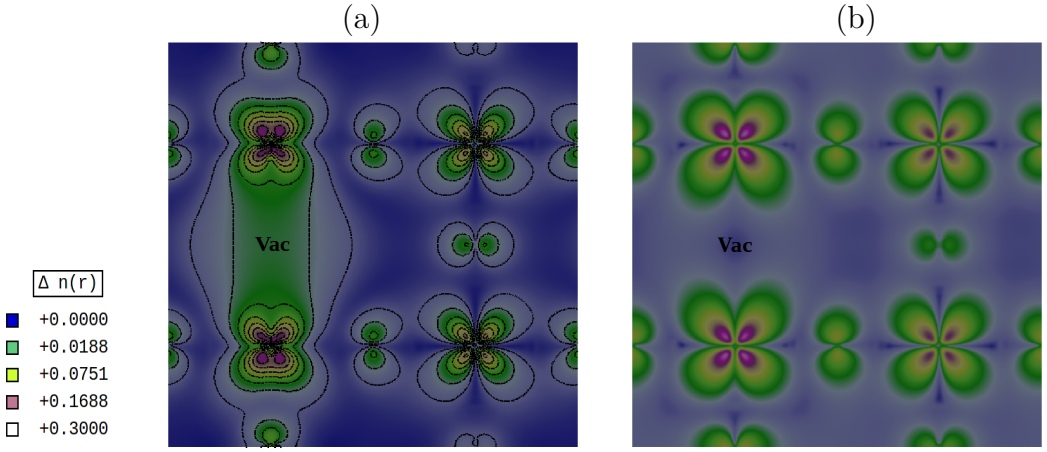

Figure 5.8: **(a)** Charge density of the oxygen vacancy induced defect state (mainly Ti $3d - e_g$ type states) and **(b)** the lowest conduction band (Ti $3d - t_{2g}$ state) above the defect state of $SrTiO_{2.875}$ in the Ti-O plane.

a similar impurity state in the band gap associated with the oxygen vacancy, although they did not see the shifting of the impurity energy due to the lack of relaxation of the internal atomic coordinates. In other papers [170] and [168] on the oxygen vacancy, it is claimed that the defect wave function changes its character from a deep to a shallow

level by going from a 40 atom supercell to a 160 atom (and 320 atom) supercell. While the defect wave function in theirs 40 and 80 atoms supercell calculations is similar to the Ti $3d - e_g$ type defect state wave function in our calculation.

5.4 Conclusion

To sum up, we have performed a detailed investigation of the structural and electronic properties of single and double oxygen vacancy defects in bulk $SrTiO_3$ using first principles LDA method.

Our first step was to examine basic properties of perfect perovskite crystal. We found for $SrTiO_3$ compound that the best agreement with experimental data on lattice constant, bulk modulus, formation energy and charge band gap is provided by the density functional theory (DFT).

Nominally pure $SrTiO_3$ is an electronic insulator at room temperature. Incorporation of point defects into the lattice can generate free charge carriers or charged ionic species. The latter treatment introduces an approximately equivalent density of oxygen vacancies which are known to exhibit significantly large lattice mobility. $SrTiO_3$ is thus considered a mixed electronic-ionic conductor.

The removal of one oxygen from the lattice reduces two Ti^{4+} to Ti^{3+} and replaces two octahedra with two square-pyramids, as shown in Figure 5.2.

In our supercell band structure calculations, the incorporation of one or two oxygen vacancies in a supercell containing eight unit cells gives rise to variety of unique density of state functions depending on the distribution of defects in the supercell. Metallic behavior is thus predicted in every case.

In the most heavily reduced case corresponding to two homogeneously distributed vacancies per unit cell (i.e., $SrTiO_{2.875}$, conduction band states were found to extend to ≈ 1 eV below the Fermi level and below ≈ 0.5 eV comparing to single oxygen vacancy. As the oxygen vacancy density increases, it is assumed that the width of this band also increases, while the formation energies decrease.

The similarity of t_{2g} orbitals (xy, xz, yz) in the defect wave function of all Ti atoms of supercell confirms the existence of an ionic conductivity in the $SrTiO_{3-x}$. However, the contribution of deep e_g ($3z^2 - r^2$) in defect wave function confirm the electronic conductivity, this state has a lower energy than Ti $3d - t_{2g}$ type conduction states. This is actually easy to understand, considering that the $3z^2 - r^2$ type orbital concentrates its charge density in a direction toward two of the nearest O atoms, while one of them (the

one in the vacancy site) is missing.
The wave functions of the other six lowest conduction bands are predominantly composed of Ti $3d - t_{2g}$ orbitals. For these six bands, all Ti atoms (no matter whether they are close to the vacancy or not) have similar contributions, which is also very similar to undoped $SrTiO_3$. Therefore we may conclude that the lowest conduction band originates from a Ti $3d - e_g$ type defect state, and the other six conduction bands are associated with the band folding states of the three lower conduction bands (mainly Ti $3d - t_{2g}$ orbitals) of the undoped $SrTiO_3$. This indicates that the effect of electron doping by introducing O vacancies cannot be correctly analyzed within a small supercell.

Chapter 6

Perovskite alloy: $Bi_{1-x}La_{-x}CoO_3$

6.1 Introduction and objective

Numerous binary AO_x and ternary ABO_x oxide systems where A and B are two different cations have been studied throughout the years, plenty of work still remains, to find new applications for old materials and to find new materials for current and new technologies based on more complex interplay between the composition, structure and properties in ternary and higher order systems. Especially for complex systems where simplified theories for magnetic interactions, conductivity, catalysis and ionic conductivity stop working, additional investigations are necessary.
At this point of time, predictions through computational simulations are still neither accurate enough nor fast enough to predict the structure and properties from only an initial input of the composition for complex systems. Thus, systematic investigations of compositional variations in, e.g., perovskite-related systems, to understand the more complex compositions, are an essential first step. One of the goals will be to improve the computational models in order to find new materials with desired properties more efficiently in the future. Synthesis of new materials based on the initial research goals is complemented by the measurement of the properties in order to improve the computational models that are used to predict new materials. However, apart from the exploratory research that is driven by curiosity to explain different phenomena or to find new ones, most of the research is often application driven and that type of research is mainly driven by the need to solve specific problems, e.g., increase efficiency, lower the

price and decrease the impact on the environment[1].

A material compositionally tuned to be at a phase boundary with a first-order transition could be viewed as being "on the brink," and it can often display a colossal response in reaction to weak external stimuli such as temperature, electric field, or magnetic field. For instance, giant piezoelectric responses are achieved in some Pb-based ferroelectrics by tuning their compositions to their morphotropic phase boundaries (MPBs)[171–175], where two different structural phases that are close by in the energy level coexist[2]

Multiferroic compounds with coexisting magnetic and ferroelectric orders [24] are the focus of current research due to their potential technological applications [176]. For technological purposes, it is desirable to have a high transition temperature as well as a reasonably high value of polarization. Perovskite-type materials of general formula ABO_3 and related materials have been discussed extensively for this purpose. Leaving aside the emerging class of improper multiferroics [177] with magnetic-order-driven ferroelectricity, for which generally both the ordering temperature as well as the magnitude of polarization are low, most of known magnetic ferroelectrics have a *lone-pair* active Pb or Bi ion at the A site and a transition metal ion having unpaired d electron at the B site. The ferroelectricity is primarily driven by the A site cation, whereas the magnetism is driven by the B site cation. Following this idea, compounds like $BiFeO_3$ [178] and $PbVO_3$ [179] have been synthesized and they show large polarization as well as large transition temperatures together with antiferromagnetic ordering of spins at the B site[3]

Along the same line of thought, Multiferroic $BiCoO_3$ has been carried out, $Bi^{3+}Co^{3+}O_3$ has the $PbTiO_3$-type structure and the Co ion is pyramidally coordinated by five oxygen ions [180]. The pyramidal coordination for Co^{3+} is caused by the noncentrosymmetric coordination for Bi^{3+} with Bi $6s$ *lone pair*. The Co^{3+} ion takes the d^6 electronic configuration which possess the possibility of low-spin, intermediate-spin, or high-spin configurations. $BiCoO_3$ is a pyroelectric insulator with antiferromagnetic long-range order below $T_N = 470K$ and takes C-type antiferromagnetic state where the magnetic moments of Co^{3+} ions are aligned antiferromagnetically in the ab-plane and are stacked ferromagnetically along the c-axis [4][4].

The presence of the Co ion in $BiCoO_3$ which is well known for its spin-state transition is expected to add another dimension to the multiferroic aspect of the compound. In ambient pressure (AP), $BiCoO_3$ is in a polar tetragonal structure with a rather high

[1]Reference text: Samrand Shafeie's thesis, "Properties in New Complex Perovskite Related Materials, a Matter of Composition and Structure", Stockholm university 2013, ISNB:978-91-7447-672-9.

[2]Reference text: D. Kan et al., Adv. Funct. Mater. 20, 1108–1115 (2010).

[3]Reference text: S. Kanungo et al., Phys. Rev. B 83, 104104 (2011).

[4]Reference text: T. Sudayama et al., Phys. Rev. B 83, 235105 (2011).

tetragonality of c/a = 1.27 characterized with a large calculated [5] polarization (170 $\mu C/cm^2$) and a high-spin (HS) state of Co^{3+}. The HS of Co is found to be retained down to the lowest temperature, preventing the temperature-driven route of the spin-state transition as in case of $LaCoO_3$ [181][3].

As Bi^{3+} has a very similar ionic size as La^{3+}, it is reasonable to assume that when the local Co-O bond lengths of $BiCoO_3$ in the HP-PE phase become identical to those of $LaCoO_3$ in the LS state at low temperature (1.925 Å at 5 K) [182], a complete transition into the LS state would be achieved in $BiCoO_3$[5].

Metamagnetism from spin-state transitions may give rise to exciting phenomena such as giant magnetoresistance [183], giant magnetocaloric effect [184], shape memory effect [185], etc. We show presently that metamagnetism can also lead to giant magnetoelectric coupling. Generally, spin-state transitions are induced by hole/electron doping, temperature, magnetic field, pressure, and/or lattice strain. For the first time P. Ravindran et al [5] has shown that spin-state transitions can also be induced by an electric field in the case of magnetoelectric materials that display magnetic instabilities.

Chemical modification of the *A*-site of the perovskite structure (ABO_3) is expected to affect the ferroelectric (FE) properties [186]. O. E. González-Vázquez et al [187], predict an enhancement of the functional responses of BLFO for compositions close to both the BFO and the LFO limits, revealing the atomistic mechanism responsible for the improved properties. Also, Kan et al. [186] have shown that an enhanced dielectric response is obtained in BFO samples in which Bi is partially substituted by a rare-earth *RE*, with *RE* = La, Sm, Gd, Dy, etc.

In fact, chemical modification of BCO has been a popular topic of investigation and there continue to be new reports of attempts at improving its FE properties. Despite the collection of literature that now exists in such studies, a comprehensive picture on the substitutional effect of rare-earth (*RE*) ions in BCO is still missing [186].

In the present study, we seek the origin of the giant tetragonal FE distortion in the ambient phase of $BiCoO_3$ and identify the nature of the La-substitution-induced spin-state transition, using local density approximation plus Hubbard U (LSDA+U) calculations. Our results show that the structural stability of this alloy between tetragonal-AFM-C and rhombohedral-NM undergoes a strongly discontinuous transition between a Tetragonal-phase and a Rhombohedral-phase at $x \simeq 0.345$, this structural transition is associated with a spin state transition from HS magnetic state to LS nonmagnetic state, these transitions are mainly due to the changes in different effects such as, crystal field, Jahn-Teller,

[3]Reference text: S. Kanungo et al., Phys. Rev. B 83, 104104 (2011).
[5]Reference text: Ting Jia et al., Phys. Rev. B 83, 174433 (2011).

and *lone pair* effects.
In this investigation, we have followed this strategy:
In first, we have studied in detail the electronic structure and magnetic stability of each parent (BCO and LCO).
Secondly, we have compared both materials in both structures (tetragonal and rhombohedric).
Finally, we have carried out a detailed study about BLCO alloy in both structures, in order to identify a magneto-structural transition.

6.2 Materials and Structure

6.2.1 Oxide Perovskites

A rare natural mineral, perovskite $CaTiO_3$, has given name to a structural class in which extensive range of materials adopt the perovskite structure or derivatives of it. The general formula of perovskites is: ABX_3 where A and B are cations and X the anion which is mostly oxygen, ABO_3 [6].
Oxide perovskites offer diverse range of properties from insulation to metallic conduction, ionic conduction, (anti-)ferroelectricity, (anti-)ferromagnetism and electrooptic responses [188–190].
In an ideal perovskite with the cubic structure and space group $Pm\bar{3}m$, the A cations are similar in size to O anions (1.4 Å) and occupy the cubo-octahedral 12-coordinated positions whereas the smaller B cations are in 6-coordinated octahedral sites. The O anions are surrounded by four A and two B cations [190, 191].

6.2.1.1 Tolerance factor, *t*

If the ions are considered as rigid spheres, an ideal perovskite structure will have the cations surrounded by as many anions as can touch them according to their coordination number. The perfectly sized ions create a structure of touching spheres where the cations cannot rattle around in the interstices between the anions. The geometrical relationship

[6] Reference text: Sara Karimi's thesis, "Structure-Property Relations in Rare Earth Doped $BiFeO_3$", Sheffield university 2011

between the ions' radii in this ideal cubic perovskite structure is expressed by Equation 6.1

$$(R_A + R_O) = \sqrt{2}(R_B + R_O) \tag{6.1}$$

However, ionic radii depend on the form of bonding and electronic configuration and actual materials rarely show ideal ionic radii. Tolerance factor, t, may therefore be introduced as a parameter on how well the ions fit into the perovskite structure, Equation 6.2 [192].

$$t = \frac{(R_A + R_O)}{\sqrt{2}(R_B + R_O)} \tag{6.2}$$

At t=1 the structure is a perfect cubic perovskite and the ions are ideally packed. Strontium titanate, $SrTiO_3$, with tolerance factor of $t = 1.002$ is one of the closest perovskites to ideal. In general when $0.8 < t < 1.05$, the perovskite structure is usually stable but deviations from the ideal value of 1 result in structural distortions of the perovskite cell that result in interesting functional properties[1, 190, 192].

6.2.1.2 Distorted perovskites

The deviation from the ideal perovskite structure can be described as a result of either ionic displacement, chemical ordering, tilting of the BO_6 octahedra or combinations thereof [193]. Generally these distortions are minor and the cubic structure will still be recognized in diffraction patterns. Line splitting, and in some cases extra lines in X-ray diffraction and extra reflections in electron diffraction will occur if the structure is distorted. These extra features in the diffraction patterns can be used to determine the true nature of the structure [1, 190].
Often for simplicity planes, directions and lattice parameters of the non-ideal perovskite are expressed in terms of the ideal cubic unit cell. This makes discussing a heavily distorted perovskite or comparison between perovskites much simpler and easier. These indices are referred to as "pseudo-cubic" and are indicated by use of a subscript 'p'[1].

Ionic displacement

There are two possibilities of displacement for any single ion: parallel and anti-parallel. For parallel displacement all ions shift from the cubic positions by equal vectors. For anti-parallel displacement neighboring ions are displaced by opposite vectors. Anti-parallel

displacement of cations results in superlattice reflections in X-ray, neutron and electron diffraction patterns due to the multiplication of the unit cell [190, 193]. Lead titanate, $PbTiO_3$, is an example of parallel displacement at room temperature. Displacement of both Ti^{4+} and O^{2-} along the $< 001 >_p$ direction, results in a tetragonal unit cell with one formula unit. Lead zirconate, $PbZrO_3$, has the anti-parallel displacement of Pb^{2+} cations along the $< 110 >_p$ direction resulting in an orthorhombic symmetry with multiple formula units.

Chemical Ordering

Chemical ordering occurs when the A-site or B-site are occupied by more than one type of cation species resulting in complex perovskites with multiplication of the unit cell. The long-range symmetry remains the same if these mixed species distribute themselves in a disordered manner. This mostly happens when mixed cations have the same valence. The symmetry reduces when the mixed cations show an environmental preference. This mainly is the case when the mixed species have different valence and cations tend to occupy the alternate 111_p planes in a ratio that depends on the formula unit of the perovskite [1].

For example lead scandium tantalate, $Pb(Sc_{1/2}Ta_{1/2})O_3$, orders in a 1:1 sequence and strontium magnesium niobate, $Sr(Mg_{1/3}Nb_{2/3})O_3$, orders in a 1:2 sequence [194, 195].

BO_6 octahedral tilting

Octahedral tilting is the mechanism responsible for the largest number of phase transitions in a perovskite. The onset of octahedral tilting usually occurs in compounds with low tolerance factor, e.g. when Sr^{2+} (1.44 Å) is substituted by Ca^{2+} (1.35 Å) in $SrTiO_3$ [196], the cation no longer completely fills the 12-fold A-site interstice and the octahedra will try and reduce the volume of the site by rotating or tilting the octahedron which ultimately results in an orthorhombic rather than the cubic structure [11, 190].

Megaw [197, 198] initiated a way to understand the distortions of the perovskite structure which was further developed by Glazer [9, 10]. Based on this system, combinations of component tilts about the three tetrad axes are used to describe the type of octahedral tilting. The component tilts are considered to be about the pseudocubic axes for small tilt angles. The letters a_p, b_p and c_p denote the tilt about $[100]_p$, $[010]_p$ and $[001]_p$ axis respectively. Where letters are repeated the magnitude of tilt around each axis is identical so that '*aaa*'refers to equal tilts about all three axes and '*abc*'refers to unequal tilts [9].

When an octahedron tilts, the neighboring octahedra in the plane normal to the tilt axis are constrained and tilt in the opposite sense, Figure 6.1, but at the same time the

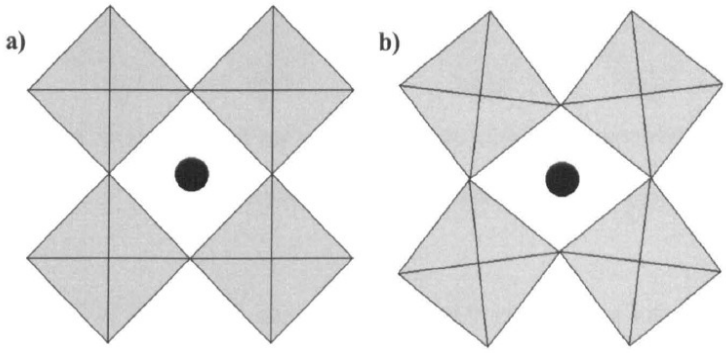

Figure 6.1: **a)** the untilted cubic perovskite viewed along a $< 100 >_p$ type axis and **b)** the tilted perovskite structure viewed parallel to the $< 100 >_p$ type tilt axis [1].

octahedra directly above and below are not constrained and this allows tilt in one of two ways possible.
The tilt is called '*in-phase*' if the octahedra rotate in the same way as the central octahedron, Figure 6.2a, and it is denoted by '$+$' superscript. An '*anti-phase*' tilt is when the octahedra above and below tilt in the opposite sense, Figure 6.2b, which is denoted by '-'superscript. Superscript '*0*'is to show that there is no tilt about an axis, e.g. $a^0a^0c^-$ shows a perovskite with anti-phase tilting only about the pseudo-cubic c axis where $a_p = b_p < c_p$.

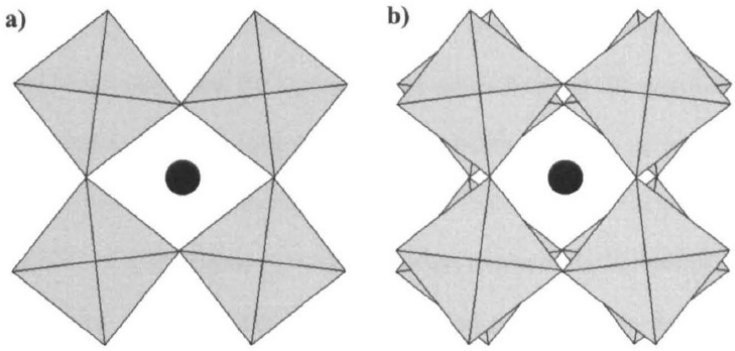

Figure 6.2: **a)** An '*in-phase*'tilted and **b)** an '*anti-phase*'tilted perovskite view parallel to the tilt axis [1].

BO_6 octahedral tilting results in doubling of the unit cell which produces extra reflections at half-integer positions in the diffraction pattern. With respect to the doubled unit cell these reflections can be indexed with some indices odd while the main reflections all have indices even. For example, c^+ creates reflections with indices odd-odd-even where $h \neq k$, e.g. 310, whereas c^- creates reflections with indices odd-odd-odd where $h \neq k$ e.g. 311 [10].

Glazer identified 23 tilt systems and consequent space groups for a unit cell based on a pseudocubic cell doubled along each axis and containing 8 formula units, Table 6.1 [9].

Table 6.1: Examples of tilt systems (e = even, o = odd indices) [9–11].

Tilt system	symbol	Reflexions	Multiple cell	Relative pseudocubic unit cell parameters	Space group
Three-tilt	$a^-a^-a^-$	eee, ooo(h$\neq k$)	$2a_p \times 2b_p \times 2c_p$	$a_p = b_p = c_p$, $\alpha = \beta = \gamma \neq 90°$	R3c
Two-tilt	$a^0b^+b^+$	eee, oeo(h$\neq k$)	$2a_p \times 2b_p \times 2c_p$	$a_p < b_p = c_p$	I4/mmm
One-tilt	$a^0a^0c^-$	eee, ooo(h$\neq k$)	$2a_p \times 2b_p \times 2c_p$	$a_p = b_p < c_p$	F4/mcm
Zero-tilt	$a^0a^0a^0$	eee	$a_p \times b_p \times c_p$	$a_p = b_p = c_p$	Pm-3m

Later Howard and Stokes demonstrated that in tilt systems $a^+a^+a^-$, $a^+b^+b^-$. $a^+a^+c^-$, $a^+b^+c^-$ and $a^0b^+b^-$ it was not possible for the tilt transition to occur while preserving a three-dimensional network without the octahedra being distorted from the perfect structure [2, 9]. It was also shown that the tilt systems with octahedral distortions were not uniquely linked to one space group and this was related to the way in which the octahedra were distorted. While none of the space groups assigned by Glazer to these tilt systems were incorrect, more information than solely the tilt system was required to identify the space group [190]. Woodward suggested that the tilt systems where all the A-sites are crystallographically equivalent are strongly favored when there is only a single A-site species, resulting in the $a^+b^-b^-$ being the most common, followed by the $a^-a^-a^-$ and the $a^0a^0a^0$. When there are two or more A-site species, tilt systems with non-equivalent A-site environments are favored [199]. Howard and Stokes argued that there could only be 15 corresponding tilt systems, since when different tilt systems result in the same space group, the tilt system with the lowest symmetry dominate. According to Howard and Stokes the unnecessary tilt systems are $a^0b^+b^-$, $a^0b^+c^+$, $a^+a^-a^-$, $a^+a^-c^-$, $a^+a^+a^-$, $a^+b^+b^-$, $a^+b^+c^-$ and $a^+b^+b^+$ and no known perovskite structures have these '*forbidden*' tilt systems. Based on this idea they established a group-subgroup relationship between these tilt systems/space groups where a tilt system is considered a subgroup of another tilt system when it can be obtained by an infinitesimal change to another, Figure 6.3 [2].

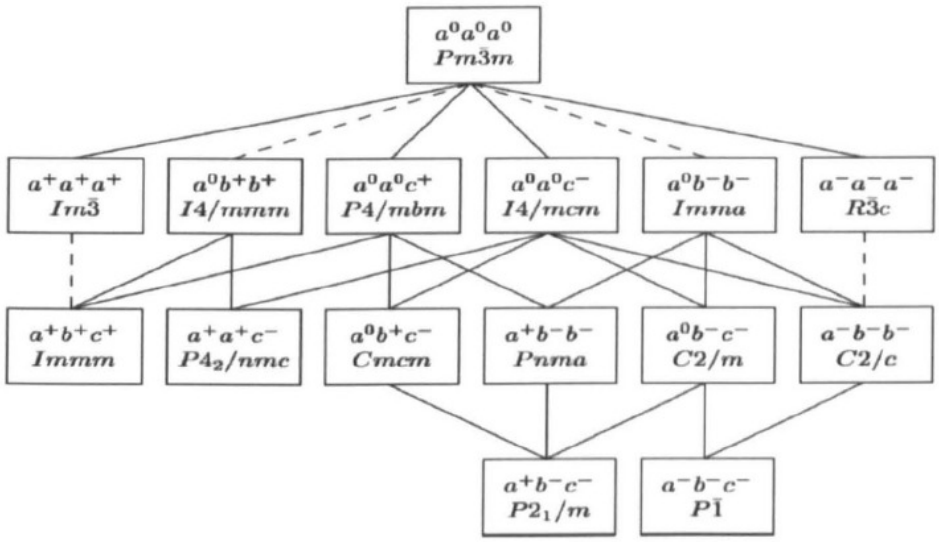

Figure 6.3: The group-subgroup relationship between the 15 perovskite space groups/tilt systems where a dashed line joining two space groups indicates that the corresponding phase transition has a discontinuous nature [2].

6.2.2 Bismuth cobaltite, $BiCoO_3$

6.2.2.1 Structure of $BiCoO_3$

$BiCoO_3$ was first synthesized in 2006 [4] and since then has been the subject of many investigations to reveal its structure and properties. $BiCoO_3$ is reported to have a tetragonally distorted perovskite structure, $P4mm$ (shown in Figure 6.4), where Bi^{3+} ions are in the cubo-octahedral positions and Co^{3+} ions are in the octahedral positions. It has parallel off-center displacement of both Co^{3+} and Bi^{3+} sublattices along the [001] direction. This tetragonal structure has the space group $P4mm$ with Bi in *1a* sites at (0, 0, 0); Co and O_1 in *1b* sites at (1/2, 1/2, z) and O_2 in *2c* sites at (1/2, 0, z). For the crystallographic facilities, we fix Bi atom at (0, 0, 0) position. However, instead of thinking in terms of shifts of the other atoms with respect to this origin, it is more physically intuitive to consider displacements of Bi and Co from the center of the distorted oxygen cuboctahedra and octahedra, respectively [200].

Figure 6.5 shows the transition from $Pm\bar{3}m$ (№221) cubic structure to $P4mm$ (№99) tetragonal structure, and the cobalt atom are displaced by 0.07 Å, producing on each of the unit cells an electrical dipole along one of the cube axes [001].

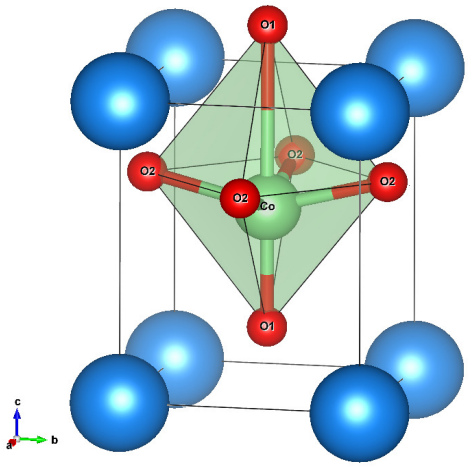

Figure 6.4: crystal structure of tetragonal $BiCoO_3$. Bi-atom (blue), Co-atom (green) and O-atom (red).

6.2.2.2 Physical properties of $BiCoO_3$

[7] The magnetoelectric properties of $BiCoO_3$ are rather unexplored. This is mainly due to the difficulties in preparing high quality samples [5]. The expected magnetoelectric properties of this material are based on *ab*-initio calculations performed on $BiCoO_3$ using DFT (density functional theory) [5, 201, 202].
Uratani et al. predicted that $BiCoO_3$ has an insulating and antiferromagnetic (G or C-type) ground state in Ref. [201]. They also predicted a giant electric polarization of 179 μC.cm^{-2} in $BiCoO_3$. In Ref. [202] Cai et al. reports that the C-AFM structure is lowest in energy and thus more stable than other possible configurations, in addition they predict a band gap of 2.11 eV in the insulating ground state of the C-AFM ordering. A giant magnetoelectric coupling in $BiCoO_3$ is predicted by Ravindran et al. in Ref. [5], which means that the magnetic state of the cobalt atom can be switched between a magnetic high spin state (HS, S=2) and a nonmagnetic low spin state (LS, S=0) by an electric field. They also predict a giant electric polarization of 170 μC.cm^{-2} in good agreement with Ref. [201]. Their calculations also show that the magnetic ground state for the ferroelectric phase of $BiCoO_3$ will be C-AFM which is in agreement with Refs. [4, 202]. In addition they report a calculated total moment of 3.10 μ_B, which is comparable with 3.24 μ_B as measured from neutron diffraction measurements at -268 C° in Ref. [4].

[7] Reference text: Knut Bjarne Gandrud, "Thin films of multiferroic $BiCoO_3$ by ALD", Thesis for the Master of Science degree in Materials, Energy and Nanotechnology, UNIVERSITY OF OSLO 2009

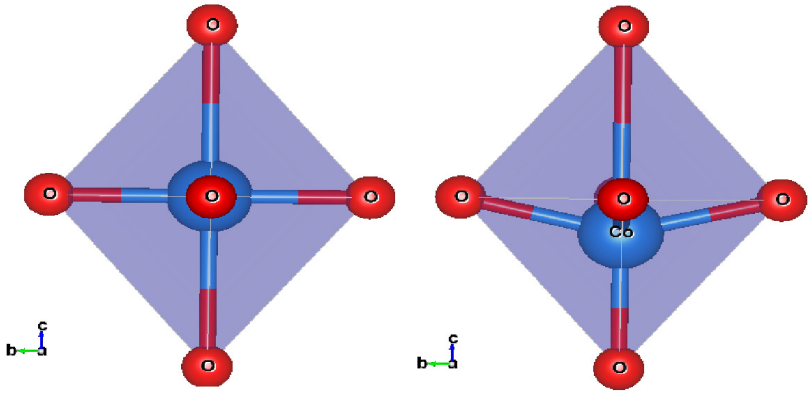

Figure 6.5: CoO_6 octahedral: **(a)** Cubic structure of $BiCoO_3$, **(b)** Tetragonal structure of $BiCoO_3$.

Multiferroics: Magnetic and electric properties

This paragraphs gives a short and general description of magnetic and electric properties which can be found in multiferroic materials. The term multiferroic is also explained, together with why there are so few multiferroic materials.

- **Magnetism**

Materials with magnetic dipoles can be divided into four different fundamental configurations: ferro-, antiferro-, ferri- and paramagnetic. Figure 2.3 of chapter 2 shows a principal sketch of how the magnetic dipoles (spins) are ordered in these four different cases.

As mentioned earlier, $BiCoO_3$ is reported to have an antiferromagnetic ordering [4], thus this configuration is explained more in detail together with ferromagnetism. Ferrimagnetism is not possible in such compounds, as it requires two subsets of magnetic moments [203], and will therefore not be discussed any further.

a/ Ferro- and antiferromagnetism

This part elaborates on the origin of ferromagnetism and antiferromagnetism

a-1/ *Origin of ferromagnetism*:

There are only nine crystals of pure elements which are ferromagnetic: three $3d$ metals, Fe, Co, and Ni, and six $4f$ metals, Gd, Dy, Tb, Ho, Er, and Tn [204]. However the number of ferromagnetic alloys and compounds is practically unlimited. A material that undergoes changes from a random distribution of its magnetic dipoles (Figure 2.3-I) to an ordered parallel magnetic structure (Figure 2.3-II), below a certain temperature, called

the Curie temperature T_C, is called ferromagnetic. The Curie-Weiss law which describes this transition is given in Eq. 6.3 [203];

$$\chi = \frac{C}{T - T_c} \tag{6.3}$$

where χ is the magnetic susceptibility, C is the Curie constant, T is the absolute temperature and T_C is explained above. The driving force for ferromagnetic ordering is the exchange energy, which gives the system a gain in free energy by ordering the magnetic moments (electron spins) parallel.
However, when the atom is introduced into a solid or a molecule another interaction, chemical bonding, is important. In general, the bonding energy is greater than the exchange energy, however the d- and f-orbitals are localized and do not extend far from the atomic nucleus, hence the bonding energy between these orbitals are weak. As a consequence they are strongly influenced by the exchange energy and ferromagnetic properties can therefore occur in materials with incompletely filled d- or f-orbitals.
a-2/ *Origin of antiferromagnetism*:
As mentioned earlier the d- and f-orbitals on the magnetic atom in a ferromagnet do only participate in weak bonding, however, for an antiferromagnet this is not the case. In an antiferromagnet, the transition metal ions are separated by a nonmetal such as oxygen, and the d orbitals on the metal ions participate in the bonding. And this interaction of the d orbitals on the cations via the intermediate anion is called superexchange, leading to a long range ordering of antiparallel spins on the metal ion. A schematic illustration of this antiparallel spin ordering, due to overlap of the metal d orbitals with the oxygen p orbitals, is shown in Figure 6.6. For an antiferromagnetic material the temperature at which the material undergoes a transition from paramagnetic to antiferromagnetic is called the Néel temperature, T_N.

- **Electric properties**

b/ Ferroelectrics
Ferroelectric materials are characterized by a spontaneous polarization in absence of an electric field. Thus a ferroelectric material has to be an insulator; otherwise any polarization in the material would be canceled out by mobile electrons. Insulating materials are often referred to as dielectrics and one of the most important parameters used to describe an insulator is its dielectric constant, properly called the relative permittivity, ε_r. The relative permittivity describes the response of a solid to an electric field. As an example, the ferroelectric crystallographic polymorph of barium titanate ($BaTiO_3$) has a relative

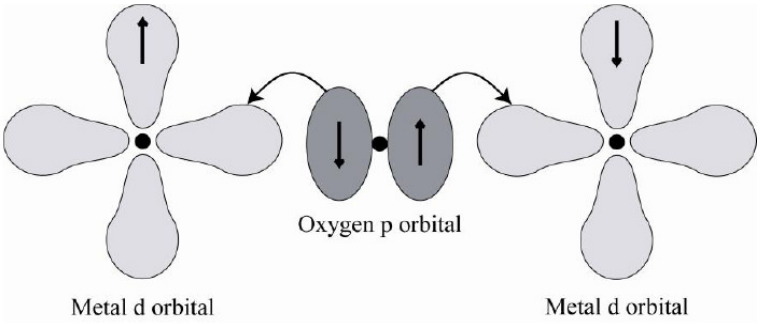

Figure 6.6: Schematic illustration of superexchange leading to antiferromagnetic alignment of spins on metal catios.

permittivity in the order of 1.10^4 [203], while silicon (Si) has a relative permittivity of 11.8 [205]. Materials with high dielectric constant can be used in a capacitor, where an increased permittivity allows the same charge to be stored with a smaller electric field (and thus a smaller voltage), leading to an increased capacitance.

b-1/ *The origin of ferroelectricity*:

The ferroelectric phase is obtained below a critical temperature called the Curie temperature. There are several different mechanisms which results in ferroelectricity, however, only the two that are relevant for this discussion in this thesis will be presented here. The first mechanism is often found in perovskites, having an ABO_3 formula, where the B-atom has a d^0 electronic configuration. In typical ferroelectrics as $BaTiO_3$ and lead titanate ($PbTiO_3$) the titanium cation is situated in an off-center position in the oxygen octahedron. It is shown for $BaTiO_3$ that the hybridization between the empty Ti-3d orbitals and O-2p orbitals stabilizes the off-centering of the Ti atom [206, 207]. As a consequence the center of gravity of the anion array will now not coincide with the positive cation, and each unit cell in the structure now contains a dipole. As a center of symmetry in the structure would force the generated dipole moment to be canceled out by symmetry, a ferroelectric material must therefore be non-centrosymmetric. In perovskite ferroelectrics this cation displacement is bi-stable with respect to the center, meaning that the displacement can take place in more than one direction, making it possible to switch the polarization by applying an external electric field.

As ferroelectricity exists in $BiCoO_3$ and other materials which do not have d^0 electronic configuration on the B atom, there must be another mechanism for the origin of ferroelectricity in these materials. In fact the *lone pair* electrons of some main group elements (Tl^+, Pb^{2+}, Sn^{2+}, Sb^{2+},Bi^{2+},Se^{2+},Te^{2+}) is known to be stereochemically active. It is shown that the Bi *lone pair* ($6s^2$) instead of remaining spherical mix with the Bi $6p$ states

and creates a space-filling localized lobe, which in turn pushes away its neighboring atoms causing a structural distortion [179, 208, 209]. This distortion stabilizes the polarization of the material, and it is also reported in the case of $BiCoO_3$ that Bi-O hybridization plays an important role in increasing and further stabilizing this polarization [5, 202]. Thus, in the perovskite structure, the properties of the A-atom can also significantly influence the formation of a ferroelectric phase in a material.

b/ Multiferroics

This section will first explain the term multiferroics, followed by an explanation for why these materials are so rare in nature. Then an explanation will be given on how the different mechanisms, resulting in antiferromagnetic and ferroelectric properties in $BiCoO_3$, can be combined together. Finally its predicted properties will be mentioned, together with some possible applications for multiferroic materials.

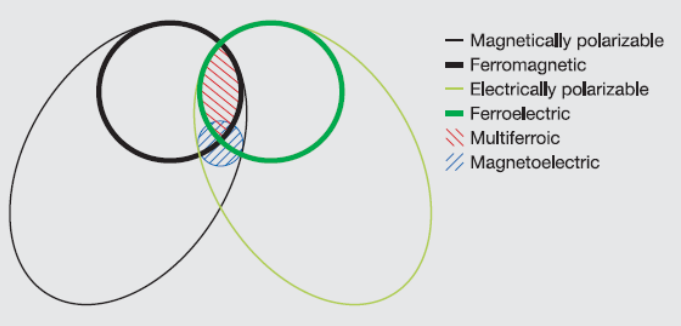

Figure 6.7: The relationship between multiferroic and magnetoelectric materials [3].

Materials in which two or all three of the properties ferroelectricity, ferromagnetism, and ferroelasticity occur in the same phase are called multiferroic [210]. By definition, a magnetoelectric multiferroic must be simultaneously both ferromagnetic and ferroelectric [3], see Figure 6.7, therefore ferroelastic materials will not be discussed any further. In a magnetoelectric materials there is also often a coupling between the two order parameters, which can give induction of magnetization by an electric field or polarization by a magnetic field [211]. The promise of coupling between the magnetic and electronic order parameters and the potential to manipulate one through the other has captured the imagination of researchers worldwide.
It should be noted, however, that the current trend is to extend the definition of multiferroics to include materials possessing two or more of any of the ferroic or corresponding antiferroic properties such as antiferroelectricity and antiferromagnetism, and it is this definition that will be used in this thesis.

Apart from that there are only 13 point groups that can give rise to multiferroic behavior, the scarcity of multiferroics can be explained by:

- A ferroelectric material must by definition be an insulator, and as earlier pointed out many ferroelectric materials have d^0 electronic configuration.
- Many ferromagnets are metals, and the magnetic ordering is only possible due to the presence of d-electrons.

Thus from these two points, there seem to exist a mutually exclusion between the conventional mechanism of off-centering in a ferroelectric and the formation of magnetic order, which explains why multiferroic materials are rare in nature.
As stated earlier the origin of ferroelectricity in $BiCoO_3$ is a result of the *lone-pair* on the Bi^{3+} ion, which hybridize with the O-2p orbital to stabilize a polarization of the structure. Resulting in a tetragonal structure with a c/a ratio of 1.27 which is remarkably large compared with ordinary perovskite-type oxides (for example, 1.06 for tetragonal $PbTiO_3$) [201]. And the calculated polarization of 179 $C.cm^{-2}$ for $BiCoO_3$ is the largest among the multiferroic materials identified so far [5]. The four unpaired electrons on the Co^{3+} ion is the origin of the magnetic properties, which by superexchange results in an (C-AFM) antiferromagnetic ordering [4], see Figure 6.8. The calculated value of 3.10 μ_B is less than the expected value of 4.00 μ_B, due to strong hybridization between Co-3d and O-2p states [201].

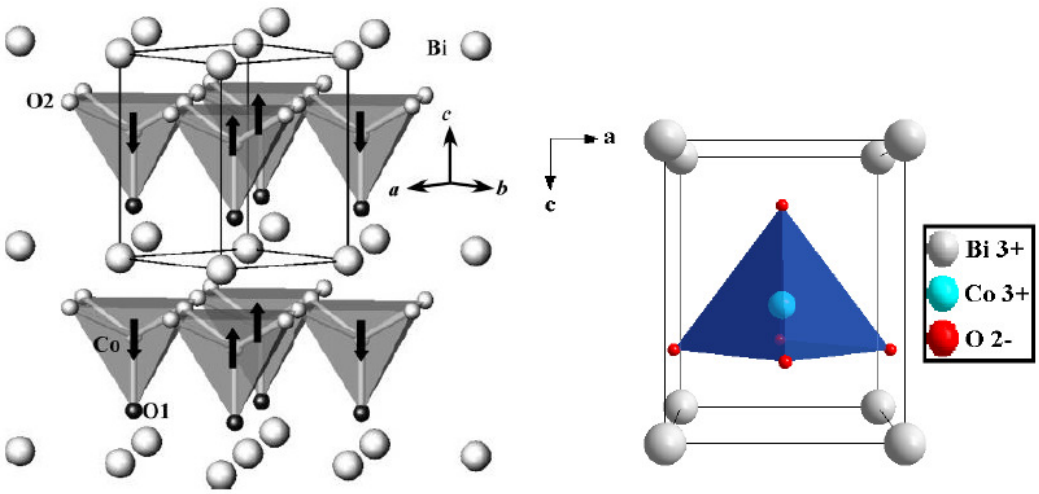

Figure 6.8: (Left picture) Crystal structure of $BiCoO_3$ with solid lines displaying the chemical cell. Arrows at the Co atoms indicate the C-type spin ordering below T_N = 197C° [4]. (Right picture) The unit cell of $BiCoO_3$ seen along the b-axis.

Design of conventional actuators, transducers, and storage devices [212]. Other applications include multiple state memory elements, in which data is stored both in the electric and magnetic polarization, or novel memory media, which might allow writing of a ferroelectric data bit, and reading of the magnetic field generated by association.
In the literature it is stated that the ultimate goal for device functionality would be a single phase multiferroic with strong coupling between ferroelectric and ferromagnetic order parameters making for simple control over the magnetic nature of the material with an applied electric field at room temperature [213]. In fact, as mentioned earlier, $BiCoO_3$ is perhaps the only material shown to be able to exhibit such strong coupling [5]. Where $BiCoO_3$ transforms from the high spin state to a nonmagnetic low spin state with 5% volume compression, which can be done by an external electric field, see Figure 6.9.

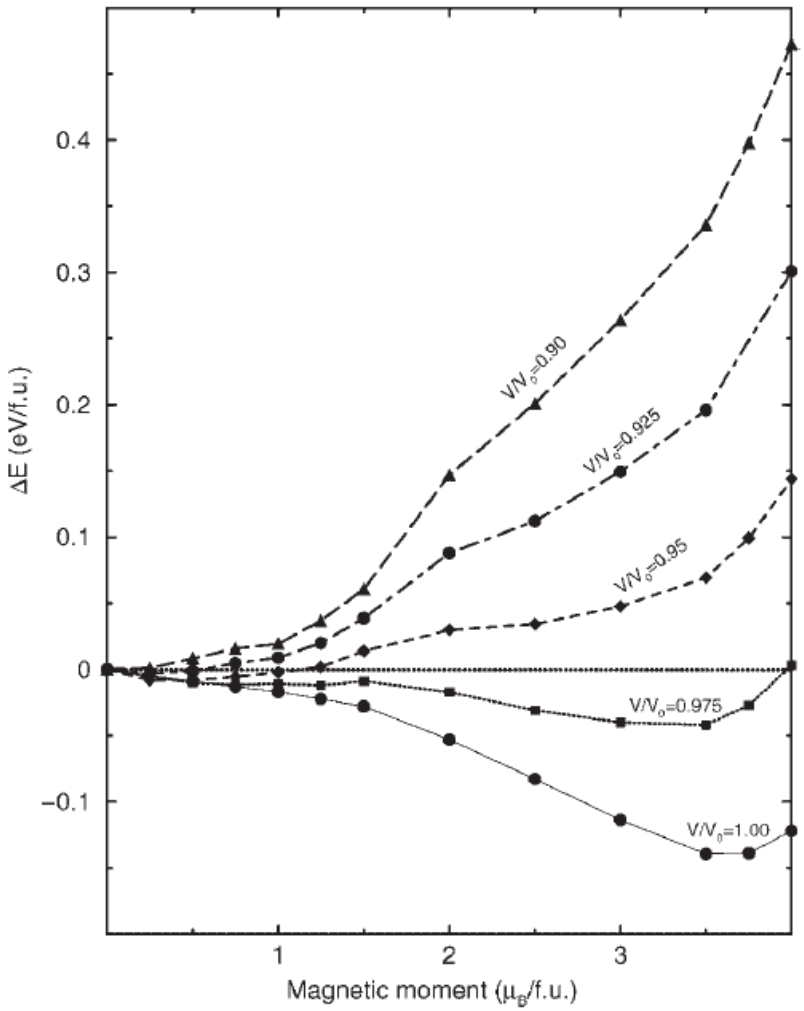

Figure 6.9: Variation of total energy with magnetic moment for $BiCoO_3$ obtained from the fixed-spin calculation for different volumes [5].

However, $BiCoO_3$ is an antiferromagnet and today the technological applications of antiferromagnets are rather limited. They are used in spin valves, where an antiferromagnet is used as a pinning layer for the magnetic spins on a ferromagnet [214]. However, aside from the potential applications, the fundamental physics of multiferroic materials are rather rich and fascinating.

6.2.3 Lanthanide cobaltite, $LaCoO_3$

6.2.3.1 Structure of $LaCoO_3$

[8] A number of different distortions exist (eg. tetragonal, orthorhombic, monoclinic) as a result of a mismatch between the radius of the B-site and the octahedral hole. One common distorted structure is the rhombohedral unit cell, which can be described as the two [100]-planes being shifted diagonally with respect to each other so that the rhombohedral angle, $\alpha < 90°$. The rhombohedral unit cell and hexagonal unit cell essentially describe the same crystal structure and the only difference is the definition of the lattice parameters. The structure is described in Figure 6.10 for $LaCoO_3$, where lattice parameters and atomic positions are designated. The rhombohedral unit cell will still arrange itself according to the cubic closed packed.

$LaCoO_3$ is known to have a rhombohedral structure with space group $R\bar{3}c$. Thornton et. al. [215] have measured the lattice parameters, bond lengths and angles accurately using neutron diffraction and found that $LaCoO_3$ maintains the $R\bar{3}c$ symmetry over the temperature region, $4 - 1248K$. Recently Maris et. al. [216] have shown neutron diffraction data suggesting a lowering of the symmetry of $R\bar{3}c$ to its monoclinic subgroup $I2/a$ which means that the Co-O distance is three-fold degenerated. This structure was also supported using EXFAS measurements [217]. The origin of this structure could perhaps explained the Jahn-Teller distortion that has been observed in several studies [217–219]. This removes the degeneracy of the $e_\alpha e_\beta$ orbitals that are filled in the intermediate and high spin states of Co^{3+}. A subsequent sections will look into this aspect in more detail.

[8] Reference text: Per Hjalmarsson, "Strontium and nickel substituted lanthanum cobaltite as cathode in Solid Oxide Fuel Cells", PhD thesis, Technical University of Denmark 2008

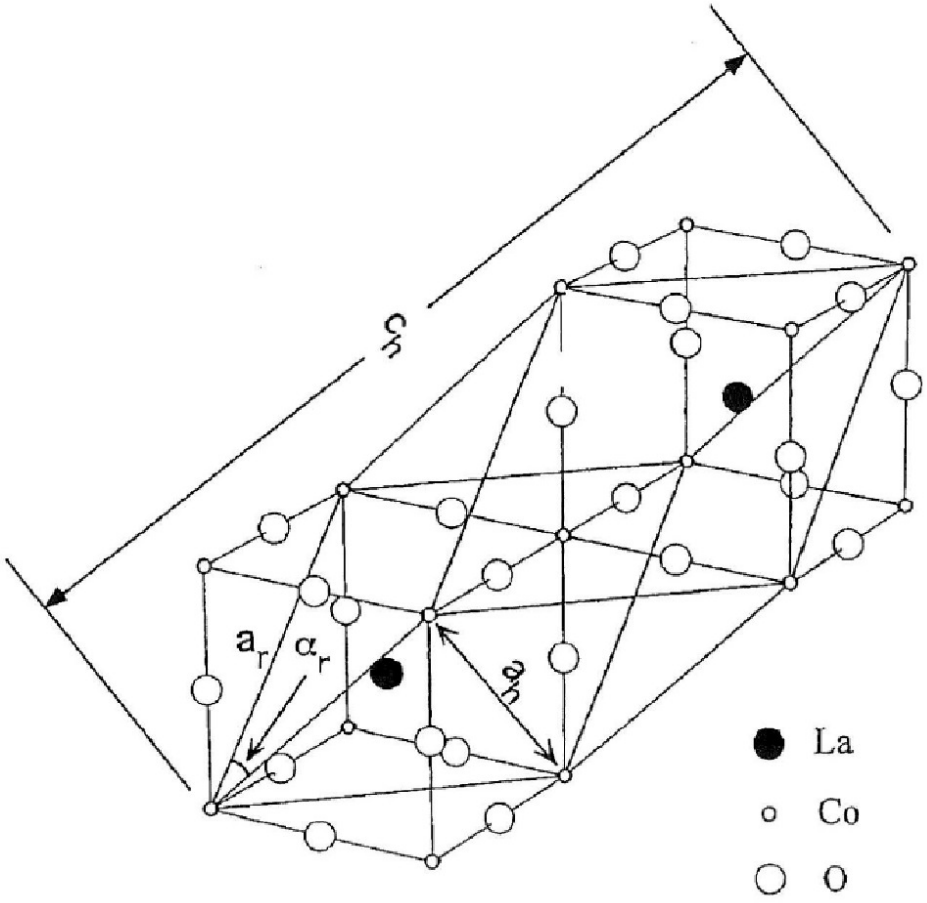

Figure 6.10: The rhombohedral structure of a perovskite where the rhombohedral unit cell parameters, α and a, are marked as well as the positions of the oxygen and metal ions. The hexagonal lattice parameters, a_h and c_h, are also marked in the figure [6].

6.2.3.2 Spin state transitions in $LaCoO_3$

[9] $LaCoO_3$ belong to the class of compounds known as Mott insulators. It appeals the scientific interest by more than 50 years. The uniqueness of $LaCoO_3$ is mostly related with its non-magnetic ground state at low temperatures and with the significant violation of the Curie-Weiss law at low temperatures [220, 221]. Most of Co compounds are magnetic, even strongly. Despite of enormous long lasting theoretical efforts the description of $LaCoO_3$ is still under very strong debate. The fundamental controversy "how to treat the d electrons" starts already at the beginning - should they be treated as localized or itinerant. Directly related with this problem is the structure of the available states: do

[9] Reference text: Z. Ropka and R. J. Radwanski, "The 3d-electron states in $LaCoO_3$", arXiv:cond-mat/0012228 [cond-mat.str-el] 2000

they form the continuous energy spectrum like it is in the band picture, schematically shown in Figure 6.11, or the discrete energy spectrum typical for the localized states.

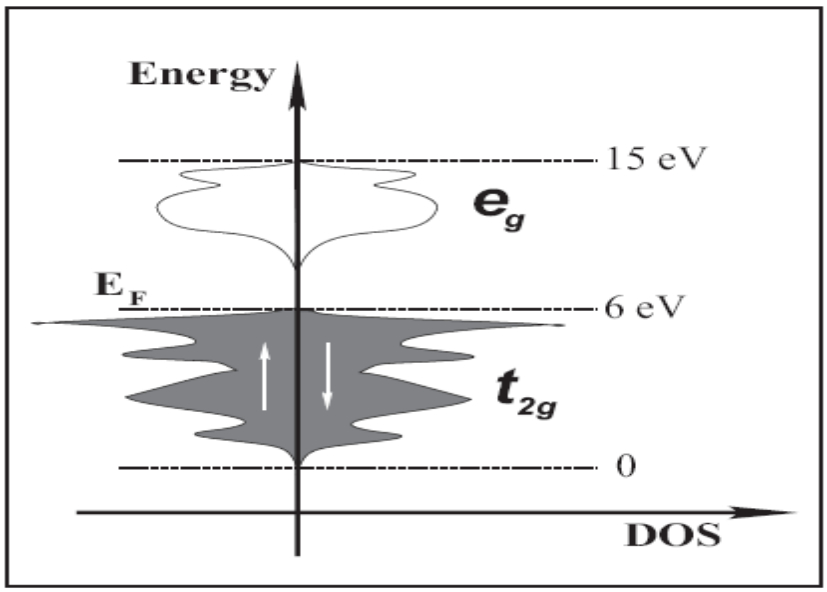

Figure 6.11: Schematic description of the d states in $LaCoO_3$ within the band approach - there is the continuous energy spectrum [7].

There is a number of band-structure calculations [222–228] and the results are schematically shown in Fig. 6.11. The bands are not polarized with respect to the spin direction as $LaCoO_3$ does not order magnetically down to lowest temperatures. The same occupancy of the spin up and down states reproduces the experimentally-observed non-magnetic (diamagnetic) state at $0K$ and is the realization of the so-called low-spin (LS) state.
In reference [7], apart of the band picture, often appears a localized electronic structure like presented in Figure 6.12 [223, 229]. At low temperatures the low-spin state (LS) is realized for $6d$ electrons (spins) that is characterized by $S = 0$. The electrons (spins) are put subsequently one by one on the single-electron states formed for $1\,d$ electron in the octahedral crystal field: lower triplet t_{2g} and higher doublet e_g. With increasing temperatures the LS state transforms to the high-spin (HS) state with $S = 2$. Korotin et al. [223] pointed out the existence of the intermediate-spin (IS) state with $S = 1$ at the middle temperature region. The temperature-induced transformation of the LS state to the HS state has been originally inferred in Refs [220] and [221] from the temperature dependence of the paramagnetic susceptibility that exhibits an intriguing maximum at about $90K$.

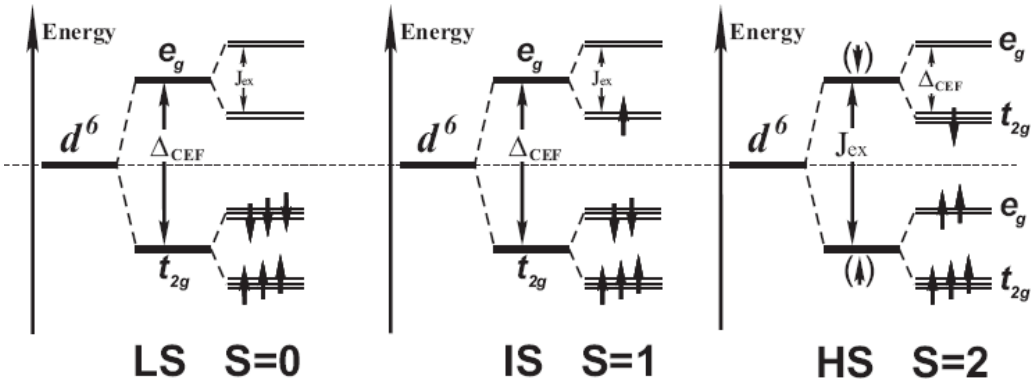

Figure 6.12: Single-electron discrete energy spectrum of the Co^{3+} ion in $LaCoO_3$ for the low-spin (LS, $S = 0$), intermediate-spin (IS, $S = 1$) and high-spin state (HS, $S = 2$). According to the current literature these spin states are subsequently realized with the increasing temperature [7].

6.2.4 Computational detail

The calculations have been performed within DFT implemented in the WIEN2K code [137]. Atoms were represented by the hybrid full-potential (linear) augmented plane-wave plus local orbitals (L/APW+lo) method [138]. In this method wave functions, charge density, and potential are expanded in spherical harmonics within non-overlapping muffin-tin (MT) spheres, and plane waves are used in the remaining interstitial region of the unit cell. In the code, the core and valence states are treated differently. Core states are treated within a multiconfiguration relativistic Dirac-Fock approach, while valence states are treated in a scalar relativistic approach. The exchange-correlation energy, E_{xc}, was calculated using the Perdew-Wang LSDA [139] and the LSDA+U [68].

Very carefully, step analysis is done to ensure convergence of the total energy in terms of the variational cutoff-energy parameter. At the same time, we have used an appropriate set of k-points to compute the total energy.

We compute equilibrium lattice constants and bulk moduli by fitting the total energy versus volume to the Murnaghan equation [140].

The standard built-in basis functions were applied with the valence configurations of (Bi: $5d^{10}6s^26p^3$), (La: $5s^25p^66s^25d^14f^0$), (Co: $3p^63d^74s^2$), and (O: $2s^22p^4$). Convergence of the calculations was checked by calculating the equilibrium structure for a number of plane wave energy cutoffs (R_{MT}*K_{MAX}) and a number of k-point grids, which were obtained using the Monkhorst–Pack method [20], and will be detailed in the table 6.2. The magnetic ordering is studied using 2×2×2 supercells to model the antiferromagnetic

(AFM) configurations. The self-consistent calculations (SCF) are considered to be converged only when the calculated total energy of the crystal converged to less than 1 mRy. We have adopted the values of 2.5 bohr for La/Bi elements 1.85 bohr for cobalt and 1.6 bohr for Oxygen, as MT radii.

Table 6.2: K-point and R_{MT}*K_{MAX} chosen in our calcul.

		K-point	R_{MT}*K_{MAX}
Tetragonal	NM/FM	$140 = 12 \times 12 \times 9$	8
	AFM-A	$84 = 12 \times 12 \times 5$	8
	AFM-C	$75 = 8 \times 8 \times 9$	8
	AFM-G	$59 = 8 \times 8 \times 8$	8
	Supercell	$36 = 4 \times 4 \times 4$	8
Rhombohedric	NM/FM	$116 = 10 \times 10 \times 10$	8
	Supercell	$40 = 6 \times 6 \times 2$	8

6.3 Results and discussion- Part-I: Parent compounds "$BiCoO_3$" and "$LaCoO_3$"

In this part, we describe some essential properties of $BiCoO_3$ and $LaCoO_3$ compounds, which can be obtained from ground state calculation; We will present the results of geometrical optimizations, electronic band structures and local magnetic moments.

6.3.1 The effect of the Hubbard U-parameter on the ground state

Density functional theory, the workhorse of modern electronic structure calculations, unfortunately, is not suitable for studying strongly correlated systems. This is traditionally accomplished by introducing to the Hohenberg-Kohn-Sham Hamiltonian, an effective on-site Coulomb interaction term referred to as the Hubbard U. In this method, the electronic correlation is associated with a small number of localized orbitals which are treated in a special way. The results thus obtained strongly depend on the definition of these localized orbitals and on the choice of the interaction parameter U used in calculations. The magnitude of U can be estimated from experiments [230]. However, the value of this parameter is uncertain for each compound, in our investigation we have supposed that the variation of this parameter gives a best description of ground state and electronic structure of this systems.

6.3.1.1 Magnetic stability of tetragonal compounds

The magnetic stability of this two materials ($BiCoO_3$ and $LaCoO_3$) is investigated using a DFT calculation to define the most favorable structure respecting the total energy of the system.

$BiCoO_3$ Bismuth cobaltite based oxide $BiCoO_3$ crystallize in tetragonal structure with *P4mm* space group №99, In order to explore the electronic and magnetic orders in the ground state, we compare the total energy of $BiCoO_3$ in different magnetic phases relative to the paramagnetic (PM) state. Calculations are done for an artificial non-spin-polarized case, as well as ferromagnetic (FM), antiferromagnetic in the ab plane stacked ferromagnetically in the c direction (AFM-C), antiferromagnetic in three

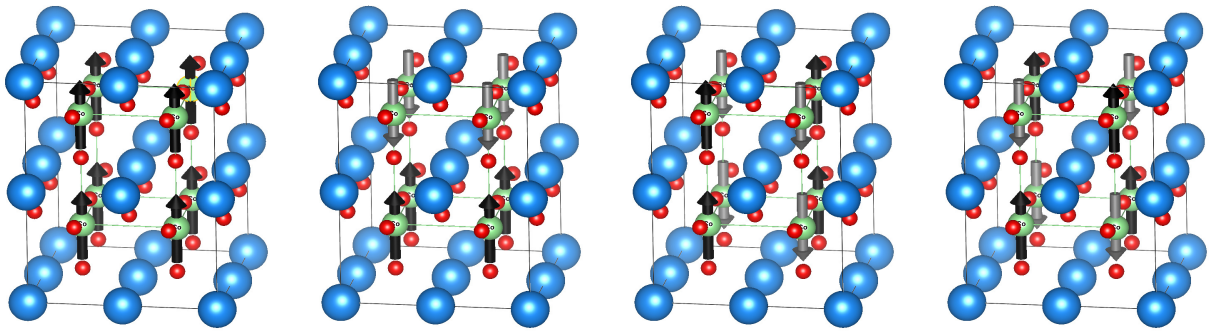

(a) (b) (c) (d)

Figure 6.13: Possible spin ordering in $BiCoO_3$ tetragonal-$P4mm$ structure: **(a)** Ferromagnetic (FM), **(b)** Antiferromagnetic type-A (AFM-A), **(c)** Antiferromagnetic type-C (AFM-C) and **(d)** Antiferromagnetic type-G (AFM-G).

directions (AFM-G), and ferromagnetic *ab* planes stacked antiferromagnetically along the *c* axis (AFM-A) (see figure. 6.13). The calculated results are listed in table 6.3 and shown in Figure 6.14. We find that the total energy of the AFM-C phase is the lowest, which is consistent with experimental observations [4, 231] and other theoretical results [5, 201, 202].

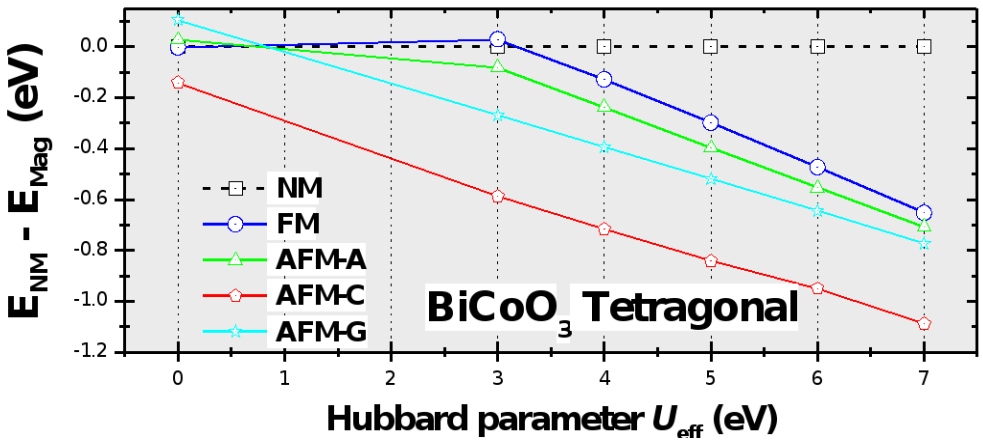

Figure 6.14: Magnetic stability: Energies of various spin configurations of $BiCoO_3$ relative to the nonmagnetic case.

According to figure 6.14 and table 6.3, we can see that AFM-C ordering is favored, and the super-exchange coupling is dominated in *ab*-plane which confirms the gain energy of AFM-G and AFM-C compared to FM and AFM-A (the *ab*-plane stacked ferromagnetically). The spin ordering priority of AFM-C compared to AFM-G due to the charge

Table 6.3: Energies of various spin configurations of $BiCoO_3$ relative to the non-spin-polarized case adopted by LSDA+U, and compared to the calculation results of the ultrasoft-pseudopotential approach (UPA+LSDA) and other full-potential LAPW calculation (FP-LAPW+GGA/LSDA). Energies are given in eV.

$BiCoO_3$	**FM**	**AFM-A**	**AFM-G**	**AFM-C**
FP-LAPW, LSDA+U, $U = 0$ [a]	-0.0027	0.0277	0.1051	-0.1409
FP-LAPW, LSDA+U, $U = 3$ [a]	0.0293	-0.081	-0.2685	-0.5854
FP-LAPW, LSDA+U, $U = 4$ [a]	-0.1284	-0.2359	-0.3938	-0.7162
FP-LAPW, LSDA+U, $U = 5$ [a]	-0.2986	-0.3974	-0.5182	-0.8409
FP-LAPW, LSDA+U, $U = 6$ [a]	-0.4726	-0.5531	-0.6440	-1.5194
FP-LAPW, LSDA+U, $U = 7$ [a]	-0.6522	-0.7059	-0.7720	-1.0877
FP-LAPW, GGA [b]	-1.338	-1.463	-1.605	-1.678
FP-LAPW, LSDA [b]	-0.889	-1.029	-1.195	-1.234
UPA, GGA [c]	-0.21	-0.12	-0.55	-0.58

[a] Present calculation
[b] Taken from Ref. [202]
[c] Taken from Ref. [201]

transfer between neighboring oxygen atoms (we will explain this point in next sections); This energy gain make AFM-C magnetic structure more favorable compared to AFM-G.

In the present study, the ground state determination, lattice parameters, electronic structure, and magnetic properties of $BiCoO_3$ are calculated by employing the LSDA+U schemes. Moreover, we discuss how the choice of U affect those properties. Figure 6.14 shows that the pure LDA fails to give the accurate magnetic structure, precisely, the meta-stable phase in $BiCoO_3$ is AFM-G ordering [202] which has corrected after using the LSDA+U. In this stage, the value of U does not affect the magnetic structure result.

$LaCoO_3$ In the following, the magnetic stability of hypothetical compound $LaCoO_3$-tetragonal was investigated with good Hubbard parameter of $BiCoO_3$-tetragonal ($U = 6$ eV). Figure 6.15 shows this magnetic stability; and its clear that the same spin ordering appears in hypothetical $LaCoO_3$-tetragonal, this result appears due to the similar atomic size of both La and Bi atoms.

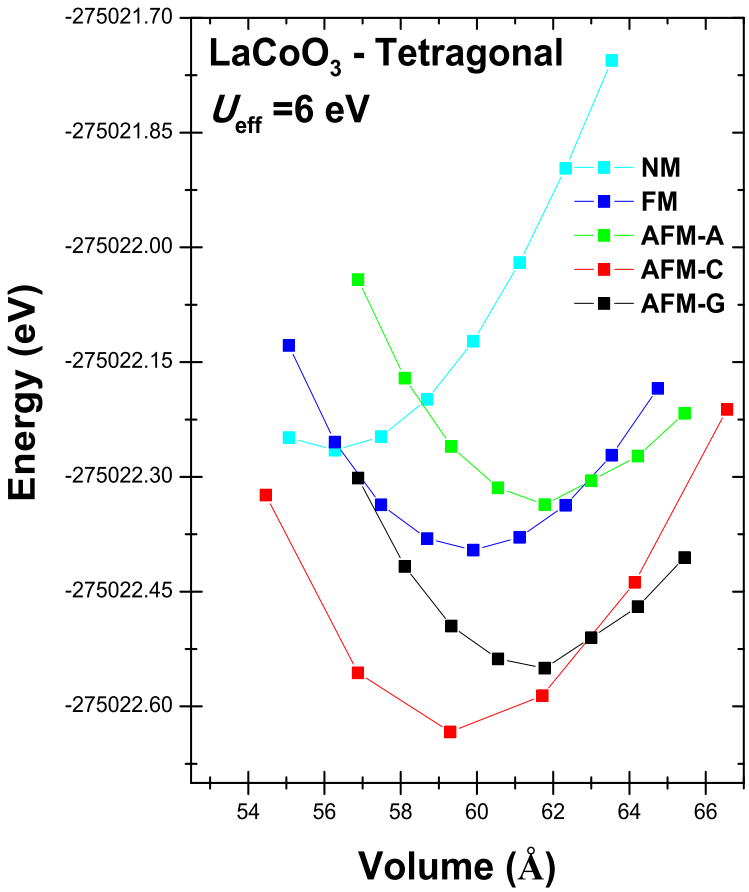

Figure 6.15: Magnetic stability: Variation of energies in various spin configurations of $LaCoO_3$ using LSDA+U ($U = 6$ eV).

6.3.1.2 Magnetic stability of rhombohedral compounds

In the family of cobalt oxides, the prototypical perovskite $LaCoO_3$ continuously attract attention of researches since late of 1950s [232]. $LaCoO_3$ has a rhombohedrally distorted pseudo-cubic perovskite structure, space group $R\bar{3}c$ compared to the cubic structure, the corner-shared CoO_6 octahedra are tilted and the point symmetry of the central Co ion is reduced from the cubic O_h to the trigonal C_{3i} one; all the Co–O bond lengths l_{Co-O} are kept the same. The ground state of $LaCoO_3$ is in diamagnetic phase in the low-spin state (LS) [220]. To confirm this result, we have done two different calculations of $LaCoO_3$, no spin-polarized (non magnetic state) calculation and spin-polarized (magnetic state) calculation.

There are three possible configurations of spin in Co^{+3} ion (see section 6.2.3.2), the non-magnetic state is derived from low spin configuration (LS); and magnetic state is derived from intermediate spin configuration (IS) or high-spin configuration (HS).

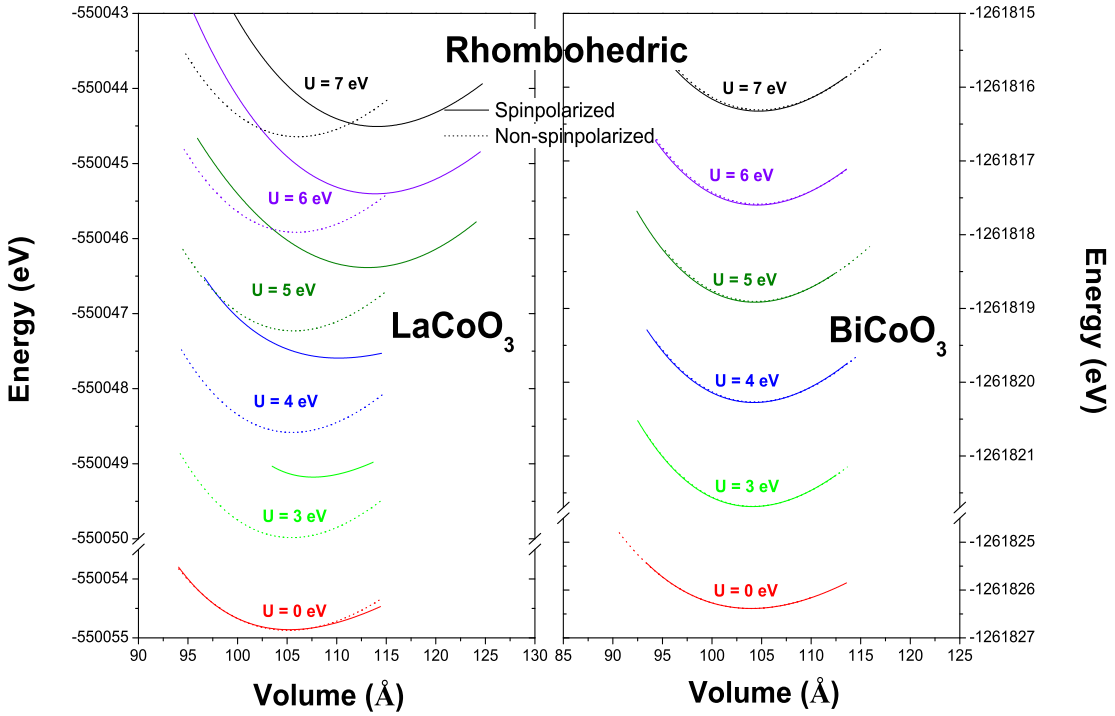

Figure 6.16: Magnetic stability: Variation of energies for nonspin-polarized/spin-polarized states for $LaCoO_3$ and $BiCoO_3$ using LSDA+U ($U = 0 - 7$ eV).

Figure 6.16 shows the nonspin-polarized and spin-polarized states for La/$BiCoO_3$. To your knowledge, $BiCoO_3$-rhombohedral is an hypothetical compound. From this figure it is clear that both materials are nonmagnetic for all values of Hubbard parameter U_{eff}.

The determination of spin state in this rhombohedral materials is an important step to understand the magnetic properties of this compounds. The nonmagnetic state in both compounds explains low spin configuration (LS, S=0). Since $LaCoO_3$ is strong correlated material, certainly, the effect of Hubbard parameter U_{eff} is clear; to confirm that, we performed the so-called fixed spin-moment (FSM) calculations [233] within the LSDA+U formalism using Wien2k-code [137] with variation of U_{eff}, this calcul is shown in figure 6.17. For both cases, the variation energy with total magnetic moment shows low spin state for all U-values ($U = 0$ to 6); beyond $U = 6$ there is change of spin state from LS to IS (intermediate spin); To clarify, the total magnetic moment correspond to IS state is around 4 μ_B which gives the Co-ion a local magnetic moment (MM) 2 μ_B.
Moreover, from past figure, we can conclude that Hubbard parameter U_{eff} affect the result and we should take the best value carefully; and finally we trying to resume our results in figure 6.18 where we must use U_{eff} value equal or less than 6 eV.

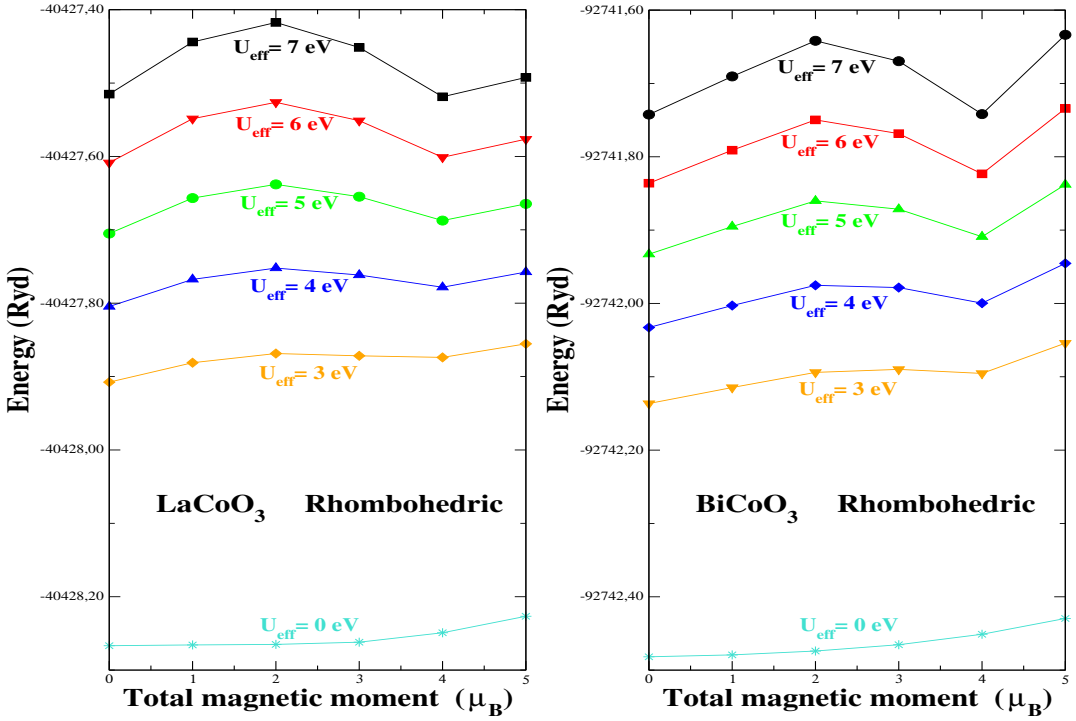

Figure 6.17: FSM curves for $LaCoO_3$ and $BiCoO_3$ ($U_{eff} = 0 to 7$) obtained by LSDA+U calculation.

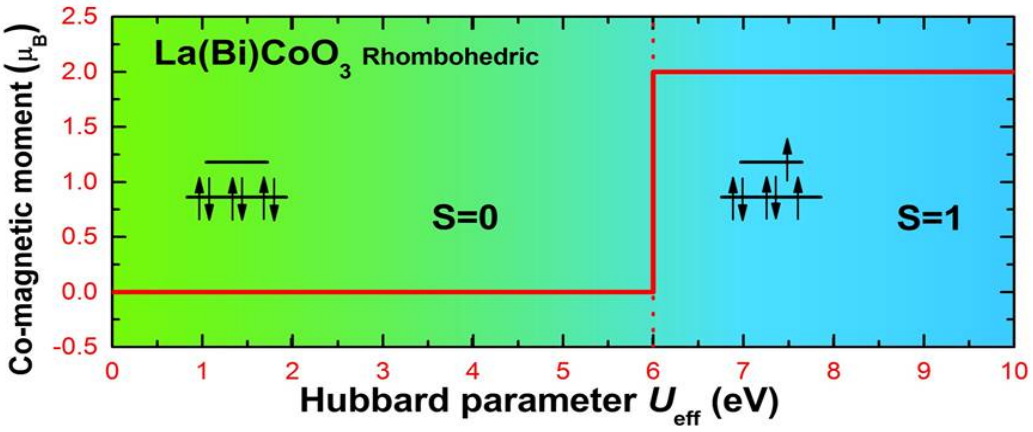

Figure 6.18: Variation of MM of Co-ion with U_{eff} value for $LaCoO_3$ and $BiCoO_3$.

6.3.1.3 Structural stability of $BiCoO_3$ and $LaCoO_3$ compounds

To characterize the structural stability of Bi/$LaCoO_3$ materials we have calculated the total energies of these compounds in tetragonal and rhombohedral structures, with and without U-Hubbard parameter application. Calculations were performed using LSDA+U for $U = 0$, 3,4,5,6 and 7 and the resulting numerical values are listed in Table 6.4. Figure 6.19 shows only the variation of total energies with LSDA+U ($U = 0$ eV) and ($U = 6$ eV).

Table 6.4: Energies values of Bi/$LaCoO_3$ compounds in tetragonal (T) and rhombohedral (R) crystalline structures in different values of U; Energies are given in eV/atom.

LSDA+U	**$BiCoO_3$-T**	**$BiCoO_3$-R**	**$LaCoO_3$-T**	**$LaCoO_3$-R**
$U = 0$	-126129.710010	-126129.775343	-54982.318654	-54982.443078
$U = 3$	-126129.287646	-126129.305323	- - -	-54981.954490
$U = 4$	-126129.165087	-126129.116397	- - -	-54981.814385
$U = 5$	-126129.048527	-126129.027615	- - -	-54981.679179
$U = 6$	-126128.934355	-126128.895852	-54981.482978	-54981.547801
$U = 7$	-126128.831424	-126128.768089	- - -	-54981.420634

The effect of U-effective on structural stability is clear in $BiCoO_3$ (BCO) than $LaCoO_3$ (LCO), In figure 6.19b, LCO perform a rhombohedric structure, this finding was confirmed experimentally [220]; Thus, U-parameter does not affect the structural stability. However, the experimental result shows a tetragonal ground state structure for $BiCoO_3$ [5, 201, 202] which is not appear in our LSDA calculation ($U = 0$ eV) (see figure 6.19a). This failure of LSDA was corrected by application of LSDA+U with large value of U_{eff} (equal or greater than 4 eV, see Table 6.4).

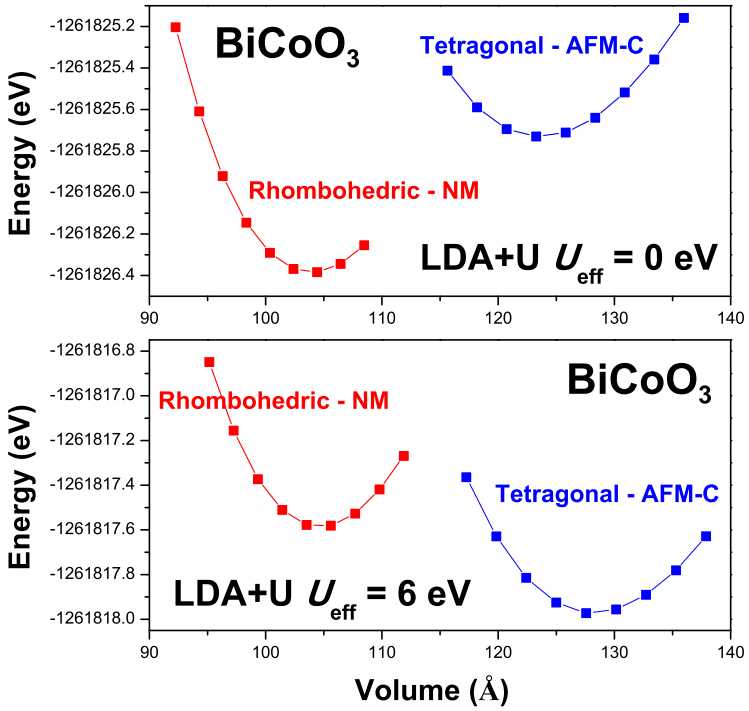

(a)

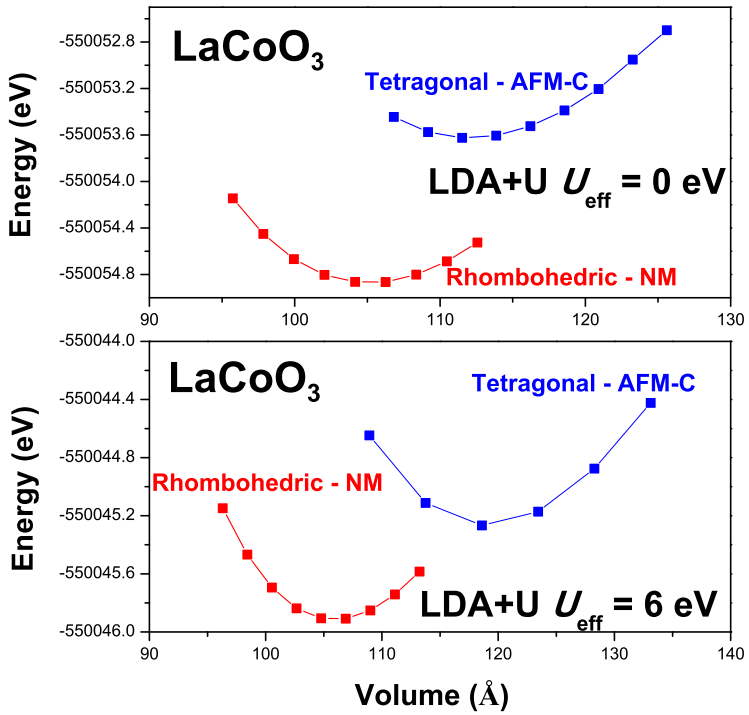

(b)

Figure 6.19: calculated variation of total energies with LSDA+U (U = 0 and 6 eV).

6.3.1.4 Structural data: Lattice and internal parameters

$BiCoO_3$ In *P4mm*-tetragonal structure, the positions of the atoms inside the unit cell are (0, 0, 0), (1/2, 1/2, z) and (1/2, 0, z) for Bi, Co and O respectively, where z is the internal parameter for the cation–anion separation (see Fig. 6.4). We began our study by optimizing the structural parameters for $BiCoO_3$ compound in AFM-C structure. This optimization was made by an iterative process as a function of the volume, V, the c/a ratio, and the internal parameter, z, until the total energy converged to within 0.01 mRy. Theoretical and experimental values of lattice parameters (a, c/a), internal parameter z are represented in table 6.5. All past works suggest that $BiCoO_3$ should rather be

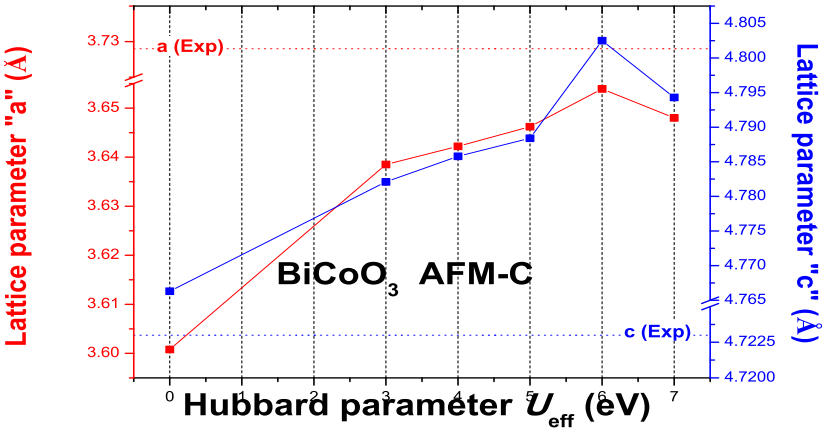

Figure 6.20: Variation of a, c versus U_{eff} value for $BiCoO_3$.

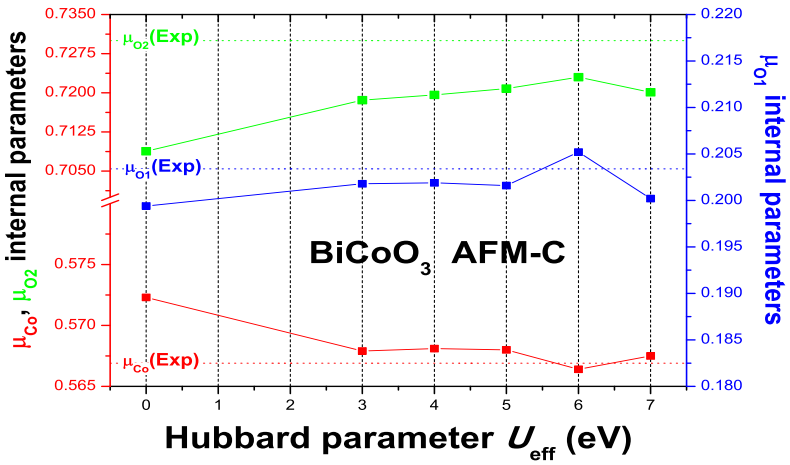

Figure 6.21: Variation of z_{Co}, z_{O1} and z_{O2} versus U_{eff} value for $BiCoO_3$.

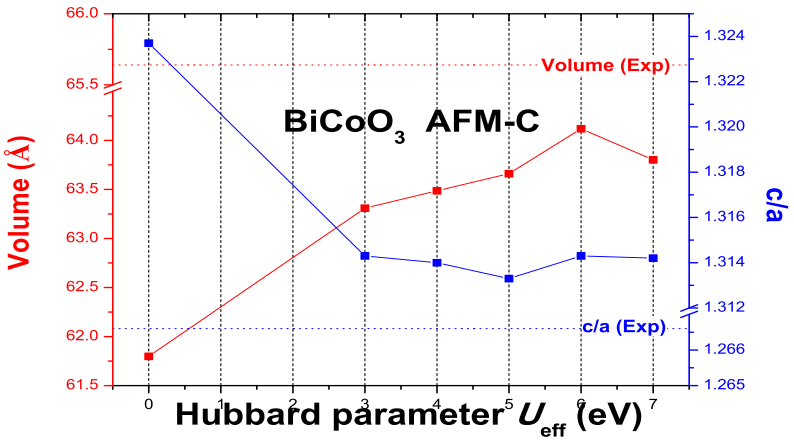

Figure 6.22: Variation of volume and c/a versus U_{eff} value for $BiCoO_3$.

categorized as a Mott insulator, which requires DFT+U calculation, but unfortunately, the application of U parameter in LSDA increases the volume and tetragonality (c/a). However, this exchange-correlation approximation gives a good results in electronic properties. Figures 6.20, 6.21 and table 6.5 show the effect of U Hubbard parameter on lattice parameters and atomic positions of $BiCoO_3$ compound; Figure 6.22 shows also the effect of U_{eff} on volume and c/a of $BiCoO_3$, these results confirm that $U_{eff} = 6$ eV is a best value which gives a good structural parameters of ground state.

$LaCoO_3$ $LaCoO_3$ perform a rhombohedric crystalline structure, In our code (Wien2k) [137], for rhombohedral (R) lattice the hexagonal lattice constants must be specified. The following relations (eq. 6.4 and eq. 6.5) help us to convert between hexagonal and rhombohedral specifications:

$$a_{hex} = 2cos(\frac{\pi - \alpha_{rhomb}}{2})a_{rhomb} \tag{6.4}$$

$$c_{hex} = 3\sqrt{a^2_{rhomb} - \frac{1}{3}a^2_{hex}} \tag{6.5}$$

Position of atom in internal units, i.e. as positive fractions of unit cell parameters. ($0 \leq x \leq 1$); the positions in the unit cell are consistent with convention used in International Tables of Crystallography [234]. For R lattice we have used rhombohedral

Table 6.5: Optimized lattice constants and atomic positions of tetragonal $BiCoO_3$ in AFM-C ordering; and comparison with theoretical and experimental data (values in bold are in good agreement with experimental data).

$BiCoO_3$-T AFM-C	**a (Å)**	**c (Å)**	z_{Co}	z_{O1}	z_{O2}
FP-LAPW, LSDA+U, $U=0$ [a]	3.6008	**4.7663**	0.5723	0.1994	0.7088
FP-LAPW, LSDA+U, $U=3$ [a]	3.6385	4.7821	0.5681	0.2018	0.7186
FP-LAPW, LSDA+U, $U=4$ [a]	3.6422	4.7858	0.5681	0.2019	0.7196
FP-LAPW, LSDA+U, $U=5$ [a]	3.6462	4.7884	0.5680	**0.2016**	0.7208
FP-LAPW, LSDA+U, $U=6$ [a]	**3.6539**	4.8025	**0.5664**	**0.2052**	**0.7230**
FP-LAPW, LSDA+U, $U=7$ [a]	3.6480	4.7943	0.5675	0.2002	0.7201
PP [b]	3.7304	4.7897	0.5718	0.2015	0.7194
FP-LAPW, LSDA+U [c]	3.748	4.710	0.5658	0.2053	0.7287
FP-LAPW, LSDA [d]	3.73055	4.72613	0.57382	0.21421	0.72207
Experiment [b]	3.7199	4.7196	0.5664	0.2024	0.7311
Experiment [e]	3.729	4.723	0.5669	0.2034	0.7300

[a] Present calculation,
[b] Taken from Ref. [5]
[c] Taken from Ref. [202]
[d] Taken from Ref. [201]
[e] Taken from Ref. [4]

coordinates. To convert from hexagonal into rhombohedral coordinates, we have used these following relations (eq. 6.6):

$$\vec{X}_{rhomb} = \vec{X}_{hex} \begin{pmatrix} -1 & 1 & 0 \\ 1 & 0 & -1 \\ 1 & 1 & 1 \end{pmatrix} \tag{6.6}$$

The space group of rhombohedral $LaCoO_3$ is $R\bar{3}c$, a Wyckoff positions inside the unit cell are $2a : (1/4, 1/4, 1/4), (3/4, 3/4, 3/4)$ for La atom, $2b : (0, 0, 0), (1/2, 1/2, 1/2)$ for Co atom and $6e : (x, -x + 1/2, 1/4), (1/4, x, -x + 1/2), (-x + 1/2, 1/4, x), (-x, x + 1/2, 3/4), (3/4, -x, x + 1/2), (x + 1/2, 3/4, -x)$ for Oxygen atom; where x is an internal parameter; we have used a structural relaxation to define a, α and x. Table 6.6 represent these structural data.

6.3.1.5 Summary

We have achieved some success in our ground state study in comparison with experimental and others theoretical investigations; $BiCoO_3$ adopt a tetragonal structure because the

Table 6.6: Optimized lattice constants and atomic positions of rhombohedral $LaCoO_3$ in NM state; and comparison with theoretical and experimental data (values in bold are in good agreement with experimental data).

$LaCoO_3$-R NM	**a (Å)**	α	x_O
LDA+U, $U = 0$ [a]	5.242	61.4226	0.19799
LDA+U, $U = 3$ [a]	5.2552	61.2266	0.19647
LDA+U, $U = 4$ [a]	5.2585	61.1533	**0.19718**
LDA+U, $U = 5$ [a]	5.2641	61.0826	0.19787
LDA+U, $U = 6$ [a]	5.2683	**61.0761**	0.19792
LDA+U, $U = 7$ [a]	**5.2777**	60.9141	0.19860
LDA+U [b]	5.4208	61.1287	—
U_{sc} [c]	5.3374	61.14	—
LDA [c]	5.3283	61.4	—
Experiment [d]	5.297	61.01	0.19735
Experiment [e]	5.3416	60.99	0.1978

[a] Present calculation,
[b] Taken from Ref. [235]
[c] Taken from Ref. [236]
[d] Taken from Ref. [182]
[e] Taken from Ref. [215]

existence of Bi-ion and especially, s orbital in valence states, this orbital promotes a shift of cobalt position from his centrosymmetric site (*lone pair* mechanism). In our knowledge, this existence of Bi is the main reason which $BiCoO_3$ adopts a tetragonal structure.

However, in $LaCoO_3$, there is no displacement of Co-atom and no *lone pair* effect in La-atom, in consequence, the CoO_6 octahedra is perfect; Although, there is a tilt of these octahedra due to large size of La-atom comparing within Alkaline earth metals.

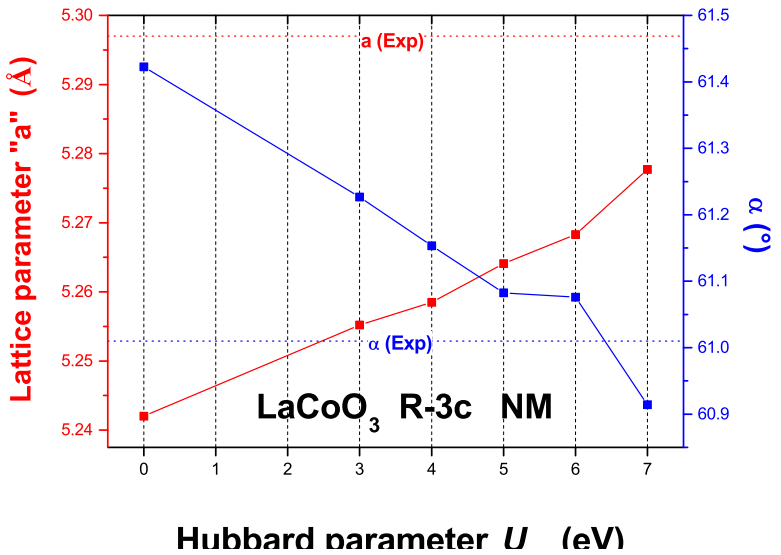

Figure 6.23: Variation of a and α versus U_{eff} value for $LaCoO_3$.

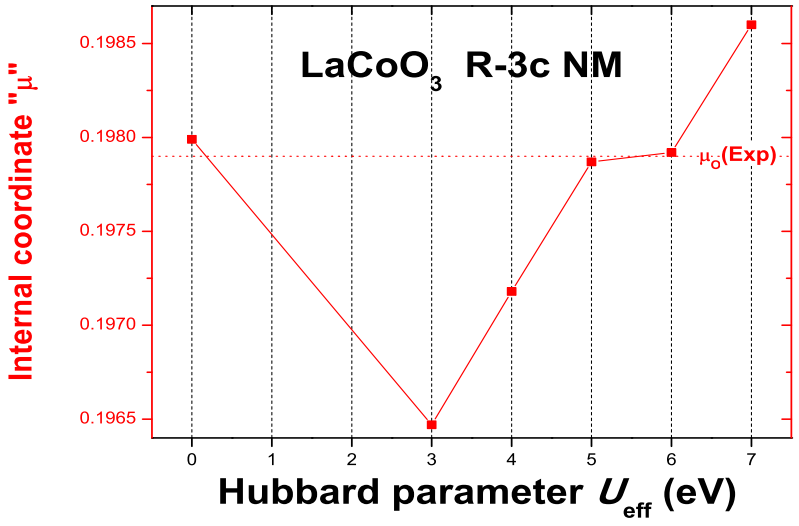

Figure 6.24: Variation of internal parameter x versus U_{eff} value for $LaCoO_3$.

6.3.2 The effect of the Hubbard *U*-parameter on electronic properties

6.3.2.1 Band structures

Band Structure (BS) can be obtained by diagonalization of the Hamiltonian matrix for each k-vector, since the eigenvalues (energies) change as a function of k, and are different along different directions in k space.
First, we will discuss the main features of the Bi/$LaCoO_3$ band structures E(k) and the effect of U parameter in the standard LSDA calculations. In Figure 6.25, Brillouin zone of tetragonal ($BiCoO_3$ (a)) and rhombohedral ($LaCoO_3$(b)) structures, as well as the most important high-symmetry k-point.
Figures 6.26 and 6.27 show the band structures E(k) along the high-symmetry lines in

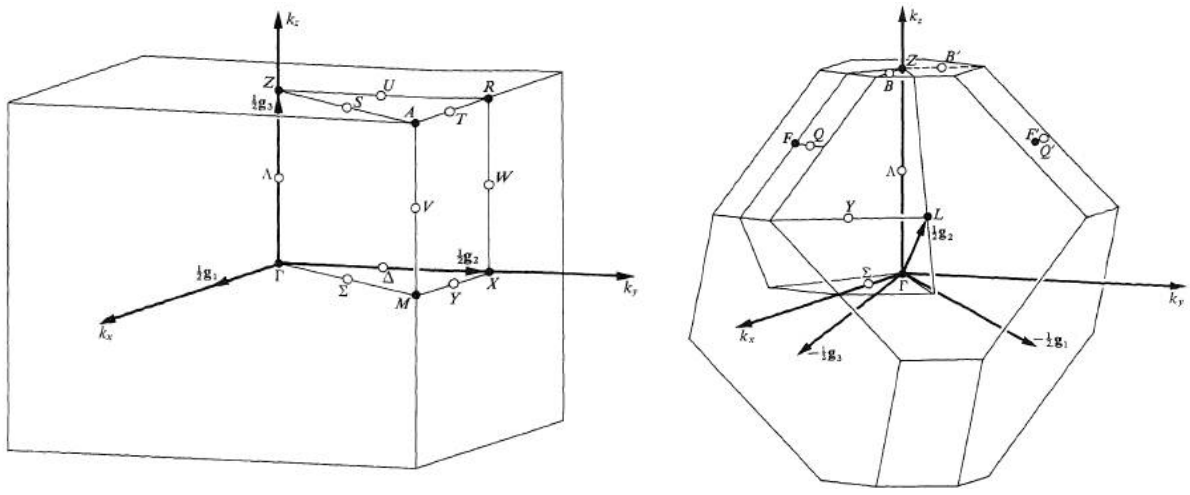

(a) (b)

Figure 6.25: Brillouin zone of (a) tetragonal-$P4mm$ structure and (b) rhombohedric-$R\bar{3}c$ structure (Taken from Ref. [8]).

an energy range close to the Fermi level of $BiCoO_3$ and $LaCoO_3$ respectively.

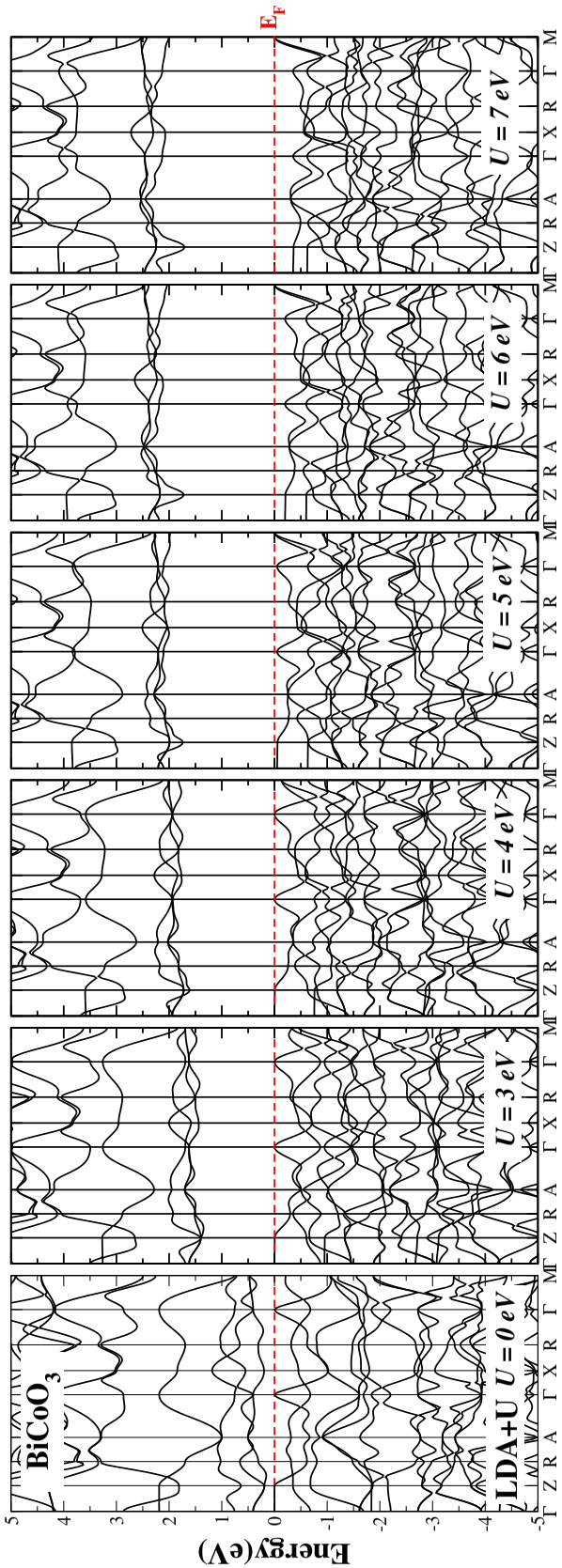

Figure 6.26: Band structures of $BiCoO_3$ in different U_{eff} values.

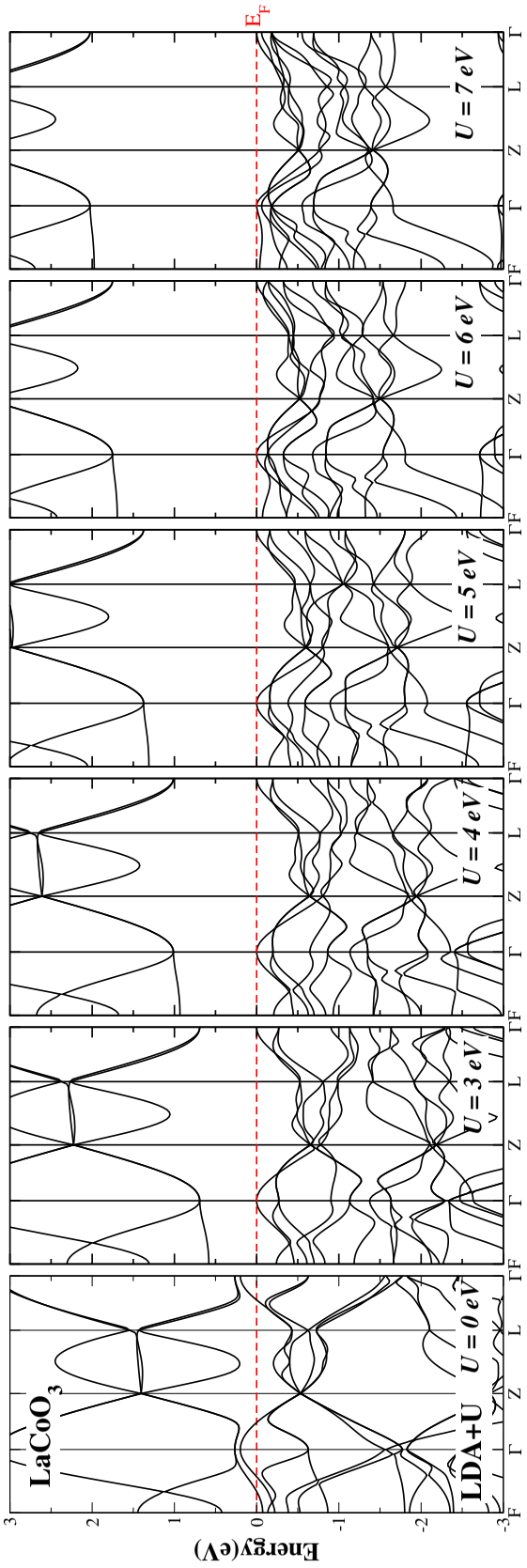

Figure 6.27: Band structures of $LaCoO_3$ in different U_{eff} values.

In addition to the U-parameter effect on structural properties, there is a clear effect of U_{eff} on band structures in both compounds, there is also an important correction of states from metallic to insulator nature. Table 6.7 presents a different values of gap energies for $Bi/LaCoO_3$ with LSDA+U ($U = 0 - 7$eV); these values are compared with experimental and theoretical results.

Our results are shown in Figures 6.28, 6.29 and table 6.6; this investigation confirm the

Table 6.7: Calculated results of gap size (E_g) and magnetic moment per Co, for BCO and LCO materials. (values in bold are in good agreement with experimental data).

	$BiCoO_3$-T AFM-C		**$LaCoO_3$-R NM**
	E_g (eV)	**Magnetic moment/Co μ_B**	**E_g (eV)**
LDA+U, $U = 0$ [a]	0.15705	2.17381	0
LDA+U, $U = 3$ [a]	1.34708	2.7548	0.58164
LDA+U, $U = 4$ [a]	1.608	2.84047	**0.9322**
LDA+U, $U = 5$ [a]	1.7388	2.84047	1.31008
LDA+U, $U = 6$ [a]	1.72282	2.97489	1.69486
LDA+U, $U = 7$ [a]	**1.7067**	**3.03908**	1.97525
LDA+U	2.11 [b]	2.48 [b]	0.7 [c], 2.06 [d]
unrestricted Hartree-Fock	3.31 [e]	3.32 [e]	—
Experiment	1.7 [f]	3.24 [g]	0.9±0.3 [h]

[a] Present calculation,
[b] Taken from Ref. [202]
[c] Taken from Ref. [237]
[d] Taken from Ref. [223]
[e] Taken from Ref. [238]
[f] Taken from Ref. [239]
[g] Taken from Ref. [4]
[h] Taken from Ref. [240]

good choice of a large U_{eff} (U=6 eV), although the accurate gap energy is difficult to determine because of the blurred onset of the conductivity perhaps due to the indirect-gap nature [241], an indirect band gap between the valence-band maximum at M and the conduction-band minimum at Z (for BCO-T), and the same case for LCO, indirect band gap between the valence-band maximum at Γ and the conduction-band minimum at F. We have determine the band gap and magnetic moment with a good accuracy, using LAPW-LSDA+U.

Since the ionic radius of La and Bi are nearly equal, and Cobalt environment are the same in both structures, we have found an equivalent band gap energies in both materials which ensures a good bowing in $Bi/LaCoO_3$ alloy and make it more stable and

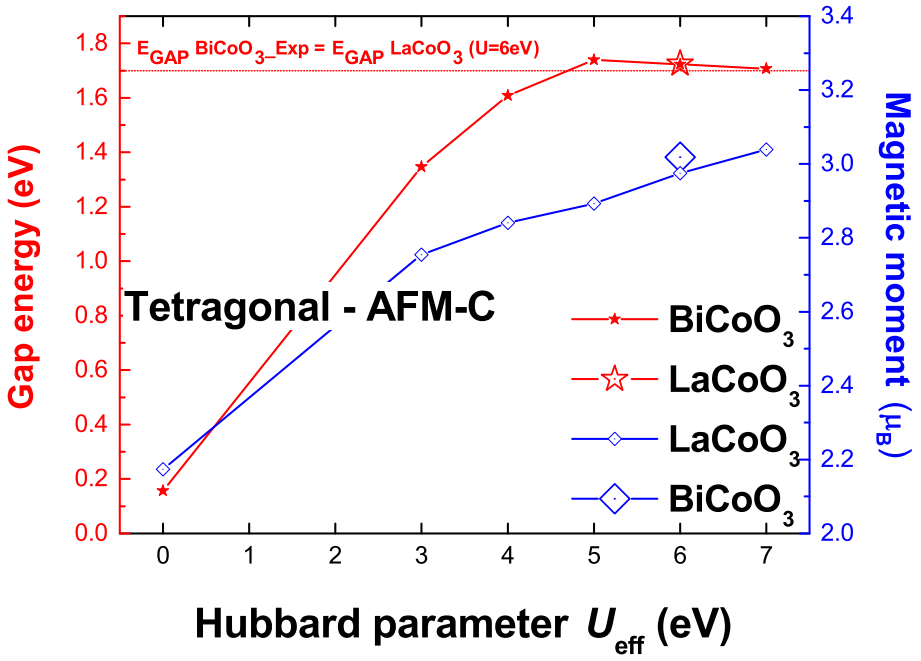

Figure 6.28: Variation of band gap and spin magnetic moment of $BiCoO_3$ and $LaCoO_3$ in tetragonal structure, with different U_{eff} values comparing with experimental data.

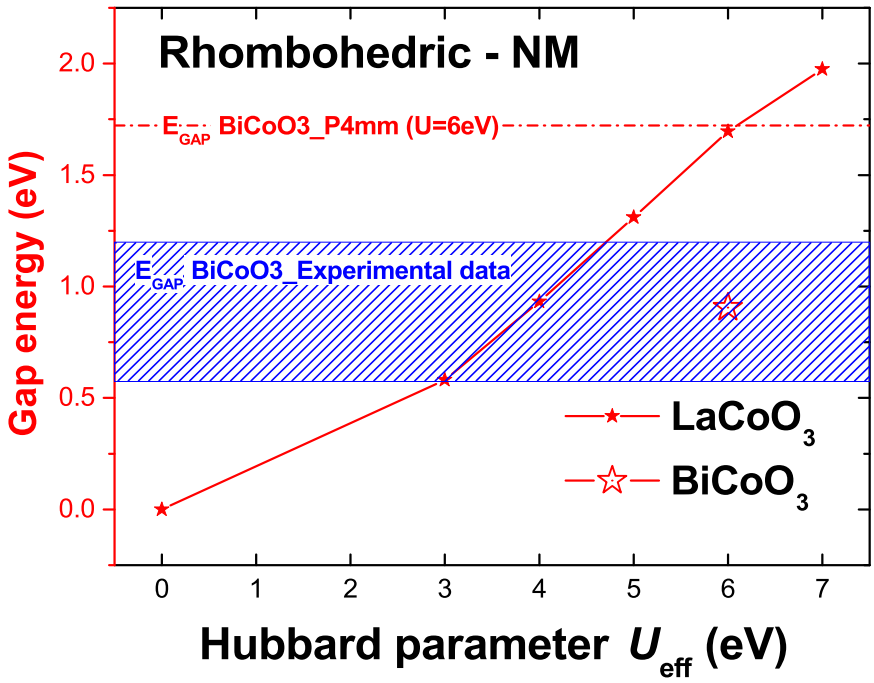

Figure 6.29: Variation of band gap of $LaCoO_3$ and $BiCoO_3$ in rhombohedric structure, with different U_{eff} values comparing with experimental data.

easy to synthesize.
Moreover, we have asked about the nature of these two compounds, insulators or semiconductors; A large gap in $LaCoO_3$ (1.69 eV) and $BiCoO_3$ (1.7 eV) indicate an insulator nature of these compounds; this result is correct for BCO (insulator), but it is not for LCO (semiconductor); Thornton et al. [215] and Korotin et al. [223] confirm the semiconducting character in $LaCoO_3$.

6.3.2.2 Density of States and magnetic moment

The density of states is an important physical quantity overwhelmingly encountered in solid state physics. It is measured by means of DFT-LSDA+U calculation. Figure 6.30 shows the total density of states (TDOS) of BCO 6.30a and LCO 6.30b with variation of U_{eff}. As the band structure, the TDOS of LCO present a metallic character with LSDA and a semiconductor character with LSDA+U. For BCO, the insulator character is present, and an increasing of band gap energy with U_{eff} application.

Tetragonal AFM-C Figure 6.31 shows the calculated density of states (DOS) with AFM C-type spin configuration. There are unoccupied Co 3d states (hybridized with O 2p orbital) extending from 2 eV to 2.8 eV. The width of this unoccupied band is about 0.8 eV.
According to partial DOS of Bi, Co, and O, there are occurrences of strong hybridization effects O 2p-Co 3d and Bi(6s, 6p) -O 2p states. It is accepted generally that the ferroelectric phase transition arises from a delicate balance between long-rang Coulomb forces (which favors the ferroelectric state) and short-range repulsions (which favors the nonpolar structure) [202]. The hybridization between Co 3d and O 2p leads to the charge transfer from O to Co; thus, O (2.535) and Co (4.5884↑ and 1.6357↓) are not fully ionized. The covalent Co–O bonds which extended from -7.5 eV to E_F, will weaken the short-range repulsions and lower the total energy, which is favorable for the ferroelectric phase transition. Moreover, the Bi s state is fully occupied and acts as a *lone pair* state causing the off-centering of Co ion [202]. The covalence of Bi–O (-10 eV - -9 eV) causes the charge transferring partially from O to both Bi, which reduces the total energy and then enhances the stability of the ferroelectric structure of $BiCoO_3$. On the other hand, the hybridizations of Co–O causes the large decrease of spin magnetic moments of Co ions 2.97 μ_B in comparison with the d^6 configuration 4 μ_B. Moreover, Fig. 6.31 shows an hybridization between Co d_{xz}, d_{yz} and O p_z, which is missing between d_{xy} and p_z, this

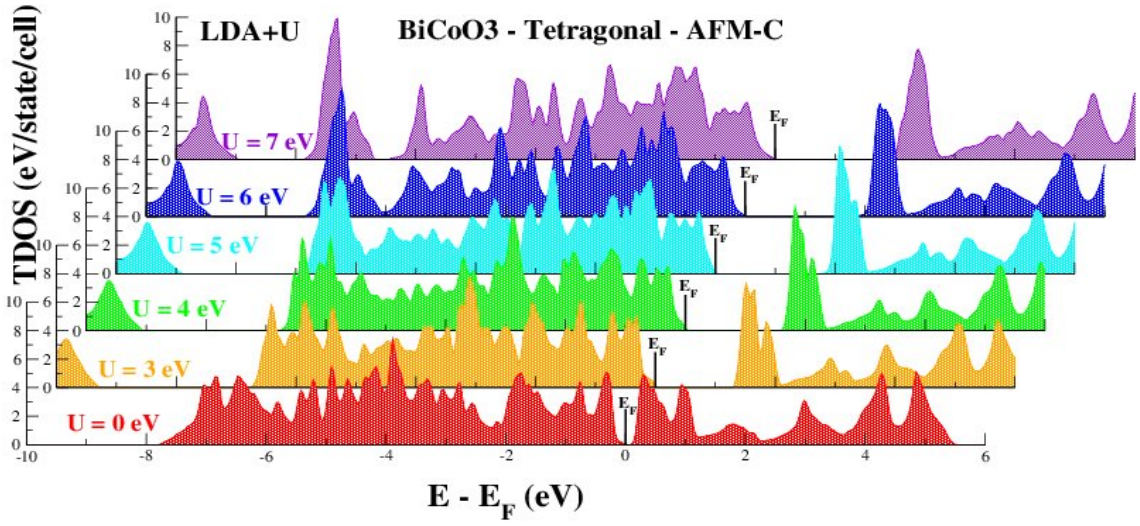

(a)

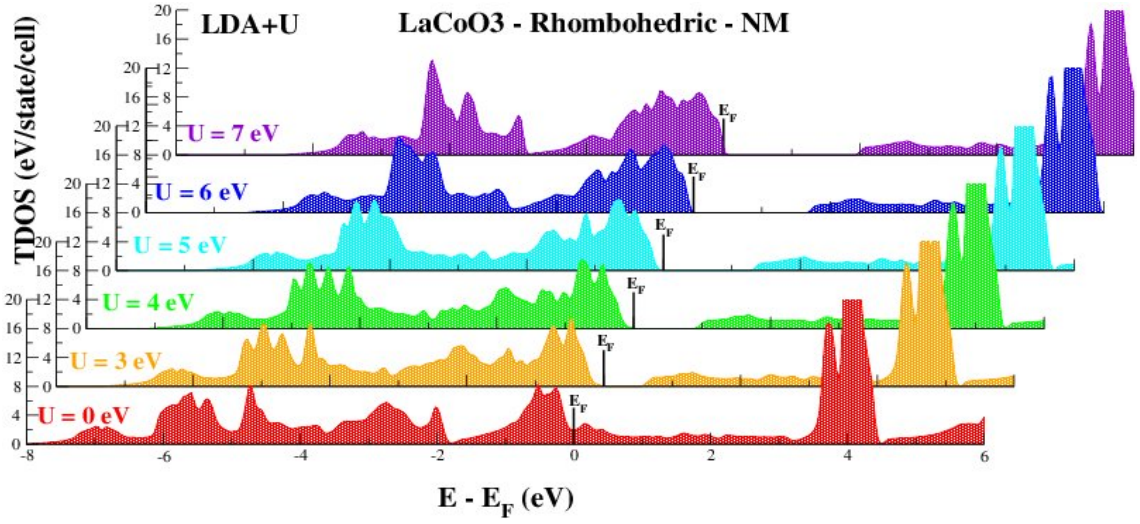

(b)

Figure 6.30: Total density of states of **(a)** $BiCoO_3$ and $LaCoO_3$ **(b)** in different U_{eff} values.

remark confirms the localization character of d_{xy} orbital. From fig. 6.31, we can observe the occupancy of Co d orbital as follows: $d_{xy}\uparrow$, $d_{xz}\uparrow$, $d_{yz}\uparrow$, $d_{z^2}\uparrow$, and $d_{x^2-y^2}\uparrow\downarrow$. This result confirms that the t_{2g} orbital is higher than e_g orbital, where the down electron prefers e_g orbital. This last result shows the high spin (HS) state in BCO-T with magnetic moment of 2.97 μ_B reduced by Co-O covalent bond.
The crystal field in BCO is present due to the octahedral environment of Co ion; also, from our BCO-DOS, there are a splitting of partial d-orbitals of Cobalt due to the Jahn-Teller effect, this effect arises because a regular octahedra deformed into a tetragonal distortion to lift the cubic symmetry.
Nevertheless, in this type of transition metal oxides, the C-type or G-type antiferromagnetic spin state is favorable due to the superexchange mechanism; In the case of $BiCoO_3$ the C-type AFM is favored because the existence of charge transfer between nearest-neighbor oxygens, where the transport properties follow Co-O-O-Co path. This O-O transfer charge reduce the total energy of system and make the AFM-C state more stable than AFM-G.
In the hypothetical tetragonal AFM-C $LaCoO_3$, the same hybridization and covalent bond between Co and O atoms (see figure 6.32). However, the missing of hybridization between La s and p orbitals and O p orbital, make the *lone pair* effect absent, which disadvantage the Co displacement and ferroelectric phase.

Rhombohedric NM For $LaCoO_3$, figure 6.33 show the calculated density of states in nonmagnetic state (LS: $t_{2g}^6e_g^0$); t_{2g} is fully occupied with triply degenerate d_{xy}, d_{xz}, and d_{yz} orbitals (same energies in DOS), the valence band is formed by a mixture of these Co states and O $2p$ orbitals. The doubly-degenerate $d_{x^2-y^2}$ and d_{z^2} orbitals which make up the e_g manifold form the conduction band.
We are agree on the fact that the valence band represents strong hybridization of electrons of O and Co atoms with some small contribution from La atom. The valence band is characterized by two peaks at -0.5 and -4.5 eV below the Fermi energy.
In hypothetical rhombohedric $BiCoO_3$, it is clear in figure 6.34 the similarities between BCO-R and LCO-R, However, there is a small hybridization between Bi s and O p orbitals, which can causing a displacement of Co atom in addition to tilt of the octahedral. This situation may produces another type of rhombohedral structure ($R3c$) which is noncentrosymmetric; the work in this type of structure is in outlook.

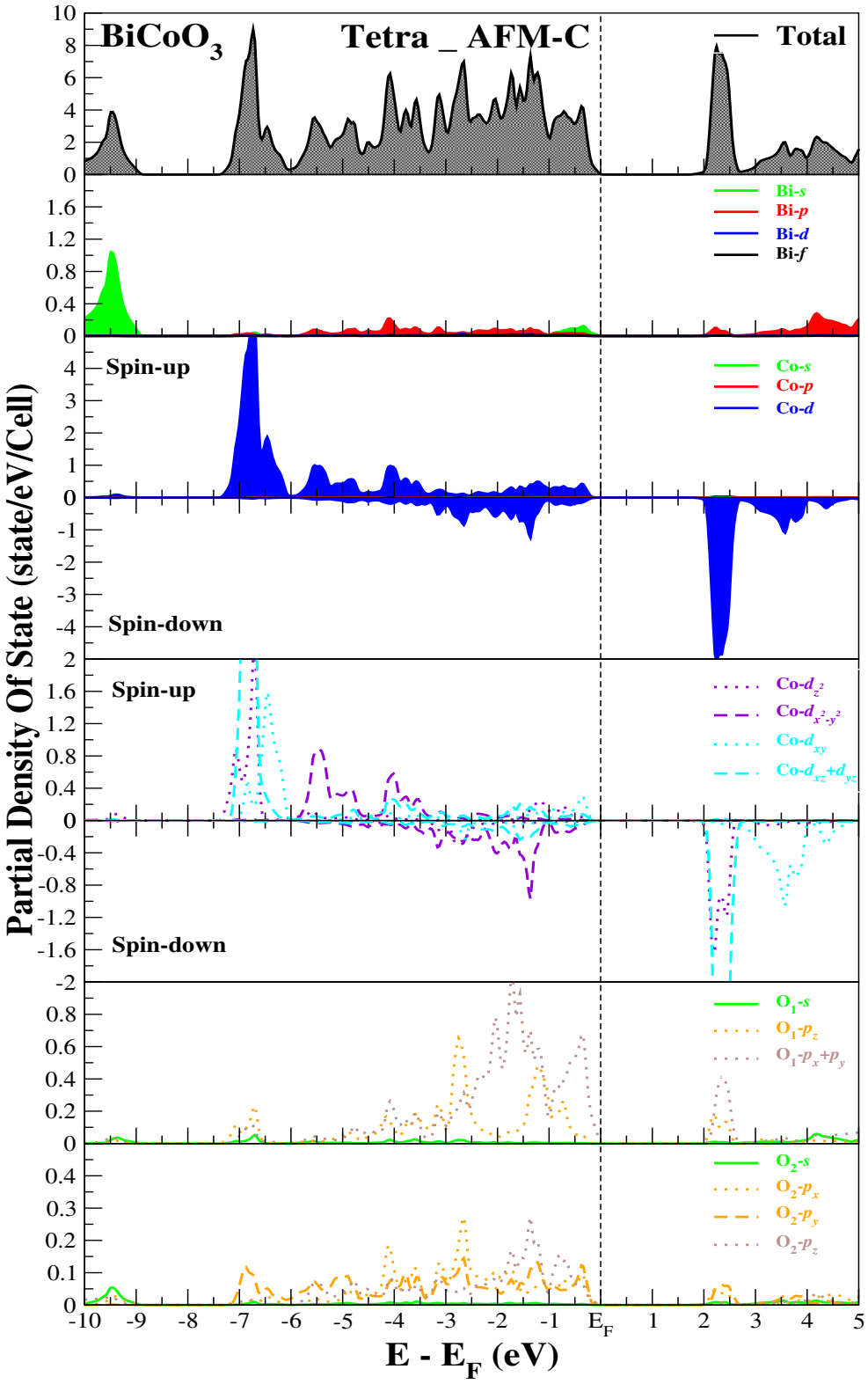

Figure 6.31: Total DOS and partial DOS of $BiCoO_3$ and partial DOS for Co, O, and Bi ions in the AFM-C tetragonal structure obtained by LSDA+U ($U = 6$ eV).

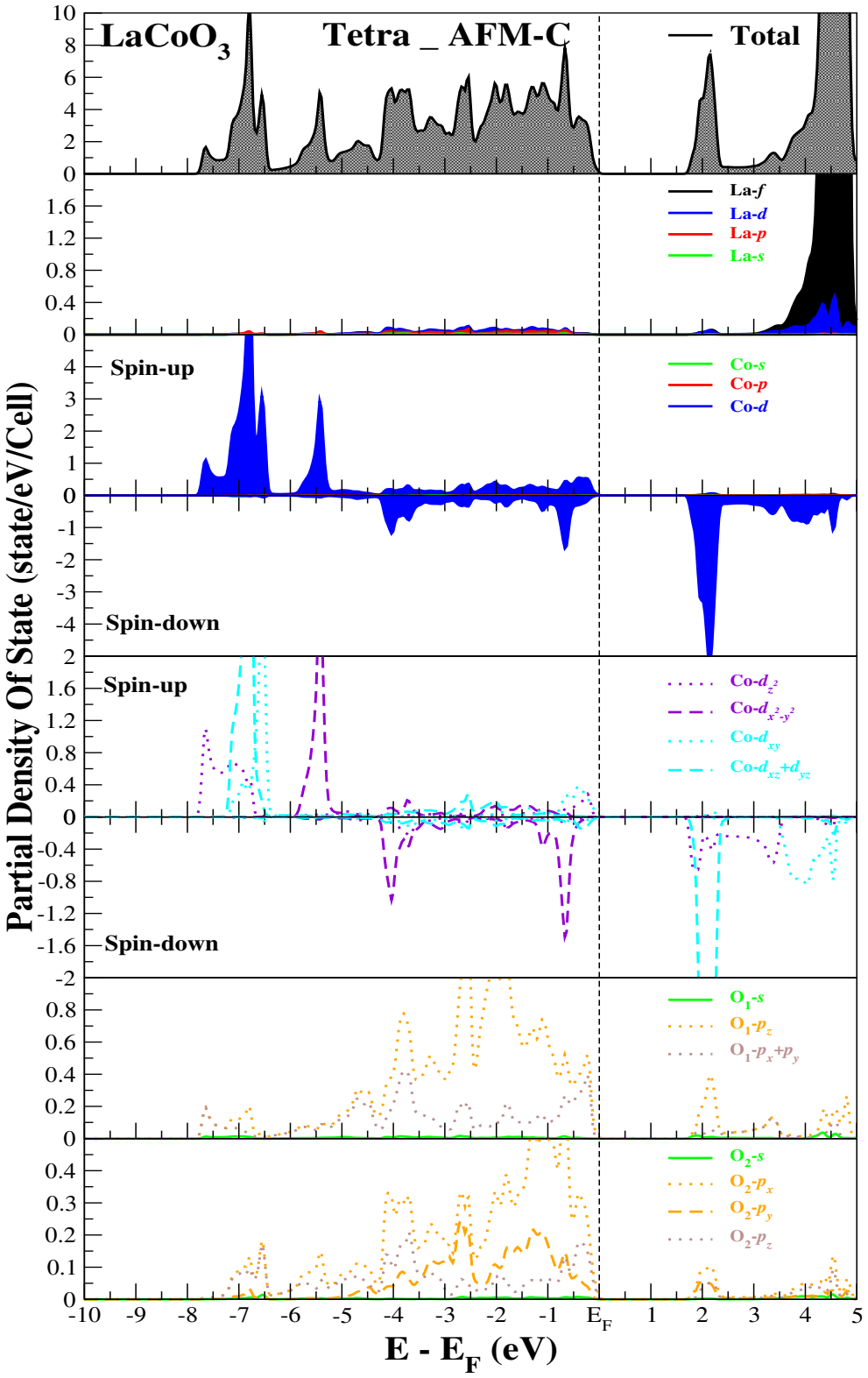

Figure 6.32: Total DOS and partial DOS of $LaCoO_3$ and partial DOS for Co, O, and La ions in the AFM-C tetragonal structure obtained by LSDA+U ($U = 6$ eV).

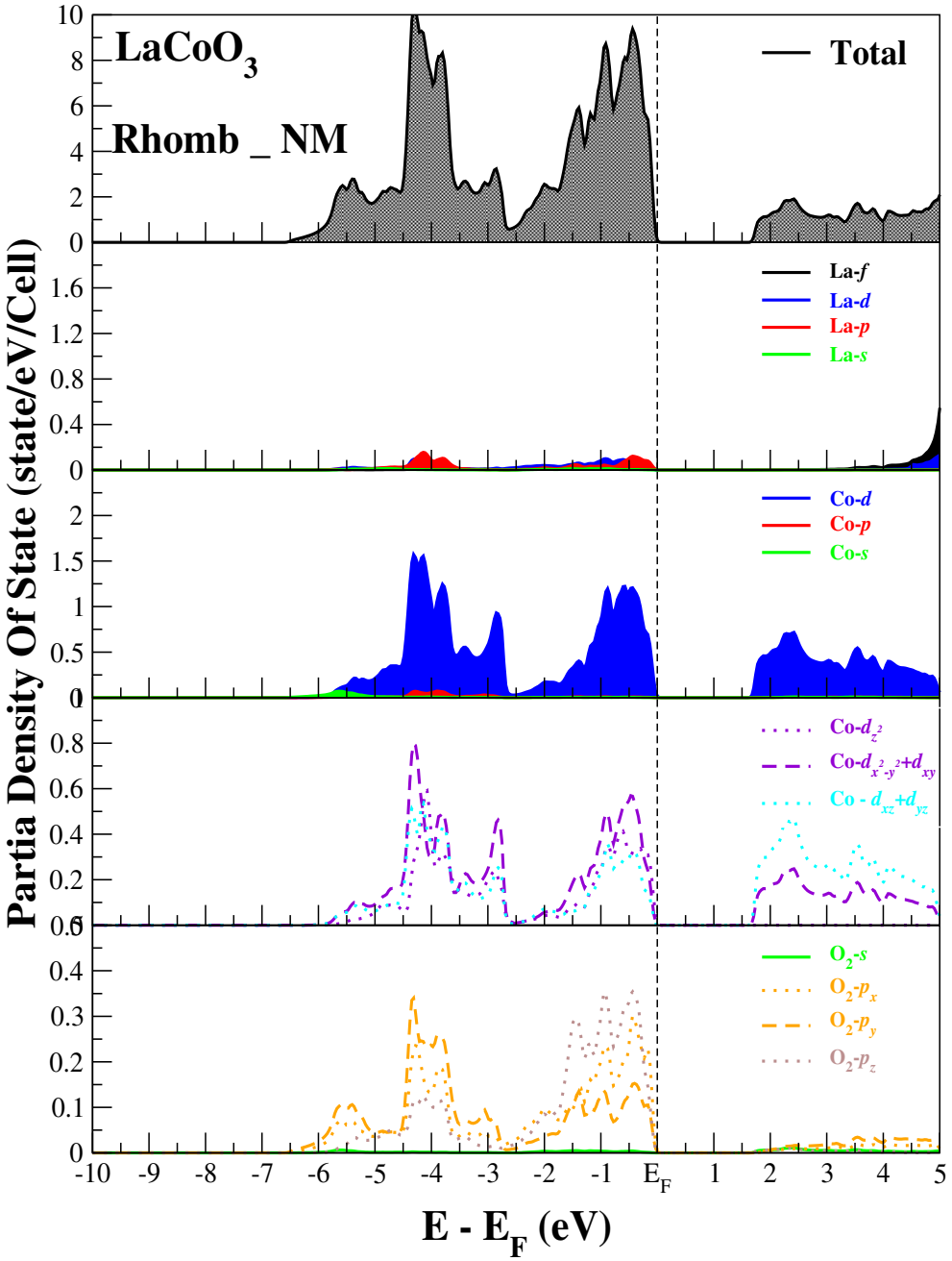

Figure 6.33: Total DOS and partial DOS of $LaCoO_3$-R and partial DOS for Co, O, and La ions in the NM rhombohedral structure obtained by LSDA+U ($U = 6$ eV).

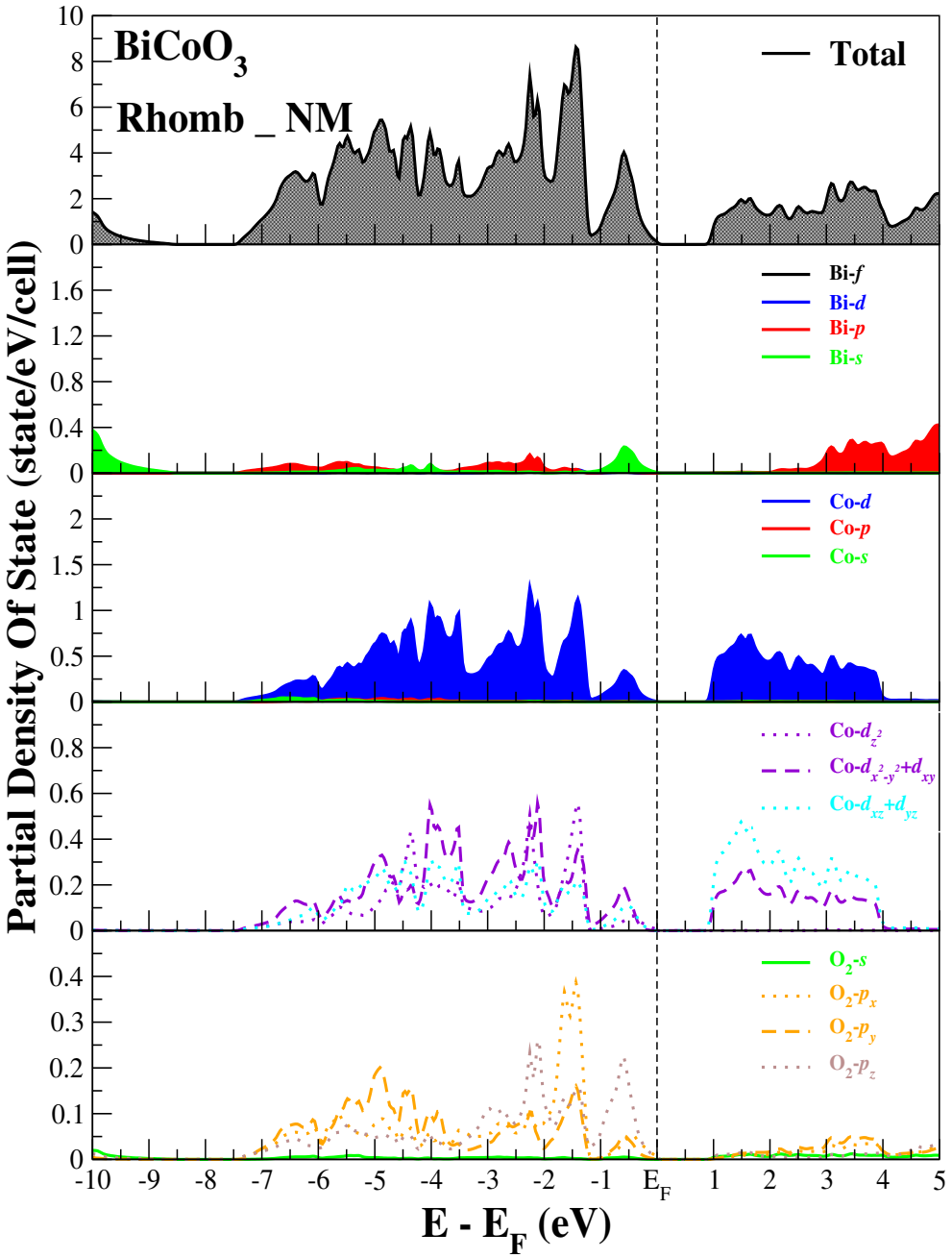

Figure 6.34: Total DOS and partial DOS of $BiCoO_3$ and partial DOS for Co, O, and Bi ions in the NM rhombohedral structure obtained by LSDA+U ($U = 6$ eV).

6.3.2.3 Structural effect on electronic structure

Table 6.8 shows the different structural data of bond lengths and angle of octahedra rotation. The bond lengths of rhombohedric CoO_6 octahedral are shorter than those of

Table 6.8: Calculated results of bond lengths and angles for BCO and LCO materials in Tetragonal and Rhombohedric structures.

	Rhombohedral	
	$BiCoO_3$	**$LaCoO_3$**
Co-O (Å)	1.9105	1.8998
Bi/La-O (Å)	2.2989	2.3873
Co-O-Co (°)	156°.66	162°.57
	Tetragonal	
	$BiCoO_3$	**$LaCoO_3$**
Co-O_1 (Å)	1.9757	1.93
Co-O_2 (Å)	1.7346	1.813
Co-O_3 (Å)	3.0679	2.3363
Bi/La-O_1 (Å)	2.26	2.4334
Bi/La-$O_{2/3}$ (Å)	2.7652	2.7122
O_1-O_2 (Å)	2.9497	2.8934

tetragonal ones, which confirm the large crystal field (CF) in rhombohedral materials in comparison with tetragonal. This large CF energy make this effect more favorable compared to exchange interaction (Hund effect J_H, CF > J_H). Therefore the low spin configuration is more stable than intermediate spin where CF ≈ J_H (Note that in high spin configuration, CF < J_H).

In tetragonal structure, the off-centering of cobalt toward O_2 makes the bond length of Co-O_3 long, and the CoO_6 octahedral yield to a pyramidal CoO_5. And the down electron prefers the $d_{x^2-y^2}$ orbital than d_{z^2}. Contrary, in $LaCoO_3$, Co-O_3 = 2.33Å keeps a octahedral environment of Co-ion.

Furthermore, the distance between La and O is longer than Bi-O which make the charge transfer impossible in LCO; So, the *lone pair* effect does not appear in LCO material.

We can conclude that the compression of tetragonal structure lead to rhombohedric structure, this compression reduce bond lengths and increase the crystal field; and for this reason, the magnetic state disappears due to spin state transition from HS (Tetragonal: CF < J_H + JT) to LS (Rhombohedral: CF > J_H).

6.4 Results and discussion- Part-II: "$Bi_{1-x}La_xCoO_3$" alloy

Doping of $BiCo0_3$ or $BiFe0_3$ often gives a beneficial effect on properties, such as an increase in dielectric constant, the decrease in the leakage current and the destruction of the space modulated spin structure. Rare earth cations are considered the most suitable substitutes for Bi^{+3} ions as they can easily be accommodated in the structure. Partial substitution of Bi^{+3} ions by lanthanides has been shown to improve ferroelectric properties and magnetization [242][6].
Rare earth oxides, RE_20_3, are dynamically very stable [243]. The RE^{+3}-O^{-2} bond is stronger than Bi^{+3}-0^{-2} which enhances the stability of the perovskite phase minimizing the bismuth volatilization and reducing the number of oxygen vacancies [244].
Several research groups have reported that La substitution at Bi-site in $BiFe0_3$ eliminates the impurity phases and enhances the magnetoelectric coupling; but to date, little works for La-doped $BiCoO_3$. It was expected having an improve in same properties, as well as magnetic properties and spin state transitions.
We chose to study the *lone-pair* dilution effect on the electronic and magnetic structures of $BiCoO_3$ by substituting La^{3+} for Bi^{3+}. Indeed both cations are isovalent, have compatible ionic radii (1.16Å for La and 1.17Å for Bi), and are nonmagnetic. At variance with Bi^{3+},the La^{3+} cation does not possess a stereochemical active electronic *lone pair*. $LaCoO_3$ crystallizes with an rhombohedric-type structure, with $R\bar{3}c$ centrosymmetric space-group symmetry. It presents a low spin configuration (nonmagnetic).
We present below the DFT study of magneto-structural stability, electronic structure, and magnetic properties of the complete alloy $Bi_{1-x}La_xCoO_3$ for $0 \leq x \leq 1$.

6.4.1 Magneto-Structural stability

Throughout condensed-matter science, disordered alloys provide unique properties which are inaccessible in pure materials. Semiconductors and ferroelectric materials are two important areas in which small changes in atomic composition dramatically change material properties. Theoretical examinations have been hampered by the difficulty of incorporating inhomogeneities into perfectly periodic systems. Several theoretical

[6]Reference text: Sara Karimi's thesis, "Structure-Property Relations in Rare Earth Doped $BiFeO_3$", Sheffield university 2011

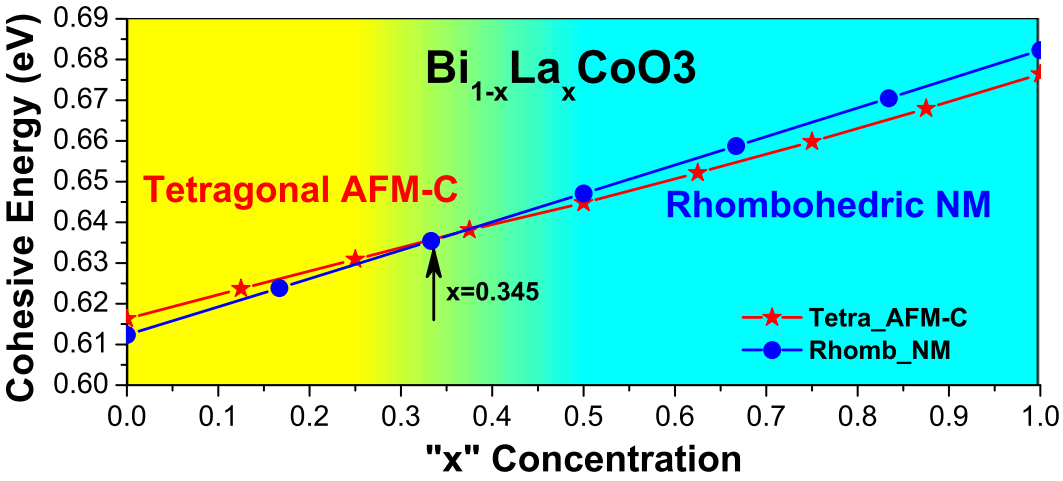

Figure 6.35: Variation of cohesive energy versus x concentration of $Bi_{1-x}La_xCoO_3$ alloy.

approaches have been formulated to address this specific issue, including the virtual crystal approximation (VCA)[245].

Firstly, an optimization of atomic coordinates and lattice parameters was performed for different x within the virtual crystal approximation (VCA) using parents structural data with LSDA+U approximation ($U = 6$ eV).

Figure 6.35 shows the variation of cohesive energy of $Bi_{1-x}La_xCoO_3$ alloy with x concentration, and indicates the structural stability of this alloy between tetragonal-AFM-C and rhombohedral-NM. We found that BLCO undergoes a strongly discontinuous transition between a T-phase and a R-phase at $x \simeq 0.345$, this structural transition is associated with a spin state transition from HS magnetic state to LS nonmagnetic state.

6.4.2 Structural properties

Figure 6.36 represents the variation of lattice parameters versus x concentration in $Bi_{1-x}La_xCoO_3$ alloy. It is clear that La-substitution in tetragonal structure decreases c parameter and increases a parameter, the same trend will be continued in rhombohedric structure with a lattice.

The incorporation of La atom reduces a tetragonality in T-phase which lead to a perfect octahedral in rhombohedral phase.

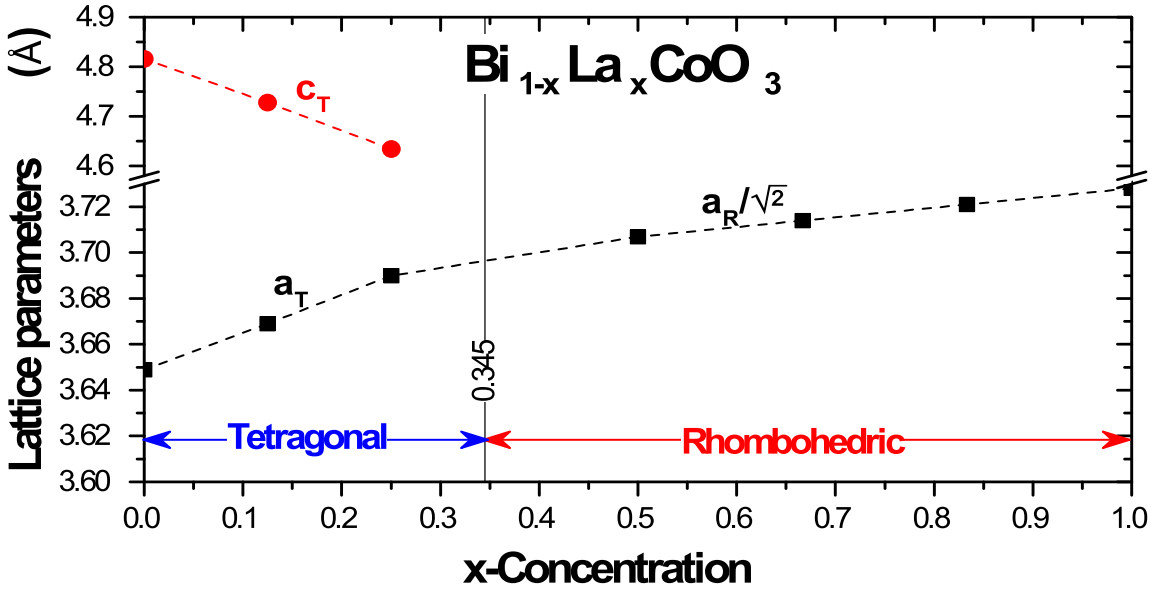

Figure 6.36: Variation of lattice parameters versus x concentration of $Bi_{1-x}La_xCoO_3$ alloy.

6.4.3 Electronic and magnetic properties

To understand this magneto-structural transition, we have calculated the density of state (DOS) of $Bi_{1-x}La_xCoO_3$ alloy in both fundamental structures (Tetragonal-AFMC and Rhombohedric-NM), using LSDA+U with $U = 6$ eV.

The density of states in Figure 6.37 shows several notices and explanations about the situation in our alloy. In tetragonal structure, we can notice that below the Fermi level, the majority up-spin is occupied by all e_g and t_{2g} bands, and the minority dn-spin by $d_{x^2-y^2}$ band; however, above the Fermi level, all bands unless $d_{x^2-y^2}$ are in minority spin. This situation make Co-atom in HS state with $d^{\uparrow}_{xy}, d^{\uparrow}_{xz}, d^{\uparrow}_{xz}, d^{\uparrow}_{z^2}$ and $d^{\uparrow\downarrow}_{x^2-y^2}$ configuration. We cannot understand the occupation of down electron e_g orbital, instead of t_{2g} orbital, perhaps due to the pyramidal environment of Co-ion.

The substitution of La-atom with Bi, reduces the Jahn-Teller effect (reducing of t_{2g} orbitals splitting), and increases the crystal field effect (increasing of $e_g - t_{2g}$ orbitals splitting). These latter remarks confirm the possible transition of $BiCoO_3$ under pressure from HS state to LS state [246]; The incorporation of La-atom reduces Co-O bond, this chemical pressure induce a geometrical transition from pyramidal to octahedral environment of Cobalt.

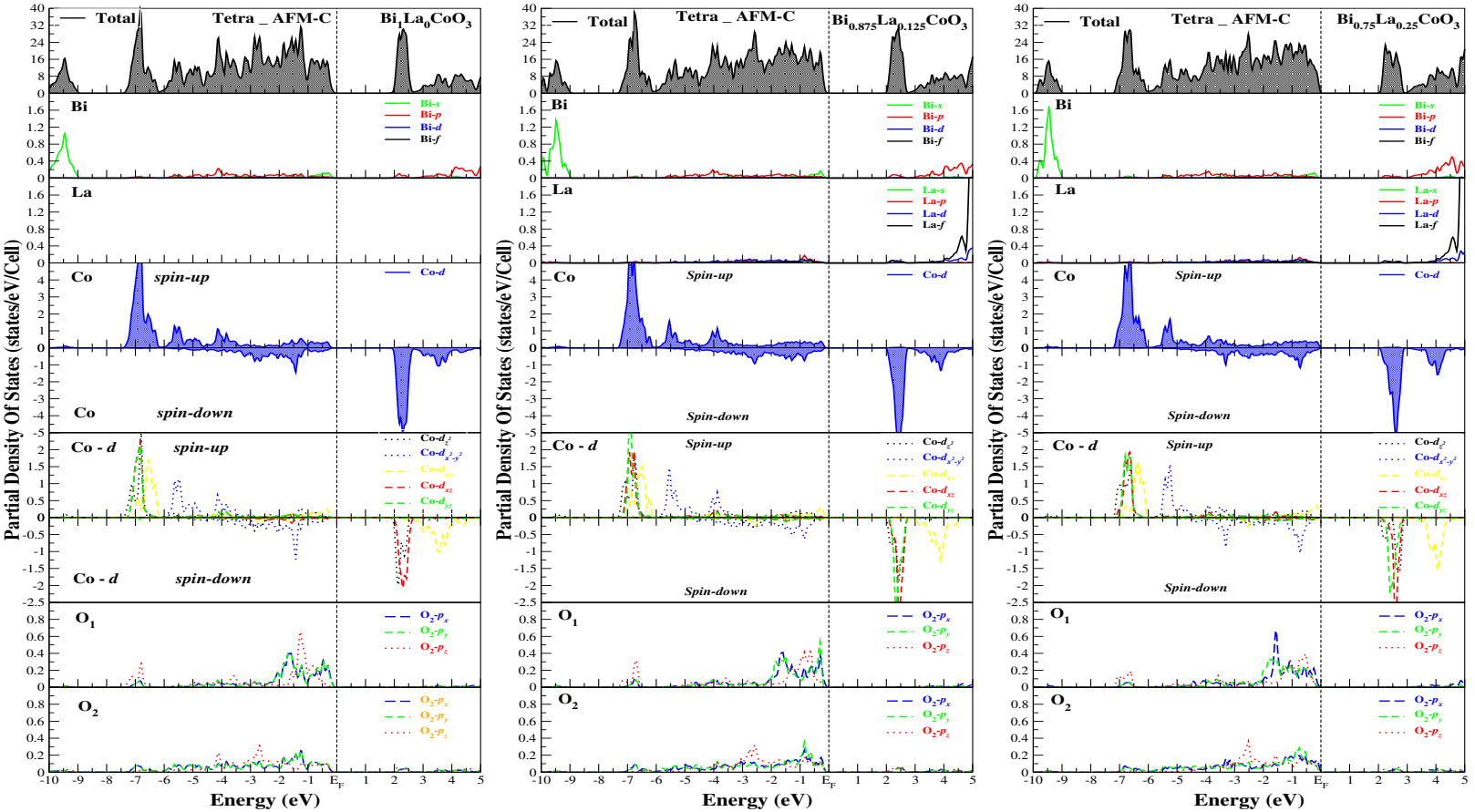

Figure 6.37: Total and Partial density of states of $Bi_{1-x}La_xCoO_3$ in tetragonal-AFM-C using LSDA+U ($U = 6$ eV).

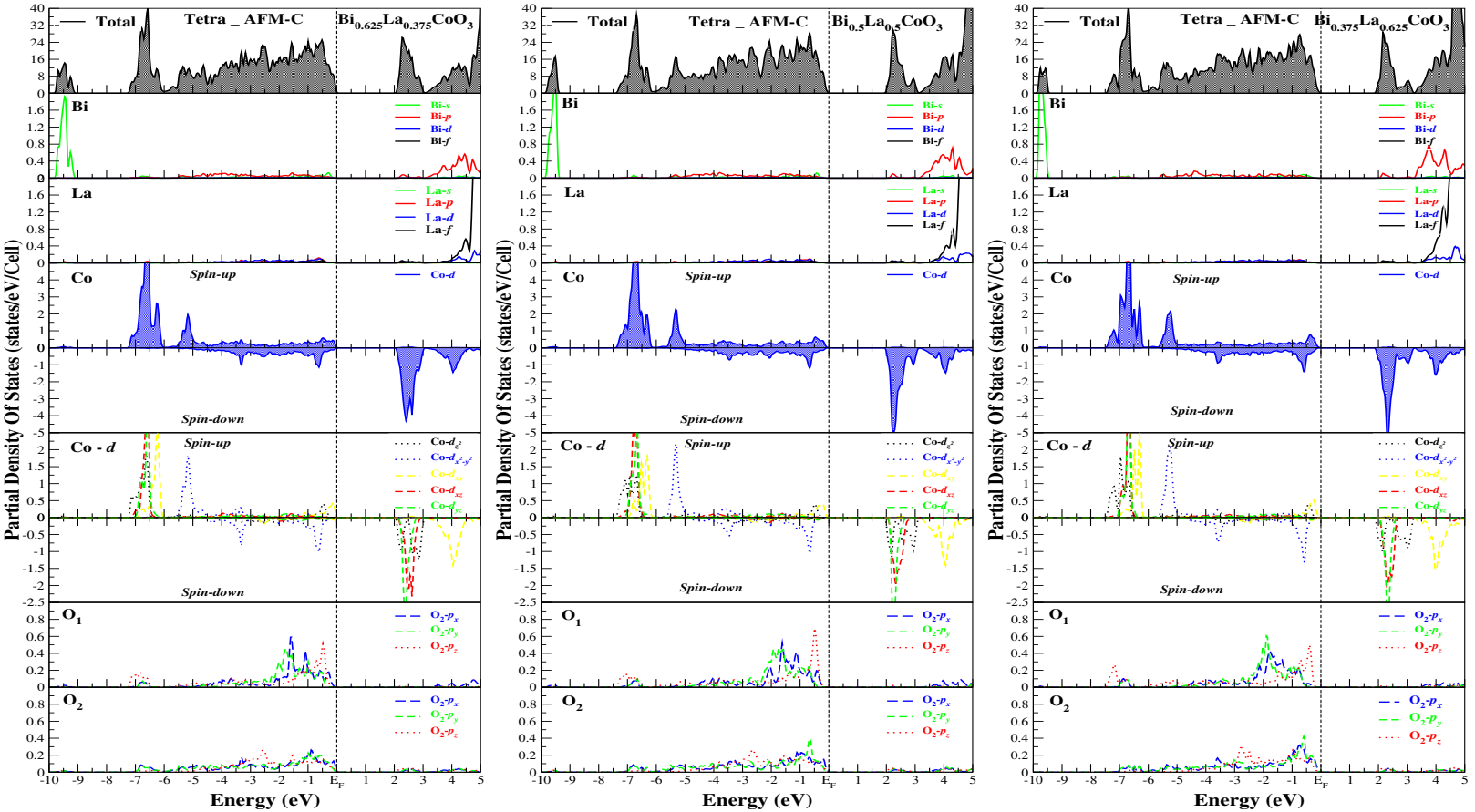

Figure 6.37: Total and Partial density of states of $Bi_{1-x}La_xCoO_3$ in tetragonal-AFM-C using LSDA+U ($U = 6$ eV).

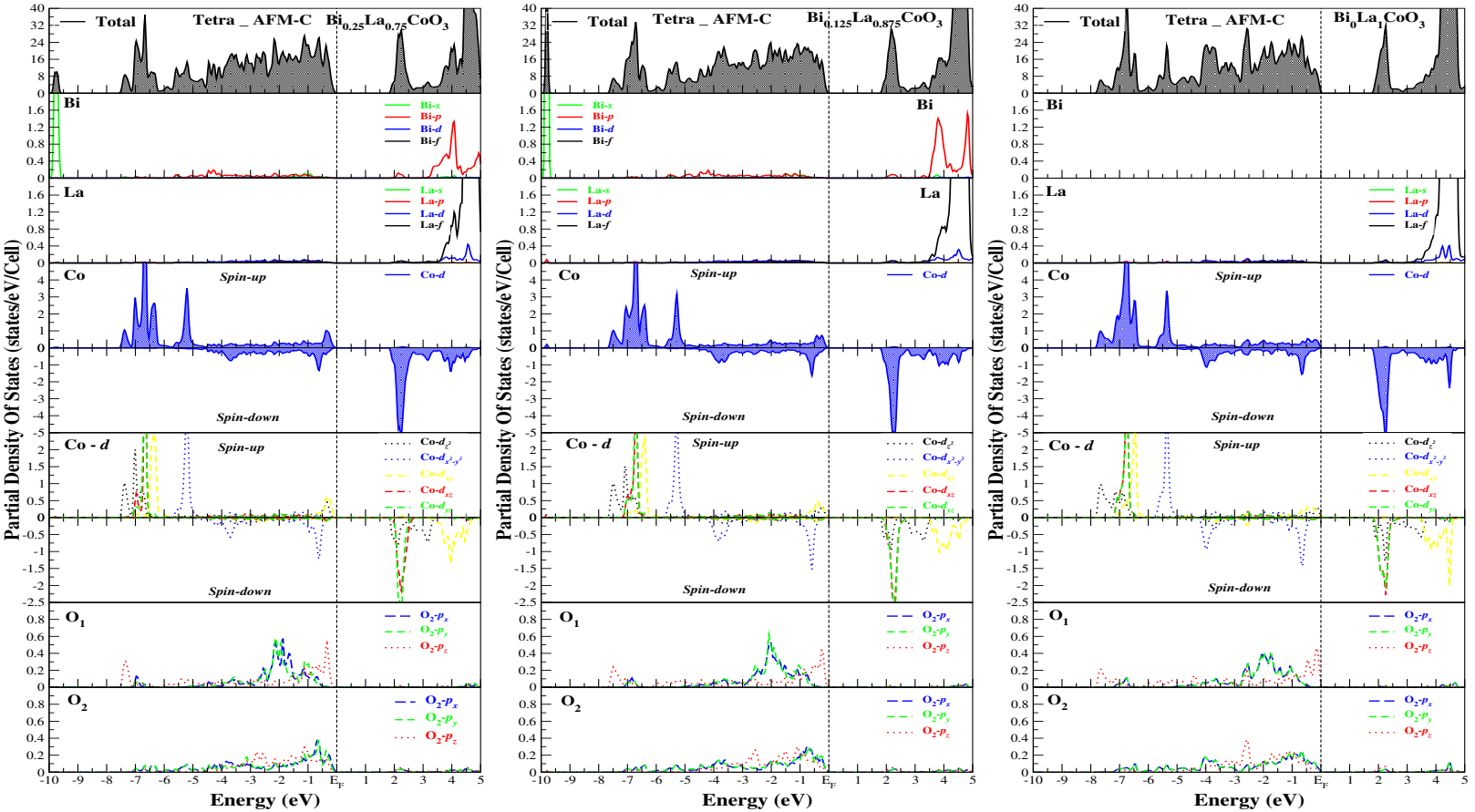

Figure 6.37: Total and Partial density of states of $Bi_{1-x}La_xCoO_3$ in tetragonal-AFM-C using LSDA+U ($U = 6$ eV).

Moreover, there is another reason for reducing Co-O bond, the absence of *lone pair* effect in La atoms. Figs. 6.37 show that band width of Bi s-like orbital decrease with increasing the La x-concentration, this change is mainly due to the increase of Bi-O distance. This latter, may predict a charge transfer reductions between Bi and O atoms; And so, reduction of *lone pair* mechanism.

We can conclude from our study of $Bi_{1-x}La_xCoO_3$ alloy in tetragonal-AFM-C structure, that this changes in different effects (Jahn-Teller, Crystal-Field, and *lone pair*) induce a structural transition from tetragonal to rhombohedral structures, as well as magnetic transition from HS antiferromagnetic to LS nonmagnetic states.

On the other hand, Fig. 6.37 show a hybridization between p_z and $d^{\downarrow}_{x^2-y^2}$ orbitals, this hybridization make a covalent bond in c direction, which make the C-type antiferromagnetic due to the superexchange mechanism. This covalency reduced with increasing La substitution (we think that reducing superexchange interactions make HS to LS transition easier).

Figure 6.38 presents the projected density of states of $Bi_{1-x}La_xCoO_3$ alloy in Rhombohedric-NM structure. As shown in rhombohedric parent compounds, the Co d electrons are localized in t_{2g} orbitals and maintains the LS nonmagnetic state.

However, the Bi-atom substitution creates a new bond between Bi s-orbital and O p_z-orbital at a top of valence band, this hybridization may causes a *lone pair* effect which can displace Co ion and induce J-T effect, but unfortunately, and due to the difficulties to realize a total relaxation, we have used a VCA approximation where we cannot see this displacement. We expect that the incorporation of Bi atom in rhombohedric $LaCoO_3$ may induce a structural transition from $R\bar{3}c$ centrosymmetric symmetry to $R3c$ noncentrosymmetric symmetry, which can shows the ferroelectricity in this system.

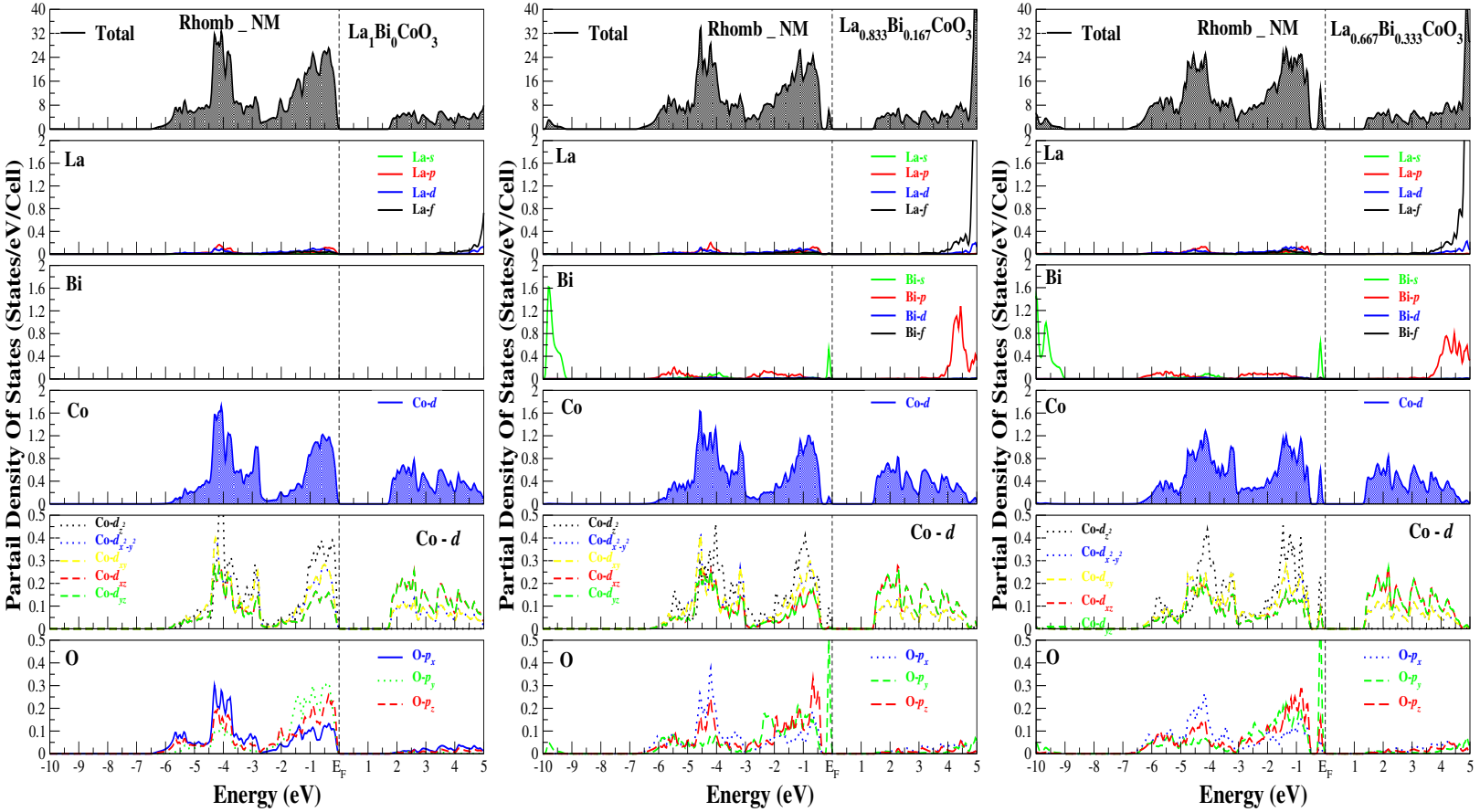

(a) (b) (c)

Figure 6.38: Total and Partial density of states of $Bi_{1-x}La_xCoO_3$ in Rhombohedric-NM using LSDA+U ($U = 6$ eV).

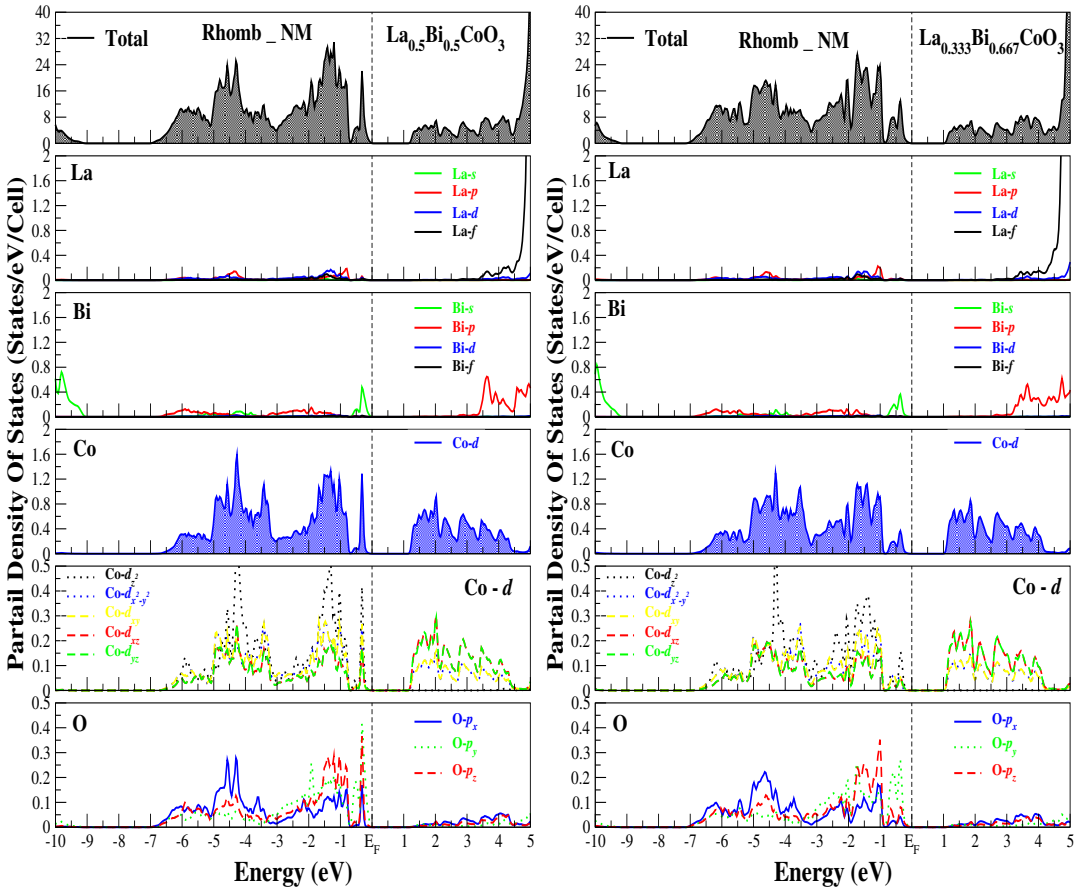

(d) (e)

Figure 6.38: Total and Partial density of states of $Bi_{1-x}La_xCoO_3$ in Rhombohedric-NM using LSDA+U ($U = 6$ eV).

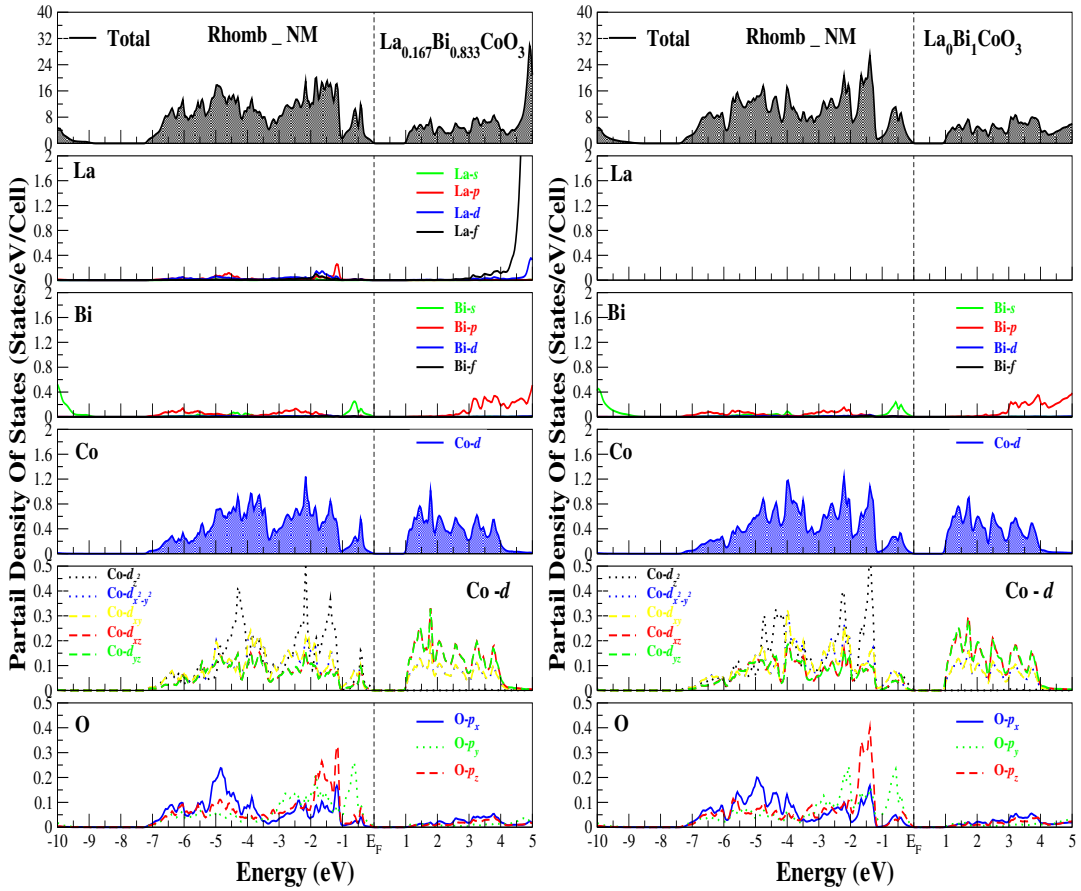

(f) (g)

Figure 6.38: Total and Partial density of states of $Bi_{1-x}La_xCoO_3$ in Rhombohedric-NM using LSDA+U ($U = 6$ eV).

6.4.4 Structural effect on electronic structure

Lanthanum substitution in tetragonal structure reduces Co-O_1 in-plane and Co-O_3 along c axis distances, and increases Co-O_2 bond, these reduction in bond increase the CF splitting and reduces the J-T effect, and consequently, a structural transition arises from tetragonal phase to rhombohedral phase.
Figure 6.39 shows a possible transition from a pyramidal to octahedral environment of cobalt atom. La-substitution induce a slight improvement in magnetic moment of Co-ion, perhaps due to a reduction in Co-O bond covalency.
Even in rhombohedric alloy, there is a reduction of Co-O distance in perfect octahedral, which induces a large crystal field splitting and improves LS state stability.

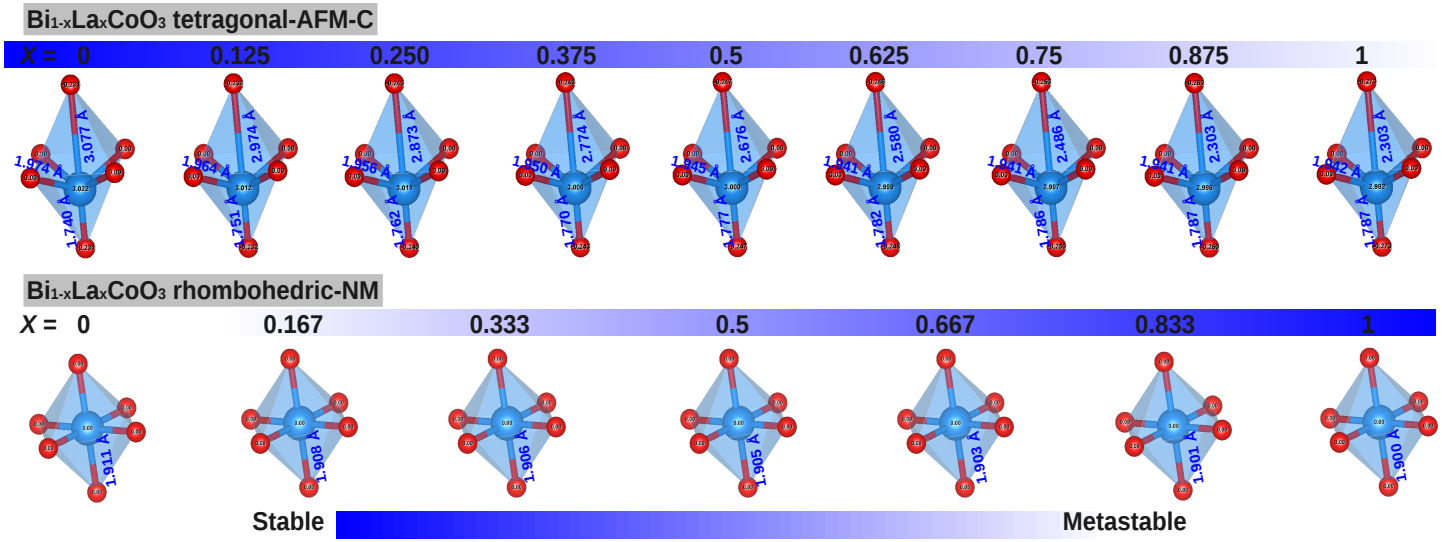

Figure 6.39: Variation of Co-O bonds and magnetic moments in CoO_6 octahedra versus x concentration of $Bi_{1-x}La_xCoO_3$ alloy.

6.5 Conclusion

To conclude, using the first-principles DFT method and LSDA+U calculations, we have performed a detailed investigation on the structural and magnetic ground states of strongly correlated perovskites, $BiCoO_3$ and $LaCoO_3$; The choice of these perovskites $ACoO_3$ (A = Bi and La) as materials of this investigation is due to the presence of the Co ion in $ACoO_3$ which is well known for its spin-state transition, is expected to add another dimension to the multiferroic aspect and magnetic behavior of these compounds. The strong correlation of the Co $3d$ electrons requires the use of the LSDA+ Hubbard U approach, it has been successful in treating strong correlations in transition-metal oxides; However, due to the discrepancies in the past works of choice U_{eff} in $BiCoO_3$ and $LaCoO_3$, in the first part of this study we revisit the effects of electron repulsion (U_{eff}) on the ground state in bulk Bi/$LaCoO_3$. We have begun by calculating the critical U value that induces a spin state transition in the bulk rhombohedral $LaCoO_3$ structure by calculating the total energies for each spin state as a function of U_{eff}, in this investigation we have found 6 eV, as a critical U_{eff}; we cannot exceed this value; beyond this critical U value, a spin state transition appears from LS to IS which disagree with the experimental. Furthermore, the variation of U induces a structural transition from rhombohedric to tetragonal in bulk $BiCoO_3$, our result shows another critical $U_{eff} = 4$ eV, the correct tetragonal AFM-C structure is only stable for U_{eff} values more than 4.0 eV.
According to these two critical values of U_{eff} (more than 4.0 eV and less than 6.0 eV), we have taken the greater one. The magnetic ground state was found in good agreement with experimental investigations, where $BiCoO_3$ was found in antiferromagnetic state with C-type spin ordering, and $LaCoO_3$ was found nonmagnetic with low spin configuration of Co d electrons.
Moreover, the crystal structure was found rhombohedric ($R\bar{3}c$) for $LaCoO_3$ and tetragonal ($P4mm$) for $BiCoO_3$; these results are in good agreement with experiments.
We continued our study by optimizing the structural parameters for $BiCoO_3$ compound in tetragonal-AFM-C structure and $LaCoO_3$ in rhombohedric-NM structure. The best results was made with $U_{eff} = 6$ eV, where a, c, c/a and z (T-AFMC) and a, α and z (R-NM) are in good agreement with others experimental and theoretical works, with an underestimation of lattice parameters, maybe due to the LSDA exchange-correction approximation choice.
The electronic structure of $ACoO_3$ (A = Bi and La) was calculated by LSDA and LSDA+U; we have calculated also the energy gap and the magnetic moments of both compounds, the best results were found for $U_{eff} = 6$ eV.

The band structures in these compounds confirms the insulator character for both materials with a large band gap; Also, we have examined the density of states for synthesized T-$BiCoO_3$-AFM-C and R-$LaCoO_3$-NM compounds, and hypothetical T-$LaCoO_3$-AFM-C and R-$BiCoO_3$-NM compounds, According to partial DOS of Bi, Co, and O, there are occurrences of strong hybridization effects O $2p$-Co $3d$ and Bi ($6s$, $6p$)-O $2p$ states. The hybridization between Co $3d$ and O $2p$ leads to the charge transfer from O to Co; thus, O (2.535) and Co (4.5884↑ and 1.6357↓) are not fully ionized. The covalent Co-O bonds will weaken the short-range repulsions and lower the total energy, which is favorable for the ferroelectric phase transition. Moreover, the Bi s state is fully occupied and acts as a *lone pair* state causing the off-centering of Co ion. The covalence of Bi-O cause the charge transferring partially from O to Bi, which reduces the total energy and then enhances the stability of the tetragonal ferroelectric structure of $BiCoO_3$. On the other hand, the hybridizations of Co-O causes the large decrease of spin magnetic moments of Co ions 2.97 μ_B in comparison with the d^6 configuration 4 μ_B. Moreover, we can observe the occupancy of Co d orbital as follows: d_{xy} ↑, d_{xz} ↑, d_{yz} ↑, d_{z^2} ↑, and $d_{x^2-y^2}$ ↑↓. This result confirms that the t_{2g} orbital is higher than e_g orbital, where the down electron prefers e_g orbital. This last result shows the high spin (HS) state in BCO-T with magnetic moment of 2.97 μ_B reduced by Co-O covalent bond.

The crystal field in BCO is present due to the octahedral environment of Co ion; also, there is a splitting of partial d-orbitals of Cobalt due to the Jahn-Teller effect, this effect arises because regular octahedra deformed into a tetragonal distortion to lift the cubic symmetry.

Nevertheless, in this type of transition metal oxides, the C-type or G-type antiferromagnetic spin state is favorable due to the superexchange mechanism; In the case of $BiCoO_3$, the C-type AFM is favored because the existence of charge transfer between nearest-neighbor oxygens, where the transport properties follow Co-O-O-Co path. This O-O transfer charge reduces the total energy of system and make the AFM-C state more stable than AFM-G.

In the hypothetical tetragonal AFM-C $LaCoO_3$, the same hybridization and covalent bond between Co and O atoms. However, the missing of hybridization between La s and p orbitals and O p orbital, make the *lone pair* effect absent, which disadvantage the Co displacement and ferroelectric phase.

For $LaCoO_3$, the calculated density of states in nonmagnetic state (LS: $t_{2g}^6 e_g^0$) show that, t_{2g} is fully occupied with triply degenerate d_{xy}, d_{xz}, and d_{yz} orbitals, the valence band is formed by a mixture of these Co states and O $2p$ orbitals. The doubly-degenerate $d_{x^2-y^2}$ and d_{z^2} orbitals which make up the e_g manifold, form the conduction band.

We are agreeing on the fact that the valence band represents strong hybridization of electrons of O and Co atoms with some small contribution from La atom.
In hypothetical rhombohedric $BiCoO_3$, there are a clear similarities between BCO-R and LCO-R, However, there is a small hybridization between Bi s and O p orbitals, which can causing a displacement of Co atom in addition to tilt of the octahedral. This situation may produces another type of rhombohedral structure ($R3c$) which is noncentrosymmetric; the work in this type of structure is in outlook.
The Co-O bond length in CoO_6 octahedral presents an important degree of freedom; The bond lengths of rhombohedric CoO_6 octahedral are shorter than those of tetragonal ones, which confirm the large crystal field (CF) in rhombohedral materials in comparison with tetragonal. This large CF energy make this effect more favorable compared to exchange interaction (Hund effect J_H, CF $> J_H$). Therefore the low spin configuration is more stable than intermediate spin where CF $\approx J_H$.
In tetragonal structure, the off-centering of cobalt toward O_2 makes the bond length of Co-O_3 long, and the CoO_6 octahedral yield to a pyramidal CoO_5. And the down electron prefers the $d_{x^2-y^2}$ orbital than d_{z^2}. Contrary, in $LaCoO_3$, Co-O_3 = 2.33 Å keeps an octahedral environment of Co-ion.
Furthermore, the distance between La and O is longer than Bi-O which makes the charge transfer impossible in LCO; So, the *lone pair* effect do not appears in LCO material.
We can conclude that the compression of tetragonal structure leads to rhombohedric structure, this compression reduces bond lengths and increases the crystal field; and for this reason, the magnetic state disappears due to spin state transition from HS (Tetragonal: CF $< J_H$ + JT) to LS (Rhombohedral: CF $> J_H$).
We have chosen to study the *lone-pair* dilution effect on the electronic and magnetic structures of $BiCoO_3$ by substituting La^{3+} for Bi^{3+}. Indeed both cations are isovalent, have compatible ionic radii and are nonmagnetic. At variance with Bi^{3+}, the La^{3+} cation does not possess an active electronic *lone pair*.
We have presented the DFT study of magneto-structural stability, electronic structure, and magnetic properties of the complete alloy $Bi_{1-x}La_xCoO_3$ for $0 \leq x \leq 1$.
We have found that the structural stability of this alloy between tetragonal-AFM-C and rhombohedral-NM undergoes a strongly discontinuous transition between a Tetragonal-phase and a Rhombohedral-phase at $x \simeq 0.345$, this structural transition is associated with a spin state transition from HS magnetic state to LS nonmagnetic state.
The same orbital occupancies were found in BLCO alloy in comparison with parent compounds for each structure. In tetragonal structure, the substitution of La-atom with Bi, reduces the Jahn-Teller effect (reducing of t_{2g} orbitals splitting), and increases the

crystal field effect (increasing of $e_g - t_{2g}$ orbitals splitting). Furthermore, the incorporation of La-atom reduces Co-O bond, this chemical pressure induce a geometrical transition from pyramidal to octahedral environment of Cobalt. Moreover, there is another reason for reducing Co-O bond, the absence of *lone pair* effect in La atoms. The band width of Bi s-like orbital decreases with increasing the La x-concentration, this change is mainly due to the increase of Bi-O distance. The latter, may predict a charge transfer reductions between Bi and O atoms; And so, reduction of *lone pair* mechanism.

We can conclude from our study of $Bi_{1-x}La_xCoO_3$ alloy in tetragonal-AFM-C structure, that these changes in different effects (Jahn-Teller, Crystal-Field, and *lone pair*) induce a structural transition from tetragonal to rhombohedral structures, as well as magnetic transition from HS antiferromagnetic to LS nonmagnetic states.

However, the hybridization between p_z and $d^{\downarrow}_{x^2-y^2}$ orbitals make a covalent bond in c direction, which make the spin ordering in C-type antiferromagnetic due to the superexchange mechanism. This covalency reduced with increasing La substitution (we think that reducing superexchange interaction makes HS to LS transition easier).

As in rhombohedric parent compounds, the calculated density of states of $Bi_{1-x}La_xCoO_3$ alloy in Rhombohedric-NM structure shows that the Co d electrons are localized in t_{2g} orbitals and maintains the LS nonmagnetic state.

However, the Bi-atom substitution creates a new bond between Bi s-orbital and O p_z-orbital at a top of valence band, this hybridization may causes a *lone pair* effect which can displace Co ion and induce J-T effect, but unfortunately, and due to the difficulties to realize a total relaxation, we have used a VCA approximation where we cannot see this displacement. We expect that the incorporation of Bi atom in rhombohedric $LaCoO_3$ may induce a structural transition from $R\bar{3}c$ centrosymmetric symmetry to $R3c$ noncentrosymmetric symmetry, which can shows the ferroelectricity in this system.

Finally, from literature, BCO compound has a critical temperature T_C about 470 K [4], and for LCO, T_C is about 95 K [182]; we can predict that La-substitution reduces T_C of $Bi_{1-x}La_xCoO_3$ alloy and improves their properties related to spin state transition.

Chapter 7

Anti Perovskites : $R\mathrm{Rh_3C}$

7.1 Introduction and objective

Materials that crystallize with a perovskite or perovskite-related structure have been widely studied, particularly after the discovery of colossal magnetoresistance [247, 248] and high-temperature superconductivity [125, 249] in layered perovskite-related ceramics. Moreover, perovskite-related materials have been shown to exhibit an extensive variety of valuable physical properties and thus are suitable for use in a wide range of applications such as electronic conductors (in particular semiconductors), ferroelectrics, ionic conductors, thermoelectric devices and battery materials.

The composition of perovskite-related materials is highly flexible, allowing huge scope for both the structure and the physical properties of the material to be controlled by exploiting the structure-property relation. Commonly, the manipulation of non-stoichiometry and substitution of cations or anions is used to control the metal oxidation state and to optimize the useful properties of the material.

The earliest description of the common atomic arrangement of perovskite structure having the general formula ABX_3 and a simple cubic structure was for the mineral known as perovskite, $CaTiO_3$ [250]. The structure of $CaTiO_3$ was later found to adopt a distorted perovskite lattice and thus an orthorhombic unit cell [197]; however the term perovskite has been universally adopted to describe the structure of ABX_3 compounds. Indeed, most structures described as perovskites are essentially orthorhombic yet still assume the ideal simple cubic unit cell at elevated temperatures.

Antiperovskites MXT_3 (M=Mg,Cu,La,..., X=B,C,N, and T a transition metal) have the same structure as the perovskite $CaTiO_3$, except for the exchanged positions of the light

atom and the transition metal. Studies on nonoxide antiperovskite-type compounds such as the ternary carbides RRh$_3$C (R=rare earth) have been comparatively rare. Among the family of antiperovskites, the superconductor MgCNi$_3$ (T$_C$=8 K) has received considerable attention (see Ref [251]). Due to the high amount of Ni, magnetic interactions are present in MgCNi$_3$ and their influence on the superconductivity mechanism is not fully understood yet. It has been shown that MgCNi$_3$ is near a ferromagnetic instability [252–254], which can be reached, for example, by hole doping at the Mg site. Unfortunately, it has been impossible so far to investigate the effect of enhanced spin fluctuations on the superconductivity in doped compounds such as Mg$_{1-x}$Li$_x$CNi$_3$ or Mg$_{1-x}$Na$_x$CNi$_3$ because all attempts to prepare such samples failed. The antiperovskite structure is cubic and centrosymmetric which give a rise to the manifestation of the 3D topological insulator (TI) phenomena, the antiperovskite 3D TI can provide a novel platform for diverse potential applications [255].

Intermetallic antiperovskites closely related to MgCNi$_3$ are therefore subject to investigations, both in the search for new superconductors and in the pursuit of a better understanding of the interplay between superconductivity and magnetism. It was suggested that carbon-containing antiperovskites may be good candidates.

Systematic investigation of the synthesis and fundamental properties of nonoxide perovskite-type compounds is necessary. The ternary carbides of rare-earth metal R-Rh-C (R=Er, Gd) system have also received considerable attention in the superconductivity and magnetism field. In the present stage of the study on perovskite-type RRh$_3$B and RRh$_3$C, it has been observed that they form a continuous solid solution, RRh$_3$B$_x$C$_{1-x}$, in the range of 0≤x≤1 with cubic structure (space group: Pm-3m) [256–261]. The introduction of smaller atoms such as carbon and boron leads in some cases to interesting changes in the physical properties of the parent compounds. The synthesis of quaternary borocarbide system RRh$_3$B$_x$C$_{1-x}$ has also been reported in the literature [261–263]. More recently, RRh$_3$X (R=rare earth; X=B, C) compounds have been studied for determining their magnetic behavior [12]. Magnetic antiperovskites show a variety of magnetic orderings and phase transitions. In the ref. [12], the magnetic behavior changed when the rare earth element changed.

So, most interest is limited to the synthesization and structural analysis and the absence in the literature of any information about the ab initio electronic and magnetic structure of these compounds has led us to study these new materials. And for comparison with Ref. [12], the magnetic stability of RRh$_3$C compounds for R=La, Ce, Pr, Nd, Pm, Sm, Eu, and Gd is studied. In particular, in the presence of rare-earth 4f orbitals, the widely used local spin-density approximation (LSDA) [139] leads to a qualitatively incorrect de-

scription of the $4f$ energy placement. A related problem is that the structural properties, due to wrongly estimated localization of the $4f$ states, are often described improperly. There are a number of approaches to minimize or overcome these limitations. Some works include a Hubbard U parameter in order to consider the Coulomb repulsion between the highly localized $4f$ electrons [68]. Traditionally, the parameters in such a model are treated as adjustable parameters and deduced from experiment. Recently, it has become very popular to calculate these parameters using the ab initio density-functional (DFT) formalism in the LSDA [15, 264].
In the present chapter, we report the results of a systematic study by means of the full-potential linearized augmented planewave (FLAPW) method of newly synthesized non-oxide antiperovskites $R\mathrm{Rh_3C}$ (R=rare earth: La-Gd) and discuss the trends in their structural, electronic and magnetic properties depending on the rare earth cations.

7.2 Materials and structure

7.2.1 Perovskite structure

The structural family of perovskites is a large family of compounds having crystal structures related to the mineral perovskite $\mathrm{CaTiO_3}$. In the ideal form the crystal structure of cubic $\mathrm{ABX_3}$ perovskite can be described as consisting of corner sharing $[\mathrm{BX_6}]$ octahedra with the A cation occupying the 12-fold coordination site formed in the middle of the cube of eight such octahedra (see figure 7.1). The ideal cubic perovskite structure is not very common and also the mineral perovskite itself is slightly distorted.
The perovskite family of oxides is probably the best studied family of oxides. The interest in compounds belonging to this family of crystal structures arise in the large and ever surprising variety of properties exhibited and the flexibility to accommodate almost all of the elements in the periodic system. Pioneering structural work on perovskites were conducted by Goldschmidt et al [192]. that formed the basis for further exploration of the perovskite family of compounds. Distorted perovskites have reduced symmetry, which is important for their magnetic and electric properties. Due to these properties, perovskites have great industrial importance.
If the large oxide ion is combined with a metal ion having a small radius, the resulting crystal structure can be looked upon as close packed oxygen ions with metal ions in the interstitials. This is observed for many compounds with oxygen ions and transition metals of valence +2, e.g. NiO, CoO, and MnO. In these crystal structures the oxygen ions form

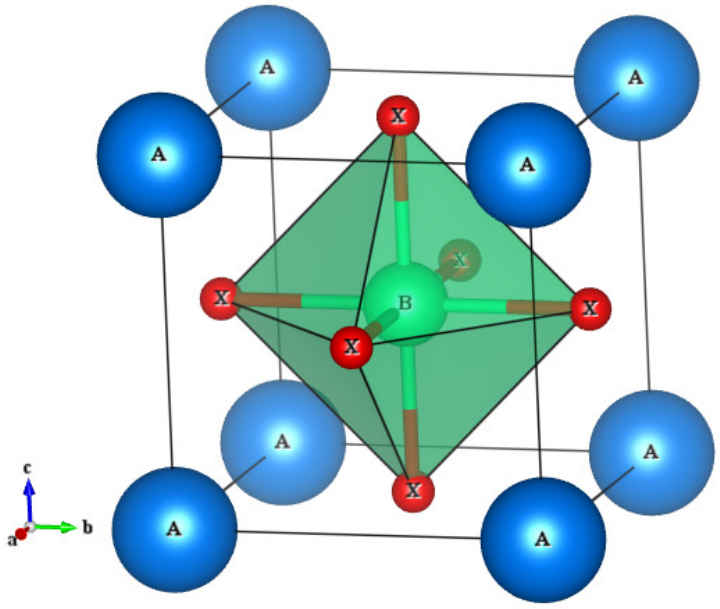

Figure 7.1: - Crystal structure of Perovskite ABX$_3$.

a cubic close packed lattice (ccp) with the metal ion in octahedral interstitials (i.e. the rock salt structure). Replacing one fourth of the oxygen with a cation of approximately the same radius as oxygen (e.g. alkali, alkali earth or rare earth element) reduces the number of octahedral voids, occupied by a small cation, to one fourth. The chemical formula can be written as ABX$_3$ and the crystal structure is called perovskite. X is often oxygen but also other large ions such as F^-, Cl^- and N^{-2} or any light elements are possible. On the other hand, the change of positions between the transition metal and the light element is possible and leads to another interesting properties. Accordingly, this composition was named Antiperovskite.

7.2.2 Antiperovskite structure

The choice of the non-oxide antiperovskites RRh$_3$C (R=rare earth: La-Gd) as materials of this investigation is due to the presence of the rare earth and transition metal elements together in this compounds.
RRh$_3$C crystallizes in the cubic antiperovskite structure with the space-group symmetry Pm-3m where the atomic positions are: R at (0,0,0), C at (0.5,0.5,0.5), and Rh at (0.5,0.5,0), (0.5,0,0.5), and (0, 0.5, 0.5) [figure 7.2].
In this structure, there are six Rh atoms at the face-centered positions of each unit cell forming a three-dimensional network of Rh$_6$ octahedron similar to oxygen octahedron in

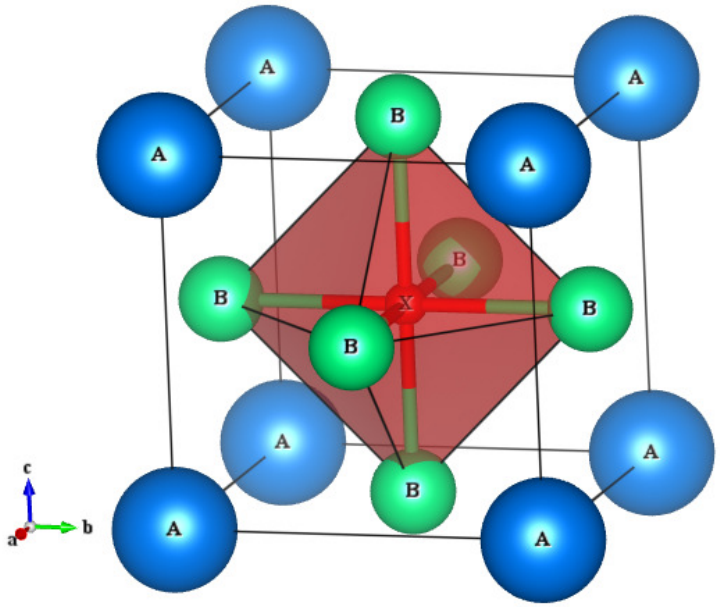

Figure 7.2: **Crystal structure of Antiperovskite AB_3X** - The positions of the ions in the unit cell are: A (000), X $(\frac{1}{2}\frac{1}{2}\frac{1}{2})$ and B at $(0\frac{1}{2}\frac{1}{2})$, $(\frac{1}{2}0\frac{1}{2})$, and $(\frac{1}{2}\frac{1}{2}0)$ respectively.

$CaTiO_3$. Each C atom is located in the body-centered cubic position surrounded by the Rh_6-octahedron cage. This is usually referred to as the cubic antiperovskite structure due to Rh atoms occupying anion positions in the $CaTiO_3$ perovskite structure [265]. In order to obtain the structural properties of $R\mathrm{Rh}_3\mathrm{C}$.

7.2.3 Antiperovskites magnetic structure

We have studied the magnetic properties in nonoxide antiperovskites $R\mathrm{Rh}_3\mathrm{C}$. It is well known that the rare earth ions present a partially filled f shell which provide a local magnetic moments. The spin ordering in this elements is in different directions.
Figure 7.3 show the different magnetic ordering; Ferromagnetic (FM) when all spin direct toward c direction (chosen as direction of magnetization), antiferromagnetic in the ab plane stacked ferromagnetically in the c direction (AFM-C), antiferromagnetic in three directions (AFM-G) , and ferromagnetic ab planes stacked antiferromagnetically along the c axis (AFM-A).

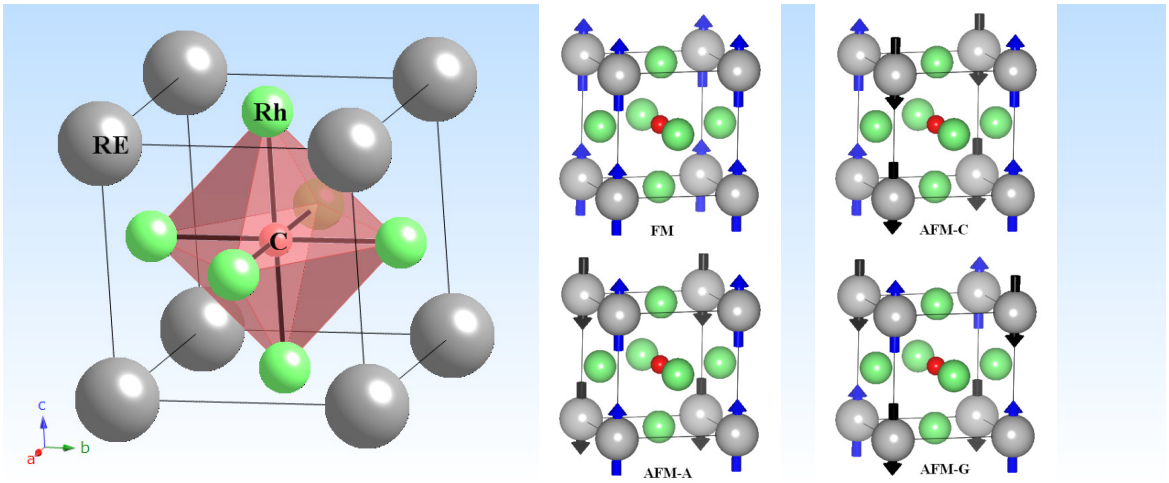

Figure 7.3: **Crystal structure and the magnetic states of RRh$_3$C compounds** - FM: Ferromagnetic, AFM: Antiferromagnetic.

7.3 Methods and functionals

7.3.1 Computational details

The calculations have been performed within DFT implemented in the WIEN2K code [137]. Atoms were represented by the hybrid full-potential (linear) augmented plane-wave plus local orbitals (L/APW+lo) method [138]. In this method wave functions, charge density, and potential are expanded in spherical harmonics within non-overlapping muffin-tin (MT) spheres, and plane waves are used in the remaining interstitial region of the unit cell. In the code, the core and valence states are treated differently. Core states are treated within a multiconfiguration relativistic Dirac-Fock approach, while valence states are treated in a scalar relativistic approach. The exchange-correlation energy, E$_{xc}$, was calculated using the Perdew-Wang LSDA [139] and the LSDA+U [68].
Very carefully, step analysis is done to ensure convergence of the total energy in terms of the variational cutoff-energy parameter. At the same time, we have used an appropriate set of k-points to compute the total energy.
We compute equilibrium lattice constants and bulk moduli by fitting the total energy versus volume to the Murnaghan equation [140].
The standard built-in basis functions were applied with the valence configurations of (R: $5s^25p^66s^25d^14f^n, 0 \leq n \leq 7$), (Rh: $4p^64d^85s^2$), and (C: $2s^22p^2$). The total energy was minimized using a set of 63 k-points in the irreducible sector of Brillouin zone, equivalent to an 11×11×11 Monkhorst- Pack [20] grid in the unit cell, and the value of 8 Ry for the

cutoff energy were used.
The magnetic ordering is studied using 2×2×2 supercells to model the antiferromagnetic (AFM) configurations. The self-consistent calculations (SCF) are considered to be converged only when the calculated total energy of the crystal converged to less than 1 mRy. We have adopted the values of 2.75 bohr for rare-earth elements, 2.25 bohr for rhodium and 1.6 bohr for carbon, as MT radii.
We consider cubic crystal structure. The crystal-structure investigation shows that it belongs to a simple cubic with space group Pm-3m. R and Rh atoms form an ordered-Cu_3Au type and the carbon atom is located at the body-centered position (as shown in figure 7.2).

7.3.2 LDA+U

We used the LSDA [139] to describe exchange and correlation potential. Since it is well known that such calculations cannot describe the strong onsite correlation between the $4f$ electrons, we added an effective Coulomb interaction $U_{eff} = U - J$. The LSDA+U method essentially consists of identifying a set of atomic-like orbitals that are treated in a non-LSDA manner (with the standard double counting correction [68]). Based on the lessons from Hubbard model studies, these orbitals are treated with an orbital-dependent potential with associated onsite Coulomb and exchange interactions, U and J.
The standard Hubbard Hamiltonian [259] is of the form

$$H = -t \sum_{\langle ij \rangle, \sigma} C^{\dagger}_{i\sigma} C_{j\sigma} + U \sum n_{i\uparrow} n_{i\downarrow}, \tag{7.1}$$

where $C^{\dagger}_{i\sigma} C_{j\sigma}$ and $C^{\dagger}_{i\sigma}(C_{j\sigma})$ creates (annihilates) an electron on site i with spin $\sigma =\uparrow$ or $\downarrow$. A nearest neighbor is denoted by $\langle i, j \rangle$.
The meaning of the U parameter was discussed by Anisimov and Gunnarsson [266], who defined it as the cost in Coulomb energy by placing two electrons on the same site.
In an atom, the U corresponds to F_0 of the unscreened Slater integrals [264]. Due to screening, the effective U in solids is much smaller than F_0 for atoms. U_{eff} can be estimated by constraint DFT calculations, where some of the valence electrons are selectively treated as core electrons to switch off any hybridization with other electrons [264]. One can artificially simulate the addition and removal of electrons to the atomic shell and observe the change in the calculated total energy in order to estimate U_{eff} (see figure 7.4). We constructed a supercell and proposed the hopping integrals connecting

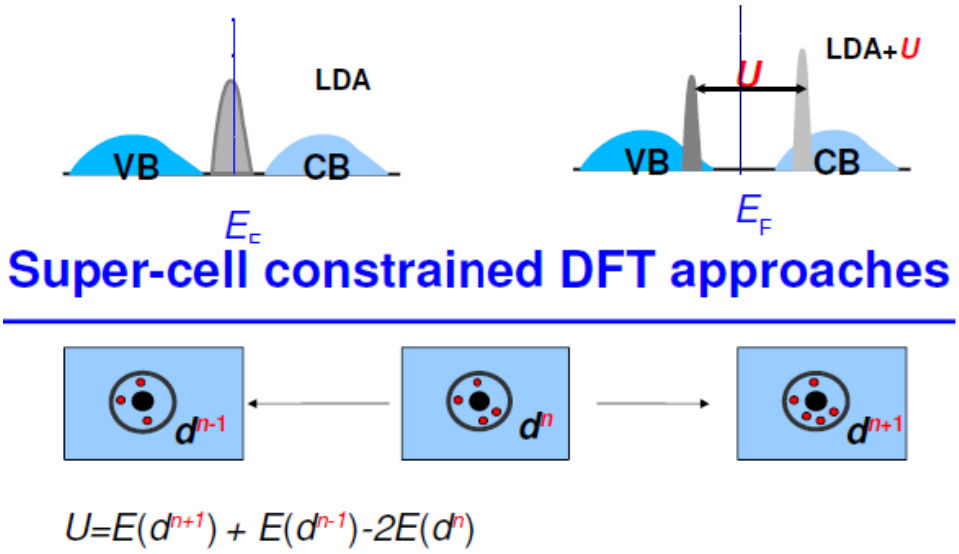

Figure 7.4: **DFT picture of U** - Anisimov and Gunnarsson [266].

the $4f$ orbital of one atom. The number of electrons in this nonhybridizing f-shell was varied and F^0_{eff} was then calculated from

$$\begin{aligned} F^0_{eff} &= \varepsilon_{4f\uparrow}\left(\frac{n+1}{2},\frac{n}{2}\right) - \varepsilon_{4f\uparrow}\left(\frac{n+1}{2},\frac{n}{2}-1\right) \\ &\quad -\varepsilon_F\left(\frac{n+1}{2},\frac{n}{2}\right) - \varepsilon_F\left(\frac{n+1}{2},\frac{n}{2}-1\right), \end{aligned} \tag{7.2}$$

where $\varepsilon_{4f\uparrow}$ stands for the $4f$ spin-up eigenvalue of the rare earth atom. The original LSDA+U method [15] was based on the LMTO basis set, where the individual orbital and hopping terms can be identified, this is not possible within the LAPW method. So, the method of Anisimov and Gunnarsson cannot be directly applied. Instead, the hybridization can be removed by putting the f states into the core or by performing a two-window calculation [15, 264] and U was then calculated from $U - J = F^0_{eff}$, where J can be calculated from the atomic values to a good approximation.

7.4 Results and discussion

7.4.1 Magnetic stability and structural properties

In order to study the magnetic stability, we compare the total energy of RRh$_3$C in different magnetic phases relative to the paramagnetic (PM) state. We have considered three kinds of AFM configurations: AFM-A, AFM-C, and AFM-G in 40 atoms/unit cell (see Figure 7.3). We restrict to the ferromagnetic (FM) and AFM-A, C, and G orderings (i.e., we neglect possible next-nearest-neighbors AFM coupling). We report total energy of AFM phases with respect to the FM phase in Figure 7.5. Moreover, from Fig. 7.5, we found that FM configuration is more stable than the three AFM phases for RRh$_3$C (R=Nd, Sm, Eu, and Gd) compounds,while PmRh$_3$C compound adopts the AFM-C configuration. Also, calculation shows that RRh$_3$C (R=La, Ce, and Pr) are nonmagnetic materials (NMs), which are consistent with experimental data [12]. For the other rare-earth inverse perovskites (R=Nd, Pm, Sm, and Eu) our results are predictions. As the first step, total energy (E_{tot}) versus cell volume calculations were carried out to determine the equilibrium structural parameters – lattice constants a, bulk moduli B, and cell volumes V. The results are listed in Table 7.1. It can be seen that our LSDA calculations reproduce the experimental data to within at least 2.6% (LaRh$_3$C), 1.76% (CeRh$_3$C), 2.97% (PrRh$_3$C), and 1.89% (GdRh$_3$C). In order to see if the effective correlation potential on R-f electrons can improve the discrepancies with experiments, we have checked the validity of LSDA+U treatment, where the Hubbard U parameters were calculated and presented in Table 7.1. It is well known that LSDA underestimates the equilibrium lattice constants by 1.76–2.97%, while LSDA+U often corrects the LSDA by predicting values 0.73–2.60% smaller than experiments.
LSDA+U is more accurate than LSDA, this implies that one should expect a perfect agreement between the experimental lattice parameters and the computed LSDA+U values. Bulk moduli of RRh$_3$C were also calculated but there is no ab initio or experimental data to compare with.

7.4.2 Electronic properties

For each magnetic state, the band structures and density of state (DOS) presented are similar, as shown in Figure 7.6a and 7.6b, so all further discussion on bonding will be

Table 7.1: The calculated equilibrium lattice parameters a (Å), the bulk modulus B (GPa), and Hubbard U parameter (eV) of the RRh$_3$C (R=La, Ce, Pr, Nd, Pm, Sm, Eu, and Gd) Antiperovskites according to FLAPW-LSDA and (LSDA+U) calculations in comparison to the data for already synthesized compounds [12] [each compound presented in his magnetic ground state (MGS)].

RERh$_3$C		MGS	E$_{XC}$	a(Å)	B(GPa)
LaRh$_3$C	this work	NM	LSDA	4.183	223.25
			LSDA+U, U_d=0.136 eV	4.194	226.96
	exp [12]			4.22	-
	theory [263]			4.27	-
CeRh$_3$C	this work	NM	LSDA	4.121	236.35
			LSDA+U, U_f=2.811 eV	4.137	237.89
	exp [12]			4.146	-
PrRh$_3$C	this work	NM	LSDA	4.150	243.82
			LSDA+U, U_f=2.332 eV	4.145	244.70
	exp [12]			4.187	-
NdRh$_3$C	this work	FM	LSDA	4.148	231.93
			LSDA+U, U_f=2.403 eV	4.150	234.56
PmRh$_3$C	this work	AFM-C	LSDA	4.143	232.62
			LSDA+U, U_f=3.015 eV	4.145	228.04
SmRh$_3$C	this work	FM	LSDA	4.141	239.55
			LSDA+U, U_f=3.083 eV	4.136	222.10
EuRh$_3$C	this work	FM	LSDA	4.136	225.63
			LSDA+U, U_f=3.898 eV	4.137	218.83
GdRh$_3$C	this work	FM	LSDA	4.122	243.90
			LSDA+U, U_f=4.154 eV	4.125	240.79
	exp [12]			4.148	-

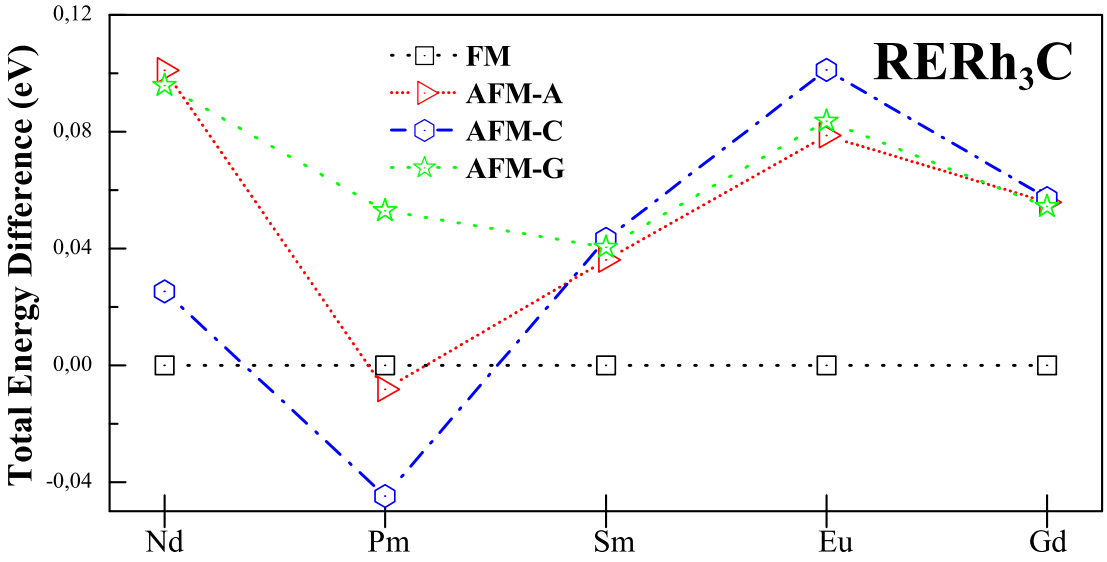

Figure 7.5: **Magnetic stability** - Total energy of AFM-A, -C, and -G phases with respect to the FM phase.

done with only one compound as a demonstrator, and we have studied the chemical bonding in more detail.

7.4.2.1 Electronic properties of Nonmagnetic structure

Figures 7.7a, 7.7b and 7.7c show the total density of states (TDOS) and partial (PDOS) of $CeRh_3C$ compound without spin polarization in the PM ordering from -15 to 10 eV and the corresponding band structures are shown in Figure 7.7 using LSDA, LSD+U, and LSDA+U+SO approach. This phase provides a useful reference for understanding the spin polarized electronic structures. A sharp peak at -12.5 eV corresponding to the C 2s states is clearly visible. It should be noted that the broad band between -8.2 and -0.5 eV is mainly composed of Rh 4d and C 2p states, but also has Ce (6s, 5d, and 4f), and Rh (4p, 5s) states, which indicate the occurrence of a strong hybridization effect in C 2p-Rh 4d states.

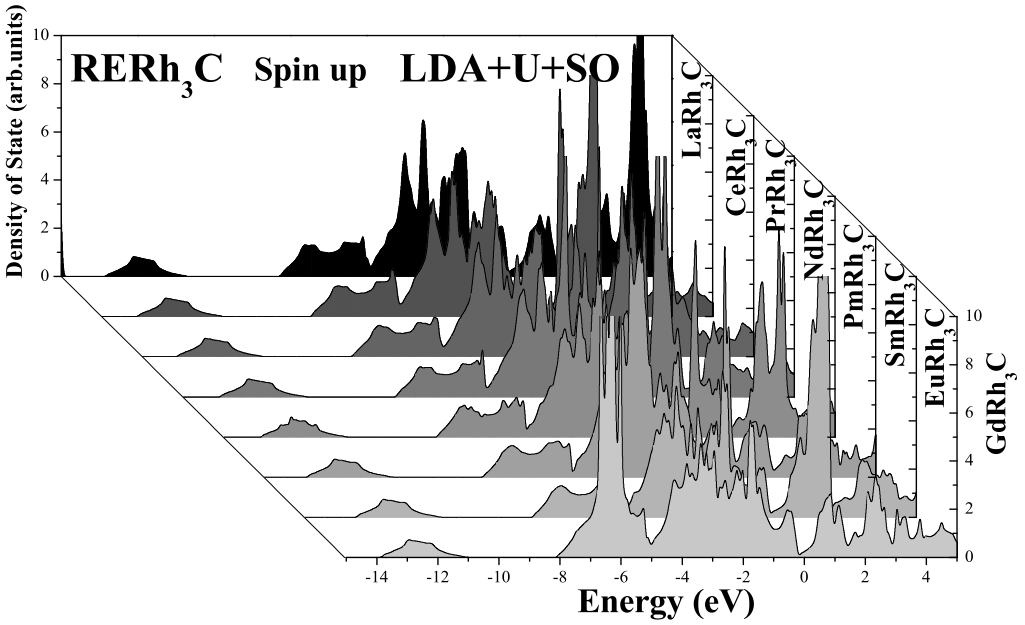

(a)

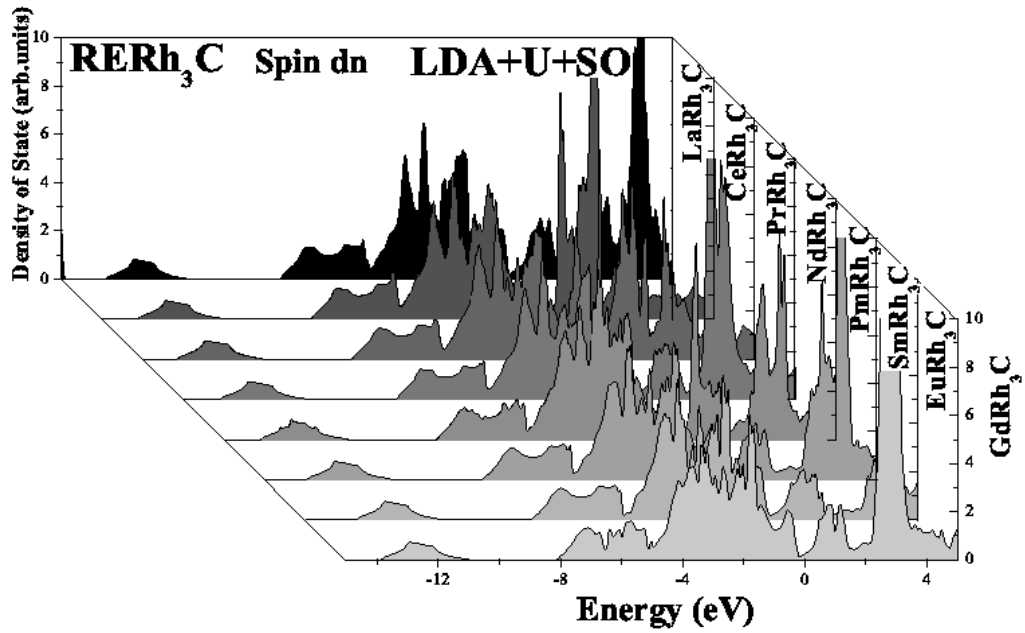

(b)

Figure 7.6: Calculated projected total DOS plots for RRh$_3$C compounds: **(a)** TDOS-up, **(b)** TDOS-down.

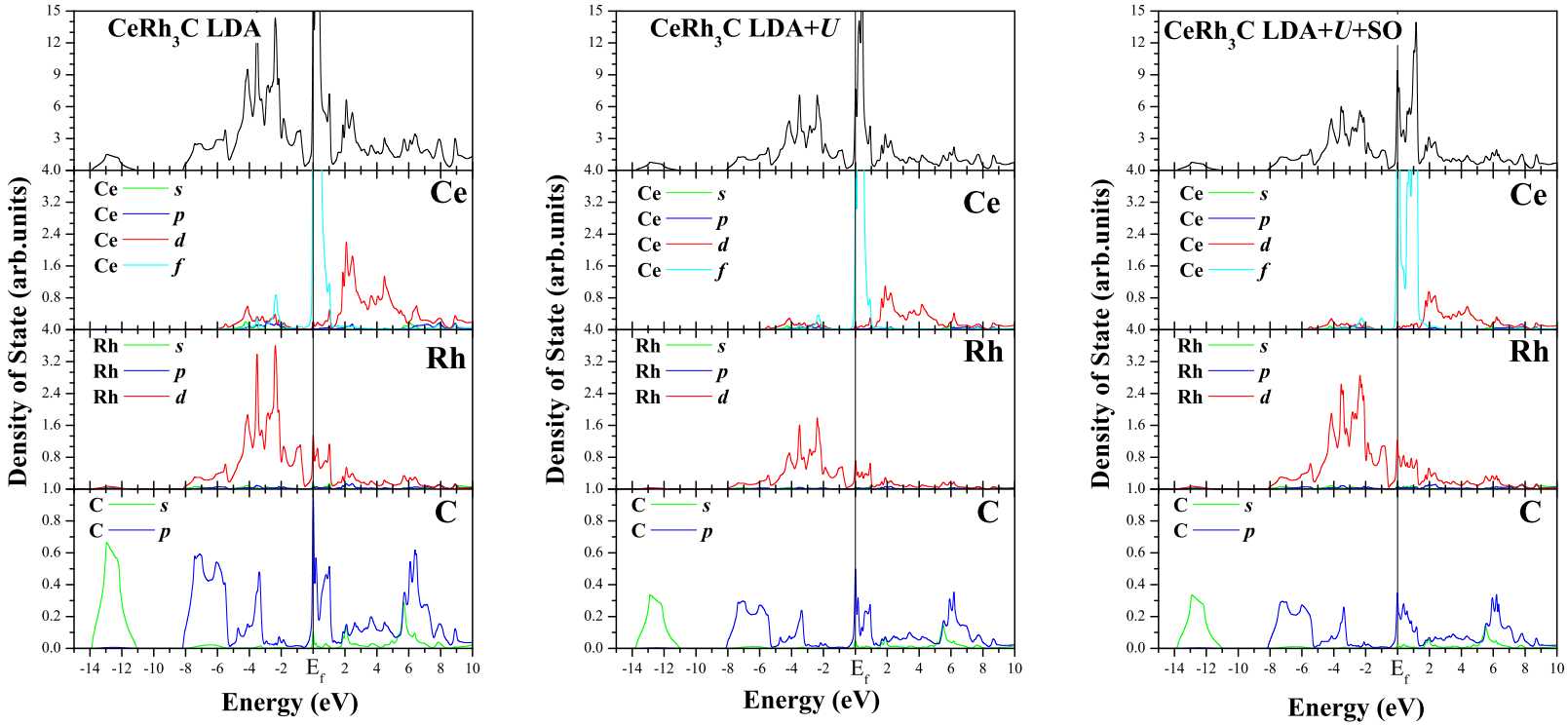

(a) (b) (c)

Figure 7.7: Calculated projected total and partial DOS plots for nonmagnetic $CeRh_3C$ using: **(a)** LSDA, **(b)** LSDA+U, and **(c)** LSDA+U+SO approach.

Hybridization between Rh 4d and the Carbon surrounding is well known to lead to superexchange interactions in magnetic perovskites.
The DOS of Rh 4d states at the Fermi level is high. At the Fermi energy, Ce 4f states dominate with a small contribution of Rh 4d and C 2p states. From 2.5 eV, there is a mixture of all states. From LSDA+U, the 4f bands are lightly modified. We also calculated the fully relativistic DOS and band structures to see the spin-orbit coupling effects, which are shown in the vicinity of the Fermi level (Fig. 7.8b). As expected SOC splits the 4f states into two manifolds. In the case of LaRh$_3$C (Fig. 7.8a) and PrRh$_3$C (Fig. 7.8c) compounds, the same features are observed with a few changes in detail. In all cases, the electronic structure is found to be metallic.

7.4.2.2 Electronic properties of Ferromagnetic structure

In this part, we present the electronic properties of EuRh$_3$C using both LSDA and LSDA+U approach by taking into account the spin-orbit coupling in the FM phase. Figures 7.9 **[a-c]** shows the TDOS and PDOS of EuRh$_3$C in the FM structure.
Majority and minority spins are shown above and below the axes. For the FM ordering, the electronic structure is found to be metallic with the near-Fermi-level DOS determined by the Eu 4f, Rh 4d, and C 2p states.

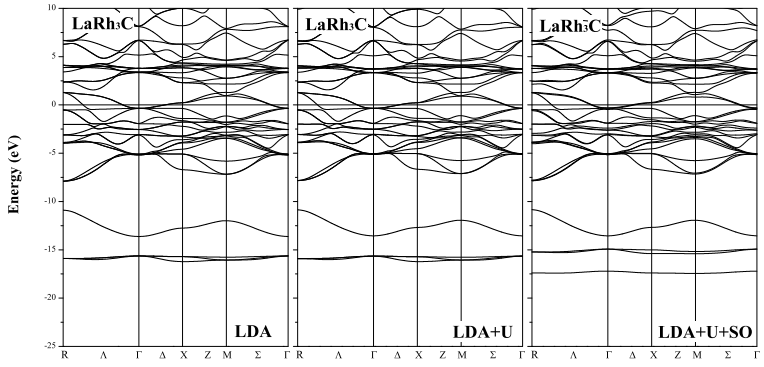

(a) $LaRh_3C$

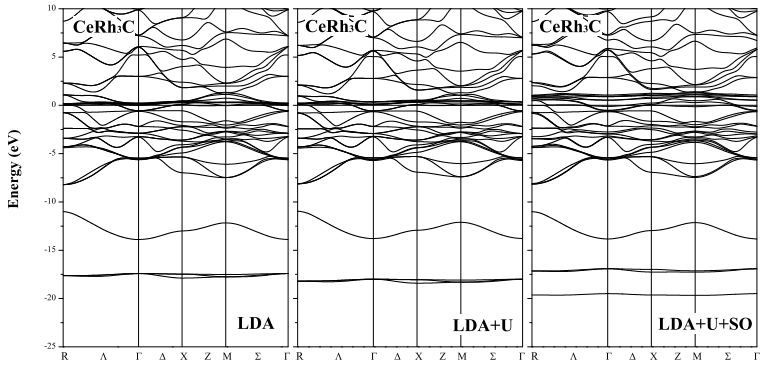

(b) $CeRh_3C$

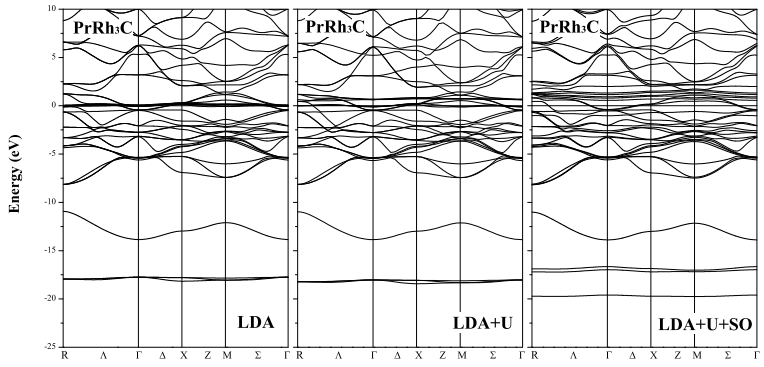

(c) $PrRh_3C$

Figure 7.8: FPLAPW-calculated band structure of nonmagnetic compounds along several high-symmetry axes using LSDA and LSDA+U approach by taking account of the spin-orbit coupling. The Fermi level is at zero energy.

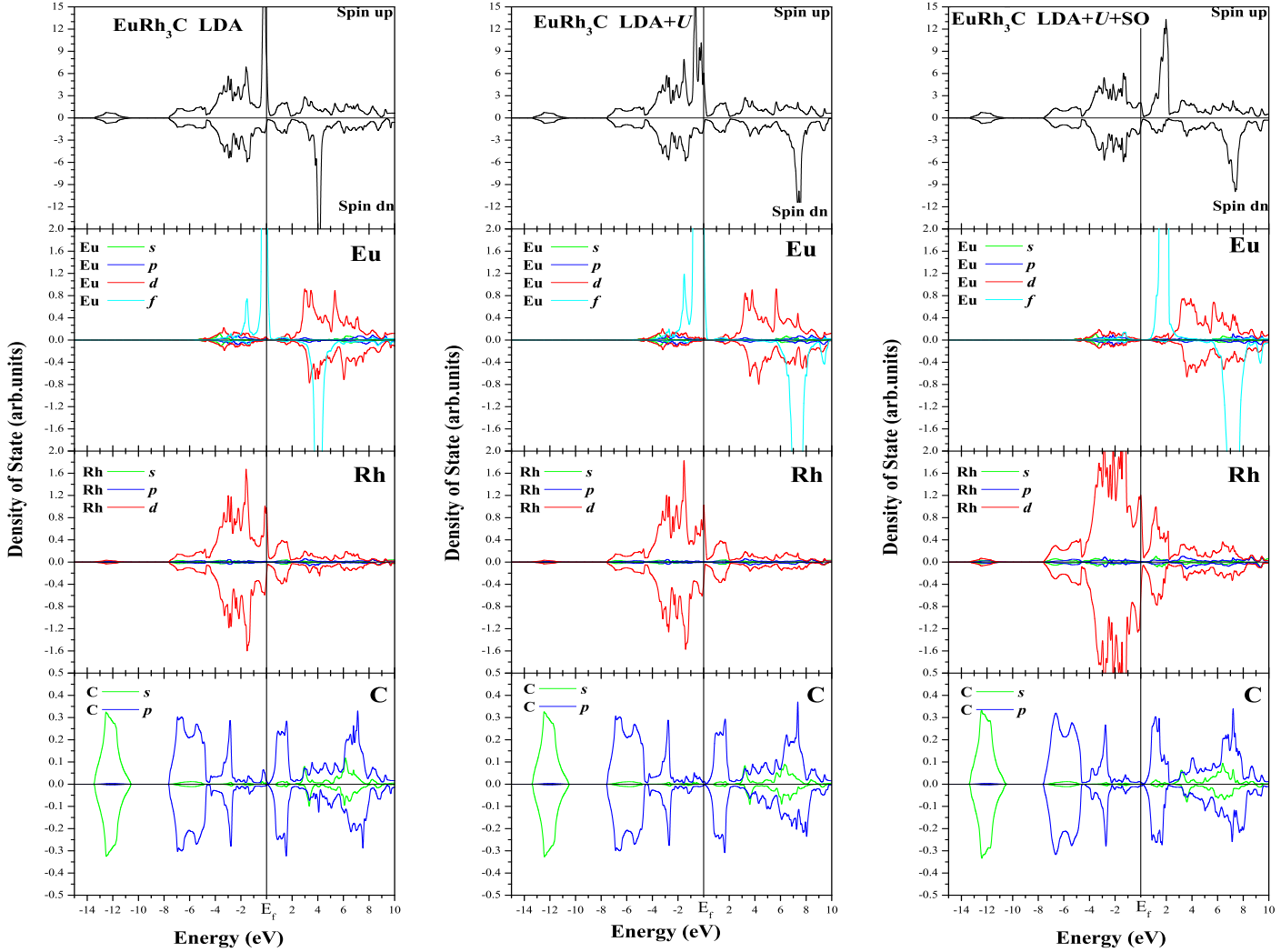

(a) (b) (c)

Figure 7.9: Calculated projected total and partial DOS plots for Ferromagnetic EuRh$_3$C using: **(a)** LSDA, **(b)** LSDA+U, and **(c)** LSDA+U+SO approach.

When the Coulomb potential is added to the Eu $4f$ orbitals, the degeneracy between the different f orbitals is lifted and they are moved at lower and upper Hubbard bands (Fig. 7.10). When the spin-orbital coupling along the axis (001) of magnetization is taken into account, the $4f$ orbitals are moved and split in three manifolds at 2.0, 7.2, and 9.5 eV. One notes that the FM $R\mathrm{Rh_3C}$ (R=Nd (Fig. 7.11a), Sm (Fig. 7.11b) and Gd (Fig. 7.11c)) compounds exhibit the same trend.

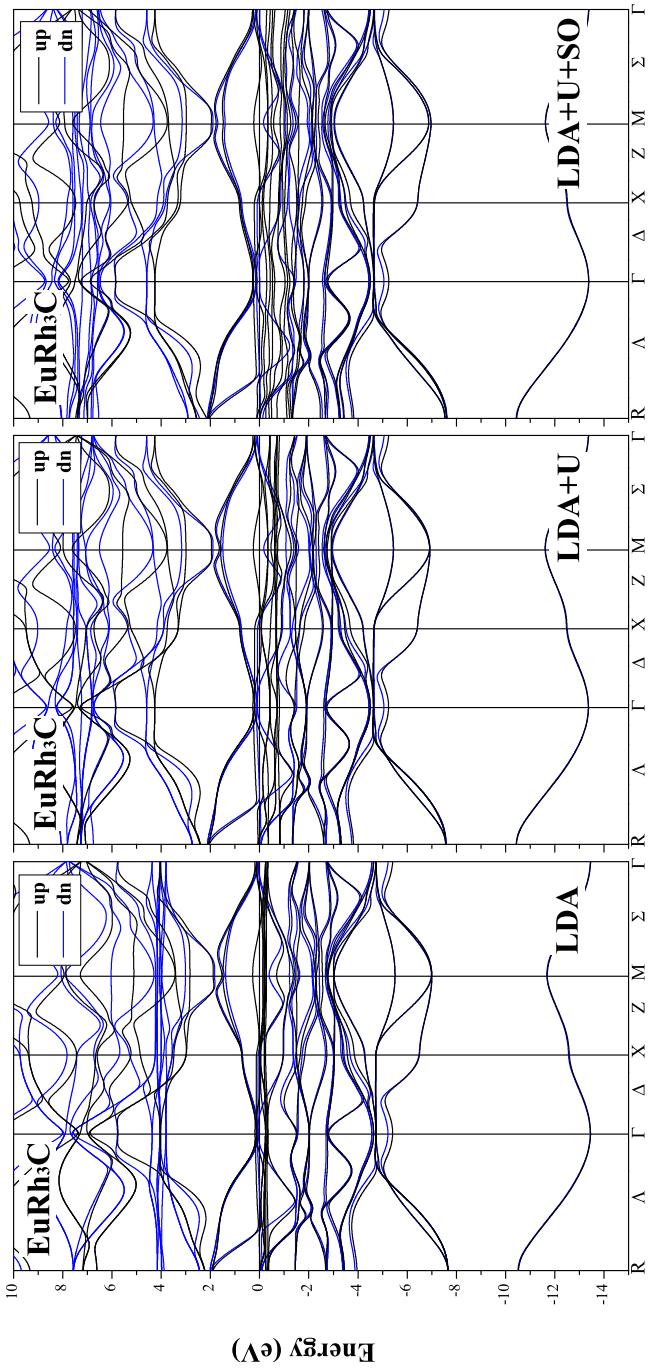

Figure 7.10: FPLAPW-calculated band structure of ferromagnetic compound $EuRh_3C$ along several high-symmetry axes using LSDA and LSDA+U approach by taking account of the spin-orbit coupling. The Fermi level is at zero energy.

7.4.2.3 Electronic properties of Antiferromagnetic structure

we discuss the specific features of the band structure of the $PmRh_3C$ in the C-AFM structure (Fig. 7.12) using the distributions of the total and partial DOS (Fig. 7.13 **a-c**) with both LSDA and LSDA+U approach by taking into account the spin-orbit coupling. Because only the DOS distribution near the Fermi level determines the magnetic properties, we concentrate our attention upon the DOS in the vicinity of this region. This range is dominated by Pm 4*f*, Rh 4*d*, and C 2*p* electrons. The Pm 4*f* orbitals are largely modified and are split into five manifolds for majority and minority spins at (-3.4, -2.8, and +1.8 eV) for Pm↑, and at (+1.7 and +3.5 eV) for Pm↓, by some combination of the crystal field and the anisotropy of the U interaction. Introducing electron correction potential changes dramatically the result of calculation in comparison with one-electron approximation. According to the partial DOS of Pm, Rh, and C, it is evident that the Rh and C states, as well as the Rh and Ce states, are hybridized. In our magnetic configurations, the effect of the SOC is very weak on the electronic structure of these materials contrary to the environment of the hexagonal structures.

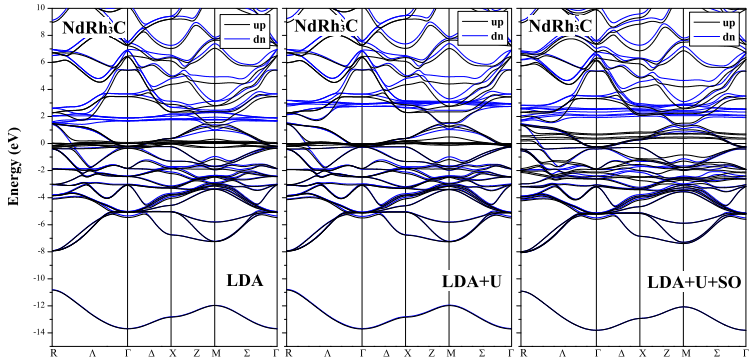

(a) NdRh$_3$C

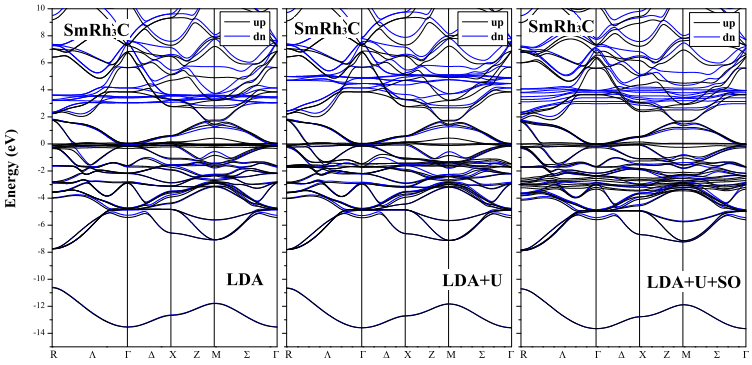

(b) SmRh$_3$C

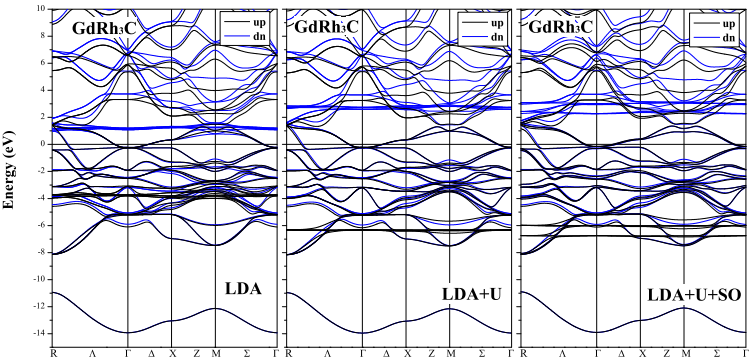

(c) GdRh$_3$C

Figure 7.11: FPLAPW-calculated band structure of Ferromagnetic compounds along several high-symmetry axes using LSDA and LSDA+U approach by taking account of the spin-orbit coupling. The Fermi level is at zero energy.

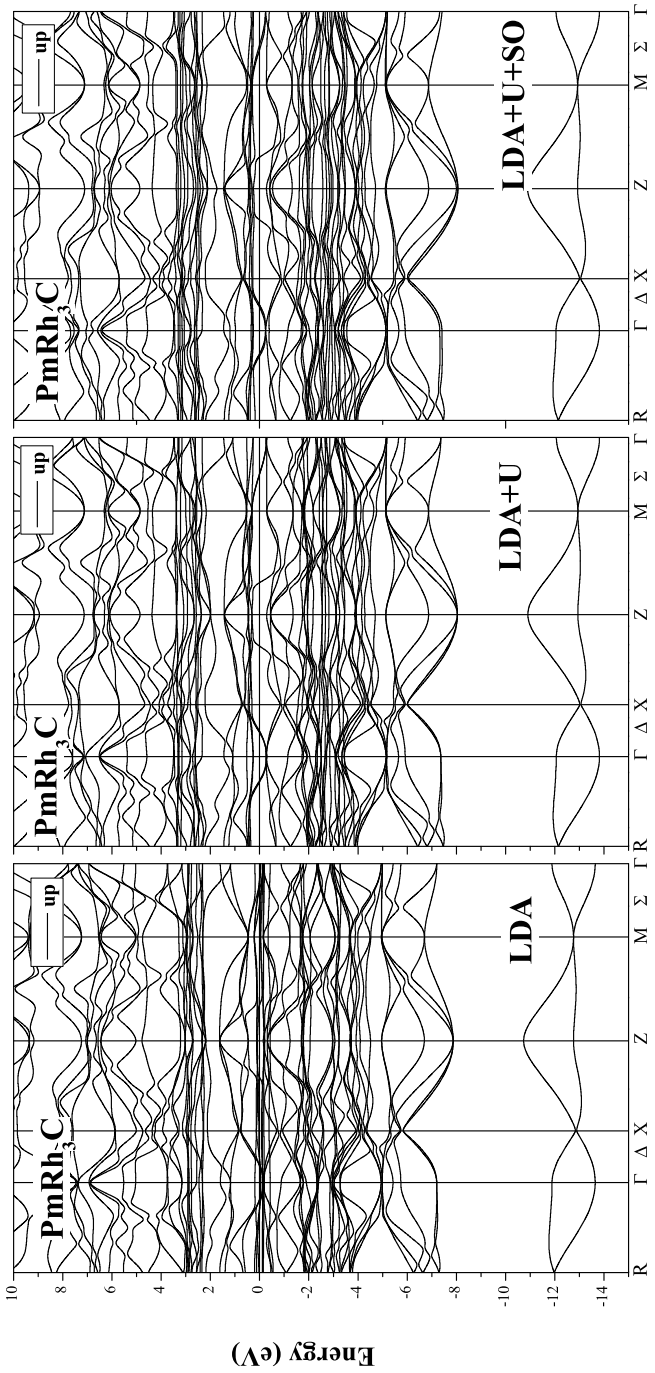

Figure 7.12: FPLAPW-calculated band structure of ferromagnetic compound $EuRh_3C$ along several high-symmetry axes using LSDA and LSDA+U approach by taking account of the spin-orbit coupling. The Fermi level is at zero energy.

7.4.2.4 Rh-C bonding in all compounds

In the past section 7.4.2, we have confirmed the contribution of the d orbital of Rh and p orbital of C in Fermi region, the relationship between this region and electronic properties of this compounds is very strong.
Accordingly, we have calculated the charge density of RRh$_3$C compounds, and we have taken in this section LaRh$_3$C compound as reference. We have presented the plane which takes into account Rh-C bonding.
Figure 7.14 shows the weak covalent bonding between Rh and C in Fermi region. We know that $t_{2g}(d_{xy}, d_{xz}, d_{yz})$ orbitals oriented toward the other Rh atoms and only d_{z^2} orbital which oriented toward C atom (see Fig. 7.14a and Fig. 7.14b). Consequently, this hybridization are created between the d_{z^2} of Rh atom and p_x, p_y of C atom (see Fig. 7.14c).

Figure 7.15 presents the total valence charge density which shows the different bonding between all atoms. There is a metallic bond between transition metal (Rh) and rare earth (La), while the bonding between Rh and C is a weak covalent as we have demonstrated later.
Finally, the d-orbital of Rh atom participates to the covalent bonding with C atom (1 electron) and the other electrons participate to metallic bonding with rare earth atoms. This particular result is not presented in the perovskites materials which make the properties of inverse perovskites (antiperovskites) different.

7.4.3 Magnetic moment

At ambient conditions the calculated magnetic moments per R atoms are shown through the spin density calculation (Figure 7.16), and listed in Table 7.2 using the different approach compared to the available experimental value (for GdRh$_3$C, 7.025 μ_B/Gd as compared to the experimental value of 7.9 μ_B/Gd at 3.5 K). It seems to be overestimated compared to the experimental value; however, extrapolation of the experimental value down to zero temperature would yield a magnetic moment close to the calculated one. A broad prediction of the calculated magnetic moment for materials remainder is shown in Table 7.2 and there is no experimental or theoretical value. We see that the magnetic moments increase along the series going from Nd to Gd. Thus, it is clear that the LSDA+U presents a better result.

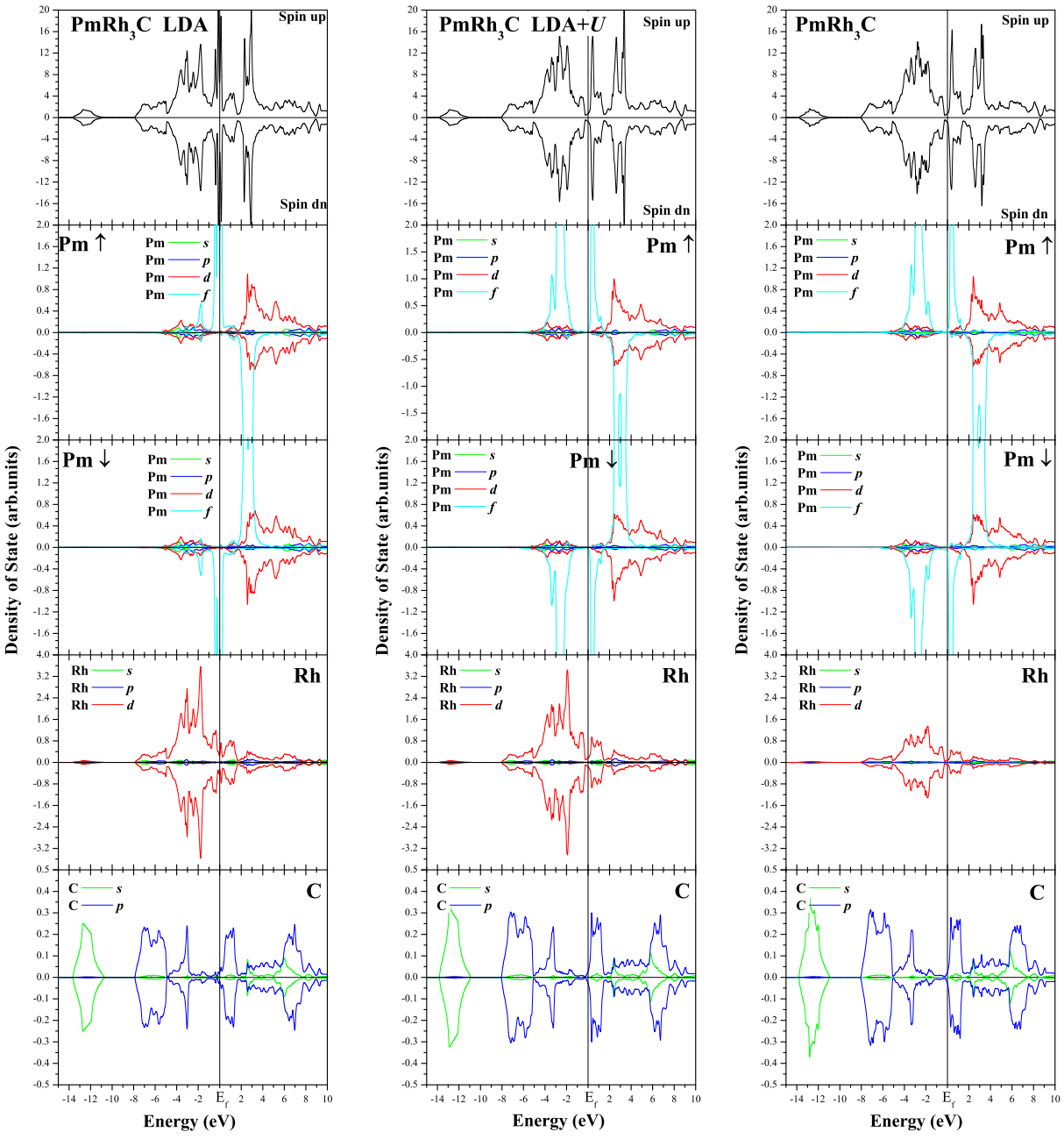

(a) (b) (c)

Figure 7.13: Calculated projected total and partial DOS plots for Ferromagnetic $EuRh_3C$ using: **(a)** LSDA, **(b)** LSDA+U, and **(c)** LSDA+U+SO approach.

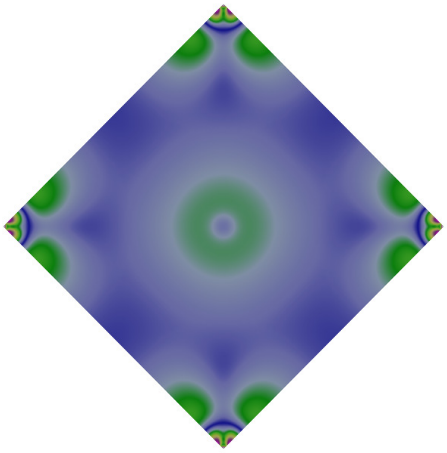

(a) C atom in center

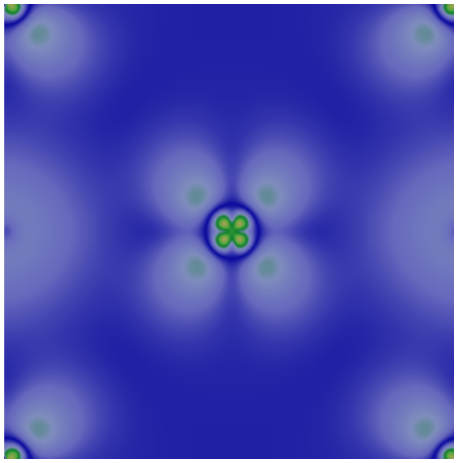

(b) Rh atom in center

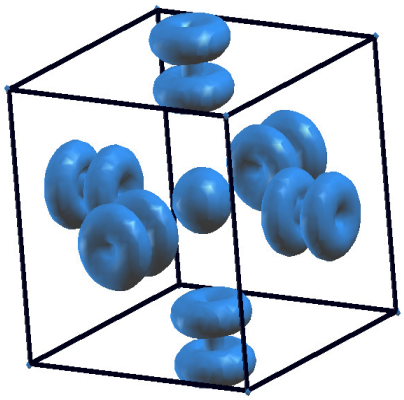

(c) 3D charge density

Figure 7.14: Valence charge density (VCD) around Fermi energy in LaRh$_3$C.

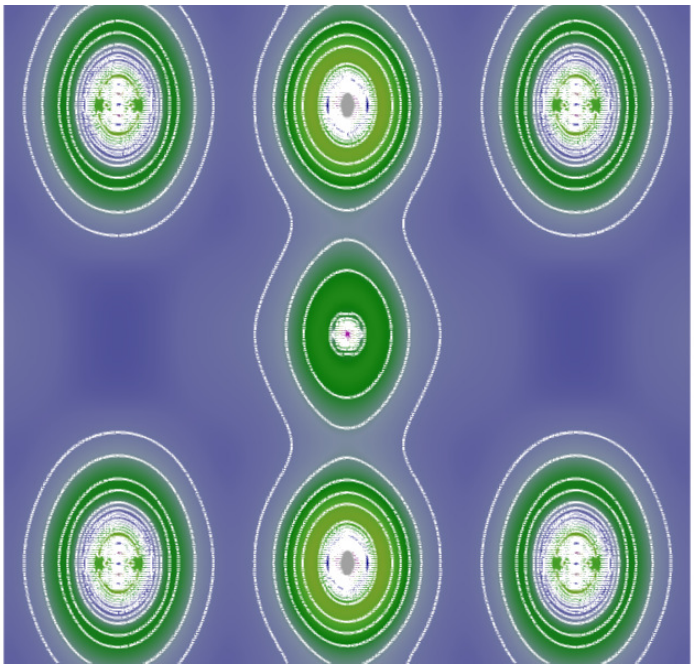

Figure 7.15: - Valence charge density in plane (110)

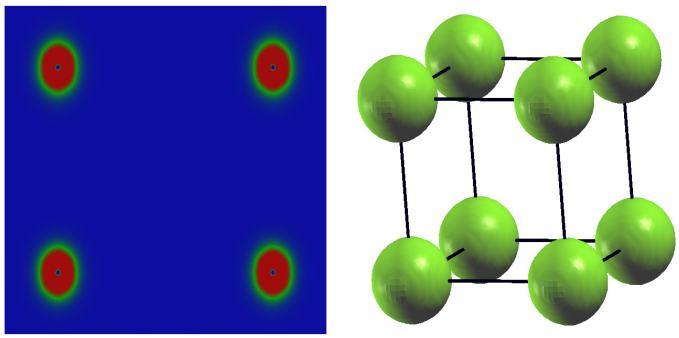

(a) 2D spin density (b) 3D spin density

Figure 7.16: Spin density calculation in $EuRh_3C$.

Table 7.2: The calculated magnetic moment of R atoms of the RRh$_3$C (R=Nd, Pm, Sm, Eu, and Gd) antiperovskite using LSDA and LSDA+U approach [each compound presented in his magnetic ground state (MGS)].

RERh$_3$C	×	MGS	E$_{XC}$	M(RE) [μ_B]
NdRh$_3$C	this work	FM	LSDA	3.058
			LSDA+U	3.114
			LSDA+U+SO	3.000
PmRh$_3$C	this work	AFM-C	LSDA	Pm$_\uparrow$:4.232/Pm$_\downarrow$:4.232
			LSDA+U	Pm$_\uparrow$:4.081/Pm$_\downarrow$:4.077
			LSDA+U+SO	Pm$_\uparrow$:4.073/Pm$_\downarrow$:4.065
SmRh$_3$C	this work	FM	LSDA	5.367
			LSDA+U	5.356
			LSDA+U+SO	5.201
EuRh$_3$C	this work	FM	LSDA	6.454
			LSDA+U	6.683
			LSDA+U+SO	6.654
GdRh$_3$C	this work	FM	LSDA	6.912
			LSDA+U	7.036
			LSDA+U+SO	7.025
	exp [12]			7.900

7.5 Conclusion

In this chapter, we have performed the first-principles DFT calculations for intermetallic antiperovskites (inverse perovskites) $R\mathrm{Rh_3C}$ (R= rare earth)compounds. The choice of nonoxide antiperovskites $R\mathrm{Rh_3C}$ (R=La-Gd) as materials of this investigation is due to the presence of the rare earth and transition metal elements together in this compounds. We have studied the magnetic properties in inverse perovskites $R\mathrm{Rh_3C}$. It is well known that the rare earth ions present a partially filled f shell which provides local magnetic moments. The spin ordering in these elements is in different directions (figure 7.3). In order to study the magnetic stability, we compared the total energy in different magnetic phases (FM, AFM-A, AFM-C and AFM-G) relative to PM state. Moreover, from figure 7.5, we have found that FM configuration is more stable than the three AFM phases for $R\mathrm{Rh_3C}$ (R=Nd, Sm, Eu and Gd) compounds, while $\mathrm{PmRh_3C}$ compound adopts the AFM-C configuration, this last result is maybe different due to instability of radioactive Pm element. However, calculation shows that $R\mathrm{Rh_3C}$ (R=La, Ce and Pr) are nonmagnetic materials (NMs), which are consistent with experimental data [12]. For the other rare earth inverse perovskites (R=Nd, Pm, Sm and Gd) our results are predictions. From the calculated band structures, densities of states and valence charge densities, the hybridization between $d - t_{2g}$ of Rh ion and $p - p_x, p_y$ of C atom creates a covalent bonding. Also, the d orbital (electron) of Rh creates the Rh-C bonding with C atom, and other electrons participate to metallic bonding with rare earth atoms. This particular result is absent in the conventional perovskites materials which make the properties of antiperovskites different.

The magnetic moment of these materials are created locally by partially filled f orbital of rare earth ions, this local magnetic moment of R atoms play an important role for the nature of the magnetism.

Chapter 8

Conclusions

The work in this thesis has focused on understanding the interrelations between the composition, structure and properties in complex perovskite related materials. These have been based on the parent compounds such as $SrTiO_3$, $LaCoO_3$, $BiCoO_3$, and inverse perovskites RRh_3C.

In this thesis, electronic and magnetic properties from selected solids in the framework of DFT were discussed.

In order to better describe correlation effects in strongly correlated systems such as compounds with transition metals ($3d$ electrons: $LaCoO_3$ and $BiCoO_3$) and lanthanides ($4f$ electrons: RRh_3C), we have used the famous LSDA+U method. In this thesis, the choice of U-Hubbard parameter has been done, based on two methods; In the first one, we have made a variation of U_{eff} depending on different properties such as structural and magnetic ground state, lattice parameters, band gap, and magnetic moments; this method was used in chapter 6. In the second one, we have calculated the U-parameter using constrained-LDA method [15]; this latter method was used in chapter 7.

In chapter 5, we have examined in detail the vacancy effect in $SrTiO_3$.

Nominally pure $SrTiO_3$ is an electronic insulator at room temperature. Incorporation of point defects into the lattice can generate free charge carriers or charged ionic species. The latter treatment introduces an approximately equivalent density of oxygen vacancies which are known to exhibit significantly large lattice mobility. $SrTiO_3$ is thus considered a mixed electronic-ionic conductor.

Removal of one oxygen from the lattice reduces two Ti^{4+} to Ti^{3+} and replaces two octahedra with two square-pyramids.

The similarity of t_{2g} orbitals (xy, xz, yz) in the defect wavefunction of all Ti atoms

of supercell confirms the existence of an ionic conductivity in the $SrTiO_{3x}$. However, the contribution of deep e_g $(3z^2 - r^2)$ in defect wavefunction confirms the electronic conductivity; this state has a lower energy than Ti $3d$-t_{2g} type conduction states. This is actually easy to understand, considering that the $3z^2 - r^2$ type orbital concentrates its charge density in a direction toward two of the nearest O atoms, while one of them (the one in the vacancy site) is missing.

In the second study, we have performed a detailed investigation on the structural and magnetic ground states of strongly correlated perovskites, $BiCoO_3$ and $LaCoO_3$ and their alloy $Bi_{1-x}La_xCoO_3$.

We have chosen to study the *lone-pair* dilution effect on the electronic and magnetic structures of $BiCoO_3$ by substituting La^{3+} for Bi^{3+}. Indeed both cations are isovalent, have compatible ionic radii and are nonmagnetic. At variance with Bi^{3+}, the La^{3+} cation does not possess an active electronic *lone pair*.

We have found that the structural stability of this alloy between tetragonal-AFM-C and rhombohedral-NM undergoes a strongly discontinuous transition between a Tetragonal-phase and a Rhombohedral-phase at $x \simeq 0.345$, this structural transition is associated with a spin state transition from HS magnetic state to LS nonmagnetic state.

We can conclude from our study of $Bi_{1-x}La_xCoO_3$ alloy in tetragonal-AFM-C structure, that the change in different effects (Jahn-Teller, Crystal-Field, and *lone pair*) induces a structural transition from tetragonal to rhombohedral structures, as well as magnetic transition from HS antiferromagnetic to LS nonmagnetic states.

However, the Bi-atom substitution in rhombohedric LCO creates a new bond between Bi s-orbital and O p_z-orbital near the top of valence band, this hybridization may causes a *lone pair* effect which can displace Co ion and induce J-T effect, and we expect that the incorporation of Bi atom in rhombohedric $LaCoO_3$ may induce a structural transition from $R\bar{3}c$ centrosymmetric symmetry to $R3c$ noncentrosymmetric symmetry, which can show the ferroelectricity in this system.

In chapter 7, we have performed the first-principles DFT calculations for intermetallic antiperovskites (inverse perovskites) $R\mathrm{Rh_3C}$ (R = rare earth) compounds. The choice of nonoxide antiperovskites $R\mathrm{Rh_3C}$ (R = La-Gd) as materials of this investigation is due to the presence of the rare earth and transition metal elements together in this compounds. We have found that FM configuration is more stable than the three AFM phases for $R\mathrm{Rh_3C}$ (R = Nd, Sm, Eu and Gd) compounds, while $\mathrm{PmRh_3C}$ compound adopts the AFM-C configuration, this last result is maybe differents due to instability of radioactive Pm element. However, the calculation shows that $R\mathrm{Rh_3C}$ (R = La, Ce and Pr) are nonmagnetic materials (NMs), which are consistent with experimental data. For the other

rare earth inverse perovskites (R = Nd, Pm, Sm and Gd) our results are predictions. From the calculated band structures, densities of states and valence charge densities, the hybridization between $d - t_{2g}$ of Rh ion and $p - p_x$, p_y of C atom creates a covalent bonding. Also, the d orbital (electron) of Rh creates the Rh-C bonding with C atom, and other electrons participate to metallic bonding with rare earth atoms. This particular result is absent in the conventional perovskites materials which make the properties of antiperovskites different.

To conclude, the work in this thesis hopefully emphasizes the need for more systematic studies of fundamental properties in complex oxides. These types of investigations are essential to understand the effects that can be manifest in perovskite related materials, and we can summarize an important competition between principles effects: crystal field effect, Jahn-Teller effect, Hund effect and *lone pair* effect.

Bibliography

[1] D. I. Woodward. *The Crystal Chemistry of Bismuth-Based Perovskite Solid Solutions*. Engineering Materials. Sheffield, The University of Sheffield, (2004).

[2] C. J. Howard and H. T. Stokes. *Acta Crystallographica*, **B54**:782, (1998).

[3] W. Eerenstein, N. D. Mathur, and J. F. Scott. *Nature*, **442**:759, (2006).

[4] A. A. Belik, S. Iikubo, K. Kodama, N. Igawa, S. I. Shamoto, S. Niitaka, M. Azuma, Y. Shimakawa, M. Takano, F. Izumi, and E. Takayama-Muromachi. *Chem. Mater.*, **18**:798, (2006).

[5] P. Ravindran, R. Vidya, O. Eriksson, and H. Fjellvag. *Adv. Mater.*, **20**:1353, (2008).

[6] Per Hjalmarsson. *Strontium and nickel substituted lanthanum cobaltite as cathode in Solid Oxide Fuel Cells*. PhD thesis, Technical University of Denmark, (2008).

[7] Z. Ropka and R. J. Radwanski. *arXiv:cond-mat/0012228*, [**cond-mat.str-el**], (2000).

[8] C. J. Bradley and A. P. Cracknell. *Mathematical theory of symmetry in solids: Representation theory for point groups and spaces groups*. Clarendon press, Oxford, (1972).

[9] A. M. Glazer. *Acta Crystallographica*, **B28**:3384, (1972).

[10] A. M. Glazer. *Acta Crystallographica*, **A31**:756, (1975).

[11] J. Knudsen. *Structure-Property Relations ar the Antiferroelectric/Ferroelectric Phase Boundary in Undoped and La Doped Pb(Zr,Ti)O_3*. Engineering Materials. Sheffield, The University of Sheffield, (2002).

[12] D. A. Joshi, N. Kumar, A. Thamizhavel, and S. K. Dhar. *Phys. Rev. B*, **80**:224404, (2009).

[13] P. Hohenberg W. Kohn. *Phys. Rev.*, **136**:B864, (1964).

[14] W. Kohn L. Sham. *Phys. Rev.*, **140**:A1133, (1965).

[15] G. K. H. Madsen and P. Novàk. *Europhys. Lett.*, **69**:777, (2005).

[16] S. A. Zumdahl and S. S. Zumdahl. Chemistry, brookes cole edition, (2006).

[17] C. Hammond. *Introduction to Crystallography*. Oxford university press edition, (1992).

[18] R. Tilley. *Crystals and Crystal Structures*. John wiley sons, ltd. edition, (2006).

[19] P. J. Brown and J. B. Forsyth. *The Crystal Structure of Solids*. Edward arnold. edition, (1973).

[20] H. J. Monkhorst and J. D. Pack. *Phys. Rev. B.*, **13**:5188, (1976).

[21] G. S. Rohrer. *Structure and Bonding in Crystalline Materials*. Campridge university press. edition, (2001).

[22] P. Weiss. *J. Phys.*, **6**:661, (1907).

[23] E. C. Stoner. *Philos. Mag.*, **15**:1080, (1933).

[24] N. A. Hill. *J. Phys. Chem.*, **104**:6694, (2000).

[25] G. K. Woodgate. *Elementary Atomic Structure*. Oxford university press. edition, USA.

[26] H. Bethe. *Ann. Physick.*, **5**:133, (1929).

[27] R. S. Mulliken. *J. Chem. Phys.*, **23**:1833, (1955).

[28] E. Jahn and H. Teller. *Proc. Royal Soc. London*, **121**:220, (1936).

[29] E. Jahn and H. Teller. *Phys. Rev.*, **49**:874, (1937).

[30] C. Zener. *Phys. Rev.*, **82**:403, (1951).

[31] W. Kohn. *Electronic Structure of Matter - Wave functions and Density Functionals*. Chemistry, 1996-2000, world scientific edition, (2003).

[32] R.O. Jones O. Gunnarsson. *Rev. Mod. Phys.*, **61**:689, (1989).

[33] E.J. Baerends O.V. Gritsenko. *J. Phys. Chem. A*, **101**:5383, (1997).

[34] U. von Barth. *Physica Scripta*, **109**:9, (2004).

[35] J. Perdew et *al.* , *J. Chem. Phys.*, **123**:62201, (2005).

[36] A.J. Cohen P. Mori-SÁnchez, W. Yang. *Science*, **321**:792, (2008).

[37] P.E. BlÖchl C.J. FÖrst, J. KÄstner. *Handbook for Materials Modeling.* Chap. Electronic Structure Methods: Augmented Waves, Pseudopotentials and the Projector augmented wave method, springer edition, (2005).

[38] P.E. BlÖchl C.J. FÖrst, J. Schimpl. *Bull. Mater. Sci.*, **26**:33, (2003).

[39] P.E. LÖdin. *Phys. Rev.*, **97**:1474, (1955).

[40] A. Coleman. *Rev. Mod. Phys.*, **35**:668, (1963).

[41] K. Burke J.P. Perdew, M. Ernzerhof. *J. Chem. Phys.*, **109**:3760, (1998).

[42] J.P. Perdew K. Burke. *Int. Quant.Chem.*, **57**:309, (1996).

[43] M. Levy. *Proc. Nat'l Acad. Sci. USA*, **76**:6062, (1979).

[44] E. Lieb. *Int. J. Quant.Chem.*, **24**:243, (1983).

[45] J.P. Perdew K. Schmidt. *AIP Conf. Proc.*, **577**:1, (2001).

[46] D.M. Ceperley B. Alder. *Phys. Rev. Lett.*, **45**:566, (1980).

[47] S.K. Ma K. Brueckner. *Phys. Rev.*, **165**:18, (1968).

[48] U. von Barth L. Hedin. *J. Phys. C: Solid State Phys.*, **5**:1629, (1972).

[49] O. Gunnarsson B.I. Lundquist. *Phys. Rev. B.*, **13**:4274, (1976).

[50] J.P. Perdew. *Phys. Rev. Lett.*, **55**:1665, (1985).

[51] D.C. Langreth M. Mehl. *Phys. Rev. B.*, **28**:1809, (1983).

[52] A.D. Becke. *Phys. Rev. A.*, **38**:3098, (1988).

[53] J.P. Perdew K. Burke, M. Ernzerhof. *Phys. Rev. Lett.*, **77**:3865, (1996).

[54] E. Proynov E. Ruiz, D.R. Salahub. *Int. J. Quant.Chem.*, **56, S29**:61, (1995).

[55] T.V. Voorhis G. Scuseria. *J. Chem. Phys.*, **109**:400, (1998).

[56] A.D. Becke. *J. Chem. Phys.*, **109**:2092, (1998).

[57] J. Tao J.P. Perdew, G.E. Scuseria. *Phys. Rev. Lett.*, **91**:146401, (2003).

[58] A.D. Becke. *J. Chem. Phys.*, **98**:1372, (1993).

[59] A.D. Becke. *J. Chem. Phys.*, **98**:5648, (1993).

[60] J. Harris R.O. Jones. *J. Phys. F: Met. Phys.*, **4**:1170, (1974).

[61] D.C. Langreth J.P. Perdew. *Sol. St. Commun.*, **17**:1425, (1975).

[62] J. P. Perdew K. Burke, M. Ernzerhof. *J. Chem. Phys.*, **105**:9982, (1996).

[63] J. Heyd G. Scuseria, M. Ernzerhof. *J. Chem. Phys.*, **118**:8207, (2003).

[64] M. Marsman J. Paier A. Stroppa, G. Kresse. *J. Phys. Chem.*, **20**:64201, (2008).

[65] P. Stephens F. Devlin C. Chabalowski, M. Frisch. *J. Phys. Chem.*, **98**:11623, (1994).

[66] M. Ernzerhof G. Scuseria. *J. Chem. Phys.*, **110**:5029, (1999).

[67] C. Adamo V. Barone. *J. Chem. Phys.*, **110**:6158, (1999).

[68] V.I. Anisimov J. Zaanen, O.K. Andersen. *Phys. Rev. B.*, **44**:943, (1991).

[69] A.I. Lichtenstein V.I. Anisimov, J. Zaanen. *Phys. Rev. B.*, **52**:5467, (1995).

[70] P. Novàk J. Kunes L. Chaput, W.E. Pickett. *Phys. Stat. Sol. B.*, **243**:563, (2006).

[71] F. Tran P. Blaha K. Schwarz, P. Novàk. *Phys. Rev. B.*, **74**:155108, (2006).

[72] M. Dion H. Rydberg E. SchrÖder D.C. Langreth, B. I. Lundqvist. *Phys. Rev. Lett.*, **92**:246401, (2004).

[73] T. Thonhauser V.R. C.S. Li A. Puzder P. Hyldgaard, D. Langreth. *Phys. Rev. B.*, **76**:125112, (2007).

[74] K. Lee E.D. Murray L. Kong B.I. Lundqvist, D.C. Langreth. *Phys. Rev. B.*, **82**:81101, (2010).

[75] J.A. Pople M. Head-Gordon D.J. Fox K. Raghavachari, L.A. Curtiss. *J. Chem. Phys.*, **90**:5622, (1989).

[76] L.A. Curtiss C. Jones-G.W. Trucks K. Raghavachari, J.A. Pople. *J. Chem. Phys.*, **93**:2537, (1990).

[77] L.A. Curtiss K. Raghavachari P.C. Redfern, J.A. Pople. *J. Chem. Phys.*, **106**:1063, (1997).

[78] L.A. Curtiss P.C. Redfern K. Raghavachari, J.A. Pople. *J. Chem. Phys.*, **109**:42, (1998).

[79] A.D. Becke. *J. Chem. Phys.*, **96**:2155, (1992).

[80] A.D. Becke. *J. Chem. Phys.*, **97**:9173, (1992).

[81] A.D. Becke. *J. Chem. Phys.*, **104**:1040, (1996).

[82] A.D. Becke. *J. Chem. Phys.*, **107**:8554, (1997).

[83] M. Marsman, G. Kresse, J. Paier, and R. Hirschl. *J. Chem. Phys.*, **122**:234102, (2005).

[84] J. Paier et al. *J. Chem. Phys.*, **124**:154709, (2006).

[85] J. Paier et al. *J. Chem. Phys.*, **125**:249901, (2006).

[86] P.E. BlÖchl. *Phys. Rev. B*, **50**:17953, (1994).

[87] K. Schwarz et al. *Computer Physics Communications*, **71**:147, (2002).

[88] F. Wohler. *Ann. Chem. Phys.*, **29**:43, (1823).

[89] L.F. Mattheiss. *Phys. Rev.*, **6**:4718, (1972).

[90] E. O. Wollan and W. C. Koehler. *Phys. Rev.*, **100**:545, (1955).

[91] F. L. Battye, H. Höchst, and A. Goldman. *Solid State Commun.*, **19**:269, (1976).

[92] M. Cardona. *Phys. Rev.*, **140**:A651, (1965).

[93] P. A. Lightsey. *Phys. Rev.*, **8**:3586, (1973).

[94] V. E. Henrich, G. Dresselhaus, and H. J. Zeiger. *Bull. Am. phys. Soc.*, **22**:364, (1977).

[95] E. A. Kraut, T. Wolfram, and W. E. Hall. *Phys. Rev. B*, **6**:1499, (1972).

[96] T. Wolfram, R. A. Hurst, and F. J. Morin. *Phys. Rev. B*, **15**:1151, (1977).

[97] T. Wolfram, E. A. Kraut, and F. J. Morin. *Phys. Rev. B*, **7**:1677, (1973).

[98] J. F. Schooley, W. R. Hosler, E. Ambler, J. H. Becker, M. L. Cohen, and O. S. Koonce. *Phys. Rev. Lett*, **14**:305, (1965).

[99] J. Hubbard. *Proc. Roy. Soc. (London) A*, **276**:238, (1963).

[100] J. B. Goodenough and P. M. Roccah. *J. Appl. Phys*, **36**:1031, (1965).

[101] A collection of papers on the applications may be found in the. *IEEE Trans. Sonics Ultrason*, **19**:2, (1972).

[102] L. A. Pedersen and W. E. Libby. *Science*, **176**:1355, (1972).

[103] D. B. Meadowcraft. *Nature*, **226**:847, (1970).

[104] T. C. Lim, E. A. Kraut, and R. B. Thompson. *Appl. Phys. Lett*, **20**:127, (1972).

[105] Z. J. Kiss. *Photochromics. Phys. Today*, **23**:42, (1970).

[106] R. J. H. Voorhoeve, D. W. Johnson, Jr., J.P. Remeika, and P. K. Gallagher. *Science*, **195**:827, (1977).

[107] R. B.Woodward and R. Hoffman. *The conservation of orbital symmetry.* Weinheim/bergstrasse, verlag-chemic edition, (1970).

[108] T. Wolfram and F. J. Morin. *Appl. Phys.*, **8**:125, (1970).

[109] D. A. Shirley. *J. Vac. Sci. Technol.*, **12**:280, (1975).

[110] A. C. C. Tseung and H. L. Beven. *J. Electroanal. Chem. Interfacial Electrochem.*, **45**:429, (1973).

[111] J. G. Mavrodies, D. I. Tchernev, J. A. Kafalas, and D. F. Kolesar. *Mater. Res. Bull.*, **10**:1023, (1975).

[112] M. S. Wrighton, A. B. Ellis, P. T. Wolczanski, D. L. Morse, H. B. Abrahamson, and D. S. Ginley. *J. Amer. Chem. Soc.*, **98**:2774, (1976).

[113] R. D. Nasby and R. K. Quinn. *Mater. Res. Bull.*, **11**:985, (1976).

[114] A. Fujishima and K. Honda. *Nature*, **238**:37, (1972).

[115] C. Kittel. *Introduction to Solid State Physics*. John Wiley Sons, inc. edition, (1996).

[116] F. Gebhard. *The Mott Metal-Insulator Transition*. Springer edition, (1997).

[117] J. H. de Boer and E. J. W. Verwey. *Proc. Phys. Soc.*, **49**:59, (1937).

[118] H. Kajueter, G. Kotliar, and G. Moeller. *Phys. Rev. B*, **53**:16214, (1996).

[119] W. S. Baer. *Phys. Rev.*, **144**:734, (1966).

[120] D. B. McWhan, T. M. Rice, and P. H. Schmidt. *Phys. Rev.*, **177**:1063, (1969).

[121] M. Imada, A. Fujimori, and Y. Tokura. *Rev. Mod. Phys.*, **70**:1039, (1998).

[122] N. Mott. *Proc. R. Soc. London, Ser*, **A 382**:1, (1982).

[123] W. Shockley, J. Bardeen, and W. H. Brattain. *Science*, **108**:678, (1948).

[124] G. E. Moore. *Electronics*, **38**:114, (1965).

[125] J. G. Bednorz and K. A. Müller. *Z. Phys. B: Condens. Matter*, **64**:189, (1986).

[126] A. Schilling, M. Cantoni, J. Guo, and H. Ott. *Nature*, **363**:56, (1993).

[127] T. Murakami and A. Yamaji. *Am. Ceram. Soc. Bull.*, **55**:572, (1976).

[128] M. Fujimoto and W. D. Kingery. *J. Am. Ceram. Soc.*, **68**:169, (1985).

[129] E. N. Bunting, G. R. Shelton, A. S. Creamer, and B. Jaffe. *J. Research NBS*, **47**:15, (1951).

[130] R. von Helmolt, J. Wecker, B. Holzapfel, L. Schultz, and K. Samwer. *Phys. Rev. Lett.*, **71**:2331, (1993).

[131] T. W. Hickmott. *J. Appl. Phys.*, **33**:2669, (1962).

[132] J. G. Simmons and R. R. Verderber. *Proc. R. Soc. London, Ser.*, **A 301**:77, (1967).

[133] C. Gerber C. Rossel A. Beck, J. G. Bednorz and D. Widmer. *Appl. Phys. Lett.*, **77**:139, (2000).

[134] G. I. Meijer. *Science*, **319**:1625, (2008).

[135] S. S. P. Parkin, C. Kaiser, A. Panchula, P. M. Rice, B. Hughes, M. Samant, and S.-H. Yang. *Nature Mater.*, **3**:862, (2004).

[136] M. Wuttig and N. Yamada. *Nature Mater.*, **6**:824, (2007).

[137] P. Blaha, K. Schwarz, G. K. H. Madsen, D. Kvasnicka, and J. Luitz. *WIEN2K, An Augmented Plane Wave Plus Local Orbitals Program for Calculating Crystal Properties*. Vienna University of Technology, Vienna, (2001).

[138] E. Sjöstedt, L. Nordstrom, and D. J. Singh. *Solid State Commun.*, **114**:15, (2000).

[139] J. P. Perdew and Y. Wang. *Phys. Rev. B.*, **45**:13244, (1992).

[140] F. D. Murnaghan. *Proc. Natl. Acad. Sci. USA*, **30**:5390, (1944).

[141] P. E. Blöchl, O. Jepsen, and O. K. Anderson. *Phys. Rev. B.*, **49**:16223, (1994).

[142] Y. A. Abramov, V. G. Tsirelson, V. E. Zavodnik, S. A. Ivanov, and I. D. Brown. *Acta Crystallogr., Sect. B: Struct. Sci.*, **51**:942, (1995).

[143] H. Unoki and T. Sakudo. *J. Phys. Soc. Jap.*, **23**:546, (1967).

[144] K. A. Müller and H. Burkard. *Phys. Rev. B.*, **19**:3593, (1979).

[145] J. F. Schooley, W. R. Hosler, and M. L. Cohen. *Phys. Rev. Lett.*, **12**:474, (1964).

[146] P. E. Blöchl and J. H. Stathis. *Phys. Rev. Lett.*, **83**:372, (1999).

[147] J. W. McPherson and H. C. Mogul. *J. Appl. Phys.*, **84**:1513, (1998).

[148] L. X. He and D. Vanderbilt. *Phys. Rev. B.*, **68**:134103, (2003).

[149] J. Robertson. *Reports on Progress in Physics*, **69**:327, (2006).

[150] A. S. Foster, F. L. Gejo, A. L. Shluger, and R. M. Nieminen. *Phys. Rev. B.*, **65**:174117, (2002).

[151] R. Merkle and J. Maier. *Angewandte Chemie-International Edition*, **47**:3874, (2008).

[152] P. J. Gellings and H. J. M. Bouwmeester. *Catalysis Today*, **58**:1, (2000).

[153] M. A. Pena and J. L. G. Fierro. *Chem. Rev.*, **101**:1981, (2001).

[154] N. Izu, W. Shin, N. Murayarna, and S. Kanzaki. *Sensors and Actuators B-Chemical*, **87**:95, (2002).

[155] G. I. Panov, K. A. Dubkov, and E. V. Starokon. *Catalysis Today*, **117**:148, (2006).

[156] N. Bickel, G. Schmidt, K. Heinz, and K. Müller. *Phys. Rev. Lett.*, **62**:2009, (1989).

[157] T. Hikita, T. Hanada, M. Kudo, and M. Kawai. *Surface Science*, **287**:377, (1993).

[158] U. Balachandran and N. G. Eror. *J. Mat. Sci.*, **17**:2133, (1982).

[159] S. Witek, D. M. Smyth, and H. Pickup. *J. Am. Ceram. Soc.*, **67**:372, (1984).

[160] I. V. Kondakova, R. O. Kuzian, L. Raymond, R. Hayn, and V. V. Lagut. *Phys. Rev. B.*, **79**:134117, (2009).

[161] R. Wahl, D. Vogtenhuber, and G. Kresse. *Phys. Rev. B.*, **78**:104116, (2008).

[162] C. Lasota, C. Z. Wang, R. Yu, and H. Krakauer. *Ferroelectrics*, **194**:109, (1997).

[163] R. D. King-Smith and D. Vanderbilt. *Phys. Rev. B.*, **49**:5828, (1994).

[164] *Ferroelectrics and Related Substances.* New Series, Springer-Verlag, Berlin.

[165] V. E. Alexandrov, E. A. Kotomin, J. Maier, and R. A. Evarestov. *Eur. Phys. J. B.*, **72**:53, (2009).

[166] Y. F. Zhukovskii et al. *Solid State Commun.*, (2009).

[167] T. Mitsui and S. Nouma. *LBIII/16a-Numerical Data and Functional Relation Relation in Science and Technology: Crystal and Solid State Physics*. Landolt-Börnstein, springer, berlin edition, (1982).

[168] W. Luo, W. Duan, S. G. Louie, and M. L. Cohen. *Phys. Rev. B.*, **70**:214109, (2004).

[169] D. Ricci, G. Bano, G. Pacchioni, and F. Illas. *Phys. Rev. B.*, **68**:224105, (2003).

[170] J. P. Buban, H. Iddir, and S. Ogut. *Phys. Rev. B.*, **69**:180102, (2004).

[171] S.-E. Park and T. R. Shrout. *J. Appl. Phys.*, **82**:1804, (1997).

[172] R. Guo, L. E. Cross, S.-E. Park, B. Noheda, D. E. Cox, and G. Shirane. *Phys. Rev. Lett.*, **84**:5423, (2000).

[173] Z. Kutnjak, J. Petzelt, and R. Blinc. *Nature*, **441**:956, (2006).

[174] H. Fu and R. E. Cohen. *Nature*, **403**:281, (2000).

[175] L. Bellaiche, A. Garcia, and D. Vanderbilt. *Phys. Rev. B*, **64**:060103, (2001).

[176] J. F. Scott. *Nat. Mat.*, **6**:256, (2007).

[177] S. Picozzi, K. Yamauchi, I. Sergienho, B. Sanyal, and E. Dagatoo. *J. Phys. Condens. Matter*, **20**:434208, (2008).

[178] A. A. Belik, M. Azuma, T. Saito, Y. Shimakawa, and M. Takano. *Chem. Mater.*, **17**:269, (2005).

[179] J. B. Neaton, C. Ederer, U. V. Waghmare, N. A. Spaldin, , and K. M. Rabe. *Phys. Rev. B*, **71**:014113, (2005).

[180] R. J. Nelmes and 721 (1985 W. F. Kuhs, Solid State Commun. 54. *Solid State Commun*, **54**:721, (1985).

[181] Y. Tokura, Y. Okimoto, S. Yamaguchi, H. Taniguchi, T. Kimura, and H. Takagi. *Phys. Rev. B*, **58**:R1699, (1998).

[182] P. G. Radaelli and S.-W. Cheong. *Phys. Rev. B*, **66**:094408, (2002).

[183] N. H. Duc, D. T. K. Anh, and P. E. Brommer. *Physica B: Condensed Matter*, **319**:1, (2002).

[184] O. Tegus, E. Bruck, K. H. J. Buschow, and F. R. de Boer. *Nature*, **415**:150, (2002).

[185] R. Kainuma, Y. Imano, W. Ito, Y. Sutou, H. Morito, S. Okamoto, O.Kitakami, K. Oikawa, A. Fujita, T. Kanomata, and K. Ishida. *Nature*, **439**:957, (2006).

[186] D. Kan, L. Palova, V. Anbusathaiah, C. J. Cheng, S. Fujino, V. Nagarajan, K. M. Rabe, and I. Takeuchi. *Adv. Funct. Mater.*, **20**:1108, (2010).

[187] Oswaldo Diéguez O. E. González-Vázquez, Jacek C. Wojdel and Jorge Í niguez. *Phys. Rev. B*, **85**:064119, (2012).

[188] A. J. Moulson and J. M. Herbert. *Electroceramics Materials. Propertis. Applications*. London, England, Chapman and Hall, (1990).

[189] A. Navrotsky. *Chem. Mater.*, **10**:2787, (1998).

[190] R. H. Mitchell. *Perovskites: Modern and Ancient*. Almaz Press, Ont., Canada, (2002).

[191] I. Sterianou. *Bismuth-Based Perovskites for High Temperature Piezoelectric Applications*. Engineering Materials. Sheffield, The University of Sheffield, (2008).

[192] V. M. Goldschmidt. *Geochemische Verteilungsgesetze Der Elemente (Geochemical Laws of Distribution of the Elements)*. Skrifter utg. av det Norske Videnskaps-akademi i Oslo. I. Mat.-naturv. klasse, (1925).

[193] B. Jaffe, W. R. J. Cook, and H. Jaffe. *Piezoelectric Ceramics*. London, Academic Press, (1971).

[194] C. A. Randall, D. J. Barber, R. W. Whatmore, and P. Groves. *Journal of Material Science*, **21**:4456, (1986).

[195] H. Zheng, H. Bagshaw, I. M. Reaney, R. Uble, and J. Yarwood. *Journal of Applied Physics*, **94**:2948, (2003).

[196] R. D. Shannon and C. T. Prewitt. *Acta Crystallographica*, **B25**:925, (1969).

[197] H. D. Megaw. *The Proceedings of the Physical Society*, **58**:132, (1946).

[198] H. D. Megaw. *Crystal Structures: A Working Approach*. London, W. B. Saunders Company, (1973).

[199] P. M. Woodward. *Acta Crystallographica*, **BS3**:44, (1997).

[200] B. Noheda, J. A. Gonzalo, L. E. Cross, R. Guo, S.-E. Park, D. E. Cox, and G. Shirane. *Phys. Rev. B*, **61**:8687, (2000).

[201] Y. Uratani, T. Shishidou, F. Ishii, and T. Oguchi. *Jpn. J. Appl. Phys.*, **44**:7130, (2005).

[202] M-Q. Cai, J-C. Liu, G-W. Yang, Y-L. Cao, X. Tan, X-Y. Chen, Y-G. Wang, L-L. Wang, and W-Y. Hu. *J. Chem. Phys.*, **126**:154708, (2007).

[203] R. Tilley. *Understanding solids*. Wiley. 593, (2004).

[204] S. V. Vonsovskii. *Magnetism*. John Wiley, (1974).

[205] Ben G. Streetman. *Solid State Electronic Devices (6th ed.)*. Prentice-Hall, Inc., (2006).

[206] A. Bussmann-Holder and H. Böttner. *Nature*, **360**:541, (1992).

[207] R. E. Cohen. *Nature*, **358**:136, (1992).

[208] N. A. Hill, P. Bättig, and C. Daul. *J. Phys. Chem. B*, **106**:3383, (2002).

[209] N. A. Hill and K. M. Rabe. *Phys. Rev. B*, **59**:8759, (1999).

[210] R. Ramesh and N. A. Spaldin. *Nature Materials*, **6**:21, (2007).

[211] M. Fiebig. *J. Phys. D: Appl. Phys.*, **38**:R123, (2005).

[212] N. A. Hill. *Annual Review of Materials Research*, **32**:1, (2002).

[213] L. W. Martin, S. P. Crane, Y-H. Chu, M. B. Holcomb, M. Gajek, M. Huijben, C-H. Yang, N. Balke, and R. Ramesh. *J. Phys.: Condens. Matter*, **20**:434220, (2008).

[214] N. A. Spaldin. *Magnetic Materials: Fundamentals and Device Applications*. Cambridge University Press, Cambridge, UK, (2003).

[215] G. Thornton, B. C. Tofield, and A. W. Hewat. *Journal of Solid State Chemistry*, **61**:301, (1986).

[216] G. Maris, Y. Ren, V. Volotchaev, C. Zobel, T. Lorenz, and T. T. M. Palstra. *Phys. Rev. B*, **67**:224423, (2003).

[217] O. Haas, R. P. W. J. Struis, and J. M. McBreen. *J. Solid State Chem.*, **177**:1000, (2004).

[218] S. Yamaguchi, Y. Okimoto, and Y. Tokura. *Phys. Rev. B*, **55**:R8666, (1997).

[219] C. Zobel, M. Kriener, D. Bruns, J. Baier, M. Gruninger, T. Lorenz, P. Reutler, and A. Revcolevschi. *Phys. Rev. B*, **66**:020402, (2002).

[220] P. M. Raccah and J. B. Goodenou. *Phys. Rev.*, **155**:932, (1967).

[221] V. G. Bhide, D. S. Rajoria, G. Rama Rao, and C. N. R. Rao. *Phys. Rev. B*, **6**:1021, (1972).

[222] S. Yamaguchi, Y. Okimoto, H. Taniguchi, and Y. Tokura. *Phys. Rev. B*, **53**:R2926, (1996).

[223] M. A. Korotin, S. Yu. Ezhov, I. V. Solovyev, V. I. Anisimov, D. I. Khomskii, and G. A. Sawatzky. *Phys. Rev. B*, **54**:5309, (1996).

[224] N. Solovyev, N. Hamada, and K. Terakura. *Phys. Rev. B*, **53**:7158, (1996).

[225] M. Zhuang, W. Zhang, C. Hu, and N. Ming. *Phys. Rev. B*, **57**:10705, (1998).

[226] P. Ravindran, P. A. Korzhavyi, H. Fjellvag, and A. Kjekshus. *Phys. Rev. B*, **60**:16423, (1999).

[227] D. D. Sarma, N. Shanti, and P. Mahadevan. *Phys. Rev. B*, **54**:1622, (1996).

[228] H. Takahashi, F. Munakata, and M. Yamanaka. *Phys. Rev. B*, **57**:15211, (1998).

[229] M. R. Ibarra, R. Mahendiran, C. Marquina, B. García-Landa, and J. Blasco. *Phys. Rev. B*, **57**:R3217, (1998).

[230] K. Tao, J. Zhou, Q. Sun, Q. Wang, V. S. Stepanyuk, and P. Jena. *Phys. Rev. B*, **89**:085103, (2014).

[231] T. Sudayama, Y. Wakisaka, K. Oka, M. Azuma, Y. Shimakawa, H. Wadati, G. A. Sawatzky, D. G. Hawthorn, T. Z. Regier, and T. Mizokawa. *Canadian Light Source*, page 128, (2009).

[232] L. Siurakshina, B. Paulus, V. Yushankhai, and E. Sivachenko. *Eur. Phys. J. B*, **74**:53, (2010).

[233] K. Schwarz and P. Mohn. *J. Phys. F*, **14**:L129, (1984).

[234] *International Tables for X-Ray Crystallography*. The Kynoch Press, Birmingham UK, (1964).

[235] S. Mukhopadhyay, M. W. Finnis, and N. M. Harrison. *Phys. Rev. B*, **87**:125132, (2013).

[236] H. Hsu, K. Umemoto, M. Cococcioni, and R. Wentzcovitch. *Phys. Rev. B*, **79**:125124, (2009).

[237] I. A. Nekrasov, S. V. Streltsov, M. A. Korotin, and V. I. Anisimov. *Phys. Rev. B*, **68**:235113, (2003).

[238] T. Sudayama, Y. Wakisaka, T. Mizokawa, H. Wadati, G. A. Sawatzky, D. G. Hawthorn, T. Z. Regier, K. Oka, M. Azuma, and Y. Shimakawa. *Phys. Rev. B*, **83**:235105, (2011).

[239] J. A. McLeod, Z. V. Pchelkina, L. D. Finkelstein, E. Z. Kurmaev, R. G. Wilks, A. Moewes, I. V. Solovyev, A. A. Belik, and E. Takayama-Muromachi. *Phys. Rev. B*, **81**:144103, (2010).

[240] M. Abbate, J. C. Fuggle, A. Fujimori, L. H. Tjeng, C. T. Chen, R. Potze, G. A. Sawatzky, H. Eisaki, and S. Uchida. *Phys. Rev. B*, **47**:16124, (1993).

[241] S. Yamaguchi, Y. Okimoto, and Y. Tokura. *Phys. Rev. B*, **54**:R11022, (1996).

[242] K. G. Yang, Y. L. Zhang, S. H. Yang, and B. Wang. *J. Appl. Phys.*, **107**:124109, (2010).

[243] H. C. Aspinall. *Chemistry of the f-block Elements*. Gordon and Breach Science, Amsterdam, (2001).

[244] V. R. Palkar, D. C. Kundaliya, and S. K Malik. *J. Appl. Phys.*, **93**:7834, (2003).

[245] N. J. Ramer and A. M. Rappe. *Phys. Rev. B*, **62**:R743, (2000).

[246] T. Jia, H. Wu, G. Zhang, X. Zhang, Y. Guo, Z. Zeng, and H-Q. Lin. *Phys. Rev. B*, **83**:174433, (2011).

[247] B. Raveau, A. Maignan, and V. Caignaert. *Journal of Solid State Chemistry*, **117**:424, (1995).

[248] A. P. Ramirez. *Journal of Physics: Condensed Matter*, **9**:8171, (1997).

[249] K. A. Müller and J. G. Bednorz. *Science*, **237**:1133, (1987).

[250] F. S. Galasso. *Structure, Properties and Preparation of Perovskite-type Compounds*. London: Pergamon Press, (1969).

[251] T. He, Q. Huang, A. P. Ramirez, Y. Wang, K. A. Regan, N. Rogado, M. A. Hayward, M. K. Haas, J. S. Slusky, K. Inumara, H. W. Zandbergen, N. P. Ong, and R. J. Cava. *Nature (London)*, **411**:54, (2001).

[252] D. J. Singh and I. I. Mazin. *Phys. Rev. B*, **64**:140507(R), (2001).

[253] S. Dugdale and T. Jarlborg. *Phys. Rev. B*, **64**:100508(R), (2001).

[254] H. Rosner, R. Weht, M. D. Johannes, W. Pickett, and E. Tosatti. *Phys. Rev. Lett.*, **88**:027001, (2001).

[255] Y. Sun, X.-Q. Chen, S. Yunoki, D. Li, and Y. Li. *Phys. Rev. Lett.*, **105**:216406, (2010).

[256] H. Horiuchi, T. Shishido, A. Saitow, M. Tanaka, and S. Hosoya. *Mater. Sci. Eng. A*, **312**:237, (2001).

[257] S. Horiike, T. Shishido, S. Yamaguchi, and Y. Yamaguchi. *J. Phys. Soc. Jpn.*, **70**:244, (2001).

[258] T. Shishido, K. Kudou, S. Okada, J. Ye, A. Yoshikawa, T. Sasaki, M. Oku, H. Horiuchi, I. Higashi, S. Kohiki, Y. Kawazoe, and K. Nakajima. *Jpn. J. Appl. Phys.*, **40**:6037, (2001).

[259] T. Shishido, J. Ye, S. Okada, K. Kudou, M. Oku, K. Obara, T. Sugawara, A. Yoshikawa, Y. Ishizawa, M. Ogawa, K. Iizumi, I. Higashi, T. Amano, S. Kohiki, Y. Kawazoe, and K. Nakajima. *Jpn. J. Appl. Phys.*, **41**:3031, (2002).

[260] P. Rogl and L. Delong. *J. Less-Common Met.*, **91**:97, (1983).

[261] T. Shishido, J. Ye, S. Okada, K. Kudou, K. Iizumi, M. Oku, Y. Ishizawa, T. Amano, S. Kohiki, Y. Kawazoe, and K. Nakajima. *J. Alloys. Compd.*, **354**:198, (2003).

[262] R. Sahara, T. Shishido, and A. Nomura. *Phys. Rev. B*, **76**:024105, (2007).

[263] R. Sahara, T. Shishido, A. Nomura, K. Kudou, S. Okada, V. Kumar, Y. Nakajima, and K. Kawazoe. *Comput. Mater. Sci.*, **36**:12, (2006).

[264] V. I. Anisimov, I. V. Solovyev, M. A. Korotin, M. T. Czyzyk, and G. A. Sawatzky. *Phys. Rev. B*, **48**:16929, (1993).

[265] D. A. Papaconstantopoulos and W. E. Pickett. *Phys. Rev. B*, **45**:4008, (1992).

[266] V.I. Anisimov and O. Gunnarsson. *Phys. Rev. B.*, **43**:10, (1991).

Declaration

I herewith declare that I have produced this research work without the prohibited assistance and without making use of aids other than those specified; notions taken over directly or indirectly from other sources have been identified as such. This thesis has not previously been presented in identical or similar form to any other Algerian or foreign examination board.

The thesis work was conducted from January 2010 to June 2015 under the supervision of Professor Ali ZAOUI at University of Sidi Bel-Abbès.

Sidi Bel-Abbès,

Mostefa DJERMOUNI
June 2015